SYNTHETIC APERTURE RADAR FOR IMAGING THE BASAL CONDITIONS OF THE POLAR ICE SHEETS

by

John Paden

B.S.Co.E., University of Kansas, 1999

M.S.E.E. (With Honors), University of Kansas, 2003

Submitted to the Department of Electrical Engineering and Computer Science and the Faculty of the Graduate School of the University of Kansas in partial fulfillment of the requirements for the degree of Doctor of Philosophy.

Dissertation Committee:

_____
Christopher Allen: Chairperson

_____
Sivaprasad Gogineni

_____
Kenneth Demarest

_____
James Stiles

_____
David Braaten

Date of Defense: Aug 30, 2006

The Dissertation Committee for John D. Paden certifies that this is the approved version of the following dissertation:

Synthetic Aperture Radar for Imaging the Basal Conditions of the Polar Ice Sheets

Dissertation Committee:

_____
Christopher Allen: Chairperson

_____
Sivaprasad Gogineni

_____
Kenneth Demarest

_____
James Stiles

_____
David Braaten

Date Approved _____

To Erin, Elijah, and Annie Paden

ACKNOWLEDGEMENTS

First of all, I want to thank my wife, Erin, for her love and support especially before field seasons and during the writing of my M. S. and Ph. D. theses. My family in general has provided unwavering support and encouragement and this journey would not have been nearly as enjoyable without them. My grandparents deserve special thanks since they provided me with a home through most of my college career and my grandmother, having also earned her PhD, gave me helpful advice and comical relief when needed from her own experiences.

Dr. Allen and Dr. Stiles are responsible for my original interest in radar development and I appreciate the many (many) long discussions we have had and the insights they provided. I also thank Dr. Allen for being my advisor and counseling me on a number of issues not always directly related to work (i.e. for putting up with me). Without, Dr. Gogineni's support I would not have been able to pursue this area of research and for that I am extremely grateful – the scientific and social value of the ice radar work done here has been and will continue to be an inspiration for me. Also I want to acknowledge the enormous help and guidance he provided me while writing my NASA fellowship proposal, publishing my first journal article, and securing my first job. Dr. Demarest and Dr. Petr also deserve my thanks for teaching some of the most exciting and challenging classes that I took during my electrical engineering career.

I want to thank Torry and Pannir for their excellent friendship and the inspiration they have been both at work and in my life. They have been very patient with me and also worked long hours helping me with my graduate work.

I also thank Thorbjorn Axelsson and Wesley Mason for providing excellent computer service support, especially while processing the large amounts of data collected. Many other people have made life very enjoyable here at the lab and in the field and the following is a truncated list: Dr. Braaten who served as team leader for both of the field experiments that I took part in, David Dunson who did the layout work and simulations for the receiver and transmitter board of the SAR, my officemate Cameron Lewis and

Tszping “Charley” Chan who helped with some of the original processing, Kelly Mason and Keron Hopkins who just helped with things in general and were always happy to do so, and Sahana Raghunandan and Adam Lohoefener for doing an amazing job of putting the MCRDS system together that I was fortunate enough to be a part of.

Finally, I am indebted to all the members of my committee for their guidance in general and for taking the time to help me with my dissertation.

TABLE OF CONTENTS

LIST OF FIGURES

LIST OF TABLES

ABSTRACT

The far-reaching impacts of future global climate change have driven both the international science community and intergovernmental cooperation to look for predictive capability of both climate-change and its impacts. One area of particular interest is sea level rise and its relationship with the massive polar ice sheets of Greenland and Antarctica. In the last several years, a number of alarming changes have been seen along the outlet glaciers and melt regions of Greenland and the outlet glaciers of the Antarctica Peninsula. The concern is that the steady-state models used in the global climate models to not include important ice dynamics that are now known to occur. Glaciologists in the last few decades have begun grappling with the problem of modeling these dynamics, including basal melting and sliding, till deformation, and ice buttressing. However, much of the work is restricted by the very limited knowledge of the basal conditions.

There are several methods that can be used to observe the basal conditions of an ice sheet. Brute-force methods that involve drilling a borehole to the bottom of the ice sheet are infeasible for wide-area coverage because the resources and time consumed for each borehole are tremendous. Even seismic experiments, which can provide better coverage, require extensive preparation and can only be conducted from the ground. Radar, and specifically side-looking synthetic aperture radar (SAR), on the other hand provides a flexible remote sensing technique that can work with very little field preparation (in comparison to seismology and drilling) and can also be installed on an airborne or space-borne platform. By producing a radar capable of producing SAR images of basal backscattering, we can bring to bear the vast literature base and toolsets developed for traditional SAR applications. To this end, the specification, design, development, fielding, and data processing of a multi-purpose VHF radar for radioglaciological work is described in this work. The purposes of the radar and subsequent data processing are to produce a map of backscatter from the basal interface, map ice thickness, and track internal layers.

The approach taken here starts with the development of an electromagnetic propagation model. This model is used to derive the radar's system specifications such as band of operation, loop sensitivity and dynamic range. It is also used in by the imaging routines for phase-history reconstruction. The system architecture chosen is a ground-based side-looking SAR operating from 120-300 MHz with VV polarization. Ground-based operation is ideal for testing purposes and very few system modifications are needed to convert to an airborne platform. Data conditioning of radar and trajectory data for the imaging algorithms is then detailed. Finally, results from both f-k migration and time-domain correlation imagers are presented and analyzed for a 6.5 km by 25 km area near Summit Camp, Greenland (72.5667° N, 38.4833° W, ~3200 m). This work represents the first successful application of side-looking SAR to the thick ice found in the ice sheets.

Chapter 1: Introduction and Literature Review

1.1 Motivation

The mean sea level, which appears to have been steady for the last 3-4000 years, has been rising between 1 to 2.6 mm per year over the past century with 1.5 mm per year being the most accepted value [1], [2], [3]. This rise in sea level has had a number of costs: abandoned islands, lost coastline and agricultural land, costly replacement of sand to eroded beachfronts, loss of marshland habitats, increased vulnerability to severe storms, and threatened aquifers [1], [5]. Since nearly 100 million people live within 1 meter of the current mean sea level [1], [2] and 37% of the world's population lives in coastal regions [1] (defined as being within 100 km of the coast), understanding possible contributions to sea level rise is of considerable practical importance. The rise in sea level has also been coupled with an ever-increasing population in the coastal regions. If these trends continue, the social and economic consequences will be severe, especially to developing countries with little resources [1].

While the precise causes of the rise in sea level are still in debate, there are three causes that seem most likely. The first is the thermal expansion of the ocean due to the concurrent rise in the mean tropospheric temperature of 0.6 ±0.2° C since the nineteenth century [4]. The second is the melting of mid-latitude temperate glaciers. The third, and most controversial because of the lack of a complete set of data, is the melting of the Antarctica and Greenland ice sheets [2]. To determine the contribution of melted ice to sea level rise, the mass balance of the ice sheet must be measured. The mass balance is the flux in ice mass. In other words, when the mass balance is positive, the net mass of the ice sheet is increasing and when the mass balance is negative, ice is being lost. If the mass balance of an ice sheet is known, its contribution to global sea level can be determined. Several methods for determining mass balance and a compilation of mass balance measurements for the polar ice sheets are given in [6]. Regardless of whether or

not the mean sea level has been affected significantly in the last century by melting ice sheets, it is certain that global climate changes could induce such behavior (e.g. mean sea level has risen as much as 120 meters since the last glacial maximum 21,000 years ago) [1], [2], [6], [7]. While the IPCC 2001 predictions for near-future ice sheet contributions to sea level rise are fairly small, the models used do not include many processes that could lead to rapid disintegration of significant portions of the ice sheet [8].

The Greenland and Antarctic ice sheets act as large reservoirs of water, holding nearly 80% of the fresh water in the world [1], [9], [10]. This water mass is equivalent to 2% of the ocean water mass [1], [11] and complete melting of the polar ice sheets would raise the global sea level by 70 meters [9], [10], [12]. A small decrease in the volume of the ice sheets (1.5%) would increase the global sea level by 1 meter. Since the polar ice sheets have the capacity to release this water under certain climatic conditions, an understanding of the process is worth pursuing. Aside from sea level issues and scientific curiosity, understanding the dynamics of ice sheets helps provide a general understanding of how the cryosphere affects and is affected by the climate of the earth system [9], [12].

Because of the ice sheets' potentially significant role, measurements of the ice sheet are made to determine their contribution to sea level rise and the global climate. Some measurements are used to directly calculate the mass balance (e.g. ice sheet surface elevation). Measurements of ice sheet properties are also made which are fed into ice sheet models which indirectly compute mass balance. Ice sheet models are important because even with a complete dataset of the current mass balance, the time over which measurements are taken is small compared to the response times of the ice sheet dynamics. The models provide the ability to decipher between short and long-term trends and identify feedback mechanisms. The models can thereby *predict future mass balance changes*.

There are several primary forcing functions that act upon the ice sheets. These are accumulation and ablation from the ice sheet surface, melting and calving along the extremity of the ice sheet, gravity acting on the ice sheet that depends on the mass of the ice and its general structure, and finally basal conditions at the glacial sole [12]. Significant effort has been put into the remote sensing of accumulation rates, surface

topography and velocities, ice thickness, and internal layering. While more complete datasets are needed, the ability to collect these parameters via remote sensing has been confirmed [13], [14], [15], [16], [17]. On the other hand, there exists no radio-glaciological technology that is able to unambiguously image bed roughness and dielectric and determine whether the bed is wet or frozen. Efforts have been made to use bedrock reflection strength as a proxy of dielectric contrast at the base [18], [19], [20], [21], [22], [23]. The bedrock echo shape [24] and the correlation of the bedrock echo [25], [26] have been used to infer roughness properties. Recently, Peters et al. combined both bedrock reflection strength and scattering characteristics to classify bed types in the Siple Coast Region in Antarctica with a monostatic nadir-looking radar [27]. The primary problem with these previous systems is that there are numerous bed and ice conditions that give similar nadir echo returns, meaning that estimates of basal conditions are ambiguous.

Ice sheets exhibit plastic flow properties when enough stress is applied. Essentially, when enough ice mass is accumulated in one area, the force of gravity acting on the ice tends to deform or flatten it. This plastic deformation tends to be slow and the majority of each ice sheet moves under this flow regime (certain fast-moving outlet glaciers, such as the Byrd glacier in Antarctica, are exceptions) [12]. On the other hand, ice streams are fast moving glaciers that are thought to move primarily through sliding[1] rather than deformation [12] (e.g. Ross ice streams in West Antarctica [28], [29]). Two mechanisms are proposed in the literature. The first is that the glacial sole is lubricated with water, which effectively lowers the basal resistance (friction) to the point that the ice can slide across the bottom [30], [31]. The average basal resistance acts with lateral drag and gradients in longitudinal stress to counteract the driving stress of gravity. Ice stream flow in this case is distinguished from plastic flow by the varying apportionments between these terms. The other proposed mechanism is a thick till layer which deforms beneath the ice sheet [32], [33]. The yield stress[2] in water-saturated till with adequate water pressure is low compared to ice. This allows the ice to move through deformation of the till alone. These two mechanisms are not necessarily mutually exclusive [34].

[1] Here sliding is used loosely to refer to motion that is not due to deformation of the ice.
[2] Yield stress is the minimum force required to cause plastic deformation.

This work is specifically aimed at assisting in the determination of the origin and migration of ice streams. Since the ice streams drain the majority (e.g. 90% in Antarctica) of the inland ice sheets [35], their understanding is crucial to understanding past mass balance changes and thereby predicting future mass balance changes. Through satellite SAR images of the glacial surface, it was found that ice streams reach hundreds of kilometers into the inland ice sheets and are laterally bounded by slow moving ice [36], [37]. As mentioned above, the primary difference between the two flow regimes relies on an understanding of the basal conditions. Knowledge of the morphology or 'roughness' of the bed [38] the distribution of subglacial water [39], the bedrock lithology [40], and the amount of rock debris and silt in the basal ice are needed to determine the basal boundary condition [41].

The science models require wide-area coverage and the ability to resolve these geophysical characteristics to within 500 to 1000 m depending on whether or not the measurement is in a transition region [41]. To properly classify the basal conditions in a region, fine resolution on the order of 10 to 100 m is required [43]. Additionally, the large scale ice flow model (also called outer flow) requires coarse knowledge of the bottom topography [44] and location of internal layers can be used to help constrain flow models [45], [46]. Table 1-1 lists the measurements required, their accuracy, and the range of values expected [43].

Table 1-1: Science requirements for the science models.

Measured Ice Parameter	Measurement Accuracy	Pixel Size	Measurement Range
Ice Thickness	5 m	10 m	500 to 5000 m
Internal layer depth	5 m	10 m	0 m to 5000 m
Wet or frozen base	95% confidence	100 m × 100 m	Wet or Dry
Basal water layer thickness	Not specified	10 m × 10 m	0.4 mm to 0.5 m
Roughness Spectrum	Not specified	10 m × 10 m	3 mm to 5 m
Bottom Topography	5 m height	10 m × 10 m	500 to 5000 m

1.2 BACKGROUND

There are several methods that can be used to observe the basal conditions of an ice sheet. One brute-force method involves drilling a borehole to the bottom of the ice sheet and passing measurement equipment down into the borehole. Many boreholes to the base of the ice sheet have been drilled [47], but wide area coverage with 100 m resolution is infeasible because the resources and time consumed for each borehole are tremendous. Seismic studies can meet many of the science requirements, but wide area coverage is still a significant challenge. Seismic studies must be ground-based and require significant setup time per measurement [48]. Radar, on the other hand, provides the ability to remotely sense the basal conditions with sufficient resolution over a large area in a comparatively short period. The physical features can be distinguished from one another through the use of wideband radar. Radar also does not require modifying the environment that is being measured. The boreholes are still necessary, however, because of the need for calibration and testing. Likewise, seismology provides additional information (e.g. bed lithography and stress [49]) that the radar system can not reliably determine and both technologies in tandem would provide the best results [50].

We designed, built, and fielded a synthetic aperture radar (SAR) whose data products include a reliable estimation of the distribution of subglacial water and the determination of the roughness of the ice-bed interface. Since, both mechanisms for fast ice flow in ice streams require a wet base, measuring the distribution of water is the primary objective of the SAR. Additionally, the data products from the radar include an ice thickness measurement needed for the SAR processing, which also satisfies the ice thickness science requirement.

The desired science outputs of the SAR data are given in Table 1-2. Since the SAR only meets a subset of the science requirements, differences are italicized. The internal layer depth measurement range starts at 150 m because a second radar, working in tandem with the SAR, has been developed for high-resolution tracking of near surface internal layers [51] that already tracks these upper layers. The measurement accuracy for wet or frozen bed, basal water layer thickness, and RMS height are determined through

simulation and were not specified. Finally, the radar should be capable of producing data that can be processed using interferometric SAR (InSAR) techniques to determine bottom topography, although InSAR is not part of this work.

Table 1-2: Subset of science requirements that the SAR should meet.

Measured Ice Parameter	Measurement Accuracy	Pixel Size	Measurement Range
Ice Thickness	5 m	10 m	500 to 5000 m
Internal layer depth	5 m *(40 dB sidelobes)*	10 m	150 m to 5000 m
Wet or frozen base	*To be determined*	100 m × 100 m	Wet or Dry
Basal water layer thickness	*To be determined*	10 m × 10 m	0.4 mm to 0.5 m
Roughness (RMS height)	*To be determined*	10 m × 10 m	3 mm to 5 m
Bottom Topography	*5 m height*	*10 m × 10 m*	*500 to 5000 m*

The key problem to be studied in this dissertation is

1. The ability to apply side-looking synthetic aperture radar concepts to map the backscatter from the ice/bed interface of the ice sheet. Several related problems that must be solved are:
    a. Determination of radar system parameters that will meet the science requirements
    b. The design, fabrication, and field testing of the radar system.
    c. Simulation of the ice sheet as a planarly stratified media (specifically interested in ice loss and refraction). This also involves creating dielectric profiles using indirect methods for areas where direct measurements are not available.
    d. Antenna network capable of providing side-looking operation over the desired bandwidth.
    e. SAR processing applied to a planarly stratified media
    f. Bistatic mode of operation for common midpoint measurements (CMP) that will provide the data necessary to determine the dielectric profile used in the planarly stratified media model

Data from one polar region are used to demonstrate the operation of the radar system and feasibility of the SAR processing and data product generation. The region is near Summit, Greenland (72.5667° N, 38.4833° W, ~3200 m) in the dry-snow zone. Summit, Greenland is known to be frozen to its base at the GRIP and GISP2 boreholes [52]. Therefore, this site does not provide the opportunity to verify the success of the "wet or frozen base" or the "basal water layer thickness" data products. However, estimates of the dielectric are necessary in the roughness analysis and may provide some way to measure the success of this part of the work since ground truth is available from the 3.4 cm diameter, 1.55-m long GISP2 bedrock core [53].

Chapter 2: ICE SHEET ANALYSIS

2.1 ELECTROMAGNETIC PROPERTIES OF THE ICE SHEET

In order to make radar system design decisions, we need an expectation of the target's scattering characteristics. To do this, we start with a geophysical model – garnered from the nearby GRIP and GISP2 ice core records. We then use the geophysical model with the proper relationships to find the electromagnetic model (i.e. the constitutive properties of the media). Finally, we describe the radar model and show how the scattered return power can be predicted from this electromagnetic model.

2.1.1 GEOPHYSICAL MODEL

Building a propagation model for the ice sheet requires knowledge of the constitutive parameters of the ice sheet. We assume that these parameters are functions only of depth and the ice sheet can be modeled, at least locally, as a planarly stratified media. This assumption has been justified in the literature, e.g. [54]. Because ice is non-magnetic, we focus on constructing a permittivity profile of the ice sheet [55]. Direct measurements of permittivity at our frequency of operation are not available. However, geophysical measurements are available that can be converted in to a permittivity profile. The geophysical properties used here are ice density, low frequency dielectric profiling (DEP), and temperature.

The radar simulations in this work use geophysical data available from the GRIP and GISP2 ice cores and drill holes. The datasets used are shown in Fig. 2-1 and Fig. 2-2 along with references to the data. Each dataset was not available for the full length of the core. The density data start at the top surface and extend to 1500 m. The density profile is extended to the bedrock with a constant value equal to the average density in the last 100 m of valid data. The same technique is used to extend the beginning and end of the DEP profile. The temperature profile is linearly extrapolated to the bed using the last 100 m of

data. The temperature profile is extrapolated to the surface using the annual mean temperature.

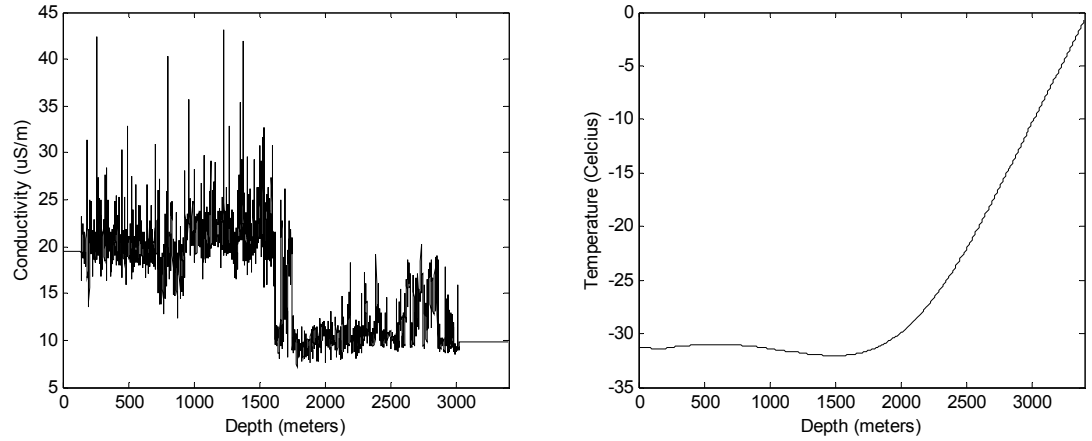

Fig. 2-1. Conductivity [56] and temperature [52] profiles from the Summit, Greenland area.

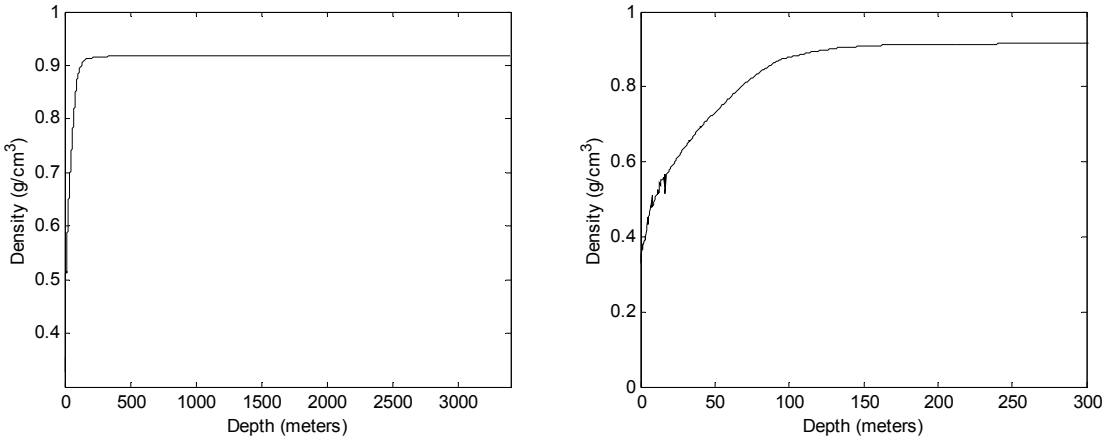

Fig. 2-2. Density [57], [58] profile from the Summit, Greenland area. Since most of the density changes occur in the top 300 m of ice, a magnified view is shown on the right.

2.1.2 ELECTROMAGNETIC MODEL

A number of factors affect the propagation of electromagnetic waves in the ice sheets. These are dielectric properties of ice which are modulated by temperature and density, increased conductivity from salt and acid impurities, volume scattering from snow grains, air bubbles, and melt events, depolarization due to the ice birefringence, and surface scattering from englacial layers [59]. In the very high frequency (VHF) and lower ultra

high frequency (UHF) bands, only temperature, density, impurity concentrations, and ice birefringence create a significant effect in the dry snow region [60]. These parameters, except for birefringence, are incorporated in our propagation model. While birefringence has been shown empirically to have an effect – lack of crystal lattice data and a direct link between ice fabric and electromagnetic wave propagation make it very difficult to quantify this effect.

The real part of the permittivity of ice is nearly independent of frequency, impurity concentration, and temperature at VHF and UHF. On the other hand, the imaginary part of the permittivity is dependent on frequency, temperature, density, and impurity concentration. Absorption in pure ice at radio frequencies comes from the high-frequency tail of the Debye-relaxation in the kHz region and the low-frequency tail of the infrared absorption bands [61]. The attenuation is controlled by the dielectric constant, which we represent by $\varepsilon = (\varepsilon' - j\varepsilon'')\varepsilon_0$, where ε_0 is the permittivity of free-space, and ε' and ε'' are the real and imaginary parts, respectively, of the relative permittivity. The justification of the following permittivity model is described in detail elsewhere [55]. For pure ice, ε can be modeled by

$$\varepsilon' = 3.1884 + 0.00091(T - 273.15)$$

and

$$\varepsilon'' = \frac{A_m}{f_G} + B_m f_G^{C_m}.$$

The first equation is based on Matzler and Wegmüller's work [61] where T is the temperature in K. The first term of the second equation accounts for Debye-relaxation loss and the second term accounts for infrared absorption loss. The frequency, f_G, is in GHz. The coefficients A_m, B_m, and C_m are temperature-dependent empirical constants and are tabulated in [62], although the form of this equation is originally from [61]. Spline interpolation with not-a-knot end conditions is used to fill in values at different temperatures.

The acid and salt impurities in the ice contribute significantly to the ice permittivity. To determine their contribution, we use the calibrated dielectric profile (DEP) from the

GRIP ice core. The DEP-derived conductivity profile from GRIP gives the high-frequency limit of conductivity measured at LF and corrected to 258 K [63]. Fujita et al. [55] suggest that the high-frequency limit conductivity is valid at our frequencies since the molar conductivity does not change from LF to UHF.

The DEP-derived conductivity is sensitive to the Debye-relaxation and impurities, but not infrared absorption. Therefore, we use the conductivity profile only to estimate the impurity component of conductivity. Because of this, we need to subtract off the LF pure ice conductivity. Using the single-frequency Debye model [63] suggests this value to be 9 $\mu S \cdot m^{-1}$ at 258 K. Due to errors in the conductivity profile, there are a few points in the profile where the total conductivity is measured to be less than 9 $\mu S \cdot m^{-1}$, leading to a negative conductivity due to impurities. We set the impurity-component of the conductivity to zero in these cases.

To determine the conductivity at other temperatures, we use an Arrenhius model (e.g., eqn. 3 of [64]):

$$\sigma_{\infty} = \sigma_{\infty,258} \exp\left(\frac{E}{R}\left(\frac{1}{T_{258}} - \frac{1}{T}\right)\right)$$

where $\sigma_{\infty,258}$ is the impurity-component of the conductivity from the profile, $E = 0.22$ eV $\left(21{,}217\ \text{J}\cdot\text{mol}^{-1}\right)$ is the activation energy suggested by [63], $R = 8.3144\ \text{J}\cdot\text{mol}^{-1}\cdot\text{K}^{-1}$ is the universal gas constant, T is the desired temperature in Kelvin, and $T_{258} = 258$ K is the temperature that the conductivity profile is given for. The conductivity is related to the imaginary part of the permittivity by $\varepsilon'' = \frac{\sigma_{\infty}}{2\pi f \varepsilon_0}$ where f is the frequency in Hz.

The above equations are for solid ice with a density of $d_{ice} = 917\ \text{kg}\cdot\text{m}^{-3}$. However, the density of the ice sheet is a function of depth in the firn/ice transition region. To account for a density of d, we scale the real part of the permittivity by [65]

$$D' = \frac{1 + 1.7d + 0.7d^2}{1 + 1.7d_{ice} + 0.7d_{ice}^2},$$

and the imaginary part of the permittivity by [65]

$$D'' = \frac{0.52d + 0.62d^2}{0.52d_{ice} + 0.62d_{ice}^2}.$$

Several issues regarding the accuracy of the permittivity must be dealt with. Fujita et al. estimates the real part of the permittivity to be accurate to 1% based on the scatter of available data [55]. The accuracy of the real part limits the maximum length of the SAR aperture that can be coherently processed since phase coherence across the entire aperture is required. We set the maximum acceptable phase error to be one eighth of a wavelength. This corresponds to a signal-to-noise degradation of 0.2 dB. The maximum synthetic apertures are 349 m, 248 m, and 177 m for 1%, 2%, and 4% velocity errors[3]. Since hyperbolas have been observed in the bed echoes, auto-focusing techniques [66], [67], [68], [69], [70], [71], [72] may improve the SAR's performance and should be investigated in the future.

The imaginary part of the permittivity, which determines the loss, has significant error bars. An example for NGRIP, Greenland is given in [60] where the difference in two-way ice loss predicted by two different sets of laboratory data for ice permittivity is approximately 30 dB. Based on this large discrepancy, we proposed to perform common midpoint measurements (CMP) utilizing a bistatic configuration to reduce the error bars on the scattering strength estimates. Unfortunately, due to system design failures described in section 7.3, the quality of the CMP data taken by the radar system was insufficient for analysis. However, once these failures are corrected, the radar system is capable of acquiring bistatic CMP data which could significantly reduce error bars.

The real part of the permittivity at 210 MHz[4] versus depth is shown in Fig. 2-3a. The loss in $\mathrm{dB \cdot km^{-1}}$ versus depth at 210 MHz is plotted in Fig. 2-3b.

[3] For small errors, a velocity error of V_{err}% corresponds to a permittivity error of $2V_{err}$%.
[4] 210 MHz is the center frequency used by the radar system.

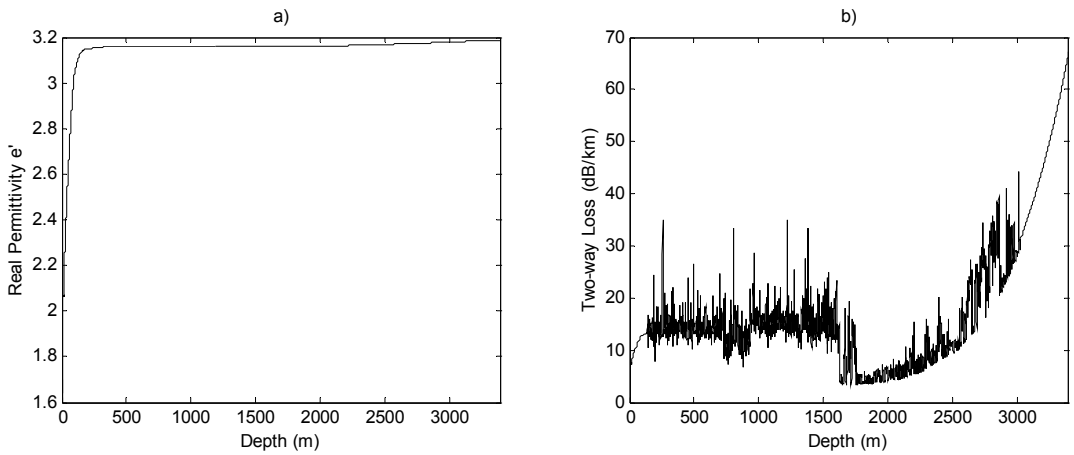

Fig. 2-3. The a) real part and b) imaginary part of the permittivity (expressed as loss) corresponding to the geophysical profiles shown in Fig. 2-1 and Fig. 2-2.

As mentioned above, to acquire more accurate velocity and attenuation profiles, the radar system will be designed so that it can operate in bistatic mode for common midpoint measurements (CMP). (Requirements imposed by bistatic operation are delineated in section 3.5.) The ice properties can be found by analyzing the reflections from the planarly stratified media at various depths as a function of antenna separation in the CMP measurements. More details are provided in section 7.3.

Without CMP measurements, we must rely on a permittivity profile derived from geophysical profiles. In areas where these direct measurements are not available, models of geophysical properties can provide a rough estimate. The density profile can be found from accumulation and mean surface temperatures [73]. Accumulation and temperature maps are readily available for Greenland and Antarctica [74], [75]. The temperature profile can be found from models of the geothermal heat flux and are also available for the Greenland and Antarctic ice sheets [76], [77]. Impurity profiles must be extrapolated from areas with known DEP measurements. This represents the largest unknown and, depending on spatial variability and proximity to an existing dataset, may represent the largest source of error.

With the permittivity profile, the solution for the propagation of a plane wave in the media can be found in closed form [78], [79]. Using simple ray-tracing approximations and this discrete layer model, the phase delay, ray-path, and attenuation can be found for

spherical waves. These are all necessary elements needed by the SAR processing algorithm, and the latter two values are also needed for solving the radar equation. Using the permittivity profile from Fig. 2-3 and a ray-tracing model, we plot the time delay in Fig. 2-4a, initial transmission angle, θ_t, in Fig. 2-4b, bed incidence angle, θ_i, in Fig. 2-4c, and attenuation, L_t, in Fig. 2-4d as a function of off-nadir position for 3000 m thick ice at 210 MHz.

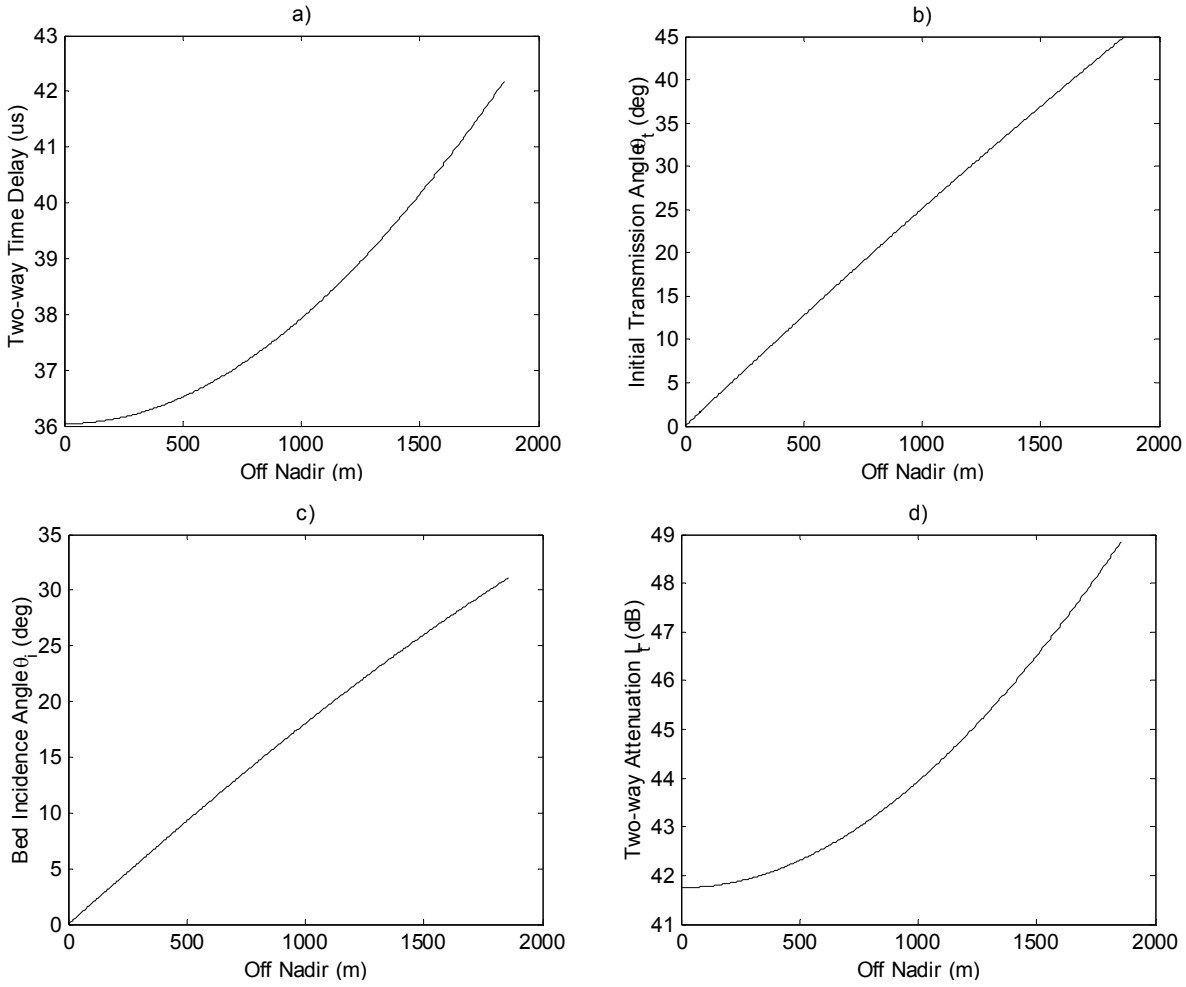

Fig. 2-4. a) Time delay, b) transmission angle, c) bed incidence angle, and d) attenuation are plotted versus off-nadir position.

2.1.3 REFRACTION

One of the characteristics of ground penetrating radar is that the antenna gain in the denser (higher permittivity) media is increased by a "focusing effect". This focusing

effect will be referred to as refraction gain, G_f. For ice sheets, which tend to start at a low permittivity near the surface and asymptotically approach a higher permittivity, the refraction gain is a function of both depth and angle of incidence. West and Demarest use a ray-tracing technique to solve for the refraction gain of an antenna on an ice sheet [80].

To solve for the refraction gain analytically, West and Demarest assume the form of the density profile to be:

$$\Delta(z) = \Delta_i - V\exp(Rz)$$

where

Δ is the density as a function of depth,

Δ_i is the density of pure ice, taken to be $0.917\ \mathrm{g\cdot cm^{-3}}$,

V is a model parameter with units of density (always less than P)

R is a model parameter with units of inverse distance (always positive)

z is the elevation (always negative).

This exponential form for the density profile is justified for ice sheets in the paper. West and Demarest use Robin et al.'s results to convert the density profile in to a permittivity profile [81] (written here in terms of the index of refraction):

$$n(z) = 1 + 0.854\Delta(z)$$

Since the permittivity conversion used in this work uses Tiuri's results to convert density to permittivity [65], the refraction gain has been re-derived for this case. Additionally, there are a number of typographical mistakes in the paper that have been corrected here (the corrected equations using Robin's results are also included in parenthesis where they differ from the equations for Tiuri's results). This proof makes use of a change of variables and two of Gradshteyn and Ryzhik's integral solutions [82]. The refraction gain is

$$G_f(z,\theta_t) = \frac{D^2\sin\theta_t}{r'\dfrac{dr'}{d\theta_i}\cos\gamma'}$$

where

$a = C + 1.7C\Delta_i + 0.7C{\Delta_i}^2 - \zeta^2$ or ($a = \left(1 + 0.854\Delta_i\right)^2 - \zeta^2$),

$b = -1.7CV - 1.4C\Delta_i V$ or ($b = -2\left(1 + 0.854\Delta_i\right)0.854$),

$d = 0.7CV^2$ or ($d = 0.854^2$),

$C = 1$ is a scaling factor to Tiuri's permittivity equation,

$\zeta = n(0)\sin\theta_t$,

$M = V\exp(Rz)$,

$X(\bullet) = a + b\bullet + d\bullet^2$,

$$r' = \int_0^z \frac{\zeta dz'}{\sqrt{n^2(z') - \zeta^2}} = -\frac{\zeta}{R\sqrt{a}} \ln \frac{V\left(2\sqrt{aX(M)} + bM + 2a\right)}{M\left(2\sqrt{aX(V)} + bV + 2a\right)},$$

$D = \sqrt{r'^2 + z^2}$,

$q = 4ad - b^2$,

$$\gamma'(z) = \sin^{-1}\left(\frac{n(0)}{n(z)}\sin\theta_t\right),$$

and

$$\frac{dr'}{d\theta_i} = r'\cot\theta_i + \frac{\zeta^2 n(0)\cos\theta_i}{R}\left[\frac{r'R}{\zeta a} - \frac{2}{aq}\left(\frac{bdM - 2ad + b^2}{\sqrt{X(M)}} - \frac{bdV - 2ad + b^2}{\sqrt{X(V)}}\right)\right].$$

Before applying these results, we need to fit our density data to the exponential function and find V and R. To do this, we take the natural log of Δ to obtain a linear relationship with respect to z

$\ln(\Delta_i - \Delta(z)) = \ln(V) + Rz$.

We then fit a first order polynomial to the log density data using the least squares technique. From the permittivity data presented in Fig. 2-3, $V = 0.601$ and $R = -0.0253$. The RMS percentage error between the exponential fit and the data is less than 1%. A plot of the refraction gain at normal incidence as a function of depth is shown in Fig.

2-5a. A plot of the refraction gain as a function of the incidence angle at 3000 m depth is shown in Fig. 2-5b.

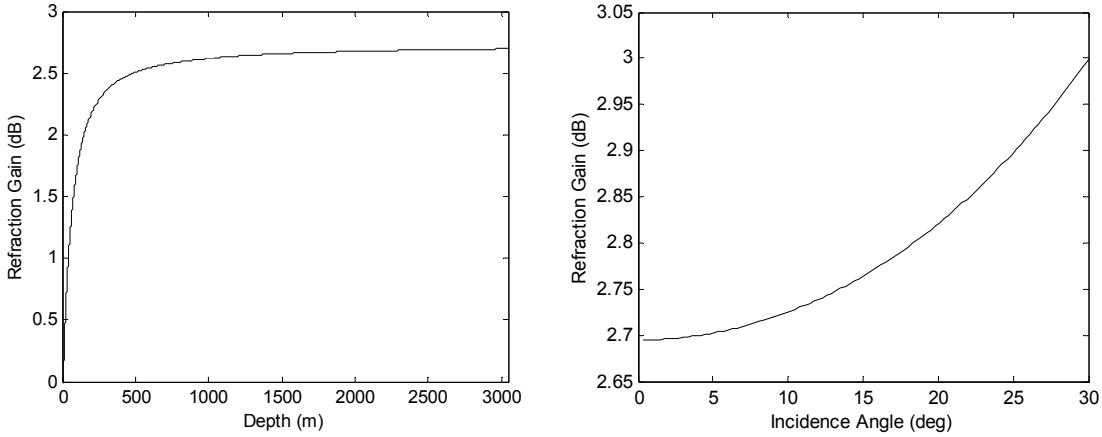

Fig. 2-5. a) Refraction gain at normal incidence as a function of depth and b) refraction gain as a function of initial transmission angle θ_t at 3000 m depth.

2.1.4 BED MATERIALS

A brief review of the dielectric properties of potential basal materials is given in this section and draws on [31], [83], [84], [85], [86], [87], [88], and [89]. Because of the expanse of the ice sheets coupled with very limited access to the base, few constraints exist that help narrow the possible selection of basal materials for a general SAR survey. Because of this wide variability and unknown moisture content at the glacial sole, dielectric values may range between 2 and 86. At the low end of the dielectric scale are dry or frozen sediments and at the high end is liquid water. Most soils and rocks in the VHF region have dielectrics below 10 and the contrast in reflectivity or scattering should be quite marked between water and rock/soil beds. However, a thin layer of water or a thawed porous bed with a mix of water can take on an effective dielectric any where between the two extremes making any clear delineation impossible.

In the case of the Summit, Greenland region, GISP2 and GRIP boreholes were drilled to the base. Only at GISP2 was substantial basal material recovered, but at both sites silty ice above the bed was recovered (although at less than 1% fraction by weight). If the study of the GISP2 core holds for the whole survey area, the region is underlain by metamorphic or granite rock with the possibility of a thin layer of soil and loose

sediments and the bed is 6 C below the pressure melting point. Since the bed is frozen to its base, large variations in backscatter are probably due to changes in roughness and surface slope rather than dielectric contrasts.

Although the GISP2 and GRIP sites are unlikely to present a chance to test the existence of subglacial water, one of the most important applications of a subglacial imaging radar is to detect the presence of basal water. We start by illustrating the results for normal incidence using a 3-layer model involving ice, water, and bed material [90]. The permittivity of ice is found using the techniques described in section 2.1.2 and is taken to be $\varepsilon_{ice} = 3.15$. The water permittivity is found using a Debye relationship [91]

$$\varepsilon_w = \varepsilon_{w\infty} + \frac{\varepsilon_{w0} - \varepsilon_{w\infty}}{1 + j2\pi f \tau_w},$$

where

$$\varepsilon_{w\infty} = 4.9,$$

$$\varepsilon_{w0} = 88.045 - 0.4147T + 6.295 \times 10^{-4} T^2 + 1.075 \times 10^{-5} T^3,$$

$$2\pi\tau_w = 1.1109 \times 10^{-10} - 3.824 \times 10^{-12} T + 6.938 \times 10^{-14} T^2 - 5.096 \times 10^{-16} T^3,$$

and T is in units of Celcius. Table 2-1 lists the values at several different frequencies for reference. The imaginary part of the permittivity scales linearly with frequency implying that the conductance is following a quadratic relation. A plot of transmissivity demonstrating this strong dependence on frequency is shown in Fig. 2-6. The oscillations are caused by the interaction of the two interfaces and are the primary reason for the variations in transmissivity for thin layers. Finally, we use a bed material permittivity of $\varepsilon_{bed} = 6.5$ – chosen to be in the mid-range of expected values.

Table 2-1: Permittivity of water at several frequencies.

Frequency (MHz)	**Real Part** ε'_w	**Imaginary Part** ε''_w
150	88.02	1.39
300	87.95	2.77
450	87.84	4.15
650	87.61	5.97

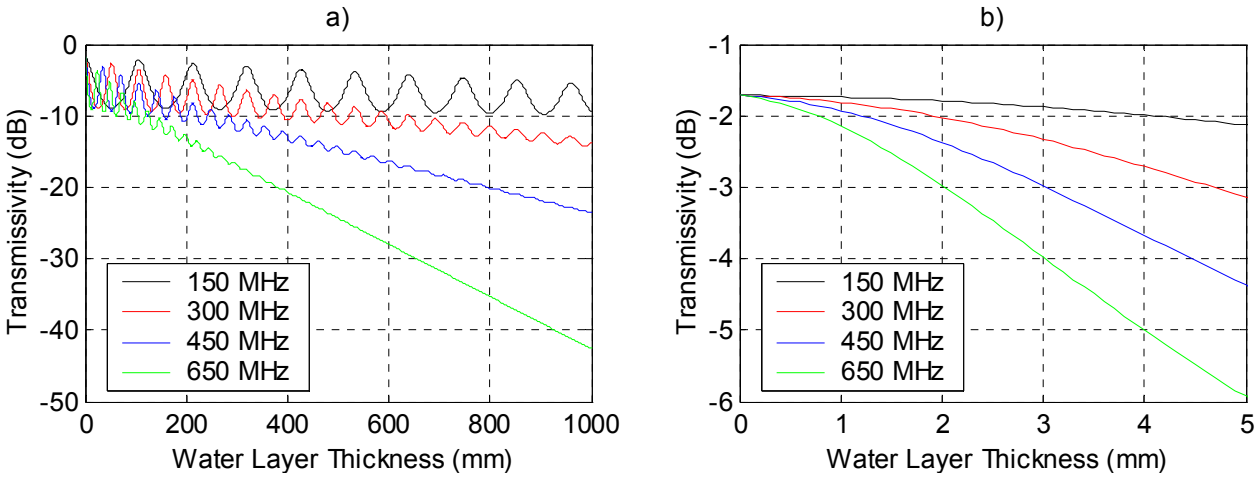

Fig. 2-6. a) Plot of transmissivity through basal water layer at normal incidence, b) Magnified view of transmissivity for thin layers.

The reflectance at normal incidence (depth sounding mode) is shown in Fig. 2-7 at several frequencies as a function of water layer thickness. These results suggest that only a 1-4 mm layer thickness is enough to change the reflectance by 6 dB depending on the frequency of operation. The reflectivity variation is strongly dependent on the constructive/destructive interference pattern. These results are of course valid when the basal interface is a planar interface, but they are also valid when the large RMS height physical optics model holds (see section 2.4). To a lesser extent they are valid for the small-slopes physical optics model since Fresnel reflections are the basis of the scattering, but this model does not directly incorporate the Fresnel reflection coefficient. The effect is less obvious on surfaces for which the small perturbation model is valid. One approach is to use radiative transfer theory for layered rough interfaces laid out by Fung [92]. This approach is very technical and a simplified approach is used here so the

results are only suggestive rather than conclusive. A water interface for very rough interfaces like those described by small perturbation theory may be more appropriately described by a mixing formula (e.g. reminiscent of permittivity variations due to soil moisture). The idea is to choose a representative bed thickness and then assume that the water layer is "mixed" into the bed material. The resultant permittivity can be used directly in the rough surface models.

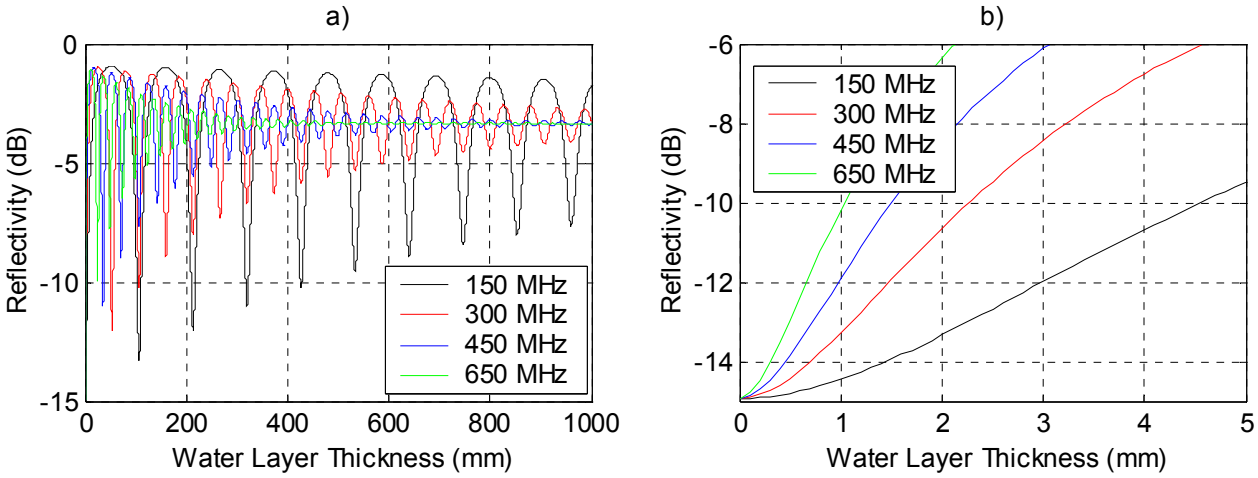

Fig. 2-7. a) Plot of reflectivity from a basal water layer at normal incidence, b) Magnified view of reflectance for thin layers.

We use the mixing formula based on Looyenga's work [93] which is developed for spherical inclusions. It is valid for low volumetric ratios of inclusions. The permittivity of the mixed material is

$$\varepsilon_r = \left[\left(\varepsilon_w^{1/3} - \varepsilon_b^{1/3}\right)v_w + \varepsilon_b^{1/3}\right],$$

where ε_w is the dielectric of water, ε_b is the dielectric of the bed material, and v_w is the volume fraction of water.

Assuming a mixture of 1 m of bedrock thickness with a water layer of t thickness we find

$$v_w = \frac{t}{1+t}.$$

A plot of permittivity versus water layer thickness is shown in Fig. 2-8 and the corresponding effect on the relative backscatter. The result is very sensitive to the bedrock layer thickness chosen and further analysis is needed to ascertain the appropriate bed material layer thickness to use. The effect of the water is insensitive to both frequency and incidence angle (this is because a mixing formula is used which only weakly depends on these parameters). The results show that if this simplified assumption is correct, the scattering would be a fairly weak function of water layer thickness. The reason for this is that a mixing formula does not include the phase-sensitive interference that occurs with a layered model. Actual measurements will likely fall between these two extremes.

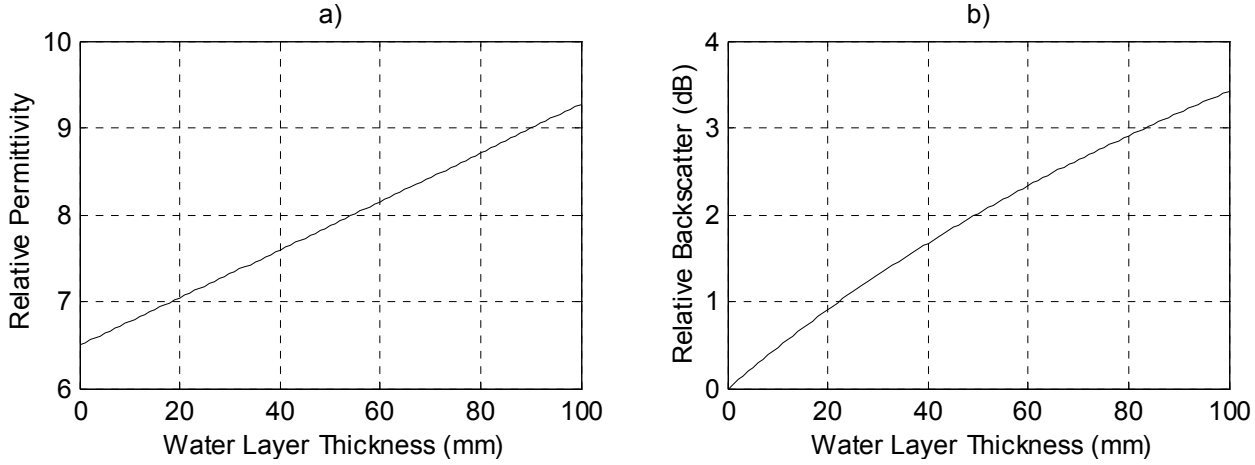

Fig. 2-8. a) Plot of the real part of the permittivity versus water layer thickness, b) Plot of relative backscatter versus water layer thickness.

2.2 RADAR SYSTEM MODEL

2.2.1 RADAR EQUATION

The geometry for the radar equation is shown in Fig. 2-9. The baseline vector, $\vec{B}$, points from the transmitter, Tx, to the receiver, Rx. The transmitter range vector, $\vec{r}_t$,

points from the transmitter to the target. The transmitter range then is $R_t = \left\| \vec{r}_t \right\|_2$.[5]

Likewise, the receiver range vector, $\vec{r}_t$, points from the receiver to the target and the receiver range is $R_r = \left\| \vec{r}_r \right\|_2$. T is the transmitter's and receiver's height above the target. Not shown are the polarization directions of the transmit antenna, η_t, and receive antenna, η_r. Using the ordinary definitions of $\vec{\theta}_i$ and $\vec{\phi}_i$ in the spherical coordinate system, η_t is the angle the E-plane[6] of the antenna makes with the plane defined by the vector $\vec{\theta}_i$ and $\vec{\phi}_i$ at the target. $\vec{\theta}_i$ is the origin and η_t increases toward $\vec{\phi}_i$. For reference, $\eta_t = 0$ implies that the polarization at the target is purely vertical and $\eta_t = \frac{\pi}{2}$ implies the polarization is horizontal. η_r is likewise defined with respect to $\vec{\theta}_s$ and $\vec{\phi}_s$. When referring to a particular Cartesian component of a vector, e.g. $\vec{r}_t$, we use the following notation [$r_{t,1} = x$, $r_{t,2} = y$, $r_{t,3} = z$].

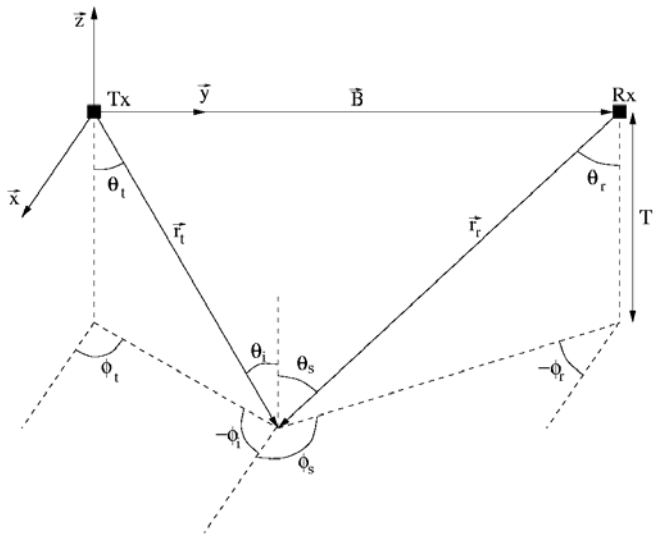

Fig. 2-9. The geometry used for the radar equation.

[5] $\left\| \bullet \right\|_2$ is the two-norm or Euclidean distance.

[6] The E-plane contains the E-field at the target and the antenna's position.

The radar system remotely senses the basal conditions of the ice sheet by illuminating the bed and measuring the radiated fields from the induced currents on the bed. The radiated fields from the ice-bed interface can be divided into coherent and incoherent components. The coherent component, also known as the specular response, is generated from currents that are correlated over the entire illuminated area. This component is described by Fresnel reflection theory. Incoherent scattering is radiation from the uncorrelated part of the currents. We will start by deriving the area-extensive form of the radar equation (incoherent form) and then specialize it to its specular or coherent scattering form.

The radar equation for an area extensive target gives the expectation of the power received from a single pixel or resolution cell in terms of radar, medium, and target parameters. The radar equation is a function of the frequency, f, and system geometry parameters, R_r, R_t, θ_t, ϕ_t, θ_r, ϕ_r, θ_i, ϕ_i, θ_s, ϕ_s, η_t, and η_r:

$$P_r = \frac{P_t(f)G_t(f,\theta_t,\phi_t)}{4\pi R_t^2} L_t(f,\theta_t,R_t) A \sigma_0(f,\theta_i,\phi_i,\theta_s,\phi_s,\eta_t,\eta_r)$$
$$L_r(f,\theta_r,R_r)\frac{G_r(f,\theta_r,\phi_r)c^2}{(4\pi f n_{ice} R_r)^2}$$

Each of the components of this equation is described in the paragraphs below. This is a generalization of the description given by Ulaby et al. [90].

The first term in the equation, $\frac{P_t(f)G_t(f,\theta_t,\phi_t)}{4\pi R_t^2}$, represents the average power density of the transmitted wave at the target. P_t is the transmitted power and is determined by the DDS generated waveform and the transfer function of the transmitter. G_t is the gain of the transmit antenna network, which is a function of frequency and the direction towards the target. The gain for the transmit antennas is found by using a finite element numerical electromagnetic solver [95] to find the fields near the antenna on the snow surface, $\varepsilon_{r,snow} \approx 1.6$. These results are extended to depth by using the results of West and Demarest [80] as described in Appendix B.

The fifth term in the equation, $\frac{G_r(f,\theta_r,\phi_r)c^2}{\varepsilon_{r,snow}(4\pi f R_r)^2}$, represents the power coupled into the receiver as a function of the power scattered. G_r is the gain of the receive antenna network and is found in the same way as for the transmit antenna network. c is the speed of light in a vacuum.

The second and fourth terms, $L(f,\theta_t,R_t)=\exp\left(\int_0^{-T}\alpha_z(f,\theta_t,z)dz\right)$ and $L(f,\theta_r,R_r)=\exp\left(\int_0^{-T}\alpha_z(f,\theta_r,z)dz\right)$ respectively, give the total extinction as the electromagnetic wave travels through the media. The integral sums the loss from the surface to the bedrock with an ice thickness of $T \approx R_t\cos\theta_t \approx R_r\cos\theta_r$[7]. $\alpha_z(f,\theta_t,z)$ is the extinction coefficient of the medium and is found using the ice sheet model detailed in section 2.1. Since the ice sheet is modeled as an inhomogeneous medium with constitutive parameters that are functions of depth only, for a plane wave source the extinction coefficient's only spatial dependence is on z. We model the point source nature of our antenna by computing the plane wave solution for each angle of incidence. The extinction coefficient changes as a function of the plane wave's incidence angle. Therefore, the extinction coefficient is a function of z and θ_t for the incidence field and θ_r for the scattered field.

The third term, $A\sigma_0(f,\theta_i,\phi_i,\theta_s,\phi_s,\eta_t,\eta_r)$, is the ratio of the power density at the target to the total scattered power times the gain of the scattered energy in the direction of the receiver. A is the size of the target pixel (backscatter is incoherent so power rather than voltage or current is added as the area is increased). $\sigma_0(f,\theta_i,\phi_i,\theta_s,\phi_s,\eta_t,\eta_r)$ is the scattering coefficient and is the ratio of the power density at the target to the total scattered power from one unit area times the gain of the scattered energy in the direction of the receiver. The scattering coefficient is found using a rough surface model. Since the terrain below an ice sheet is so extensive, no one model can adequately explain the scattering for the entire bed of the ice sheet. For this reason, the results from several

[7] These are only approximations since the permittivity is a function of depth. The exact thickness is related to the incidence angle and range using a ray-tracing model.

rough surface scattering models with various surface statistical parameters are considered.

The two applications of the radar equation to this work are monostatic backscattering and bistatic specular scattering where both the transmitter and receiver are at the same height above the scattering surface. Under these conditions several of the terms become equal. These terms are $\theta_t = \theta_r$, $\phi_t = \phi_r$, $\theta_i = \theta_s$, $\phi_i = \phi_s$, and $R_t = R_r$, which further implies that $L(f, \theta_t, R_t) = L(f, \theta_r, R_r)$. Additionally, for monostatic backscattering with co-polarized antennas, the scattering coefficient is simplified so that $\sigma_0(f, \theta_i, \phi_i, \theta_s, \phi_s, \eta_t, \eta_r)$'s functional dependency is $\sigma_0(f, \theta_i, \eta_t)$. The removal of the ϕ dependency is due to the cylindrical symmetry of the monostatic geometry and the assumption that the rough surface characteristics are isotropic.

As written, the radar equation does not explicitly show the time dependence of the received power. Moore and Williams discuss this dependency and show that the expectation of the received power can be modeled as an integration of the transmitted signal represented in power with a weighting term which embodies all of the other components of the radar equation [96]. The simulations in section 3.3 are based on this analysis. Note that the effect of surface relief which is resolvable in range is not dealt with here. This can be accounted for by a convolution of these results with the surface height probability function [97]. For most standard surface height probability density functions (e.g. Gaussian or two-sided exponential), this has the effect of spreading or smearing the results slightly. This additional convolution does not affect our loop sensitivity analysis, but is useful for predicting surface roughness properties [24].

For the rough surface models used here, we calculate the expected received power for each of the cross-track pixels of the SAR image. The pixel's total signal power is determined from an integration of the pixel's scattered energy along the SAR's aperture length, $L_{SAR} = 300\ \text{m}$ [8], as shown in Fig. 2-10. The size of the effective integration area is $A = L_{SAR} r_c$, where $r_c \approx \dfrac{c}{2B\sqrt{\varepsilon_{r,ice}}\sin\theta_i}$ is the cross-track dimension of the pixel, and

[8] The derivation of the SAR aperture length is done later in this section.

$B = 180$ MHz is the bandwidth. Since the radar and scattering parameters are functions of the radar's position in the SAR aperture, the area is subdivided into smaller areas over which these parameters are essentially constant. Various rough surface models are reviewed and their results using the radar equation developed here are given in section 2.4.

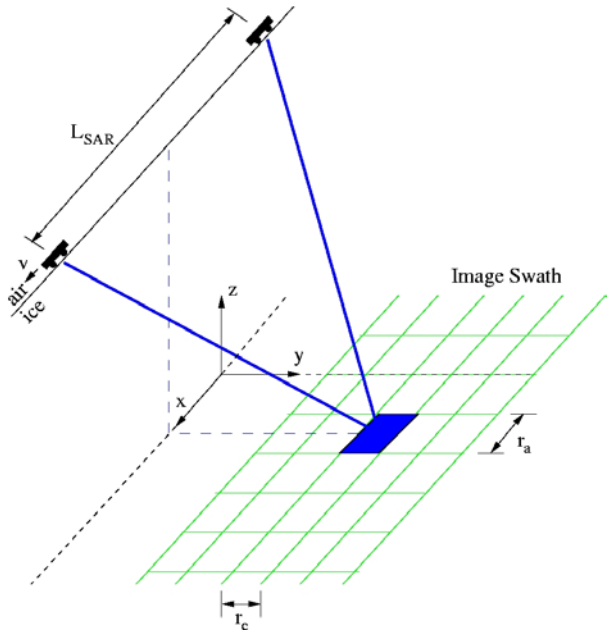

Fig. 2-10. The SAR imaging geometry. The along-track direction is x, the cross-track or ground range direction is y, and the elevation is z. The radar's synthetic aperture length is L_{SAR}. *The dimensions of a single pixel are* r_c *by* r_a.

2.2.2 SPECULAR RADAR EQUATION

For a specular surface, transmitter and receiver a fixed distance above the surface implying $R_r = R_t$, and a planarly stratified media implying $L_r = L_t$, the radar equation simplifies to

$$P_r = \frac{P_t(f)G_t(f,\theta_t,\phi_t)G_r(f,\theta_r,\phi_r)c^2}{64\pi^2(fn_{ice}R_t)^2} L_t^2(f,\theta_t,R_t)\left\langle\left|\Gamma_{pp}\right|^2\right\rangle.$$

This equation follows from an application of image theory [98] which translates the radar geometry into an equivalent direct path geometry.

If a rough interface is sufficiently smooth, it can also be approximated by a planar interface [99], [100], [101]. In this case, the scattering follows a modified Fresnel reflection. For both horizontal and vertical polarization, the modification takes the form of a power reflection coefficient weighting according to $\exp\left(-2k^2 \sin\theta_i^2 h^2\right)$. Letting $\left|\Gamma_s\right|^2$ be the Fresnel reflection coefficient for a flat surface, then the modified Fresnel coefficient is given by

$$\left\langle \left|\Gamma_s\right|^2 \right\rangle = \left|\Gamma_s\right|^2 \exp\left(-2k^2 \sin\theta_i^2 h^2\right)$$

Note that the modified Fresnel coefficient is the average or expected power reflection coefficient where the expectation is taken over the ensemble of surface functions.

2.3 INTERNAL LAYERS

The specular radar equation is used to describe the scattering from layers within the ice sheet. These layers are known as isochrones because they are caused by snow deposition that occurred in the same time frame over a large area. Three primary causes of reflections have been hypothesized in the literature: density changes, acidity changes, and ice crystal fabric changes between layers [55]. While all three undoubtedly occur, only the former two have been directly matched to radar reflections [102], [103][9]. Using this ice sheet model and observations from previous field work, a range of expected power reflections from these layers is given in this section.

Density changes in the ice sheet through two mechanisms. The first is caused by seasonal changes in temperature and accumulation rate and the other is due to the ice overburden pressure which transforms snow into ice as the snow is buried deeper in the ice sheet by new accumulation. These density changes are responsible for most of the reflections in the top of the ice sheet, but do not show up below about 300 m, since at this point the snow has been compacted into ice. As reported earlier in this chapter, the density is almost linearly related to the real and imaginary parts of the permittivity. Since the real part of the permittivity is many orders of magnitude greater than the imaginary

[9] A number of attempts have been made to characterize the effects of crystal fabric on radar returns [104], [105], [106], [107], [108], [109], [110], [111], [112], [113], [114], [115], but no work has made a conclusive link.

part, these reflections are real as opposed to complex and not functions of frequency (closely spaced layers can create frequency dependency through constructive and destructive interference) [55].

Impurity concentration changes relate to the atmospheric conditions when the snow was deposited. For example, large volcanoes or volcanoes in close proximity increase the amount of sulfuric acid in the atmosphere above the ice sheet. These impurities are deposited with the snow and change the snow's conductivity. The impurities migrate very slowly in the snow once deposited and therefore can be observed to the bed of the ice sheet where the oldest snow lies. Since only the conductivity changes, these reflections are imaginary and are functions of frequency [55].

To determine our instantaneous dynamic range requirements and the loop sensitivity, we need to know the expected strength of the reflection from these layers as a function of depth. Using the ice model described in section 2.1 and the specular radar equation, the predicted impulse response of a point source is plotted in Fig. 2-11a. These values are significantly lower than what has been observed in the field. The main problem is that the sampling rate of the geophysical profiles is 0.5-1 m at best and the parameters are averaged measurements over this length. Because of the low pass filtering and under-sampling of the original data, much of the high-frequency permittivity changes are removed and proper re-interpolation to a common depth axis is problematic. A filtered set of previous field data, $\left|\Gamma_{filt}(z)\right|^2$, is plotted in Fig. 2-11b and is used for the loop sensitivity and dynamic range calculations. A fourth degree polynomial, $\left|\Gamma_{poly}(z)\right|^2$, is fitted to $\left|\Gamma_{filt}(z)\right|^2$ using the least squares solution. If we make the assumption that any reflection profile, $\left|\Gamma(z)\right|^2$, will satisfy

$$10^{-4}\left|\Gamma_{poly}(z)\right|^2 < \left|\Gamma(z)\right|^2 < 10^{4}\left|\Gamma_{poly}(z)\right|^2$$

then we can constrain our dynamic range and loop sensitivity. The limits, $10^{-4}\left|\Gamma_{poly}(z)\right|^2$ and $10^{4}\left|\Gamma_{poly}(z)\right|^2$, along with the fitted polynomial $\left|\Gamma_{poly}(z)\right|^2$ are plotted in Fig. 2-11b.

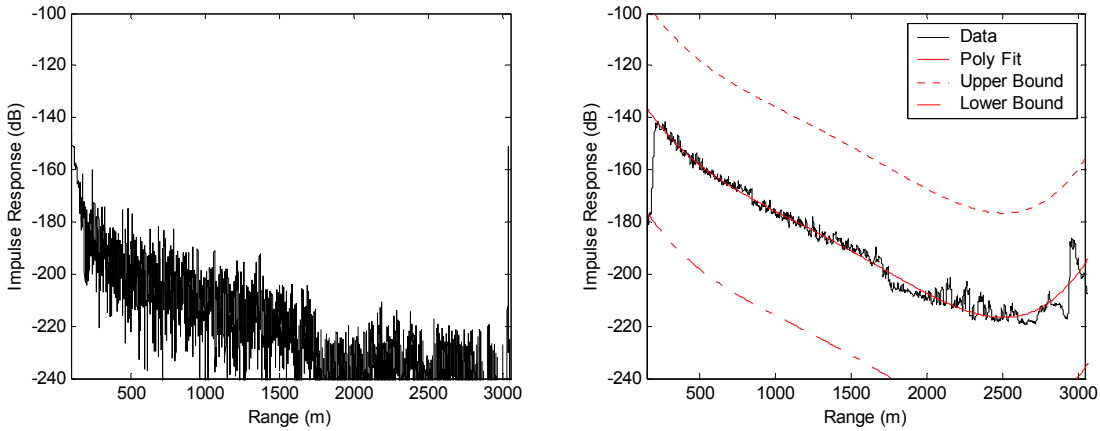

Fig. 2-11. a) Impulse response using the geophysical profiles and b) the impulse response using field data. The upturn in the data at ~3000 m depth is due to the bedrock return.

2.4 BASAL SCATTERING

Rough Surface Terminology

The rough surface models reviewed here follow the results from Ulaby et al. [116] and Ruck et al. [117]. These models treat rough surfaces that are described by a two-dimensional random process of surface height. The random process is assumed to be zero-mean and Gaussian in all the models described in this proposal. The RMS height of the surface, h, is then the standard deviation of the Gaussian random process. The autocorrelation function of the surface is taken to be isotropic so that it is dependent only on the radial distance ρ. Two forms are considered below and these are Gaussian, $\exp\left(\rho^2/l^2\right)$, and exponential, $\exp\left(|\rho|/l\right)$. The parameter l is called the correlation length. The final parameter used to describe the surface is the RMS surface slope, s, which can be derived once the surface random process is known.

Several terms show up in all or most of the rough surface scattering coefficient calculations and are listed here for ease of reference

k_1 is the wavenumber of the incident media

η_1 is the intrinsic impedance of the incident media

k_2 is the wavenumber of the media beneath the interface

η_2 is the intrinsic impedance of the media beneath the interface

$$q_x = k_1\left(\sin\theta_s \cos\phi_s + \sin\theta_i \cos\phi_i\right),$$

$$q_y = k_1\left(\sin\theta_s \sin\phi_s + \sin\theta_i \sin\phi_i\right),$$

$$q_z = k_1\left(\cos\theta_s + \cos\theta_i\right),$$

and

$$q^2 = q_x^2 + q_y^2 + q_z^2 .$$

The equation for q_z is incorrect in Ruck et al. Also, Ulaby et al.'s definition for ϕ_i does not match the standard coordinate spherical system definition as it is shifted by π (this is not stated explicitly in their text). The correct form for q_z is given here and the standard definition of ϕ_i is used. For monostatic (i.e. backscatter) these equations simplify to

$$q_x = 2k_1 \sin\theta_i \cos\phi_i ,$$

$$q_y = 2k_1 \sin\theta_i \sin\phi_i ,$$

and

$$q_z = 2k_1 \cos\theta_i .$$

Although there is still a ϕ dependency, in all the scattering coefficient results below this dependency cancels out in the backscattering case.

Finally, we must consider the antennas' polarization. In all cases in this work, we are interested in arbitrary linear polarization so this is the only type of polarization that will be considered. Typically the incident and scattered fields are divided into horizontal and vertical components. The scattered fields are then solved for with respect to each of these components. Let α_{pq} be the ratio of the q-polarized transmit field to the p-polarized receive field. The principle of superposition allows us to add these four field components together to find the ratio of the actual receiver to transmitter polarizations, α_{η_t,η_r}. The

apportionment between each of the components is dependent on the orientation of the antennas, η_t and η_r, according to (Ruck et al.)

$$\alpha_{\eta_t,\eta_r} = \alpha_{vv}\cos\eta_t\cos\eta_r + \alpha_{vh}\sin\eta_t\cos\eta_r + \alpha_{hv}\cos\eta_t\sin\eta_r + \alpha_{hh}\sin\eta_t\sin\eta_r .$$

Note that this result considers ratios of fields and not powers, whereas the scattering coefficient represents ratios of powers.

Small Perturbation Model

The small perturbation model predicts the power scattered from a surface with a small RMS height. A complete derivation of the monostatic (backscatter) result for a rough surface satisfying the conditions described below and a Gaussian correlation coefficient is given in Ulaby et al. Most of the derivation for the more general bistatic situation is given as well. However, the surface power spectral density needed to calculate the scattering coefficient is not provided. Ruck et al. present these results and their results match Ulaby et al.'s where direct comparisons can be made. In addition, the result for an exponential correlation function is also given in Ruck et al.

This surface model is applicable to surfaces which satisfy the following assumptions

1. Surface RMS height satisfies $k_0 h < 0.3$. (Ruck et al. suggests a slightly less restrictive criteria with $k_0 h < 1$). When determining h for this model, only the frequency components of the surface responsible for scattering should be considered. These are roughly the frequency components with wavelengths equal to the radar's operating wavelength.
2. Average surface slope, s, is less than 0.3. For a Gaussian correlation function, Ulaby et al. shows that $s = \sqrt{2}\frac{h}{l}$. (Ruck et al. suggests a slightly less restrictive criteria with slope less than 1).

The scattering coefficient is given by

$$\sigma_{pq} = \frac{4}{\pi}k_1^4 h^2 \cos^2\theta_i \cos^2\theta_s \left|\alpha_{pq}\right|^2 I$$

where

k_1 is the wave number of the incidence media,

ε_r is the permittivity of medium 2 relative to medium 1,

μ_r is the permeability of medium 2 relative to medium 1,

$$\alpha_{vh} = \sin(\phi_s - \phi_i)\frac{\mu_r(\varepsilon_r - 1)\sqrt{\varepsilon_r\mu_r - \sin^2\theta_s} - \varepsilon_r(\mu_r - 1)\sqrt{\varepsilon_r\mu_r - \sin^2\theta_i}}{\left[\mu_r\cos\theta_i + \sqrt{\varepsilon_r\mu_r - \sin^2\theta_i}\right]\left[\varepsilon_r\cos\theta_s + \sqrt{\varepsilon_r\mu_r - \sin^2\theta_s}\right]},$$

$$\alpha_{hv} = \sin(\phi_s - \phi_i)\frac{\varepsilon_r(\mu_r - 1)\sqrt{\varepsilon_r\mu_r - \sin^2\theta_s} - \mu_r(\varepsilon_r - 1)\sqrt{\varepsilon_r\mu_r - \sin^2\theta_i}}{\left[\varepsilon_r\cos\theta_i + \sqrt{\varepsilon_r\mu_r - \sin^2\theta_i}\right]\left[\mu_r\cos\theta_s + \sqrt{\varepsilon_r\mu_r - \sin^2\theta_s}\right]},$$

$$\alpha_{vv} = \frac{\left[\begin{array}{r}(\varepsilon_r - 1)\left(\varepsilon_r\sin\theta_i\sin\theta_s + \cos(\phi_s - \phi_i)\sqrt{\varepsilon_r\mu_r - \sin^2\theta_i}\sqrt{\varepsilon_r\mu_r - \sin^2\theta_s}\right) \\ -\varepsilon_r^2(\mu_r - 1)\cos(\phi_s - \phi_i)\end{array}\right]}{\left[\varepsilon_r\cos\theta_i + \sqrt{\varepsilon_r\mu_r - \sin^2\theta_i}\right]\left[\varepsilon_r\cos\theta_s + \sqrt{\varepsilon_r\mu_r - \sin^2\theta_s}\right]},$$

$I = \pi l^2 \exp\left(\frac{-l^2\left(q_x^2 + q_y^2\right)}{4}\right)$ for a Gaussian correlation function,

and $I = 2\pi l^2 \frac{1}{\left[1 + l^2\left(q_x^2 + q_y^2\right)\right]^{1.5}}$ for an exponential correlation function.

As a side note, Ulaby et al. has a sign error in α_{vv} that has been corrected here and is also correct in Ruck et al. Additionally, both Ulaby et al and Ruck et al assume $\phi_i = \pi$ and the equations above are generalized for arbitrary ϕ_i. For monostatic or backscatter, we note that

$$q_x^2 + q_y^2 = 4k_1^2\sin^2\theta_i$$

and the scattering coefficients for a Gaussian correlation function are

$$\sigma_{hh} = 4k_1^4h^2l^2\cos^4\theta_i\left|\frac{(\mu_r - 1)\left((\mu_r - 1)\sin^2\theta_i + \varepsilon_r\mu_r\right) - \mu_r^2(\varepsilon_r - 1)}{\left[\mu_r\cos\theta_i + \sqrt{\varepsilon_r\mu_r - \sin^2\theta_i}\right]^2}\right|^2 \exp\left(-l^2k_1^2\sin^2\theta_i\right)$$

$$\sigma_{vv} = 4k_1^4 h^2 l^2 \cos^4\theta_i \left| \frac{(\varepsilon_r - 1)\left((\varepsilon_r - 1)\sin^2\theta_i + \varepsilon_r \mu_r\right) - \varepsilon_r^2 (\varepsilon_r - 1)}{\left[\varepsilon_r \cos\theta_i + \sqrt{\varepsilon_r \mu_r - \sin^2\theta_i}\right]^2} \right|^2 \exp\left(-l^2 k_1^2 \sin^2\theta_i\right)$$

and

$$\sigma_{vh} = \sigma_{hv} = 0 .$$

These equations show polarization dependence even for the backscatter scenario. Furthermore, for oblique scattering, vertical polarization is larger than horizontal polarization for scattering surfaces with higher permittivities and equal permeabilities (we assume that the constitutive parameters of the majority of the bed underlying the ice sheets satisfy this condition). Both Ruck et al. and Ulaby et al. show examples of this polarization dependence.

Because the RMS height of any surface that satisfies the conditions listed above is small, there is always a significant specular or coherent component with this type of surface. The specular component is given as a modification to the Fresnel reflection coefficient which is described in section 2.2.2.

This model is strongly frequency dependent due to the k_1^4 term and the exponential term $\exp\left(-l^2 k_1^2 \sin^2\theta_i\right)$. For small correlation lengths with respect to frequency, the exponential term's effect is small and scattering increases with the fourth power of frequency for all angles of incidence. For longer correlation lengths, scattering still increases at the fourth power of frequency for angles near normal incidence, but decrease for angles near grazing despite the k_1^4 term.

Fig. 2-12 shows the average loss predicted by the radar equation for the monostatic case with SAR processing. The other terms in the radar equation used in this simulation, including the dielectric properties of the ice and the bedrock, are described in section 2.1.

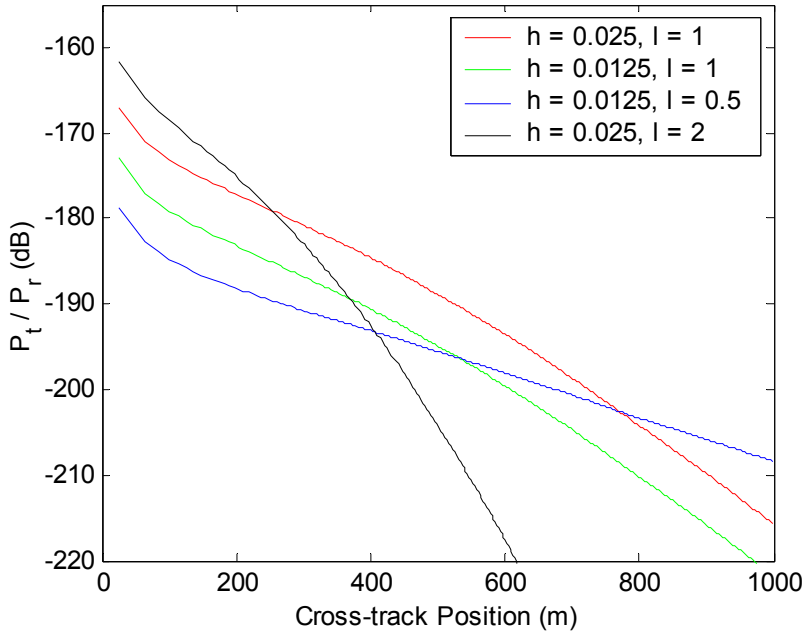

Fig. 2-12. Total loss at the radar's center frequency, 210 MHz, predicted by the radar equation using the small perturbation model for the bed surface. The results for four different surface characteristics are plotted.

Physical Optics, Large RMS Heights Model

This physical optics model predicts the surface scattering from surfaces with large radiuses of curvature and a large RMS height with respect to wavelength. The complete derivation for this scattering model with Gaussian height and correlation surface statistics is given in Ulaby et al. Ruck et al presents results for Gaussian and exponential correlation coefficients. However, the results in Ruck et al include a factor of 2 everywhere the surface slope variance enters the equation. This error enters because Ruck et al.'s RMS surface slope definition on page 705 has a factor of $\sqrt{2}$ error. For a correct derivation, see pages 1011-2 from Ulaby et al. with $\rho''(0) = -2/l^2$ for the Gaussian correlation function.

This surface model is applicable to surfaces which satisfy the following assumptions

3. Surface features are larger than a wavelength so that $l > \lambda$.
4. Surface RMS height is large with respect to wavelength $q_z h > 10$.

5. Radius of curvature (derived on pages 1011-1013 of Ulaby et al.) for the surface is large with respect to wavelength $\frac{l^2}{2h}\sqrt{\frac{\pi}{6}} > \lambda$.

The scattering coefficient is given by

$$\sigma_{pq} = \frac{\left(k_1 q \left|\alpha_{pq}\right|\right)^2}{2q_z^4 \sigma^2 \left|\rho''(0)\right|} \exp\left[-\frac{q_x^2 + q_y^2}{2q_z^2 \sigma^2 \left|\rho''(0)\right|}\right]$$

where

$$\sigma^2 \left|\rho''(0)\right| = s^2 = \frac{2\sigma^2}{l^2},$$

$$p_1 = \sin\theta \sin(\phi_s - \phi_i),$$

$$p_2 = -\sin\theta_s \sin(\phi_s - \phi_i),$$

$$p_3 = -\sin\theta_i \cos\theta_s \cos(\phi_s - \phi_i) - \cos\theta_i \sin\theta_s,$$

$$p_4 = \cos\theta_i \sin\theta_s \cos(\phi_s - \phi_i) - \sin\theta_i \cos\theta_s,$$

$$\theta_{li} = \cos^{-1}\left(\frac{q|q_z|}{2k_1 q_z}\right) \text{ (local angle of incidence)},$$

$$\theta_{lt} \approx \sin^{-1}\left(\text{Re}\left(\frac{k_1}{k_2}\right)\sin\theta_{li}\right) \text{ (local angle of transmission)},$$

$$\Gamma_\perp(\theta_l) = \frac{\eta_2 \cos\theta_{li} - \eta_1 \cos\theta_{lt}}{\eta_2 \cos\theta_{li} + \eta_1 \cos\theta_{lt}},$$

$$\Gamma_\parallel(\theta_l) = \frac{\eta_1 \cos\theta_{li} - \eta_2 \cos\theta_{lt}}{\eta_1 \cos\theta_{li} + \eta_2 \cos\theta_{lt}},$$

$$\alpha_{hh} = \frac{q|q_z|\left(\Gamma_\parallel(\theta_l) p_1 p_2 + \Gamma_\perp(\theta_l) p_3 p_4\right)}{k_1 q_z \left(p_1^2 + p_3^2\right)},$$

$$\alpha_{vh} = \frac{q|q_z|\left(\Gamma_\parallel(\theta_l) p_3 p_2 + \Gamma_\perp(\theta_l) p_1 p_4\right)}{k_1 q_z \left(p_1^2 + p_3^2\right)},$$

$$\alpha_{hv} = \frac{q|q_z|\left(\Gamma_{\parallel}(\theta_l)p_1p_4 + \Gamma_{\perp}(\theta_l)p_3p_2\right)}{k_1 q_z\left(p_1^2 + p_3^2\right)},$$

and

$$\alpha_{vv} = \frac{q|q_z|\left(\Gamma_{\parallel}(\theta_l)p_3p_4 + \Gamma_{\perp}(\theta_l)p_1p_2\right)}{k_1 q_z\left(p_1^2 + p_3^2\right)}.$$

For monostatic or backscatter, the scattering coefficient is found by taking the limit as $\theta_s \to \theta_i$ when $\phi_i = \phi_s$ [10]. The result is reproduced here as

$$\sigma_{hh} = \sigma_{vv} = \frac{\left|\Gamma_{\parallel}(0)\right|^2 \exp\left[-\dfrac{\tan^2\theta_i}{2\sigma^2\left|\rho''(0)\right|}\right]}{2\sigma^2\left|\rho''(0)\right|\cos^4\theta_i}$$

and

$$\sigma_{vh} = \sigma_{hv} = 0.$$

Unlike the small perturbation model, the physical optics model for large RMS heights has effectively no coherent component. This is because the RMS height extends over a wavelength so that the distribution of random phases from the surface is nearly uniform on 0 to 2π. Additionally, because of the stationary phase approximation used in Ulaby et al.'s derivation, all the scattered power comes from localized specular scattering. In other words, only portions of the surface oriented to give a specular response are included. For backscatter, specular scattering implies normal incidence so that there is no polarization dependence in this model.

The model is also referred to as the high frequency model because it applies for all frequencies above a threshold value (see assumptions above). Fung shows that the general integral equation method (IEM) model for rough surfaces converges to this model in the high frequency limit [118]. Therefore, scattering predicted by this model is frequency independent. (Although the wavenumber appears in this "edition" of the equations, it always cancels out.)

[10] The limit from only one direction needs to be considered because the scattering function is continuous almost everywhere and only one singular point in the finite plane exists.

Fig. 2-13 shows the average loss predicted by the radar equation for the monostatic case with SAR processing. The other terms in the radar equation used in this simulation, including the dielectric properties of the ice and the bedrock, are described in section 2.1.

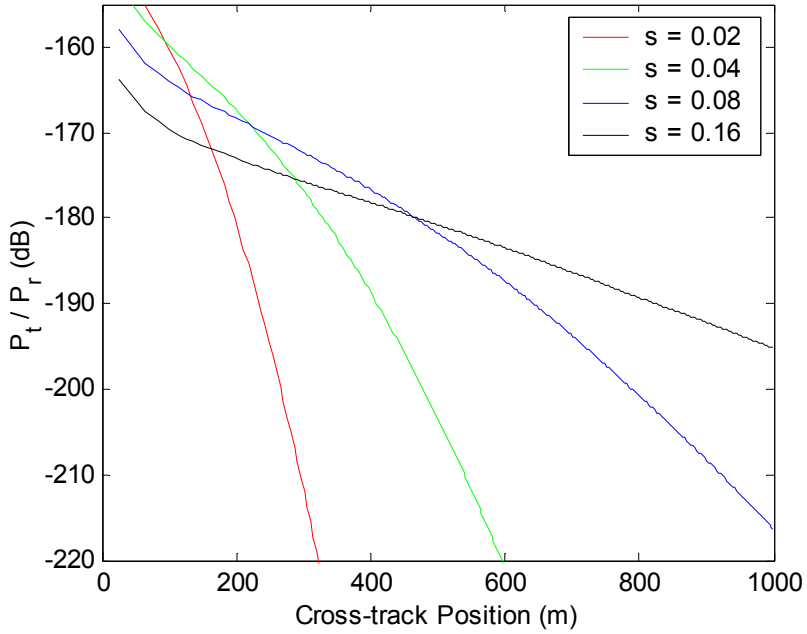

Fig. 2-13. Total loss at the radar's center frequency, 210 MHz, predicted by the radar equation using the physical optics for large RMS height model for the bed surface. The results for four different surface characteristics are plotted.

Physical Optics, Small Slopes Model

Unlike the physical optics model for large RMS surface heights, the small slope model puts no direct constraints on h. However, the RMS slope must be small for this model to applicable. The derivation of the model is given in Ulaby et al.

The scattering coefficient for this model is divided in to three parts: the noncoherent scattering σ_{pqn}, scattering due to slopes σ_{pqs}, and the coherent component σ_{pqc}. The total scattering coefficient is given by:

$$\sigma_{pq} = \sigma_{pqn} + \sigma_{pqs} + \sigma_{pqc}$$

where

$$\sigma_{pqn} = \left(\frac{k_1 l \left| \alpha_{0,pq} \right|}{2} \right)^2 \exp\left(- q_z^2 \sigma^2 \right) \sum_{n=1}^{\infty} \frac{\left(q_z^2 \sigma^2 \right)^n}{n! n} \exp\left[- \frac{\left(q_x^2 + q_y^2 \right) l^2}{4n} \right]$$

$$\sigma_{pqs} = - \left(k_1 l \left| \alpha_{0,pq} \right| \right)^2 \frac{q_z}{2} \exp\left(- q_z^2 \sigma^2 \right) \left| \alpha_{1,pq} \right|^2 \sum_{n=1}^{\infty} \frac{\left(q_z^2 \sigma^2 \right)^{n-1}}{n! n} \exp\left[- \frac{\left(q_x^2 + q_y^2 \right) l^2}{4n} \right]$$

$$\sigma_{pqc} = \pi \left(k_1 \left| \alpha_{0,pq} \right| \right)^2 \delta(q_x) \delta(q_y) \exp\left(- q_z^2 \sigma^2 \right)$$

$$\theta_t \approx \sin^{-1}\left(\mathrm{Re}\left(\frac{k_1}{k_2} \right) \sin\theta_i \right) \text{ (local angle of transmission),}$$

$$R_{\perp 0} = \frac{\eta_2 \cos\theta_i - \eta_1 \cos\theta_t}{\eta_2 \cos\theta_i + \eta_1 \cos\theta_t}$$

$$R_{\perp 1} = -R_{\perp 0} \frac{\eta_2 \sin\theta_i + \eta_1 \sin\theta_t}{\eta_2 \cos\theta_i + \eta_1 \cos\theta_t}$$

$$R_{\| 0} = \frac{\eta_1 \cos\theta_i - \eta_2 \cos\theta_t}{\eta_1 \cos\theta_i + \eta_2 \cos\theta_t}$$

$$R_{\| 1} = \frac{R_{\| 0} \left(\eta_1 \sin\theta_i + \eta_2 \sin\theta_t \right) + \eta_2 \sin\theta_t - \eta_1 \sin\theta_i}{\eta_1 \cos\theta_i + \eta_2 \cos\theta_t}$$

$$\alpha_{0,hh} = -R_{\perp 0} \left(\cos\theta_i + \cos\theta_s \right) \cos\left(\phi_s - \phi_i \right),$$

$$\alpha_{1,hh} = \mathrm{Re}\left\{ \begin{matrix} \alpha_{0,hh} \left[R_{\perp 0}^* \left(\sin\theta_s - \sin\theta_i \cos\left(\phi_s - \phi_i \right) \right) - R_{\perp 1}^* \left(\cos\theta_s + \cos\theta_i \right) \cos\left(\phi_s - \phi_i \right) \right] \\ \left(q_x \cos\phi_i + q_y \sin\phi_i \right) \end{matrix} \right\},$$

$$\alpha_{0,vh} = -R_{\perp 0} \left(1 + \cos\theta_i \cos\theta_s \right) \sin\left(\phi_s - \phi_i \right),$$

$$\alpha_{1,vh} = \mathrm{Re}\left\{ \begin{matrix} \alpha_{0,vh} \left[- R_{\perp 0}^* \sin\theta_i \cos\theta_s - R_{\perp 1}^* \left(1 + \cos\theta_i \cos\theta_s \right) \sin\left(\phi_s - \phi_i \right) \right] \\ \left(q_x \cos\phi_i + q_y \sin\phi_i \right) \end{matrix} \right\},$$

$$\alpha_{0,hv} = -R_{\| 0} \left(1 + \cos\theta_i \cos\theta_s \right) \sin\left(\phi_s - \phi_i \right),$$

$$\alpha_{1,hv} = \mathrm{Re}\left\{ \begin{matrix} \alpha_{0,hv} \left[- R_{\| 0}^* \sin\theta_i \cos\theta_s - R_{\| 1}^* \left(1 + \cos\theta_i \cos\theta_s \right) \sin\left(\phi_s - \phi_i \right) \right] \\ \left(q_x \cos\phi_i + q_y \sin\phi_i \right) \end{matrix} \right\},$$

$$\alpha_{0,vv} = -R_{\|0}\left(\cos\theta_i + \cos\theta_s\right)\cos\left(\phi_s - \phi_i\right),$$

$$\alpha_{1,vv} = \mathrm{Re}\left\{\begin{array}{l}\alpha_{0,vv}\left[R^*_{\|1}\left(\cos\theta_s + \cos\theta_i\right)\cos\left(\phi_s - \phi_i\right) - R^*_{\|0}\left(\sin\theta_s - \sin\theta_i\cos\left(\phi_s - \phi_i\right)\right)\right] \\ \left(q_x\cos\phi_i + q_y\sin\phi_i\right)\end{array}\right\}.$$

For monostatic or backscatter, the scattering coefficient reduces to

$$\sigma_{hhn} = \left(k_1 l\cos\theta_i\left|\Gamma_{\|0}\right|\right)^2\exp\left(-q_z^2\sigma^2\right)\sum_{n=1}^{\infty}\frac{\left(q_z^2\sigma^2\right)^n}{n!\,n}\exp\left[-\frac{\left(k_1 l\sin\theta_i\right)^2}{4n}\right]$$

$$\sigma_{vvn} = \left(k_1 l\cos\theta_i\left|\Gamma_{\perp 0}\right|\right)^2\exp\left(-q_z^2\sigma^2\right)\sum_{n=1}^{\infty}\frac{\left(q_z^2\sigma^2\right)^n}{n!\,n}\exp\left[-\frac{\left(k_1 l\sin\theta_i\right)^2}{4n}\right]$$

$$\sigma_{hhs} = -2q_z\sin\theta_i\left(k_1 l\right)^2\exp\left(-q_z^2\sigma^2\right)\left[\left|\Gamma_{\|0}\right|^2\sin\theta_i + \mathrm{Re}\left\{\Gamma_{\|0}\Gamma^*_{\|1}\right\}\cos\theta_i\right]$$
$$\sum_{n=1}^{\infty}\frac{\left(q_z^2\sigma^2\right)^{n-1}}{n!\,n}\exp\left[-\frac{\left(k_1 l\sin\theta_i\right)^2}{4n}\right]$$

$$\sigma_{vvs} = -2q_z\sin\theta_i\left(k_1 l\right)^2\exp\left(-q_z^2\sigma^2\right)\left[\left|\Gamma_{\perp 0}\right|^2\sin\theta_i + \mathrm{Re}\left\{\Gamma_{\perp 0}\Gamma^*_{\perp 1}\right\}\cos\theta_i\right]$$
$$\sum_{n=1}^{\infty}\frac{\left(q_z^2\sigma^2\right)^{n-1}}{n!\,n}\exp\left[-\frac{\left(k_1 l\sin\theta_i\right)^2}{4n}\right]$$

and

$$\sigma_{vh} = \sigma_{hv} = 0.$$

These equations show polarization dependence even for the backscatter scenario. Furthermore, for oblique scattering, horizontal polarization is larger than vertical polarization for scattering surfaces with higher permittivities and equal permeabilities. This is due to the Brewster angle effect. This polarization dependence is the opposite of the small perturbation model. Ulaby et al. provides several illustrations of the polarization dependence.

Because there is no restriction on the RMS height, there may be a significant coherent component with this type of surface. The coherent component can either be included as the scattering coefficient σ_{pqc}, or a modified Fresnel coefficient can be used: $\Gamma_{\|} = \left|R_{\|0}\right|^2 e^{-q_z^2\sigma^2}$ and $\Gamma_{\perp} = \left|R_{\perp 0}\right|^2 e^{-q_z^2\sigma^2}$. This modification differs by a factor of two in the

exponent as compared to the modified Fresnel coefficient for the small perturbation model.

This scattering model is also frequency dependent. Increasing frequency increases scattering near normal incidence and decreases scattering for near grazing angles. As frequency increases, this model approaches the physical optics model for large RMS heights.

Fig. 2-14 shows the average loss predicted by the radar equation for the monostatic case with SAR processing. The other terms in the radar equation used in this simulation, including the dielectric properties of the ice and the bedrock, are described in section 2.1.

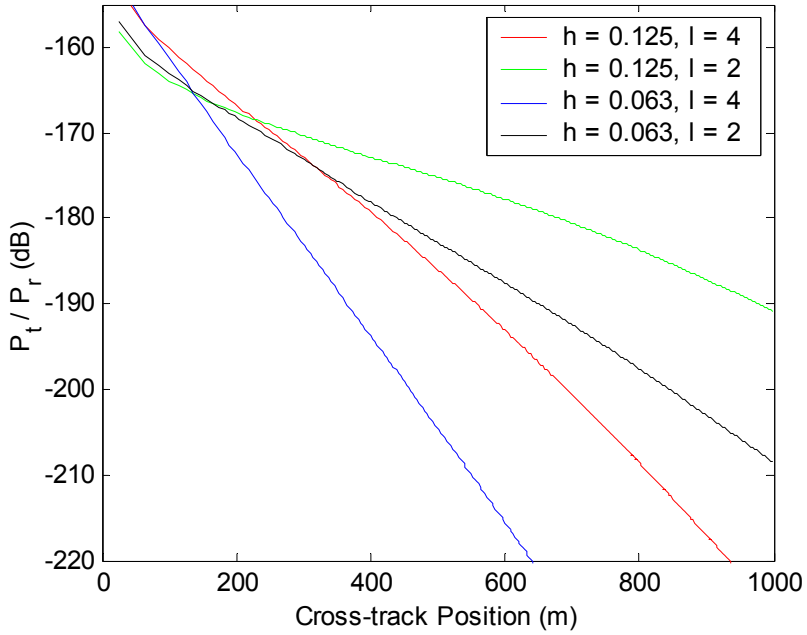

Fig. 2-14. Total loss at the radar's center frequency, 210 MHz, predicted by the radar equation using the physical optics for small slopes model for the bed surface. The results for four different surface characteristics are plotted.

Two-Scale Roughness

Each of the models covered thus far are limited to certain classes of surfaces. Many natural surfaces do not fall into only one of these categories. One extension to the above models is to combine the physical optics model for large RMS heights with the small

perturbation model. This model can represent surfaces with two-scale roughness (a large low frequency component and a small perturbation component). Ulaby et al. show that for the proposed work where the angles of incidence are far from grazing, the solution for this model is to simply add the scattering results of the two models together. The one modification that is made to the large RMS height result is to use the small perturbation's modified Fresnel coefficients rather than the Fresnel coefficients for a flat surface. Note that the small perturbation model has a coherent component which is not included in the two-scale roughness model (the coherent component is effectively replaced by the physical optics results).

Chapter 3: RADAR SYSTEM DESIGN

3.1 INTRODUCTION

The radar specifications are laid out in this chapter. The first section sets the general frame-work (e.g. selection of a side-looking SAR) and lists constraints on the system design such as size, coverage rate, etc. The next section details how the loop sensitivity and dynamic range specifications were determined from simulation. This is followed by a discussion of the antenna network. Finally, the requirements imposed by the bistatic operation needed to provide CMP measurements are considered. In the final two sections, a table summarizing the radar specifications and a set of block diagrams of the radar system are given.

3.2 PRINCIPLE DESIGN DECISIONS

The initial framework for the radar design is a ground based side-looking synthetic aperture radar. The ground-based operation provides flexibility and ease of testing as compared to an airborne platform. Side-looking synthetic aperture radar enables the radar to satisfy coverage and resolution requirements. Previous bedrock mapping missions have for the most part been restricted to nadir-looking sounder operation. Musil's work near the grounding line on the Bach Ice Shelf is an exception [119], [120], [121]. This system was operated along two very short traverses and for thin ice due to limitations of available technology. The concept of side-looking operation has also been reviewed briefly in [122]. Other efforts to apply synthetic aperture radar techniques have also been reported in the literature, but these are all nadir-sounding [123], [124], [125], [126], [127], [128], [129].

Ideally, the radar system would measure the full frequency spectrum with infinite signal to interference and noise ratio. However, finite resources constrain the design and concessions must be made. Due to design-time limitations we chose to use a proven antenna design and digital system. The antenna we used is a TEM horn antenna [130],

[131]. The antenna dimensions could be scaled with frequency, but the weight and shape of the antennas set a limit to the maximum number of elements and the minimum spacing between elements. The digital system uses a direct digital synthesis (DDS) waveform generator which can produce a fixed set of simple functions (e.g. linear FM chirp). The data acquisition system set the dynamic range, the maximum throughput (a function of PRF, sample word size, and number of samples), the maximum number of simultaneously sampled channels, and the maximum sampling frequency. For shipping and mobility considerations, the maximum cross-track dimension of the antenna network was set to be 4 m. Likewise, the maximum along-track dimension of the antenna network was set to 10 meters.

To achieve wide-area coverage in a reasonable time-frame, we chose a minimum coverage rate of $10\ \mathrm{km}^2 \cdot \mathrm{hour}^{-1}$. Due to vehicle limitations, our platform velocity is $\sim 3\ \mathrm{m} \cdot \mathrm{s}^{-1}$, so our total swath width needs to be $\sim 1\ \mathrm{km}$. Due to the high loss through the ice and the low backscatter expected in some regions (details given later in this section), the maximum cross-track distance to an image pixel must be less than or equal to $1\mathrm{km}$ from the radar. Considering that a side-looking radar cannot image in the nadir direction because the ground-range resolution goes to infinity for normal incidence[11], to meet the coverage rate requirement the radar should image both sides of the platform to achieve our desired total swath width. By imaging both sides of the platform simultaneously rather than just one side, the effective swath width is doubled as shown in Fig. 3-1. Since we additionally require nadir sounding and broadband operation, a cross-track antenna array with multiple transmit and receive channels is used. With multiple channels we can apply spatial filters to focus the beam towards nadir for depth sounder data collection while simultaneously steering beams to the left and right side of the platform for side-looking data collection. Additionally, digitally combining channels circumvents the problem of controlling the antenna's radiation pattern over a broad

[11] The cross-track resolution is $r_c = \frac{v\tau_c}{2\sin\theta_i}$, where v is the speed of electromagnetic waves in the media, τ_c is the compressed pulse width of the radar , and θ_i is the incidence angle [132].

bandwidth since spatial filters can be applied as a function of time-frequency and incidence angle to target.

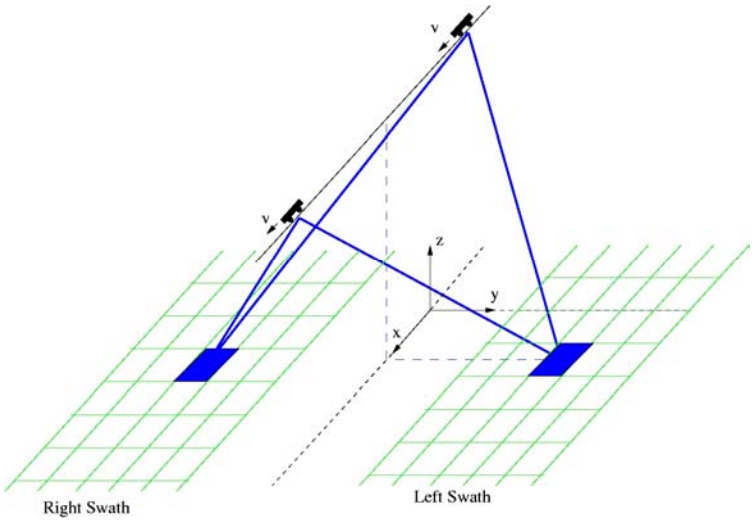

Fig. 3-1. The SAR imaging geometry for left and right swaths. The y-axis aligns with the cross-track dimension.

The selection of the frequency band depends on a number of factors. First, the spectrum used should have wavelengths that correspond to the roughness parameters of interest. Given the broad limits of the roughness parameters in Table 1-2, this frequency range covers VHF and UHF bands. Additionally, the spectrum should span at least an octave in the frequency range to measure frequency sensitive parameters. Finally, ice loss increases rapidly above 500 MHz (details in section 2.1), suggesting the use of frequencies lower than this. Given that the maximum cross-track dimension of the antenna network is 4 m and using both a receive and transmit array, the lowest frequency of operation that will allow sufficient left-side to right-side isolation during SAR operation is 120 MHz. At 120 MHz, this corresponds to a 12.5 degree beamwidth (details in section 3.4).

The low frequency sets the minimum size of the TEM horn antenna element as defined by a return loss of 10 dB. The TEM horn antenna element is broadband and does not, in terms of return loss, practically limit the upper frequency. However, the size of the individual elements, 0.61 m on a side, restricts the minimum spatial sampling rate. The need to meet the Nyquist spatial sampling rate, half of one wavelength, coupled with

the digital system's maximum sampling frequency of 720 MHz, suggested an upper frequency of 300 MHz. The unambiguous range of directions of arrival at 300 MHz is $\pm\sin^{-1}\left(\frac{c}{2df\sqrt{\varepsilon_{r,snow}}}\right) = \pm 39$ deg [12]. Due to the small topographic slopes expected for the bed and high ice loss, scattered energy is not expected beyond these angles. Regarding the waveform generation, 300 MHz is 42 percent of 720 MHz, which provides a sufficient guard band for proper alias rejection.

The design analysis above considers direct digitization only. This imposes an artificial upper limit set by the sampling frequency of the digital system. Heterodyne operation circumvents this limitation. However, there are several reasons why direct digitization is chosen. The primary advantage to direct digitization is the simplification of the transmitter and receiver since no mixing stages are required. Another advantage is that we cover more octaves of the frequency range given a fixed bandwidth when using lower frequencies; an important feature when measuring frequency sensitive parameters. Furthermore, antenna position resolution and dielectric error tolerance for phase sensitive processing increases inversely proportional to frequency. On the other hand, the restriction to lower frequencies implies poorer spatial resolution given the fixed antenna array dimensions.

The final system parameters that are considered in this section are the loop sensitivity and dynamic range. To determine the required loop sensitivity and dynamic range, the radar equation is used to find the expected received signal power as a function of depth in the ice sheet. Loop sensitivity and dynamic range requirements are derived from these results. Since the expected received signal power is a function of time, the requirements on these two parameters will likewise be functions of time.

3.3 LOOP SENSITIVITY AND DYNAMIC RANGE

The required loop sensitivity is a function both of the expected signal-to-noise ratio determined from the radar equation and the required signal-to-noise ratio needed to

[12] $\varepsilon_{r,snow} \approx 1.7$

appropriately process the data. In other words, the radar must not only overcome the loss from spherical spreading, dielectric loss, etc., there must be sufficient SNR to perform analysis. Therefore, the required loop sensitivity is the maximum expected loss times the SNR requirement. With the SAR images of the bed, we plan to perform both roughness-dielectric analysis and interferometric techniques on the data. For interferometric SAR, a 10 dB SNR is necessary to keep the interferogram coherence level sufficiently high for elevation extraction [133], [134], [135]. We will investigate the effect of SNR on the roughness-dielectric analysis (currently this SNR requirement is left open).

The required SNR for internal layer detection depends on our desired probability of detection and false alarm rates. For example, to detect an internal layer with a probability of detection of 95% and false alarm rate of less than 5%, we need an SNR of ~12 dB [136]. The proposed work does not consider analysis of the internal layer reflections to estimate the cause of the reflection, but it is worth noting that this analysis will likely set more stringent SNR requirements than reported here.

The loop sensitivity for internal layer detection and the maximum expected signal power as a function of time are shown in Fig. 3-2a. Likewise, the loop sensitivity and maximum expected signal power for imaging as a function of cross-track position are shown in Fig. 3-2b. For the latter plot, the loop sensitivity is the minimum of Fig. 2-12 through Fig. 2-14 and the maximum expected power is the reflection from a specular bed of water, $\varepsilon_{r,bed} = 81$. The dynamic range is the maximum expected signal power divided by the loop sensitivity. It is plotted in Fig. 3-3a and Fig. 3-3b respectively.

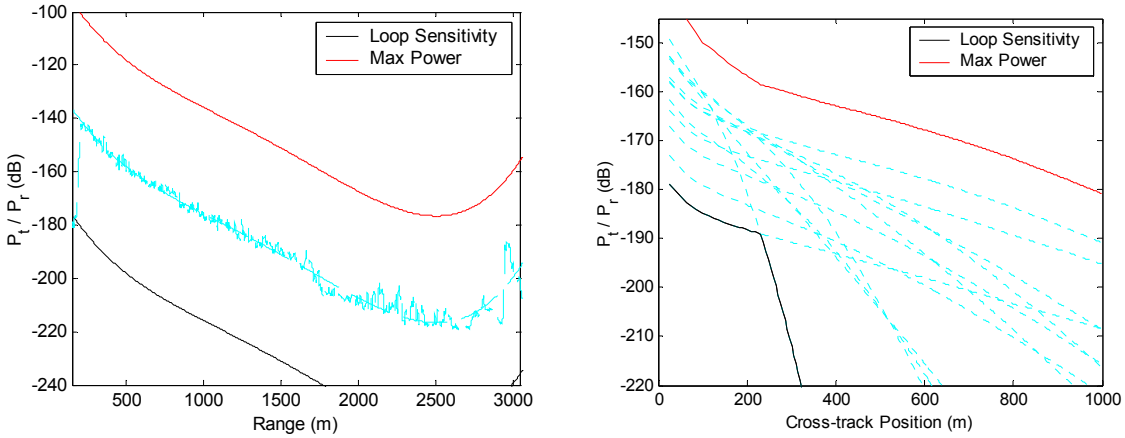

Fig. 3-2. a) Loop sensitivity and maximum expected power from internal layer reflections plotted versus time. b) Loop sensitivity and maximum expected power from basal scattering plotted versus cross-track dimension (individual test cases are shown as dashed lines in the background).

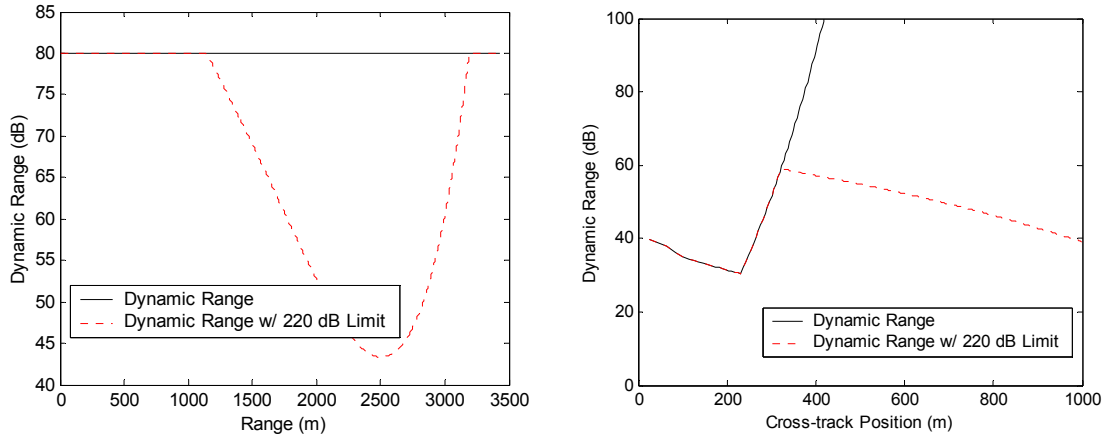

Fig. 3-3. a) Dynamic range plotted versus time. b) Dynamic range plotted versus cross-track dimension.

A further complication arises when pulse compression is used to increase signal-to-noise ratio. In this case, a long pulse of length τ_{pulse} is generated that simultaneously engages many layers of the ice sheet. See Fig. 3-4 for an illustration of this. In this example, the radar must be sensitive to the weak return from layer B while not saturating when receiving the return from layer A.

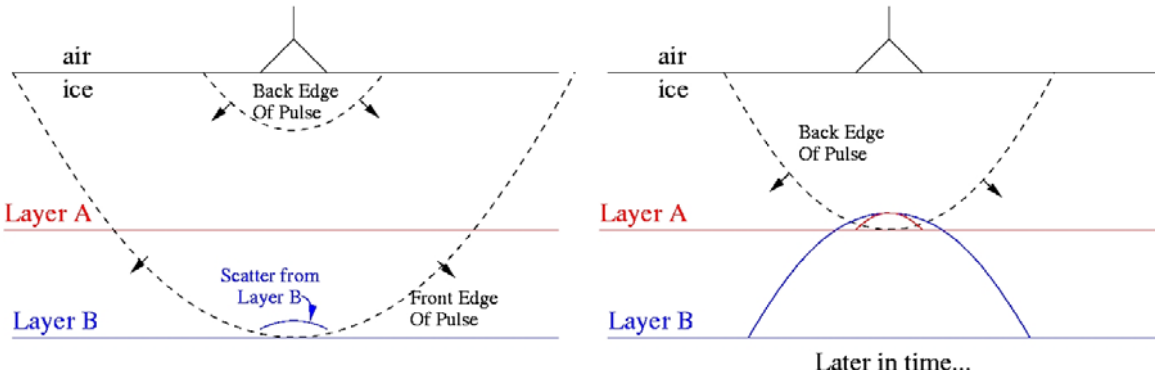

Fig. 3-4. Illustration of pulse compression's effect on dynamic range. The scattering from layer A is typically larger than the scattering from layer B because there is less spherical spreading loss and extinction of the wave. Because of the long pulse duration, these two scattering sources concurrently arrive at the receiver.

Based solely on the above simulations and measurements, the required loop sensitivity to image all bedrock types and all internal layers to the base is not possible given our (or any) budget and space requirements. Therefore, the budget and space constraints must also be considered. The space requirement of a 4-m wide antenna array set the maximum antenna gain that we could achieve. Our budget was able to afford two 400-W pulsed linear AB amplifiers. The reason for choosing two amplifiers of lower power rather than a single high power amplifier is two fold. First, with two amplifiers we can drive two separate antennas simultaneously and thus achieve the effect of 800 W without the cost of a power combiner. Second, if one amplifier failed we would have a spare. Another constraint on the system was that we could only support two data acquisition systems, which required that we multiplex our eight receive channels through two data acquisition channels.

Based on these competing constraints, we set our required loop sensitivity to 220 dB. This loop sensitivity appears to be sufficient for many of the rough surfaces that we might encounter in Greenland. Clearly, there are some locations where this loop sensitivity will be insufficient to image the bed.

The loop sensitivity, LS, of the radar system is a function of numerous system parameters according to:

$$LS = \frac{P_t N_{chan} N_{ave} G_{pc}}{kTBF}$$

where

$P_t = 800$ W is transmit power,

$N_{chan} = 2$ is the number of data acquisition channels,

$N_{ave} = \frac{\lambda f_{PRF}}{2\sin(\theta_t(L_{SAR}))v_{platform}} = 8490$ is the number of coherent averages,

$\lambda = \left.\frac{c}{f\sqrt{\varepsilon_{r,snow}}}\right|_{f=120\text{ MHz}} = 1.1$ m is the wavelength in snow at the radar's center frequency of 210 MHz,

$f_{PRF} = 6900$ Hz is the pulse repetition frequency set by the data acquisition system,

$v_{platform} = 3\ \text{m}\cdot\text{s}^{-1}$ is the velocity of the platform,

$G_{pc} = \tau_{pulse} B$ is the pulse compression gain,

$k = 1.3806505(24)\times 10^{-23}\ \text{J}\cdot\text{K}^{-1}$ is Boltzmann's constant,

$T = 298$ K is the receiver temperature,

$B = 180$ MHz is the receiver bandwidth,

and

F is the noise figure of the receiver.

Most of the constants above are self-explanatory, but the origin of N_{ave} needs further explanation. The number of coherent averages is determined by calculating the longest length of pre-summations, referred to hereafter as the unfocussed SAR aperture, which does not impact the SAR resolution and then accounting for the number of radar pulses which are transmitted in this aperture. From the science requirements, we must provide a pixel size of 10 m. Since the raw SAR image should be incoherently averaged to reduce the effects of speckle or fading, we chose an along track resolution of $r_a = 5$ m. The SAR

aperture length, L_{SAR}, is defined here as the length at which the beam-pattern of the SAR places a null in the adjacent pixel (5 m away). This corresponds to a $\frac{\lambda}{2}$ phase shift across the aperture from a wave originating from an adjacent pixel (see Fig. 3-5). The half-beamwidth as defined by the first null is a more complicated function than the simple geometry shown in Fig. 3-5 due to refraction and we thus define it as $\theta_t(r_a)$. This SAR aperture length is then $L_{SAR} = \frac{\lambda}{2\sin(\theta_t(r_a))} = 586$ m. This SAR aperture length now becomes the finest unfocussed SAR resolution allowed. Any finer resolution will begin to destructively cancel the pixel energy that the SAR processing uses. The half-beamwidth for the unfocussed SAR resolution, as defined by the first null, is $\theta_t(L_{SAR})$. Using the same $\frac{\lambda}{2}$ phase shift criterion, the largest unfocussed SAR aperture is $L_{unfocused} = \frac{\lambda}{2\sin(\theta_t(L_{SAR}))} = 3.7$ m. The number of pulses taken in the aperture is $N_{ave} = \frac{L_{unfocused} f_{PRF}}{v_{platform}} = 8490$.

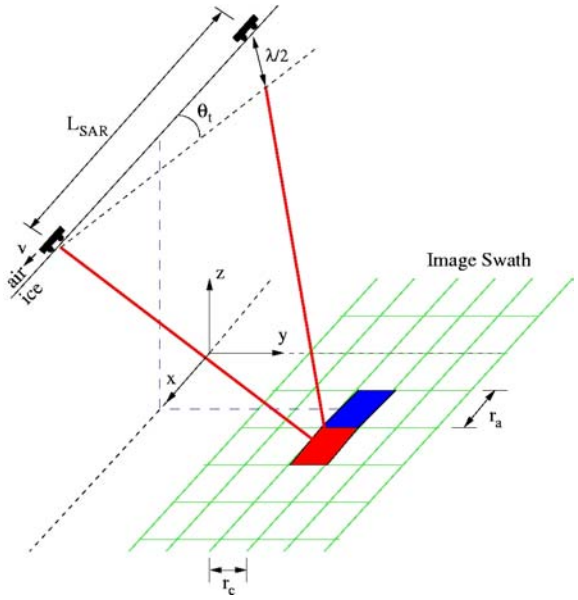

Fig. 3-5. Demonstration of beamwidth (defined null to null) requirement to achieve an along track resolution of r_a.

The two unknowns in the loop sensitivity equation are the pulse compression gain and the noise figure of the receiver. Since the bandwidth is 180 MHz, we only need to know the transmit pulse duration to calculate the pulse compression gain. We would like to maximize the pulse duration subject to the dynamic range requirement. Based on the analysis described in the following dynamic range discussion, we set the pulse duration to $\tau_{pulse} = 10\ \mu s$, which provides a pulse compression gain of $G_{pc} = \tau_{pulse} B = 32.6\ \text{dB}$. Based on available technology, we were able to achieve a receiver noise figure of 2 dB (includes band-pass-filter and limiter insertion losses used to protect the receiver). The loop sensitivity is then 223 dB. However, the following factors must be considered:

6. 10 μs pulse only transmitted 8 out of 9 pulses (see dynamic range discussion for the reason for this)
7. Power amplifier has non-flat gain and the average power is 50% of peak power[13].
8. Antenna feed network, including the low pass filter and transmit antenna switches which followed the power amp add 2 dB of loss.

The new loop sensitivity calculation is 218 dB, which is 2 dB short of our desired loop sensitivity.

The dynamic range is a function of the analog-to-digital converter, compression gain, number of channels, coherent averages, receiver blanking, transmit waveform, and thermal noise to quantizer noise ratio. The analog-to-digital converter is a 9-bit converter, with approximately 8 effective bits [137]. This gives a raw dynamic range of

$$D_{ADC} = 8(6\ \text{dB}) = 48\ \text{dB}.$$

The compression gain adds

$$D_{pc} = 10\log_{10}(G_{pc}) = 10\log_{10}(B) + 10\log_{10}(\tau_{pulse}) = 82.6\ \text{dB} + 10\log_{10}(\tau_{pulse}).$$

The two receiver channels add

$$D_{chan} = 10\log_{10}(N_{chan}) = 3\ \text{dB}.$$

The coherent averages add

[13] With predistortion of the transmit pulse, this power loss could have been circumvented. However, our transmit waveform was generated by a DDS which could only produce a simple linear FM chirp.

$D_{ave} = 10\log_{10}(N_{ave}) = 39.3 \text{ dB}$.

Receiver blanking does not change the dynamic range, but protects the receiver during transmission. The length of the blanking period is set by the transmit waveform's pulse duration τ_{pulse} and the scattering properties of the scene. The thermal noise to quantizer noise floor ratio must be sufficiently large to allow effective coherent averages (i.e. dithering) [138]. Essentially, the maximum number of effective coherent averages is set by this ratio and can be determined by laboratory measurements of the analog-to-digital converter[14]. To determine our required maximum number of averages, we consider two constraints. The first is that we wanted to be able to slow, and even stop, the platform to allow more coherent averages when an increased SNR was desired. Also, when calibrating the radar system via loopback tests, we take many averages to determine the transfer function of the system. To accommodate this functionality, we set the desired coherent averaging capability to one million averages (2.5 minutes of averaging at a PRF of 6900 Hz). Based on lab measurements, we set our minimum thermal noise to quantizer noise floor to $D_{dither} = 20 \text{ dB}$.

We consider two pulse durations here, $\tau_{pulse} = 1\,\mu\text{s}$ and $\tau_{pulse} = 10\,\mu\text{s}$:

$$D_{1\,\mu s} = D_{ADC} + D_{pc}\Big|_{\tau_{pulse}=1\,\mu\text{s}} + D_{chan} + D_{ave} - D_{dither} = 92.9 \text{ dB}$$

$$D_{10\,\mu s} = D_{ADC} + D_{pc}\Big|_{\tau_{pulse}=10\,\mu\text{s}} + D_{chan} + D_{ave} - D_{dither} = 102.9 \text{ dB}$$

By adjusting the receiver gain and transmitter pulse width of three different radar configurations, we found we were able to meet most of the dynamic range and loop sensitivity requirements. The three configuration settings are given in Table 3-1. The transmitter transmits 9 different waveforms. The first waveform is 1 μs and the second through ninth are 10 μs. When the 1 μs waveform is transmitted, the two receivers/data acquisition channels have different gain settings to cover different regions of the required dynamic range. The low-gain channel's gain does not raise the thermal noise floor above the quantizer noise floor, so its dynamic range is less because of this. Also, $D_{1\,\mu s} = 83 \text{ dB}$ because this transmit waveform is only sent about 10% of the time. Almost 90% of the

[14] The digital system employs zero-pi modulation which is essential to taking advantage of dithering.

time, the 10 μs waveform is transmitted and both receive channels are being used to sample at maximum gain. The sixteen combinations possible with the 10 μs waveforms (8 transmit pulses with 2 receivers) are used to sample each of the possible antenna configurations (see section 3.4 below for more detail on the antenna network). This technique of utilizing multiple radar configurations required creating software and hardware that allowed the radar configuration (e.g. digital attenuator settings, transmit waveform, etc) to change on a pulse-to-pulse basis.

Table 3-1: Radar Waveforms

Configuration	Transmit Waveform	Receiver Channel	Start Range	Max. Loss	Min. Loss
1 μs low-gain	1	1	150 m	160 dB	90 dB
1 μs high-gain	1	2	1200 m	200 dB	117 dB
10 μs high-gain/SAR	2-9	1 & 2	1700 m	218 dB	116 dB

3.4 ANTENNA NETWORK

Both the transmitter and receiver use an array of elements where each element is a TEM horn antenna [130], [131]. To ease shipping and manufacturing problems, we chose the same element type and size for both arrays. The minimum frequency of operation was determined by the antenna networks' ability to provide sufficient left/right isolation and suppression of the nadir (specular) echo while meeting our maximum cross-track array dimension of 4 m. The isolation and suppression requirement translated to an approximate footprint size of 500 m (footprint size on the bed defined by the null to null spacing). A plot of footprint size versus frequency is shown in Fig. 3-6 for a 4-m long transmit and receive antenna array. Only the outside elements of the transmit array are used. The reason for this is discussed later. Based on these results, the low frequency was set to 120 MHz. The footprint is ~700 m, which is larger than desired, but simulations showed that this still provided 10 dB of nadir suppression.

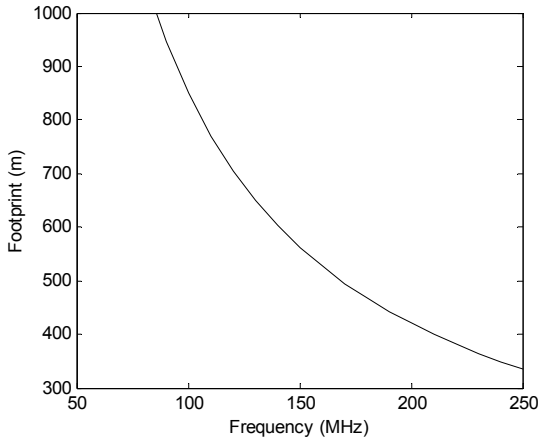

Fig. 3-6. Footprint of antenna array versus frequency. This assumes that only the outside elements of the transmit array are used.

Based on data taken in 2004 with the TEM horn antennas, we found that the antenna element size would need to be ~24 inches on a side to provide sufficient matching at 120 MHz. This meant that we could place eight elements in the array. Because we need the ability to electronically scan with our array, we cannot simultaneously excite transmit elements arrayed in the cross-track dimension since this would fix the main lobe of the transmit array. Therefore, each element of the transmit array must be excited one at a time. Due to data system limitations, we could not meet our Nyquist sampling rate and multiplex across both transmit and receive elements (8 receive elements times 8 transmit elements equals 64 configurations). To solve this problem, we used a sparse transmit array with two elements, one on each end of the array. This technique produces a cross-track beam pattern that is approximately half as large, but the side lobe performance is similar to a single element. An analogous situation arises when a real aperture is compared to a SAR aperture. The SAR aperture has twice as fine resolution (half the beamwidth), but the side lobe performance is worse. The reason for this difference is that both the transmitter and receiver move together which doubles the phase-delay.

To increase our transmit power and gain and to improve the return loss of our transmit antennas, we arrayed two transmit antennas in the along track direction. This also allowed for a convenient way to combine the power of our two amplifiers. The TEM horn elements have significantly better return loss when arrayed in the H-plane rather

than fed as single elements. This improvement in return loss is shown in Fig. 3-7 (based on S-parameter measurements taken at Summit, Greenland).

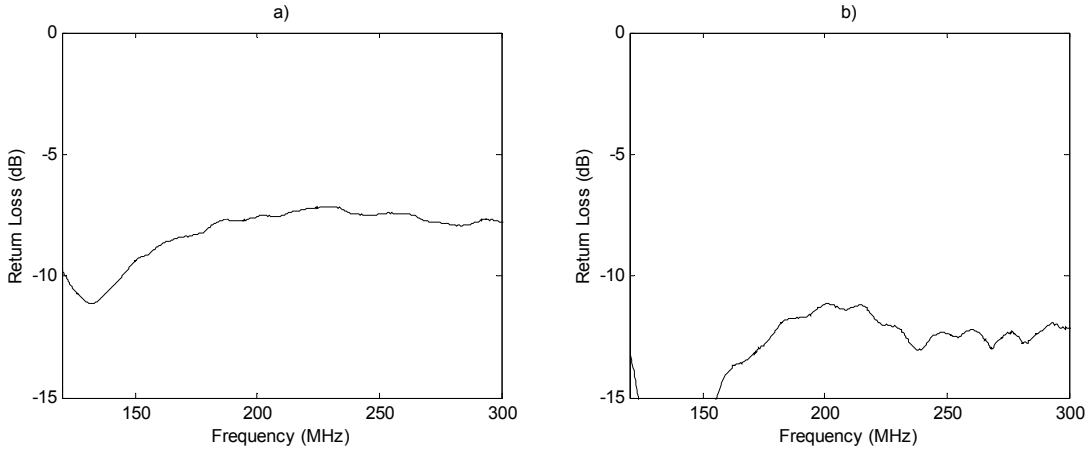

Fig. 3-7. Return loss of a) a single antenna and b) two H-plane arrayed antennas fed simultaneously.

Another technique for improving both the noise figure of the receiver and improving the matching to the receive elements is to place the low noise amplifier at the input to the antenna. Any mismatches or "ringing" that occurs between the antenna and the low noise amplifier settles rapidly because the transmission line connecting the two is very short[15]. A DC bias on the RF feed cables is used to power the amplifiers.

The E-plane and H-plane simulations of the antennas at our center frequency are shown in Fig. 3-8 [95]. A diagram of the antenna network is given in Fig. 3-9.

[15] The reverse isolation of the LNA is more than 10 dB which reduces reflections through the LNA to a tolerable level.

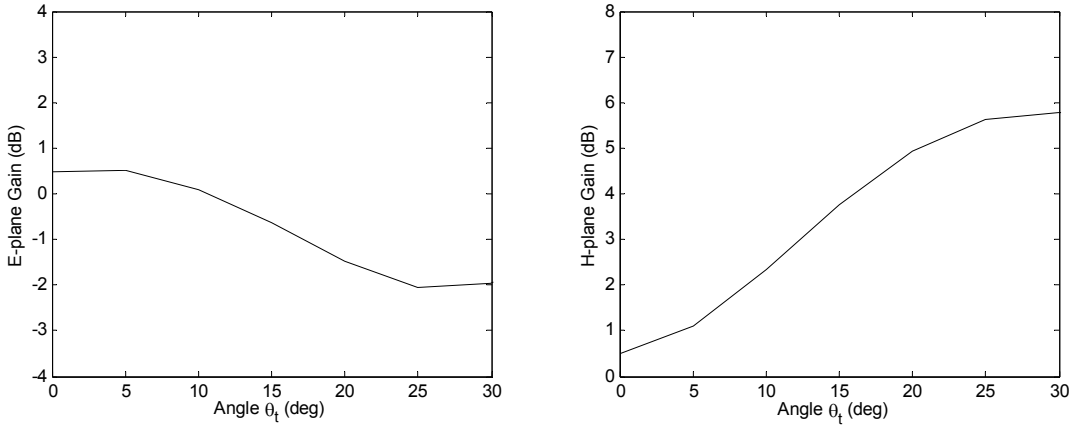

Fig. 3-8. Simulated a) E-plane and b) H-plane antenna gain patterns of TEM horn antennas at 210 MHz (main lobe is at zero degrees and patterns are nearly symmetrical about the main lobe).

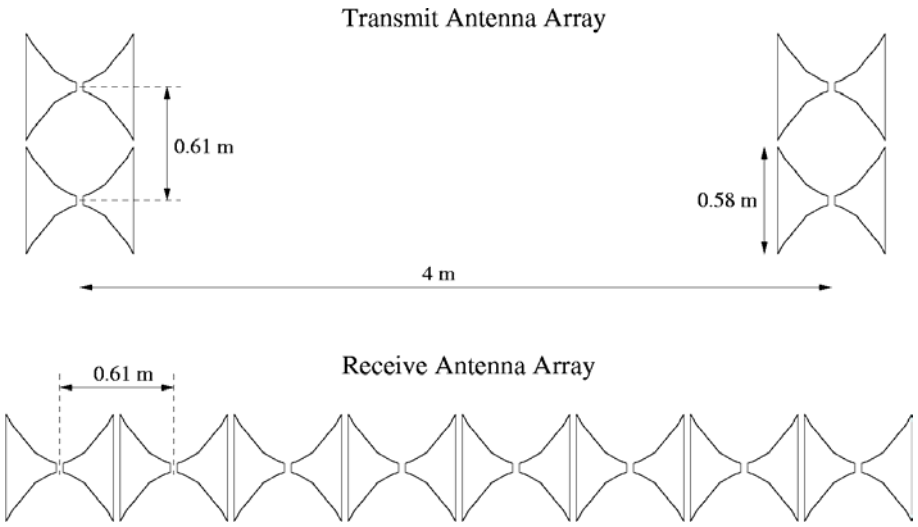

Fig. 3-9. Diagram of antenna network configuration.

3.5 BISTATIC RECEIVER

For the bistatic receiver to operate, it must synchronize control and timing signals with the transmitter. It also needs to provide phase synchronization even when the raw signal (uncompressed and minimal coherent averages) is 30-50 dB beneath the noise floor. This is provided through two mechanisms. The first is an IEEE 802.11 wireless network that provides a link to synchronize the radar control parameters such as pulse repetition frequency, transmit waveform, position and heading information, etc. The

second mechanism provides the timing synchronization (locking the PRF signal and locking the phase). To do this, both the monostatic transmitter and bistatic receiver are referenced off an atomic standard, programmable, 10-MHz Rubidium source. Additionally, the PRF signal is programmable.

The radar control parameters are transported through the network so that each end of the system (transmitter and bistatic receiver) knows what the transmitted pulse will be, the PRF, and other pertinent radar settings. After the transmitter begins transmitting, the bistatic receiver software scans the entire pulse period (equal to the time between pulses) into a temporary buffer by adjusting the offset of the data capture trigger in reference to the PRF signal. Once the entire pulse period has been captured, the temporary buffer is analyzed to find the direct path signal. Then, using high-precision position and heading information, the range between transmit and receive antennas is found. This range is then used to offset the location of the direct path signal in the data capture window so that the bistatic receiver's PRF signal is aligned with the transmitter's PRF signal.

Once the PRF signals are locked, the bistatic receiver software begins monitoring the phase and range bin of the direct path signal. As the radar system moves, new range and heading information is used to provide accurate range information to the software. Using this range information and the phase/range-bin of the direct path signal, the Rubidium source's frequency is adjusted until the unexpected phase/range-bin drift in the direct path is zero. After phase locking, the bistatic software allows data to be recorded to disk, but continues monitoring the direct-path signal and making adjustments to the Rubidium source as needed.

The phase synchronization requires a very accurate estimate of the range between the transmit and receive antennas. Using a twentieth of a wavelength as a guideline for maximum position error, at 300 MHz, the position accuracy should be better than 3 cm. To provide this quality of ranging information, a differential global positioning system is used. This provides position information with an error standard deviation of 1 cm in latitude and longitude, and 2 cm in elevation.

3.6 RADAR SPECIFICATIONS

A consolidated list of the radar system specifications is given in Table 3-2. The only parameter that is not discussed above is the maximum device-to-device reflection level. This was set to 30 dB to ensure low side lobes due to these reflections.

Table 3-2: Radar System Specifications

Specification	Value
Frequency Band	120-300 MHz
Loop Sensitivity	220 dB
Dynamic Range	130 dB
Pulse Repetition Frequency	6900 Hz
Transmit Power	800 W
Receiver Noise Figure	2 dB
Maximum Device to Device Reflection	-30 dB
Number of ADC Channels	2
Transmit Channels	2
Receive Channels	8
Others	– Multiple transmit waveforms – Radar parameters configurable on a pulse to pulse basis -- PRF and stable local oscillator configurable from software for bistatic operation

3.7 BLOCK DIAGRAMS AND SYSTEM INSTALLATION

This section gives an overview of the radar system and its workings. For an in-depth description of each component of the radar system, please see [139]. Fig. 3-10 shows the flow of control and data to and from the various sections of the radar system. To aid in the discussion, the system is divided into seven sections as shown in Fig. 3-10: computer, digital, receiver, transmitter, clock synthesizer, power-amp, and multiplexer sections. Dashed lines indicate the flow of control/timing information and solid lines illustrate signal flow (whether in analog or quantized form).

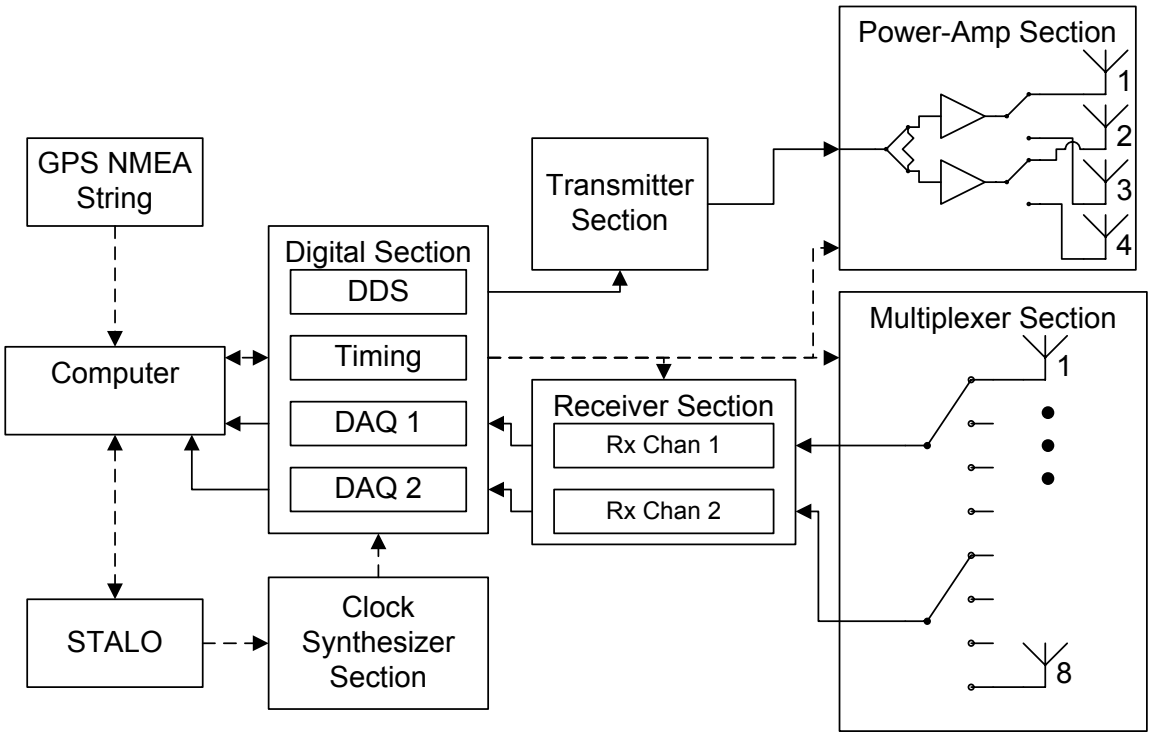

Fig. 3-10. Radar system diagram.

The computer interfaces directly to the serial port and to the digital section. One serial port is configured to be receive-only and the software simply records GPS strings as they are transmitted from the GPS receiver. The string is interpreted to give the radar operator live updates of position. Another serial port is used to program the stable local oscillator (STALO). The computer's primary functions are to control the digital section and capture and record radar data. Several features of the software are specific to this radar system and therefore warrant explanation. In the following discussion, we use the term "waveform" to signify the radar settings, waveform data points, and data acquisition settings associated with a particular pulse period. We required that these waveforms be user configurable for ease of use and adaptability in the field. Because of the large number of waveform settings (over a hundred individual settings in a typical configuration), we implemented a configuration file interface. Secondly, because the number of waveforms is user configurable, the real-time data display was implemented to allow for an arbitrary number of plots to be loaded. Each plot can display multiple waveforms with user-settable post-processing options: coherent integrations, incoherent integrations, pulse compression, signal-to-noise markers and frequency markers.

Another potential pitfall that the software has to avoid is digital section buffer overflows. The buffers in the digital section can only hold a single record in memory. Therefore, the software must upload the data immediately to prevent buffer overflows. To guarantee the highest level of responsiveness, the data-upload and recording tasks were each given their own thread. Also, a large first-in-first-out (FIFO) was implemented in the recording thread to hold many data records at once. In case a write to the hard drive stalls, the data thread can continue to write to the FIFO. The FIFO also held data for display to the graphical user interface. Since the real-time display was secondary to data capture, all post-processing besides coherent integrations is performed inside the graphical user interface thread.

The digital section is comprised of three parts: timing, DDS, and DAQ. The timing subsystem not only generates all the timing signals for the DDS and two DAQs, it also configures the timing backplane for the radar system and generates all the radar control signals. The DDS generates the linear FM chirp waveforms and its output is connected to the transmitter section. The two DAQs capture waveforms from each of the respective receivers in the receiver section. The clocking of samples for both the DDS and DAQs is from the 720 MHz clock synthesizer.

The clock synthesizer section is shown in Fig. 3-11. The phase locked oscillator is implemented inside a configurable Silicon Labs part which is loaded on power-up by an on-board programmable logic device. The signal is then amplified and filtered before being distributed to each DAQ and the DDS. To minimize channel mismatch, power dividers with very tight amplitude and phase balance specifications were used.

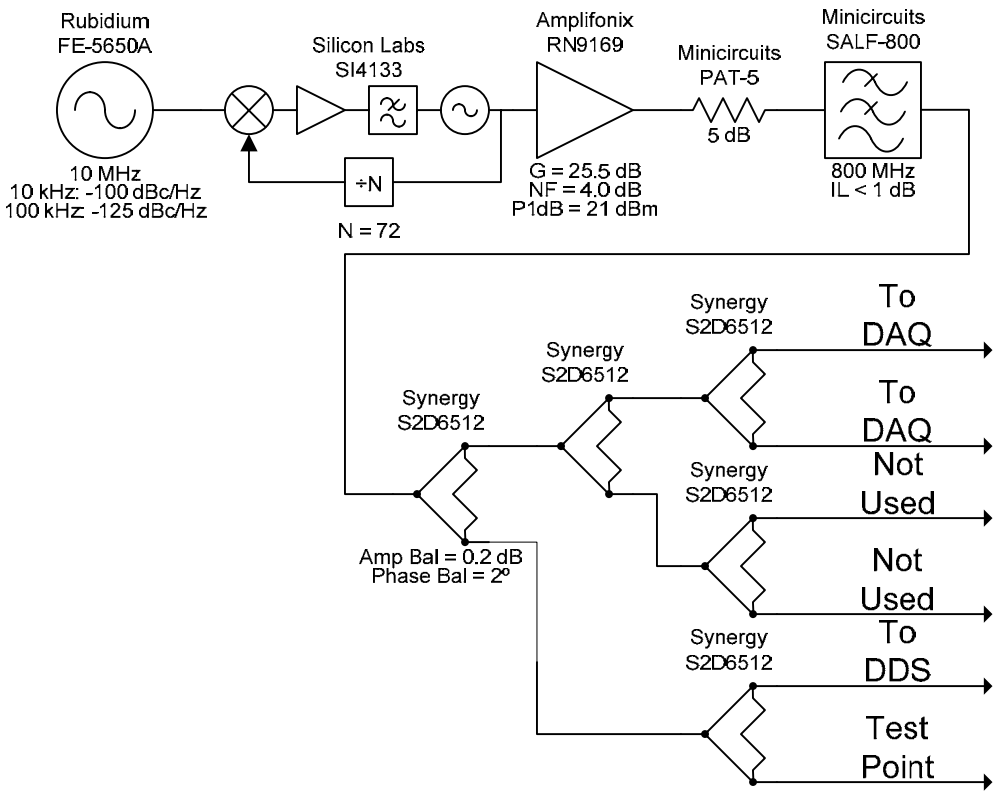

Fig. 3-11. Block diagram of clock synthesizer.

The DDS generates the pulse which is then filtered, amplified, and filtered again by the transmitter section, shown in Fig. 3-12, before being sent to the power-amp section. The DDS also generates a calibration tone after the linear FM chirp is generated. The single-pole double-throw (SPDT) switch is used to pass this calibration signal to the receiver, bypassing the power-amp section. Thus, the calibration tone passes through the transmitter and receiver sections, but is slightly outside the band of interest so that it does not interfere with the signal. The calibration tone is used to verify the phase and amplitude stability of the radar and to verify that the timing section was not producing any jitter in the data.

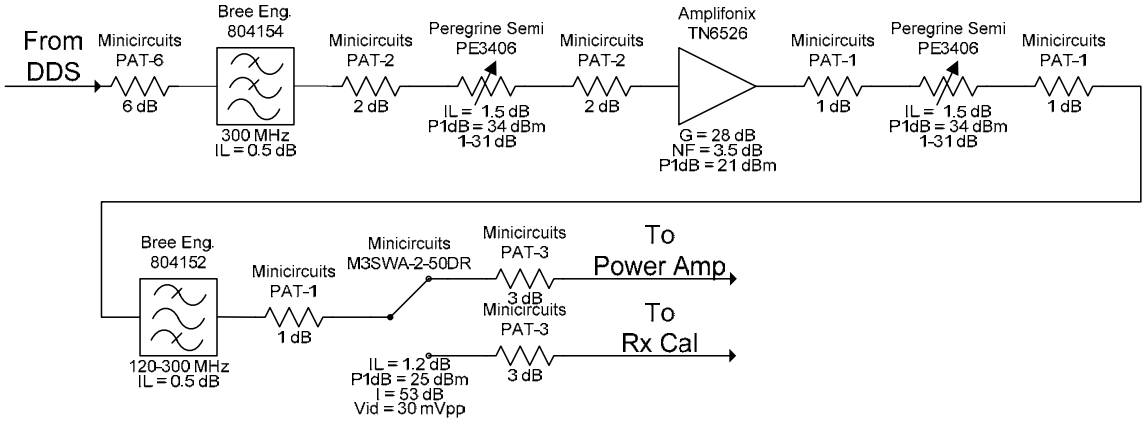

Fig. 3-12. Block diagram of transmitter.

The transmitter section, shown in Fig. 3-13, feeds into the power-amp section. The power-amp section amplifies the signal using two 400-W power amplifiers operating in parallel. The switches then control which pair of antennas are active. A picture of the transmit antenna array in the field is shown in Fig. 3-14. Since the switches share the same control line, the same pair of antennas (1 and 2) or (3 and 4) are always enabled together. Two important notes about this section are warranted. First, because power amps tend to have very large harmonics, a high-power filter is essential after the power amp. Secondly, the off-port of high-power switches (pin diode construction) do not usually have absorptive outputs. Because of coupling between the active pair of antennas and the inactive pair, an additional switching stage was added in the switch so that the off port would be terminated into a high-power 50-Ω load.

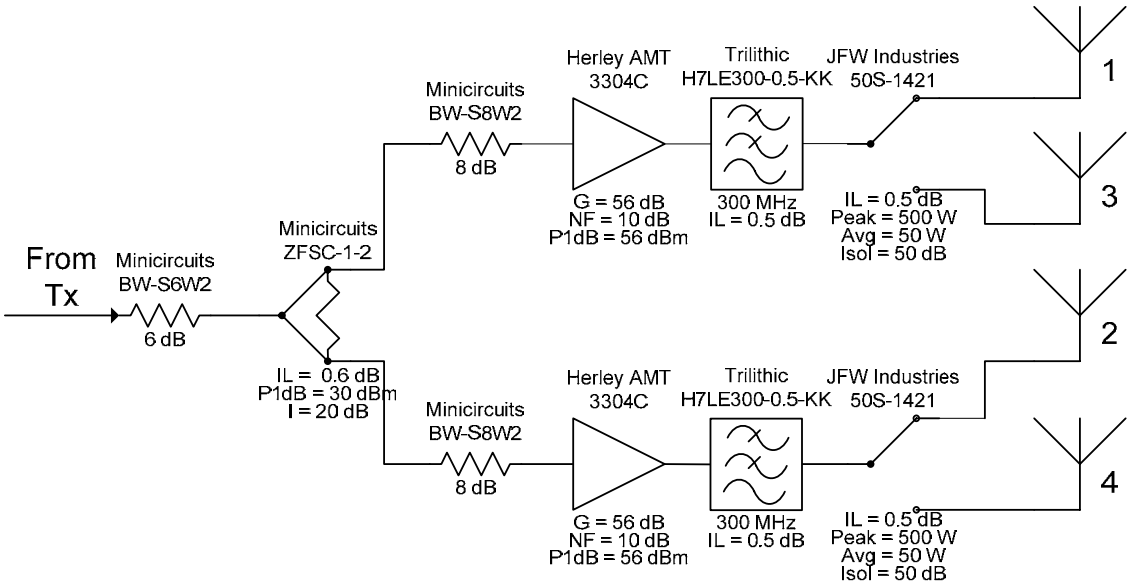

Fig. 3-13. Block diagram of power-amp section which includes the antenna feed network.

Fig. 3-14. Transmit antenna array with 4 TEM horn antennas. The transmit array really consists of two pairs of antennas which operate in parallel for improved return loss characteristics.

After the signal is transmitted, it scatters off englacial and subglacial features and is coupled into one of the eight antennas, see Fig. 3-16. The eight antennas are attached to the multiplexer section of the radar. The block diagram of the multiplexer section is shown in Fig. 3-15. The band-selection filter and low noise amplifier (LNA) is placed at the output of the antenna to reduce reflections off the antenna and to improve the noise figure of the receiver chain. The LNA has a built in limiter to protect the receiver circuitry. Power to the LNA is supplied from the main radar system via a DC-bias. Finally, the eight receive channels are multiplexed onto two channels and passed to one of the two receivers. Similar to the switch in the power amp section, an *absorptive* SP4T switch is used to perform the multiplexing operation.

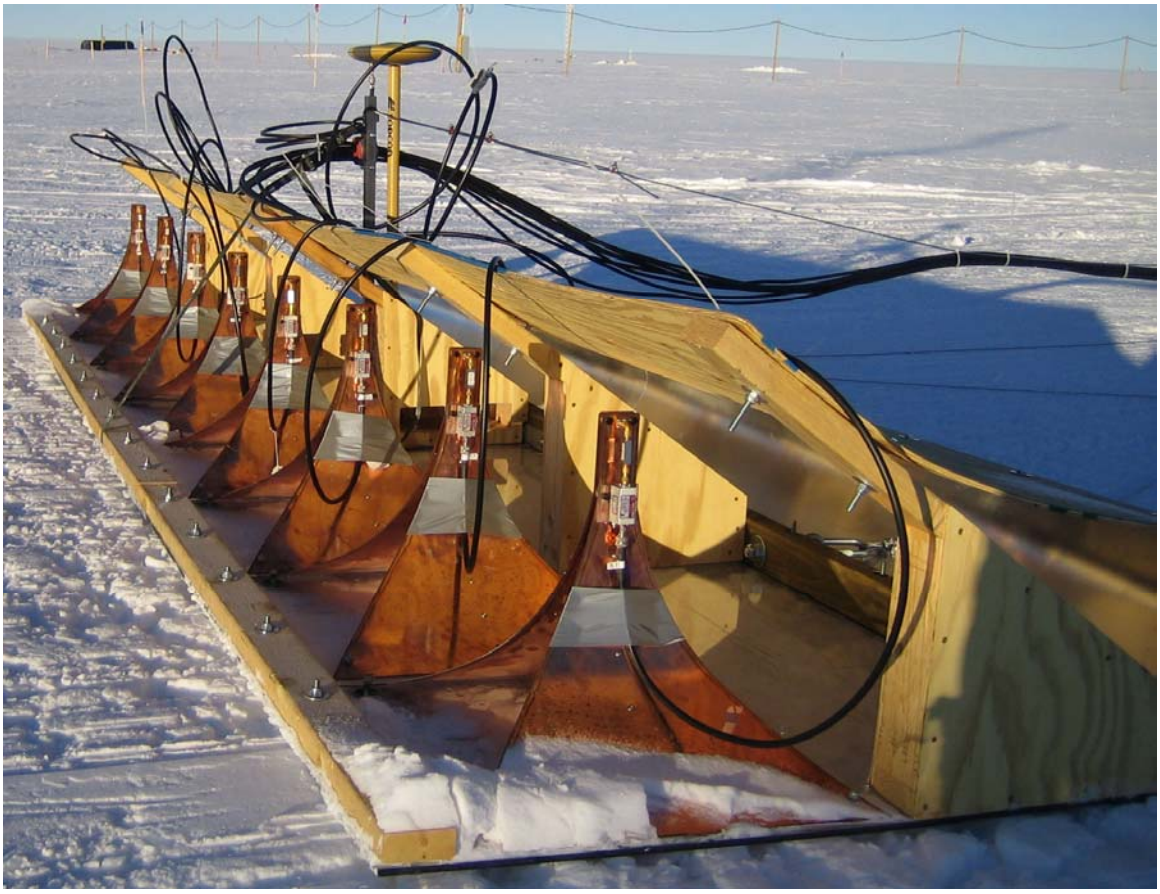

Fig. 3-15. Receiver antenna array with 8 TEM horn antennas. The front-end band pass filter and low noise amplifier are fastened directly to the antenna connector.

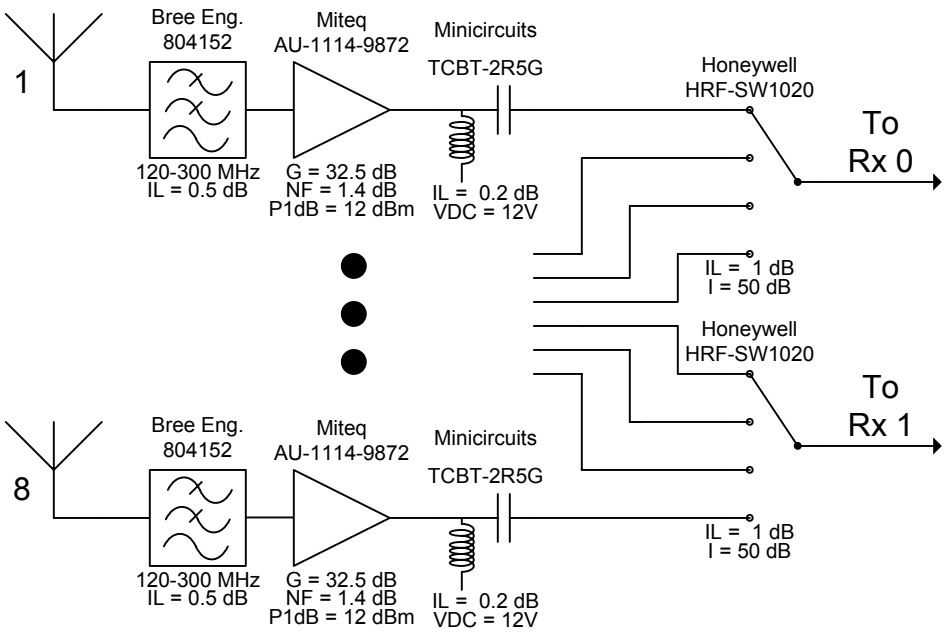

Fig. 3-16. Block diagram of receiver front-end and multiplexer.

The two signal paths from the multiplexer section are passed into the two receive channels in the receive section. Both receive channels are identical so that the block diagram of only one receive channel is shown in Fig. 3-17.

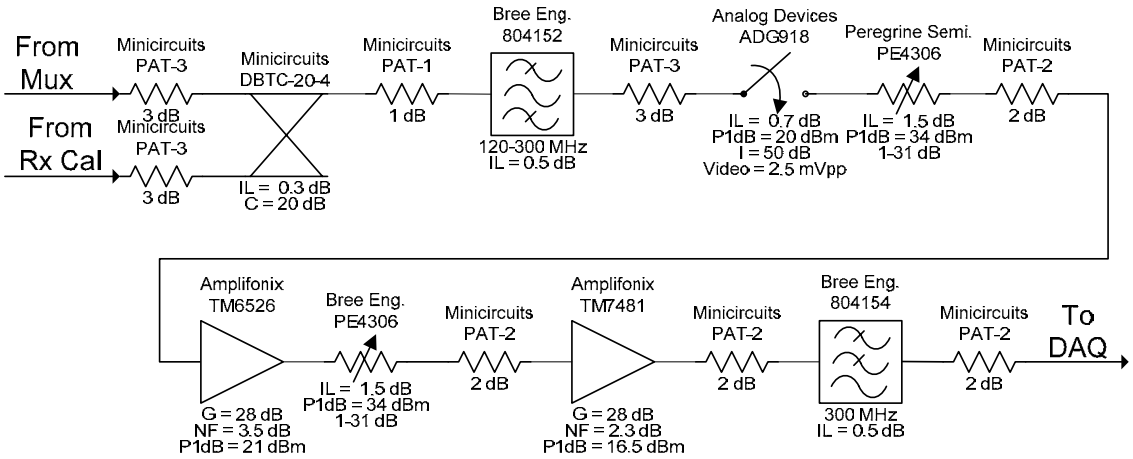

Fig. 3-17. Block diagram of a single receiver channel.

The radar system installed on the tracked vehicle (Tucker Sno-Cat) is shown in Fig. 3-18. The transmit antennas are carried on the front sled and the receive antennas are carried on the back sled. The separation between front and back sleds is approximately 10 m. This

pseudo-bistatic configuration provides over 70 dB of isolation between the two systems and helps protect the receive circuitry from the high power transmit pulse without the need for a circulator or T/R switch. A close-up picture of the rack-mounted portion of the radar system installed in the cab is shown in Fig. 3-19. A gasoline-powered electric generator with high quality sine wave output is strapped to the top of the cab. The output of the generator is passed through an uninterrupted power supply (UPS) with automatic voltage regulation (AVR). All electronics are powered from the UPS. The power-amps take 220 V and an additional transformer is used to step-up the voltage. Finally the carrier-phase DGPS receivers for each of the antenna arrays are housed in the cab as well. A laptop running windows was used to remotely run the radar software and collect the DGPS data. The DGPS data collection is done by PCCDU, a Microsoft Windows recording program written by the DGPS receiver's manufacturer.

Fig. 3-18. Radar system and antenna network.

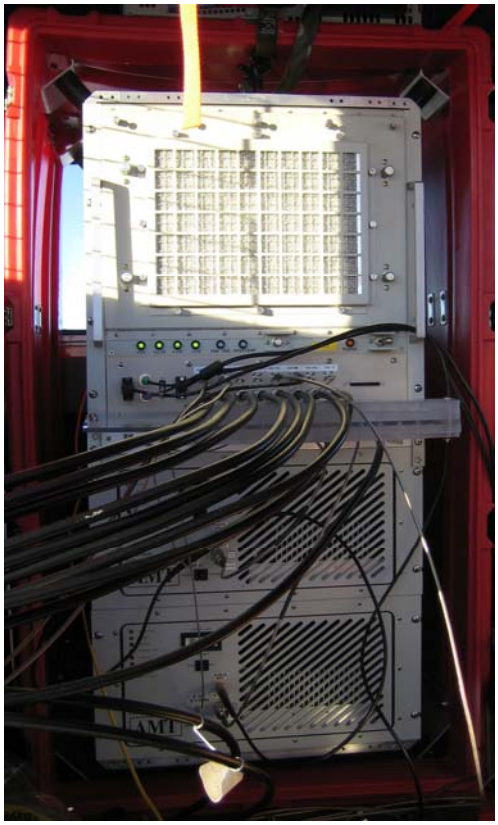

Fig. 3-19. Radar system installed in the tracked vehicle. The system fits inside a rugged 21U 19" rack which is installed inside the cab of the tracked vehicle. The UPS is mounted on top of the rack, and the carrier sensitive DGPS systems and step-up transformers are mounted on the floor of the cab.

Chapter 4: DATA PRECONDITIONING

4.1 INTRODUCTION

This chapter describes the various steps involved in the preparation of the data before they are passed to the imaging algorithms (f-k migration or SAR processing). These steps include synchronization of the radar and DGPS data, calibration of the radar data which is equivalent to a matched filter that removes all cable delays so that all channels have a common time zero reference, grouping of data into sequences for management purposes, and finally, the uniform along-track re-sampling of the data for wavenumber domain filtering.

4.2 TRAJECTORY DATA

To enable image processing and position tagging of data, two Topcon global positioning system (GPS) units were used to record GPS data. The carrier-phase GPS data from each unit are recorded by Topcon's PCCDU Microsoft Windows software. One unit also outputs a National Marine Electronics Association (NMEA) string to the radar system computer. This string's primary purpose is to provide a coarse synchronization between the radar system and GPS time. This is done by time-stamping the arrival of each new NMEA string (10 NMEA strings are sent per second). The radar data are likewise time-stamped by the computer upon arrival. By comparing these time-stamps we can synchronize the GPS data with the radar data. Due to unknown delays in the serial port and data acquisition path, this method has limited resolution – probably on the order of a hundred milliseconds or less. While this delay may be problematic for airborne applications, it is insignificant considering our slow-moving platform, which is both unable to change heading or speed rapidly. While a detailed explanation of every step of the DGPS processing is available in [140], there are several important points and assumptions that should be pointed out.

The primary problem encountered during post-processing the Summit, Greenland data is that the post-processor provides poor accuracy for substantial portions of the traverse. Topcon representatives were unable to provide insight and an in-house heuristic algorithm was generated to alleviate the problem. Parts of the algorithm are automated, but some portions involve manual and best-guess work. This algorithm for correcting the data has the important feature that it produces continuous position records. The imaging algorithms tend to be more tolerant to continuous and slowly varying position errors – as these types of errors usually cause minor defocusing and shifting of target locations. Sudden jumps in position errors can result in severe target decorrelation since they do not correspond to a simple shift of the Doppler centroid. The steps of the process are outlined here:

Step One…

Instead of passing a single DGPS file to the post-processor, we concatenated the files into groups of three (the largest size that the post-processor could handle). We then post-processed the data in overlapping segments. For example, assume we collected five DGPS files and label these files A, B, C, D, and E. We would then create three concatenated files: {A,B,C}, {B,C,D}, and {C,D,E}. Each of these files would be post-processed so that each location would have up to three solutions (see how file C is in all three concatenated files).

The post-processor provides a solution-type tag for each position: fixed or float. A location tagged as fixed should be high-precision and a location tagged as float has low-precision. The problem with passing a single DGPS file, e.g. file C, into the post-processor was that the output would have many float solution-types. These offending positions tended to be at the beginning of the file: the DGPS routine is similar to a filter and suffers from transients. Furthermore, the float solution-types are usually clumped together and the post-processed position would make a sudden "jump" when the solution type switched between fixed and float. This jump in position was usually between 0.1 and 2 meters which could cause significant problems to the phase-sensitive imaging algorithms. The jumps also only occurred at solution-type transitions. In other words, no jumps occurred in contiguous groups of fixed or float solutions.

Step Two…

After post-processing, the multiple results for each location are combined using the following algorithm:

1. If fixed solution-types are available, the mean of the fixed solutions is taken as the final result.
2. When a group of float solution-types are encountered, we apply an affine correction to the group based on the fixed solution-types that surround the group of bad data. Since the correction method is identical and is the applied independently along each basis of the coordinate system, we consider only a single axis. As noted above, a jump in position occurs at the transition from fixed to float solution-type. The same occurs at the transition from float back to fixed solution-type. The affine correction is based on this jump. First, we create a first-order polynomial fit to the last three seconds of good data. This polynomial is used to predict what the next position should have been. The difference between this predicted position and the float solution is the starting error of the affine correction. The same is done at the end of the group of float solutions and this becomes the ending error. A line is then fit to these two errors and added to the float solution types.

This method is accurate if the post-processor's fixed solutions are good and the GPS errors have low spatiotemporal bandwidth. The latter assumption is what DGPS post-processing uses to improve relative position accuracy. An example of data before and after the correction is shown in Fig. 4-1.

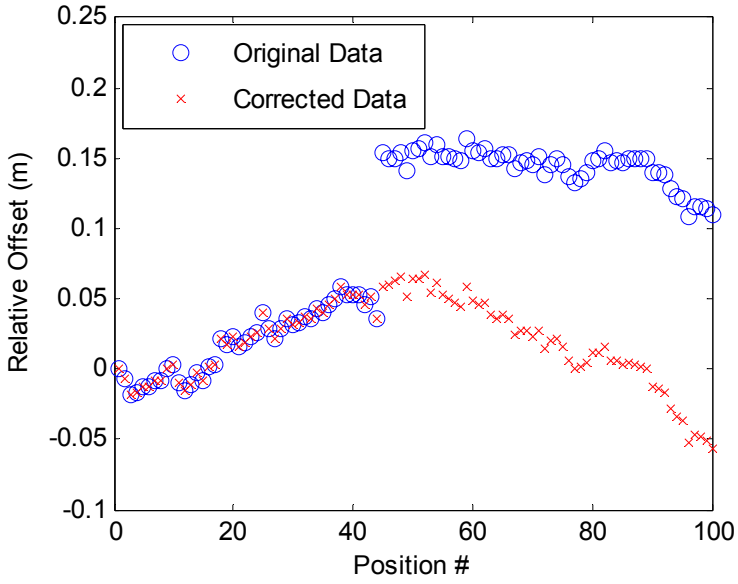

Fig. 4-1. Example of automated correction at fixed-float solution-type transition.

Step Three…

The final step is to apply manual corrections to locations that are clearly in error, but that the post-processor still marked as fixed solution-type. To this end, a graphical user interface in Matlab was created that allows the user to apply three different types of corrections. The first is a linear correction which allows the locations-in-error to be replaced with a line. The second is a jump correction identical to what is described in step two only the jumps are replaced manually. (The jumps are easily identified by sudden changes in position, but do not occur at fixed-float solution-type transitions.) The third correction type is a substitution of locations from another source. Since both transmit antenna array and receive antenna array sleds have DGPS receivers mounted on them, and these sleds track each other fairly closely, we can exploit this redundancy. If only one of the DGPS receivers is in error and the error can not be fixed with just a linear or jump correction, we use a substitute correction. This involves determining a heading vector from the DGPS data and applying an affine offset to the good set of DGPS data which is used to replace the bad DGPS data. Fig. 4-2 through Fig. 4-4 show examples of all three of these corrections.

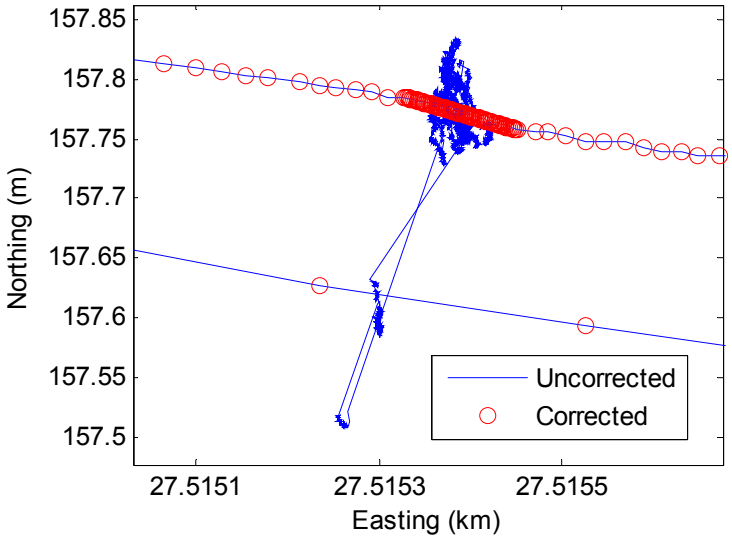

Fig. 4-2. Example of linear correction when vehicle was stationary.

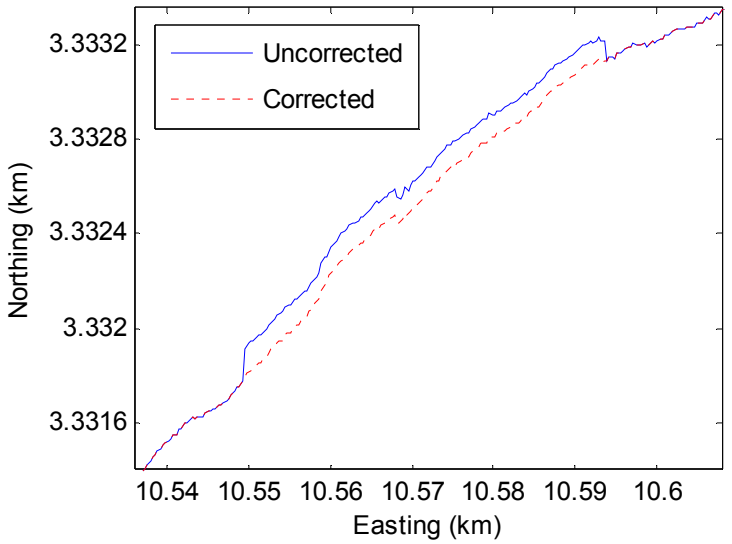

Fig. 4-3. Example of jump correction.

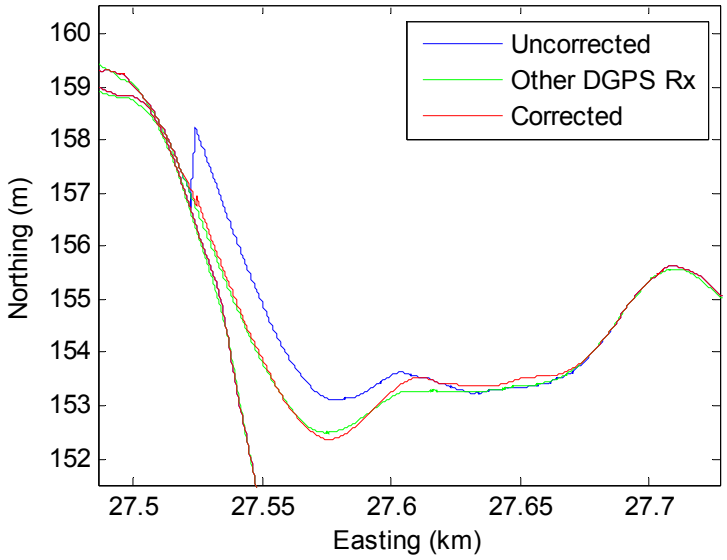

Fig. 4-4. Example of substitute correction.

One final filtering step is applied to the trajectory data: when the SAR processor loads the trajectory data, the cross-track and along-track positions are averaged over 4 m of along-track movement and the elevation is averaged over 400 m of along-track movement. The long average for the elevation vector is justified based on observations made while taking the measurements.

4.3 CALIBRATION

4.3.1 CALIBRATION MEASUREMENTS

The calibration of the radar involves taking a loopback measurement of the radar system. The loopback measurement ideally connects the transmit antenna cable to the receive antenna cable for every channel combination so that all components in the system are measured. However, because of the high power amplifier and the high gain of the receiver, attenuation must be added to protect the receiver's circuitry. Also, there is significant direct coupling from the power amp into the receiver. This direct coupling is essentially internal electromagnetic interference (EMI) and is coherent since it is the pulse energy from the power amp coupling into the receiver. To record a signal that consists only of the desired loopback signal, we include a fiber delay line that delays the

loopback pulse by more than 10 us. Ten microseconds is chosen because this is the longest pulse width we use with the system and the EMI occurs with almost no time delay. The calibration setup is shown in Fig. 4-5. Note that each of the unused transmit ports is terminated into a 50 Ω high power load.

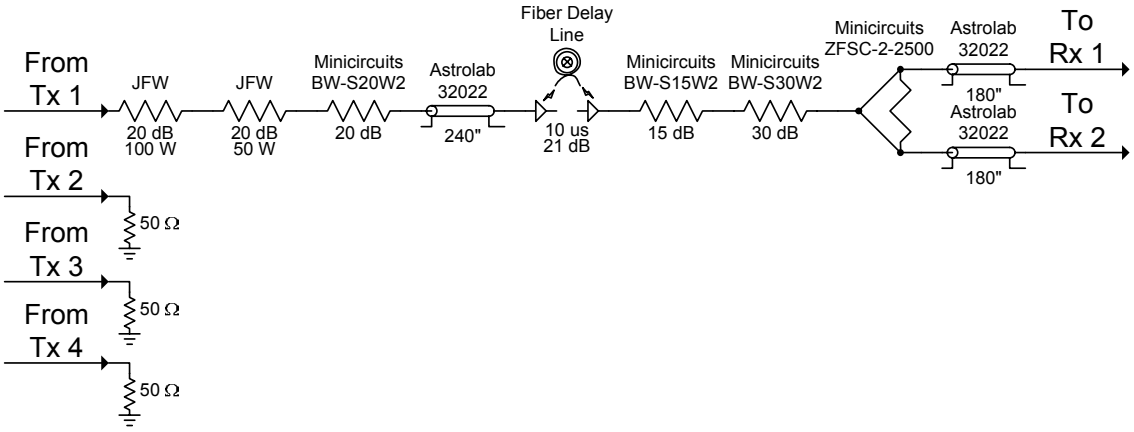

Fig. 4-5. Block diagram of calibration setup.

Because the calibration setup is not normally in the signal path, we must remove the effect these components have from our calibration measurements. This is done by taking network analyzer measurements of each of the components and dividing out the transfer function in the frequency domain. In general, let us assume that there are N devices in the calibration setup that need to be removed. Let the S-parameters of the N^{th} device be defined as $[S_i(f)]$. We then approximate the transfer function of the calibration as:

$$H_{cal}(f) = [S_1(f)]_{21}[S_2(f)]_{21}[S_3(f)]_{21}\cdots[S_N(f)]_{21}.$$

There are two possible $H_{cal}(f)$ – one for each path of the splitter. Because of this, S_{21} for the splitter should be along the path of interest (i.e. one of the paths will actually use S_{31} of the splitter if port 1 is the input port and port 2 and 3 are the output ports). The transfer function, $H_{Meas}(f)$, of the calibration measurement is

$$H_{Meas}(f) = H_{Tx}(f)H_{Cal}(f)H_{Rx}(f) = H_{Sys}(f)H_{Cal}(f)$$

where $H_{Tx}(f)$ is the transfer function of the transmitter, $H_{Rx}(f)$ is the transfer function

of the receiver, and $H_{Sys}(f) = H_{Tx}(f)H_{Rx}(f)$ is the desired transfer function. Solving for $H_{Sys}(f)$ we find

$$H_{Sys}(f) = \frac{H_{Meas}(f)}{H_{Cal}(f)}$$

This is an appropriate technique when the following is satisfied: 1) the signal-to-noise ratio (SNR) is very large at all frequencies, and 2) inter-device reflections in the calibration setup are insignificant. When measuring the calibration setup with the network analyzer, the setup is broken in to multiple low-attenuation sections and averaging is used to ensure a large SNR. Furthermore, the return loss of the attenuators used in the calibration is very high, >40 dB, at our low frequencies of operation.

The radar system captures $H_{Meas}(f)$ indirectly by capturing a discrete time-domain signal, $h_{Sys}(n)$. The discrete Fourier transform is used to find a discrete version of $H_{Meas}(f)$. The frequency samples of $H_{Meas}(f)$ do not necessarily line up with the frequency samples of the device measurements, $[S_i(f)]_{21}$. Since the amplitude of each $[S_i(f)]_{21}$ is a slowly varying function of frequency and the phases are nearly linear, we use linear interpolation to find the values of $[S_i(f)]_{21}$ at the frequency points $H_{Meas}(f)$ is known at. Also, because of hardware limitations the frequency range covered by each $[S_i(f)]_{21}$ does not cover the same frequency range as $H_{Meas}(f)$ which is a baseband signal. Because $[S_i(f)]_{21}$ *is* evaluated at all frequencies where significant energy is present in the system, we only need to make sure that there are no sudden transitions in its spectrum. In other words, we can not just zero-pad $[S_i(f)]_{21}$. The method we use is to linearly extrapolate the phase and to extrapolate the amplitude with the nearest neighbor method. Fig. 4-6 shows $[S_i(f)]_{21}$ before and after extrapolation. We also force conjugate symmetry as shown in the figure.

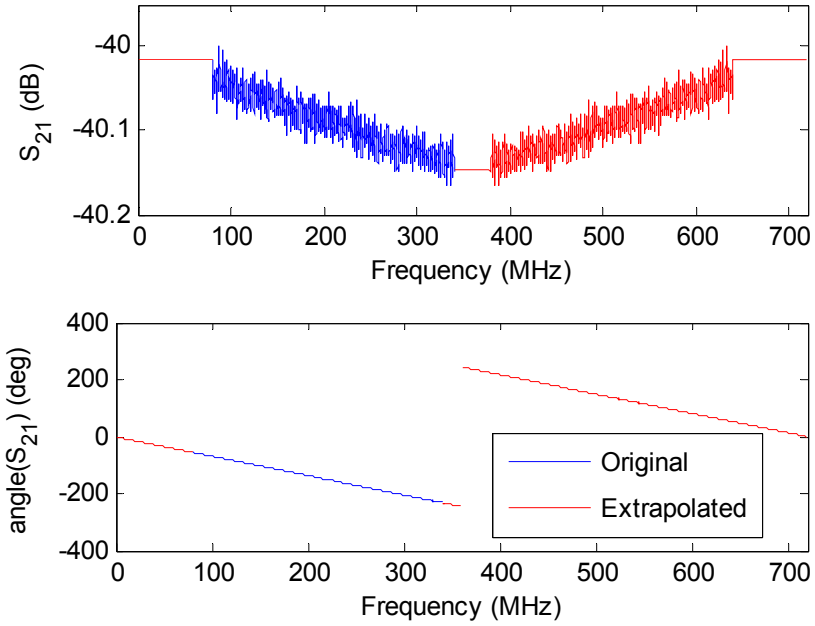

Fig. 4-6. $[S_i(f)]_{21}$ *before and after extrapolation.*

Since there are two transmit antennas active at any given time and each signal path has its own phase and amplitude distortions we measure both of these paths. In the actual measurements these two paths are essentially added together in phase (all targets of interest are in the main lobe of the two-element array). Therefore the reference function is simply the summation of these two paths as well.

To ensure a high SNR for the calibration measurements, 1000000+ pulses are coherently averaged. After averaging and deconvolution as described above, we truncate the end of the time-domain record to remove unwanted time-domain noise as well as circular convolution effects from the deconvolution step. The signal is then down-converted to baseband, $h_{Sys}(n)\exp(-j2\pi f_c t(n))$ where $t(n)$ is the time-axis. The next step is to normalize the baseband signal to create a reference function for matched filter pulse compression: $h_{Ref}(n)=\dfrac{h_{Sys}(n)\exp(-j2\pi f_c t(n))}{\left\|h_{Sys}(n)\exp(-j2\pi f_c t(n))\right\|_2^2}$. The normalization ensures that system effects are removed. For example, a power level of 0.01 at the output of the properly normalized matched filter implies that the signal has undergone 20 dB of loss. Because of

the small signal levels expected (< -200 dB) and rounding errors resulting from limited computer precision, we add in a 100 dB offset during the normalization process. This keeps the signal levels closer to the center of the double precision range. Finally, this process is repeated for every channel combination so that each channel has its own reference function and any channel phase or amplitude mismatch can be removed.

4.3.2 PRE-PROCESSING AND MATCHED FILTER

Before the matched filter is applied to the radar data, several steps are applied for memory and speed reasons. The first is pre-summing which is the process of averaging adjacent records and then decimating the result. This process is shown in Fig. 4-7 for clarity. Essentially, this is equivalent to time-domain convolution with a boxcar window and decimation at a rate equal to the width of the boxcar window. The reason for the pre-summing is to reduce the amount of data that must be dealt with in the later and more time-consuming image processing.

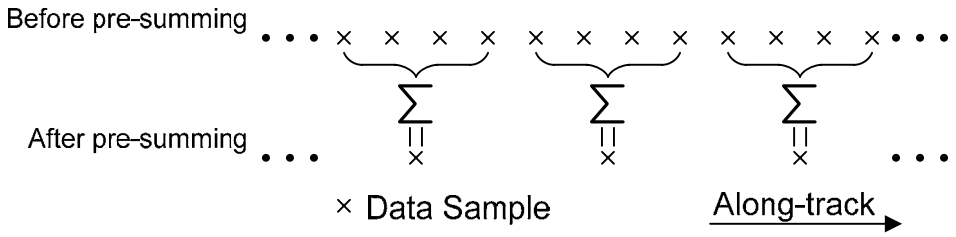

Fig. 4-7. Example of pre-summing as along-track filtering and decimation when $M_x = 4$.

After pre-summing, the data are down-converted to complex baseband via time domain multiplication with $\exp(-j2\pi f_c t(n))$ as shown in Fig. 4-8. Note that the effective frequency axis is shifted: the imaging algorithms use the shifted frequency axis when applying phase shifts.

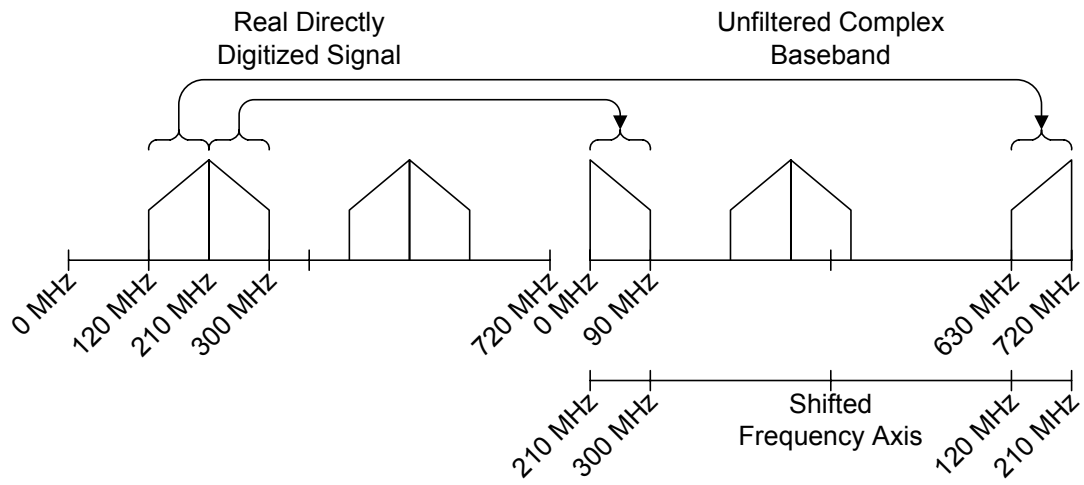

Fig. 4-8. Down-conversion and shifted frequency axis.

The data are then filtered and decimated in time by M_t. This is done by zero-padding the time-domain radar record to a multiple of M_t and then taking the discrete Fourier transform (for efficiency the record length is actually zero-padded so that the factorization of the number of samples is of the form $2^n M_t$). Since the number of samples is a multiple of M_t, we can decimate in the frequency domain as shown in Fig. 4-9 since the discrete frequency axes uses the same points. Filtering (or windowing) is performed after decimation with a Hanning window. The same steps are performed on the reference functions when these are loaded. During the filtering and decimation process the data are also pulse compressed since the data are already in the frequency domain. Pulse-compression is performed by multiplying the radar record with the complex conjugate of the corresponding reference function.

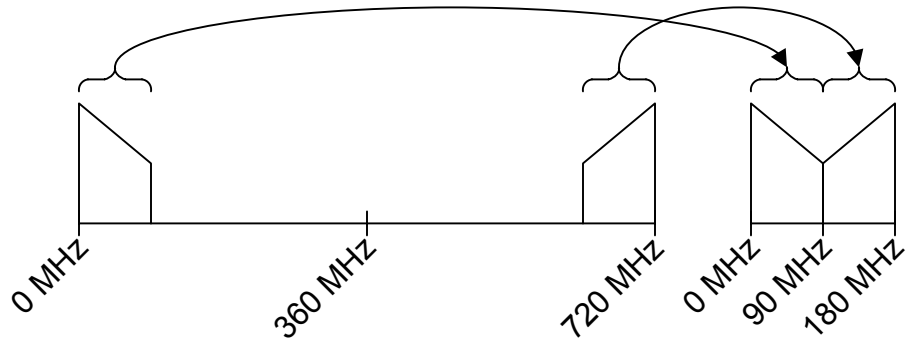

Fig. 4-9. Decimation applied in the frequency domain where $M_t = 4$.

4.4 DATA INDEXING METHOD: SEQUENCES

To ease data management and to allow the image processing algorithms to be independent of this particular set of radar data, a data indexing scheme is laid on top of the actual data. This indexing scheme takes care of loading the radar and trajectory data and also identifies sequences of similar data. For example, in a given day, we have to move the radar platform to the scene of interest, take a few swaths of data, and then return to the camp. When applying f-k migration and SAR processing, we want to be able to identify turns, straight segments, and the transits to and from the scene. To this end, a graphical user interface (GUI) was created in Matlab to identify and tag groups of data. The GUI is shown in Fig. 4-10. We define a *sequence* to be a contiguous group of data where all the data in the group should have the same processing applied to it. A set of functions, e.g. sequenceOpen, sequenceLoad, sequenceGet, etc. allow generic access to the data and also provide transparent synchronization to the trajectory data.

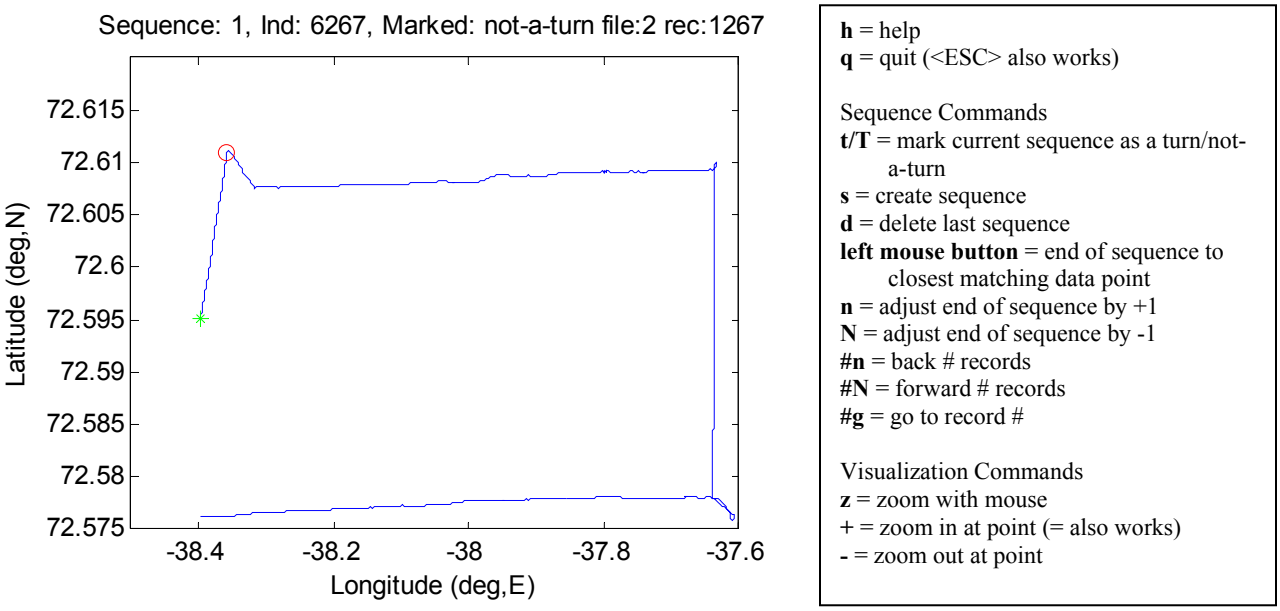

Fig. 4-10. GUI for creating sequences. The platform's trajectory is shown in blue. The user clicks on the graph of the trajectory to identify the start and stop of each sequence. Attributes such as platform "turning" can be set which allow automated processing of the data (this could be expanded for aerial work to identify regions over land, percolation zone, etc.).

4.5 Selection of an Along-track Resampling Method

The platform velocity is not constant so that the along-track sampling is non-uniform[16]. Since both the f-k migration and the SAR processing algorithm perform operations in the frequency domain, some form of uniform sampling is desired to allow the fast Fourier transform and traditional filters to be used. This problem can be looked at as a complex spectral estimation problem where the input to the spectral estimator is non-uniformly sampled, but the output in the frequency domain is uniformly sampled. We assume the data satisfy the following framework used to derive the estimators:

$$\mathbf{x} = \mathbf{G}\mathbf{s} + \mathbf{n}$$

where $\mathbf{x}$ is an N-by-1 vector of non-uniformly-spaced spatial measurements, $\mathbf{G}$ is an N-by-M matrix relating the frequency domain samples to the spatial-domain samples, $\mathbf{s}$ is

[16] The PRF is also constant (i.e. the PRF is not slaved to the platform velocity)

an M-by-1 random vector of uniformly-spaced frequency samples with cross-correlation matrix $\Sigma_s = E\{\mathbf{s}\mathbf{s}^H\}$, and $\mathbf{n}$ is an N-by-1 random vector of time-domain zero-mean additive Gaussian noise with cross-correlation matrix $\Sigma_n = E\{\mathbf{n}\mathbf{n}^H\}$. All vectors and matrices are complex. The signal and noise variances (i.e. diagonal elements of Σ_s and Σ_n) are denoted $\sigma_{s,1}^2$, through $\sigma_{s,M}^2$ and $\sigma_{n,1}^2$ through $\sigma_{n,N}^2$. The signal and noise are assumed to be independent of each other. The matrix, $\mathbf{G}$, is given by:

$$\mathbf{G} = \exp\left(j\mathbf{x}\mathbf{k}^T\right)$$

where $\mathbf{x}$ is the N-by-1 vector of spatial positions and $\mathbf{k}$ is the M-by-1 vector of spatial frequency points. For uniformly sampled space and frequency data where N = M, $\mathbf{G}$ is the traditional inverse discrete Fourier transform matrix.

Three different methods are derived in the following subsections. This is followed by a description of the simulation setup and a comparison between each method using simulated data.

4.5.1 MATCHED ESTIMATOR

The matched filter estimator maximizes the SNR of a particular estimate. It does not consider the correlation of other frequencies with the frequency of interest. With uniformly sampled spatial data, the frequencies are orthogonal because $\mathbf{G}$ is a unitary matrix. Orthogonal in this context means that the Euclidean inner product between the space-domain representations of two frequencies is zero. Therefore, there is no need to consider correlation from other frequencies. With nonuniformly sampled spatial data, the frequencies are not necessarily orthogonal since $\mathbf{G}$ is not necessarily unitary. Therefore, this correlation limits the performance of the matched filter.

We start by considering the estimate of a single frequency component, $\hat{s}_m = \mathbf{l}_{MF,m}^H \mathbf{x}$ where $\mathbf{l}_{MF,m}$ is an N-by-1 vector containing the filter coefficients (note that we have implicitly forced the estimator to be linear). We define the matched filter to be $\mathbf{l}_{MF,m}$ such

that the SNR, $E\left\{\frac{\left|\mathbf{l}_{MF,m}^{H}\mathbf{G}_{:,m}\mathbf{s}_{m}\right|^{2}}{\left|\mathbf{l}_{MF,m}^{H}\mathbf{n}\right|^{2}}\right\}$, is maximized. Since we would like the output to equal s_m when there is zero noise and zero interference from other frequencies ($s_k = 0$ when $k \neq m$), we enforce the constraint[17] that $\mathbf{l}_{MF,m}^{H}\mathbf{G}_{:,m}\sigma_{s,m}^{2} = 1$. The optimization equation is now $\min_{\mathbf{l}_{MF,m}^{H}\mathbf{G}_{:,m}\sigma_{s,m}^{2}=1} E\left\{\left|\mathbf{l}_{MF,m}^{H}\mathbf{n}\right|^{2}\right\} = \min_{\mathbf{l}_{MF,m}^{H}\mathbf{G}_{:,m}\sigma_{s,m}^{2}=1} \mathbf{l}_{MF,m}^{H}\Sigma_{n}\mathbf{l}_{MF,m}$. This is a constrained optimization problem that can be solved using the Lagrangian multiplier method. The Lagrangian is $\mathbf{l}_{MF,m}^{H}\Sigma_{n}\mathbf{l}_{MF,m} + \lambda\left(\mathbf{l}_{MF,m}^{H}\mathbf{G}_{:,m}\sigma_{s,m}^{2} - 1\right)$. Taking the derivative of the Lagrangian with respect to $\mathbf{l}_{MF,m}^{H}$, we find that the stationary point satisfies $\Sigma_{n}\mathbf{l}_{MF,m} + \lambda\mathbf{G}_{:,m}\sigma_{s,m}^{2} = 0$. Because the optimization function is quadratic and positive, its stationary point must be a minimum. Solving we get $\mathbf{l}_{MF,m} = -\lambda\Sigma_{n}^{-1}\mathbf{G}_{:,m}\sigma_{s,m}^{2}$. To find λ, we enforce the constraint,

$\mathbf{G}_{:,m}^{H}\mathbf{l}_{MF,m} = -\lambda\mathbf{G}_{:,m}^{H}\Sigma_{n}^{-1}\mathbf{G}_{:,m}\sigma_{s,m}^{2} = 1$, which gives $\lambda = \frac{-1}{\mathbf{G}_{:,m}^{H}\Sigma_{n}^{-1}\mathbf{G}_{:,m}\sigma_{s,m}^{2}}$. Therefore, the matched filter is

$$\mathbf{l}_{MF,m} = \frac{\Sigma_{n}^{-1}\mathbf{G}_{:,m}}{\mathbf{G}_{:,m}^{H}\Sigma_{n}^{-1}\mathbf{G}_{:,m}\sigma_{s,m}^{2}}.$$

When the noise is independent and identically distributed, Σ_n is the identity matrix and the matched filter simplifies to

$$\mathbf{l}_{MF,m} = \frac{\mathbf{G}_{:,m}}{\left|\mathbf{G}_{:,m}\right|^{2}\sigma_{s,m}^{2}}.$$

The matched filter for this special case contains no matrix inverses and its computational complexity is $O(N^2)$ since it involves a simple matrix multiply.

4.5.2 LINEAR MINIMUM MEAN SQUARED ERROR ESTIMATOR

As the name indicates, the minimum mean squared error (MMSE) estimator minimizes the mean squared error. As with the matched filter, we force the estimator to

[17] This constraint has no effect on the SNR and is essentially a scaling factor that cancels out.

be a linear operator[18]. We again start by considering the estimation of just the mth frequency component, $\hat{s}_m = \mathbf{l}_{MF,m}^H \mathbf{x}$. We define the optimization problem to be $\min_{\mathbf{l}_{MF,m}} = E\left\{\left|\hat{s}_m - s_m\right|^2\right\}$. Inserting the filter into the optimization equation gives:

$$E\left\{\left|\mathbf{l}_{MF,m}^H(\mathbf{Gs}+\mathbf{n}) - s_m\right|^2\right\}$$

$$= E\left\{\left(\mathbf{l}_{MF,m}^H(\mathbf{Gs}+\mathbf{n}) - s_m\right)\left(\left(\mathbf{s}^H\mathbf{G}^H + \mathbf{n}^H\right)\mathbf{l}_{MF,m} - s_m^H\right)\right\}$$

$$= E\left\{\mathbf{l}_{MF,m}^H(\mathbf{Gs}+\mathbf{n})\left(\mathbf{s}^H\mathbf{G}^H + \mathbf{n}^H\right)\mathbf{l}_{MF,m} - \left(\mathbf{s}^H\mathbf{G}^H + \mathbf{n}^H\right)\mathbf{l}_{MF,m}s_m - \mathbf{l}_{MF,m}^H(\mathbf{Gs}+\mathbf{n})s_m^H + \left|s_m\right|^2\right\}$$

Taking the derivative with respect to $\mathbf{l}_{MF,m}^H$, we find that the stationary point satisfies

$$E\left\{(\mathbf{Gs}+\mathbf{n})\left(\mathbf{s}^H\mathbf{G}^H + \mathbf{n}^H\right)\mathbf{l}_{MF,m} - (\mathbf{Gs}+\mathbf{n})s_m^H\right\} = 0\,.$$

Now solving for $\mathbf{l}_{MF,m}$ we find

$$E\left\{(\mathbf{Gs}+\mathbf{n})\left(\mathbf{s}^H\mathbf{G}^H + \mathbf{n}^H\right)\mathbf{l}_{MF,m} - (\mathbf{Gs}+\mathbf{n})s_m^H\right\} = 0$$

$$\Leftrightarrow \left(\mathbf{G}E\left\{\mathbf{ss}^H\right\}\mathbf{G}^H + \mathbf{G}E\left\{\mathbf{sn}^H\right\} + E\left\{\mathbf{ns}^H\right\}\mathbf{G}^H + E\left\{\mathbf{nn}^H\right\}\right)\mathbf{l}_{MF,m} - \mathbf{G}E\left\{\mathbf{s}s_m^H\right\} - E\left\{\mathbf{n}s_m^H\right\} = 0$$

$$\Leftrightarrow \left(\mathbf{G}\Sigma_s\mathbf{G}^H + \Sigma_n\right)\mathbf{l}_{MF,m} - \mathbf{G}\Sigma_{s_k s} = 0$$

$$\Leftrightarrow \mathbf{l}_{MF,m} = \left(\mathbf{G}\Sigma_s\mathbf{G}^H + \Sigma_n\right)^{-1}\mathbf{G}\Sigma_{s_k s}\,,$$

where we have used the independence of $\mathbf{s}$ and $\mathbf{n}$. As with the matched filter, the optimization function is quadratic and positive and therefore its stationary point must be a minimum.

Although the filter coefficients only need to be found once, the matrix inversion is O(N^3). Once the filter coefficients are found, applying the filter involves a matrix multiplication which has computational complexity of O(N^2). This method requires the most knowledge about the signal's statistics and also has the highest computational burden.

[18] For AWGN, the linear estimator is also the overall optimal estimator.

4.5.3 SPLINE INTERPOLATION

The final method considered is spline interpolation to uniform samples in the time-domain followed by a fast Fourier transform (FFT). This method is considered because spline interpolation is very efficient as is the FFT. There are a number of textbooks which cover spline interpolation as it is applied here (e.g. [141]) and therefore its derivation will be skipped. The end conditions used for the spline are "not-a-knot" – the first two and last two segments are each fit to a single cubic spline.

The matrix inverse required to compute the spline is tridiagonal and diagonally dominant making the computational complexity O(N). The fast Fourier transform's computational complexity is O(NlogN). Therefore the overall complexity is just $O(N\log_2 N)$.

4.5.4 RESULTS

In this section, the three methods presented above are compared. This is done by creating a variety of sequences of non-uniformly sampled data and comparing the mean squared error of the three methods. First a uniformly sampled spatial-axis is established

$$x_i = 0, \Delta, 2\Delta, \ldots, (N_x - 1)\Delta .$$

Then the non-uniform spatial-axis is created. To do this, we create a Gaussian random sequence, $\tilde{\Delta}_0, \tilde{\Delta}_1, \tilde{\Delta}_2, \ldots, \tilde{\Delta}_{2N_t-1}$, with mean Δ and variance σ_x. This sequence is passed through a low pass filter which preserves the variance giving a new sequence $\Delta_0, \Delta_1, \Delta_2, \ldots, \Delta_{2N_t-1}$. If $\Delta_n \le 0$ for any n, new sequences are generated until $\Delta_n > 0 \; \forall \; n$. Then the spatial-axis is generated similar to a random-walk:

$$x = 0, \Delta_0, \Delta_0 + \Delta_1, \ldots, \sum_{n=0}^{2N_t-1} \Delta_n .$$

This spatial-axis is then truncated at the point, K, where $\sum_{n=0}^{K} \Delta_n > (N_x - 1)\Delta$ and $\sum_{n=0}^{K-1} \Delta_n \le (N_x - 1)\Delta$: The non-uniform spatial-axis is contained within the uniform spatial-axis. Next, independent additive white Gaussian signal and noise discrete random

processes are created on the uniform spatial-axis with variances σ_s and σ_n. These are Fourier interpolated to the non-uniform spatial-axis using an over-sampling rate of 40 times (zero-padding in the frequency domain).

Each of the three methods is then applied to the data while varying the variance σ_x, the low pass filter cutoff frequency, and the SNR $\frac{\sigma_s}{\sigma_n}$. The results are shown in Fig. 4-11 through Fig. 4-14. These results are the average mean squared error of 20 simulation runs. There is still some variance left in the results, but the general trends are clear.

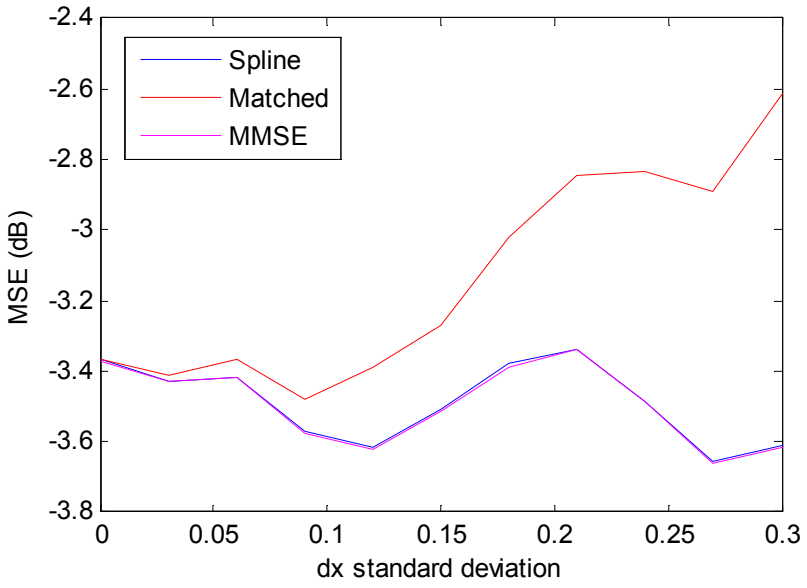

Fig. 4-11. Mean-squared error as a function of the standard deviation of the spatial-sampling rate. Standard deviation is relative to the average spatial sampling rate (e.g. if average sampling rate is 0.5 m, 0.2 on the scale above would imply a standard deviation of 0.1 m). The sample spacing is not filtered and the SNR is 10.

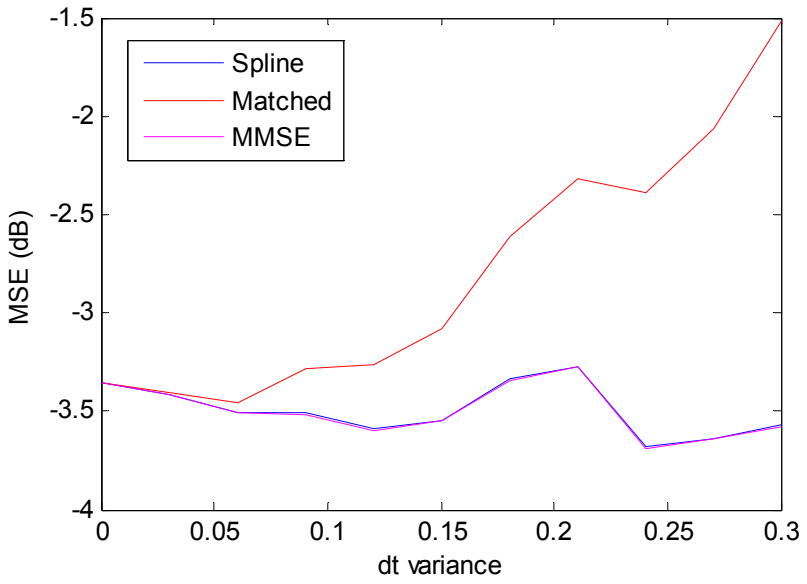

Fig. 4-12. Mean-squared error as a function of the standard deviation of the spatial-sampling rate. Standard deviation is relative to the average spatial sampling rate (e.g. if average sampling rate is 0.5 m, 0.2 on the scale above would imply a standard deviation of 0.1 m). This plot is the same as above, but the sample spacing is low pass filtered with a normalized bandwidth of 0.1 (1 being half the sampling rate).

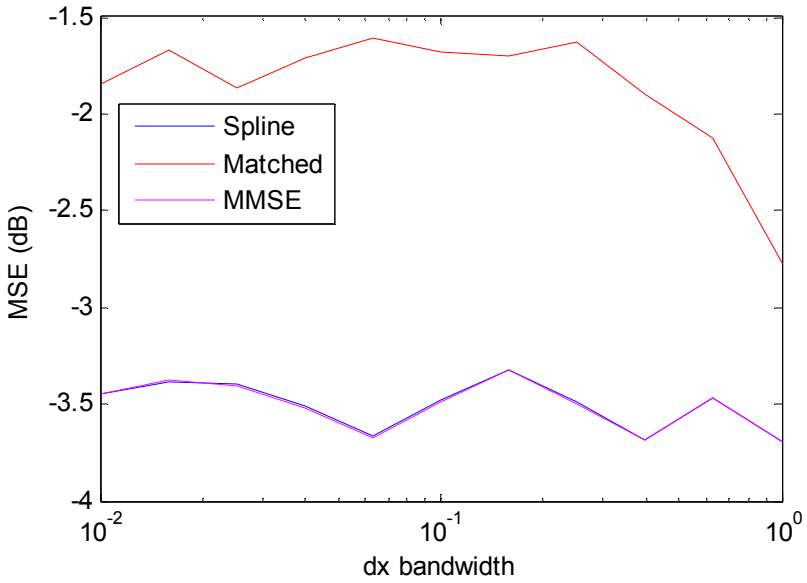

Fig. 4-13. Mean-squared error as a function of the normalized bandwidth of the spatial-sampling rate. A bandwidth of 1 (or 10^0) is equivalent to no filtering. The standard deviation of the sample-spacing is 0.3 and the SNR is 10. The filter coefficients are modified so that the standard deviation of the sample-spacing output is equivalent to the standard deviation of the input.

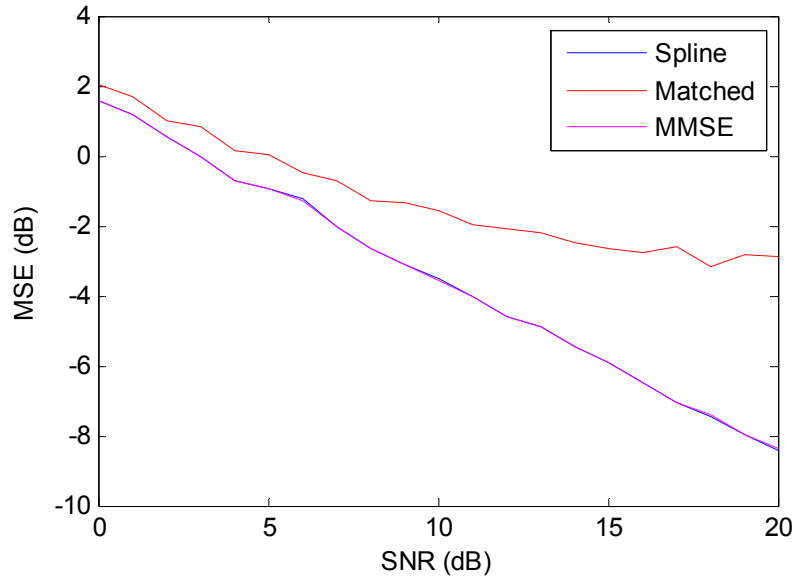

Fig. 4-14. Mean-squared error as a function of the SNR. The standard deviation of the sample spacing is 0.3 and the normalized bandwidth is 0.1.

The spline method is very attractive due to its computational efficiency and near-MMSE performance. For example, the inversion required by the MMSE algorithm takes over an hour to compute using available computer resources where as the spline method finishes in seconds. Also, the MMSE requires knowledge of the signal and noise variance which are space-varying. The matched filter always performs worse than both the spline and MMSE methods and is not considered because it is also more computationally expensive than the spline. Therefore, for both the f-k migration and SAR algorithms, the spline-interpolation method is used for spatial filtering and decimation.

Chapter 5: FREQUENCY-WAVENUMBER MIGRATION

5.1 CONCEPT

Frequency-wavenumber migration (f-k migration) as applied here is a synthetic aperture radar (SAR) algorithm which provides fine along-track resolution of scattering from the nadir direction. Using a simple detector, ice thickness and bed elevation data products are garnered from this scattering information. These data products satisfy the altimetry information needed by the side-looking SAR to generate the system geometry. The reason f-k migration is used is that it is much more efficient than the side-looking SAR algorithm described in the next chapter. This is primarily because convolution-like operations applied in the space-time domain are replaced by multiplication operations in the frequency-wavenumber domain. In fact, f-k migration is the frequency-wavenumber domain equivalent of space-time synthetic aperture radar [141], [143]. The algorithm includes spherical wavefront curvature (i.e. exact range migration) in addition to ordinary phase correction. Another very useful property of the algorithm is that it efficiently computes the frequency-wavenumber filter coefficients for layered media[19]. The approach taken here for ice sounding is similar to Leuschen et al.'s work with the CoRDS system used to sound ice in Greenland [125].

To use the multi-dimensional FFT required for f-k migration, the data must be uniformly spaced in both the time and space domains. The radar provides uniform sampling in time and the required spatial re-sampling is described in section 4.5. The FFT also requires the spatial data be taken along a line. However, no motion compensation is performed before the algorithm. The reason for this is that cross-track motion has virtually no effect on the focusing of nadir targets. Elevation motion does have an effect, but the surface slope is very small and nearly constant at the location the measurements were made as shown in Fig. 5-1. Slopes are about 0.1% or 1 m elevation change for every 1000 m of along-track movement. A constant gradient in the elevation causes a shift in

[19] Refraction and velocity changes are incorporated, but the effect of reflection and transmission at interfaces is ignored.

the doppler centroid which results in a rotation of the migrated image and degradation in signal-power for non-isotropic scatterers. Since the shift is so small in this case, signal loss can be ignored. The rotation is equal to the slope: for 3000 m of ice this results in a 3 m along-track shift in position. This is less than the along-track resolution of the final image product.

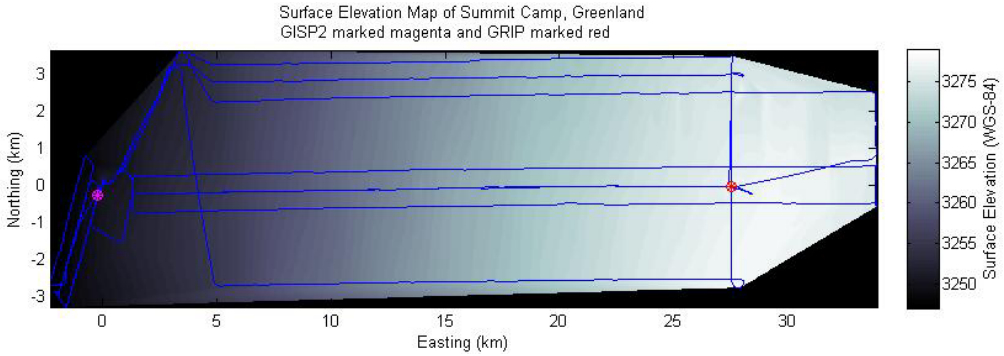

Fig. 5-1. Surface elevation derived from the DGPS measurements taken while collecting the radar data. Surface is interpolated from discrete DGPS measurements (blue lines) using linear Delaunay triangulation.

To explain the f-k migration algorithm, an analogy restricted to a single dimension is helpful. Suppose that a plane-wave is traveling in the positive x-direction so that $\|\mathbf{k}\|_2 = k_x = -\frac{2\pi}{\lambda}$. Since the direction of the wave is set, the wave can be completely described by its frequency response. Consider a receiver at the origin as shown in Fig. 5-2.

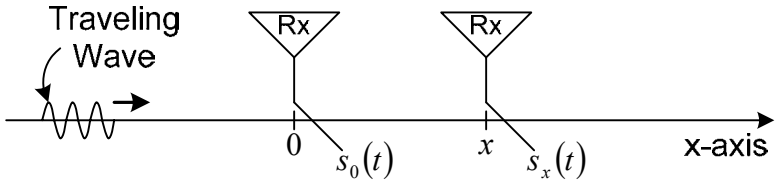

Fig. 5-2. Spatial shift in one dimension.

Let $s_0(t)$ denote the signal recorded by the receiver. To determine the signal recorded by a receiver at position x on the x-axis, $s_x(t)$, we only need to add a delay of $\frac{x}{v}$ so that

$s_x(t) = s_0\left(t - \frac{x}{v}\right)$ where v is the velocity of the wave in the medium. In the frequency domain, using the time-shift property, this corresponds to

$$S_x(f) = S_0(f)\exp\left(j2\pi f\left(\frac{-x}{v}\right)\right)$$

$$= S_0(f)\exp\left(-j\frac{2\pi f}{v}x\right)$$

$$= S_0(f)\exp(jk_x x).$$

Therefore to determine the frequency response at a position x, we need to multiply $S_x(f)$ with $\exp(jk_x x)$. In the general case, $\|\mathbf{k}\|_2 = \frac{2\pi}{\lambda} = \sqrt{k_x^2 + k_y^2 + k_z^2}$. From the assumptions we have $k_y = k_z = 0$ and the wave is traveling in the positive direction so that $k_x = -\frac{2\pi}{\lambda}$. To determine the value at zero-time from the frequency domain response (this will be needed later) we sum all the frequency components together,

$$s_x(0) = \int_{-\infty}^{\infty} S_x(f)\exp(j2\pi f \cdot 0)df = \int_{-\infty}^{\infty} S_x(f)df .$$

Or if the signal is discrete and of finite length N we have

$$s_x(0) = \frac{1}{N}\sum_{n=0}^{N-1} S_x(n)\exp(j2\pi n f_0 \cdot 0) = \frac{1}{N}\sum_{n=0}^{N-1} S_x(n).$$

If the plane-wave is allowed to travel in three dimensions, there are three free variables k_x, k_y, and k_z but only one constraint equation. However, if the x and y domain are sampled, this information can be used to determine k_x and k_y. This leaves only k_z which can be solved as

$$k_z = \pm\sqrt{\left(\frac{2\pi}{\lambda}\right)^2 - k_x^2 - k_y^2} .$$

Assuming that the waves are coming from the negative z direction and substituting in frequency for wavelength this becomes

$$k_z\left(f,k_x,k_y\right)=-\sqrt{\left(\frac{2\pi f}{v}\right)^2-k_x^2-k_y^2}\ .$$

Now consider a two dimensional mesh of space-time data collected on the surface of the ice sheet (e.g. by using a synthetic aperture approach). Let the z-axis be normal to the surface and point out of the ice. The signal, $S_0\left(t,x,y\right)$, at each receiver is a function of time and the receiver's position. Also, since all scatterers are located in the ice, **k** will always have a positive z component. These data can be transformed to the frequency-wavenumber domain through a three-dimensional FFT. Each output element of the three-dimensional FFT is associated with a particular f, k_x, and k_y given by[20]:

$$f=f_c+\left\{0,\frac{1}{\Delta_t},\frac{2}{\Delta_t},\ldots,\frac{N_t-1}{2\Delta_t},\frac{-N_t}{2\Delta_t},\frac{-N_t+1}{2\Delta_t},\ldots,\frac{-2}{\Delta_t},\frac{-1}{\Delta_t}\right\},$$

$$k_x=2\pi\left\{0,\frac{1}{\Delta_x},\frac{2}{\Delta_x},\ldots,\frac{N_x-1}{2\Delta_x},\frac{-N_x}{2\Delta_x},\frac{-N_x+1}{2\Delta_x},\ldots,\frac{-2}{\Delta_x},\frac{-1}{\Delta_x}\right\},$$

$$k_y=2\pi\left\{0,\frac{1}{\Delta_y},\frac{2}{\Delta_y},\ldots,\frac{N_y-1}{2\Delta_y},\frac{-N_y}{2\Delta_y},\frac{-N_y+1}{2\Delta_y},\ldots,\frac{-2}{\Delta_y},\frac{-1}{\Delta_y}\right\},$$

where Δ_t, Δ_x, and Δ_y are the spacings in the original space-time domain and N_t, N_x, and N_y are the number of samples in each dimension. The space-time data are assumed to be in the complex baseband form for representing a bandpass signal with a center frequency of f_c. To predict the signal that would have been measured if the mesh of receivers were moved 1 m in the negative z-direction from their original position, we solve for k_z and then apply a phase shift

$$S_{-1\mathrm{m}}\left(f,k_x,k_y\right)=S_0\left(f,k_x,k_y\right)\exp\left(jk_z\left(f,k_x,k_y\right)\cdot-1\right).$$

[20] Assumes an even number of samples (odd number of samples requires the usual simple perturbation).

The result is the predicted frequency response that would have been observed if the receivers had been placed 1 m below their actual positions. This process can be used to find the predicted waveform at any position by multiplying by the appropriate spatial phase shift. Note that this shifts all the spatial measurements simultaneously, which is key to f-k migration's speed advantage over space or time domain processing. It is analogous to filtering by multiplying by the transfer function with O(N) operations rather than convolving with an impulse response with $O(N^2)$ operations.

To apply this spatial shifting to radar processing, we must consider the position of the transmitter, which generates the original signal $s(t)$. In the monostatic case, the transmitter and receiver are collocated – if the receiver is moved, the transmitter must also be moved. The original signal $s(t)$ is delayed by the transmitter movement and the received signal is delayed further by the receiver movement. This collocation effectively doubles the effect of the radar movement. This can be dealt with by doubling the index of refraction of the medium. Using the simplified example from above, the delay for the receiver movement is $\frac{x}{v}$. The delay for the transmitter movement is also $\frac{x}{v}$. Therefore the total delay is $\frac{2x}{v}$. Since the doubling factor appears everywhere the velocity or wavelength is used, we can interpret the effect as a doubling of the index of refraction.

The f-k migration technique involves moving the radar to each of the target positions of interest via phase shifts and reading the zero-time response. If there is a strong response at zero-time after "moving" (phase shifting) the radar, this is interpreted to mean that there is a target in the immediate vicinity of the radar since a zero-time delay corresponds to zero range. Since we generally treat the scene as a lattice of isotropic point targets, the f-k migration technique can process whole sections of the lattice simultaneously. This is because the entire SAR aperture is moved when the phase shift is applied rather than each "receiver" being moved individually. Since each "receiver" in the SAR aperture gives the response at that point we have simultaneously determined the response at N new points. In other words, if the SAR aperture has N elements in it, we can process N targets after each phase shift (assuming the SAR aperture lines up with the lattice of isotropic point targets).

The final response needed by the processing is in the space-domain. As mentioned above, the value at zero-time can be found by summing all of the frequency points. This should be done before transforming from the wavenumber domain to the space domain using the IFFT. By summing first, the number of IFFTs is reduced by a factor of $N_t - 1$.

There are two caveats that need to be mentioned when using the f-k migration algorithm. The first is that the process above assumes that the signal is band-limited in space and time. If the signal were truly band-limited (infinite time signal) then there would be no energy in parts of the data matrix that correspond to $\sqrt{k_x^2 + k_y^2 + k_z^2} > \|\mathbf{k}\|_2 = \frac{2\pi}{\lambda}$. However, there are portions of the frequency-wavenumber data matrix that represent a combination of k_x, k_y, k_z, and λ that require the wave to be evanescent. In our case, the energy from the portions of the data matrix corresponding to evanescent waves will be filtered out because wavenumber domain filtering is employed.

The second issue comes from the periodic nature of the discrete Fourier transform. Because the signal is being represented discretely and circular convolution is being used in the frequency domain, zero-padding may be necessary in some cases to remove artifacts due to the non-linear nature of circular convolution (i.e. aliasing). This is handled in the usual way by processing overlapping segments, truncating the segments so that only the valid part is kept, and then concatenating these segments such that the effective result is ordinary linear convolution.

The example above considered a mesh of space-time data. For this work, the data are collected along a single line. Therefore only the time and x domain are sampled. To solve for k_z, k_y is forced to be zero. While the restriction of data to a single line certainly introduces errors, there are two reasons why this approach still produces a good quality data product. The first is that the backscattering seen by the radar is primarily from the negative z-direction suggesting that the k_y component will be small. Secondly, the radar employs cross-track (y-dimension) antenna arrays which narrow the beamwidth significantly so that the k_y domain is effectively low pass filtered. However, since we do

not fully sample the y-dimension there is still some ambiguity and this can be seen in the migrated images shown in section 5.3.

Another technique we use is k-domain filtering and decimation. Filtering removes noise energy (and evanescent wave energy as explained above) and decimation reduces the number of operations performed by the migration routine. The procedure is identical to the time/frequency-domain windowing and decimation described in section 4.3 – only it is applied along the space/wavenumber-domain. The geometric interpretation of this filter is worth describing since it provides a more intuitive understanding of the process. The link between wavenumber and angle of arrival, θ, is illustrated in Fig. 5-3 and given by

$$\theta = \sin^{-1}\left(\frac{k_x}{\|\mathbf{k}\|_2}\right).$$

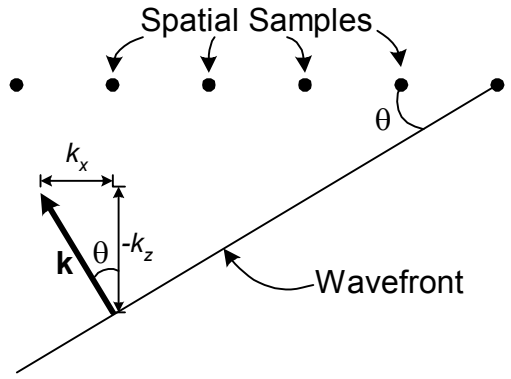

Fig. 5-3. Shows the relationship between the wavenumber and the angle of arrival.

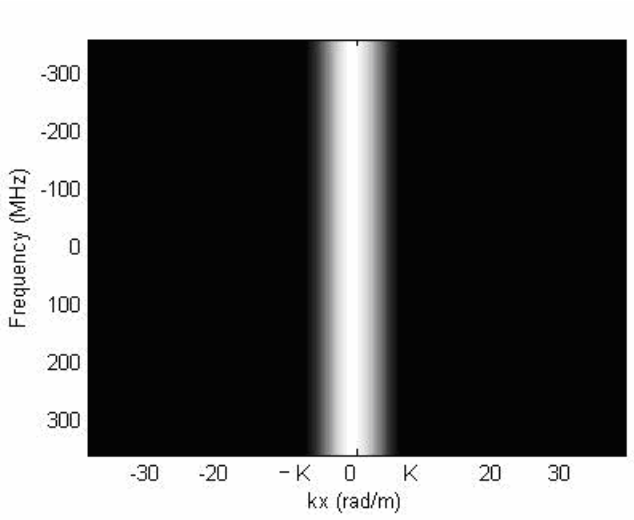

Fig. 5-4. Frequency-wavenumber domain filter.

The frequency-wavenumber domain filter used is shown in Fig. 5-4. The filter is a low pass filter using a Hanning window. As indicated in the figure, $|k_x| \le K$. Therefore, the angles of arrival are restricted to a beamwidth set by $\theta_{\max} = \sin^{-1}\left(\frac{K}{\|\mathbf{k}\|_2}\right)$. Note that K is not a function of frequency and $\mathbf{k}$ is. Therefore, $\theta_{\max}$ is a function of frequency and

$$\theta_{\max}(f) = \sin^{-1}\left(\frac{Kc}{2\pi f(2n)}\right),$$

where c is the speed of light in a vacuum and n is the real part of the index of refraction of the medium. The synthetic aperture length, L, for a fixed beamwidth is illustrated in Fig. 5-5 and given by

$$L = 2D\tan(\theta_{\max}) = 2D\tan\left(\sin^{-1}\left(\frac{Kc}{2\pi f(2n)}\right)\right) \approx \frac{DKc}{2\pi fn},$$

where D is the depth of the target. Note that the synthetic aperture length is a linear function of the depth and approximately inversely proportional to the frequency. Since the beamwidth is restricted according to the spatial domain bandwidth, K, which is not a function of frequency, the along-track resolution of the migrated image using the wavenumber filter in Fig. 5-4 is not a function of D or f.

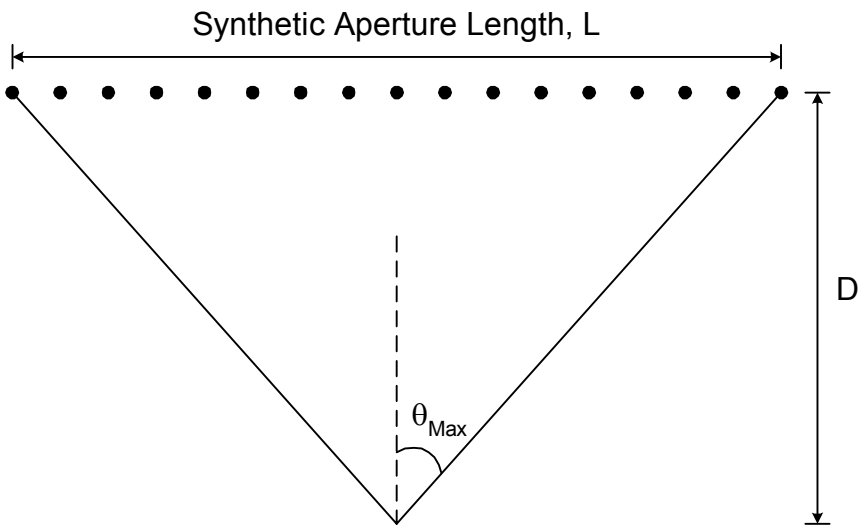

Fig. 5-5. Shows the relationship between the synthetic aperture length, L, and the maximum angle of arrival $\theta_{\max}$.

As mentioned in the introduction, f-k migration handles propagation in layered media very naturally. We use the dielectric models developed in section 2.1 to generate an approximated discrete depth-permittivity profile. Let $\Delta_{z,1}, \Delta_{z,2}, \ldots, \Delta_{z,n}$ be a sequence denoting the thickness of each layer and $n_1, n_2, \ldots, n_n$ be the corresponding index of refraction for each layer. Only the real part of the index of refraction is used so that the migration algorithm corrects for phase only. The filter coefficients for the f-k migration algorithm are then generated in an iterative manner by finding the transfer function matrix for each layer and then multiplying these together. Using the development described above to find the phase shift for each layer, we find the signal after the mth layer to be

$$S_m(f,k_x) = S_0(f,k_x)\prod_{p=1}^{m}\exp\left(-jk_{z,p}(f,k_x)\cdot\Delta_{z,p}\right),$$

where the solution for the z-component of the wavenumber, $k_{z,p}(f,k_x)$, is now a function of the layer number.

The final adaptation to the algorithm was to incorporate the radar's sample window delay. Because of data rate limitations, the radar does not begin to record data at time

zero (i.e. at the start of transmission). In fact, data are not recorded until 20 microseconds have passed. This delay is called the sample window delay. The f-k migration described above expects data to start at zero time. To compensate for the sample window delay, two options were considered. The first is to zero-pad the data from time zero up to the sample window delay. The problem with this approach is that it requires significantly more memory to store the large number of zeros and also hurts computation time by increasing the number of data points. The approach used here is to perform a time domain circular shift on the data equal to the sample window delay. The phase delays applied by the migration algorithm undo this shift. Essentially we have taken advantage of one of the properties of circular convolution – when the transform domain is used to apply filters the effect is to convolve periodic versions of the filter and the input. So instead of padding with zeros we have padded with the data itself. As long as the spatial and temporal extent of the migration filter do not corrupt the rest of the data, this is not a problem.

5.2 SIMULATIONS

To test the algorithm as well as to quantify the effects of pre-summing, sample window delays, and the filtering-decimation operations, we created a simple point target simulator for layered media. The point target simulator makes use of the propagation model described in section 2.1. The propagation model is used to determine the phase delay to the target from each of the radar positions. A noise-free example of a single point target is shown in Fig. 5-6 where the traditional hyperbolic delay response is easily recognized.

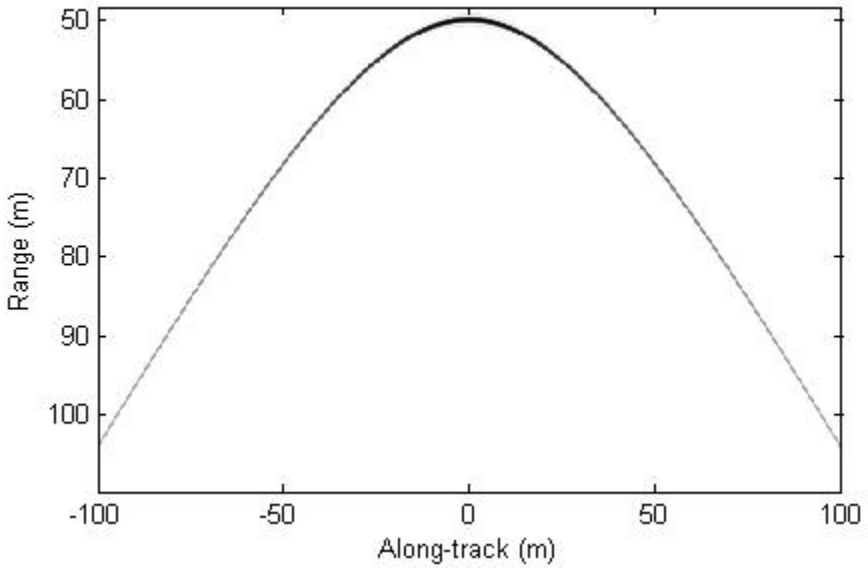

Fig. 5-6. Example of a simulated point target with along-track hardware averages and pulse compression. The target is located at a depth of 50 m and an along-track position of 0 m.

The migration algorithm applied without pre-summing, sample window delay, and the filtering-decimation is shown in Fig. 5-7.

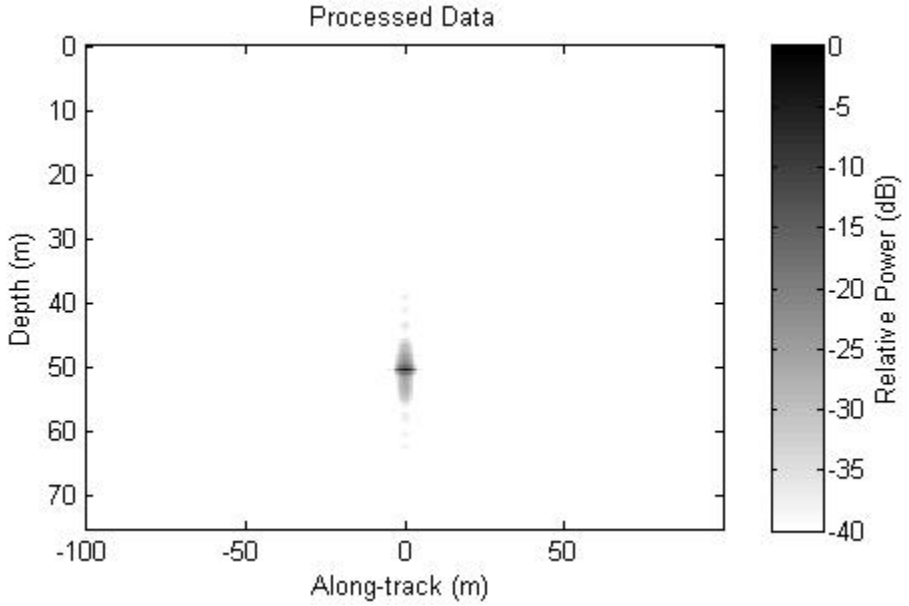

Fig. 5-7. Ideal migration with Hanning along-track windowing and boxcar time-domain windowing.

Pre-summing as explained in section 4.3 is effectively convolution in the spatial domain with a boxcar window. This creates a sinc-squared radiation pattern in the along-track dimension. Fig. 5-8 a) and b) show the transform domain before and after pre-summing. The signal is bandpass between 120-300 MHz. The hour glass shape is because of the evanescent waves (note that at DC there is no spatial bandwidth since DC waves do not "travel"). If decimation is applied without proper space-domain filtering, the large sidelobes will alias into the visual region and degrade the migrated image. Fig. 5-8 c) shows the transform domain after low-pass filtering with a Hanning window. Decimation can now be applied to the data.

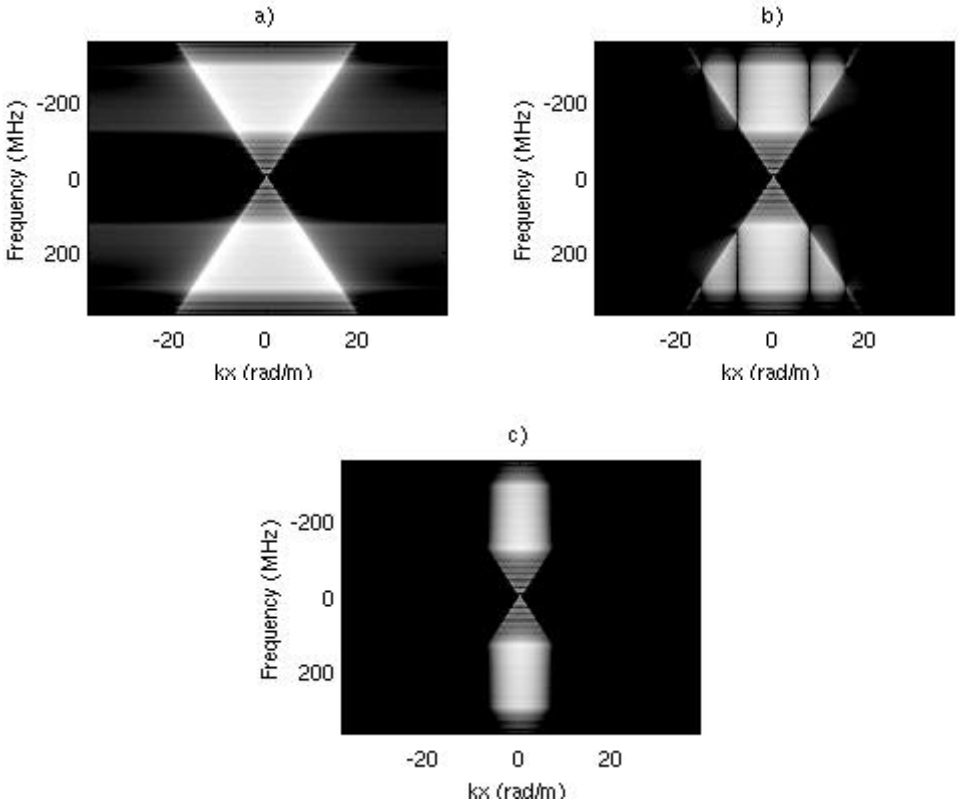

Fig. 5-8. Example of pre-summing in the transform domain a) before pre-summing b) after pre-summing and c) after spatial filtering.

The migrated image with pre-summing and spatial filtering is shown in Fig. 5-9. Time-domain filtering and decimation has also been applied. Note that by lowering the spatial bandwidth of the signal we have degraded the resolution since this shortens the

synthetic aperture length. Ordinarily this is not desirable unless signal characteristics or processing requirements limit the aperture that can be used.

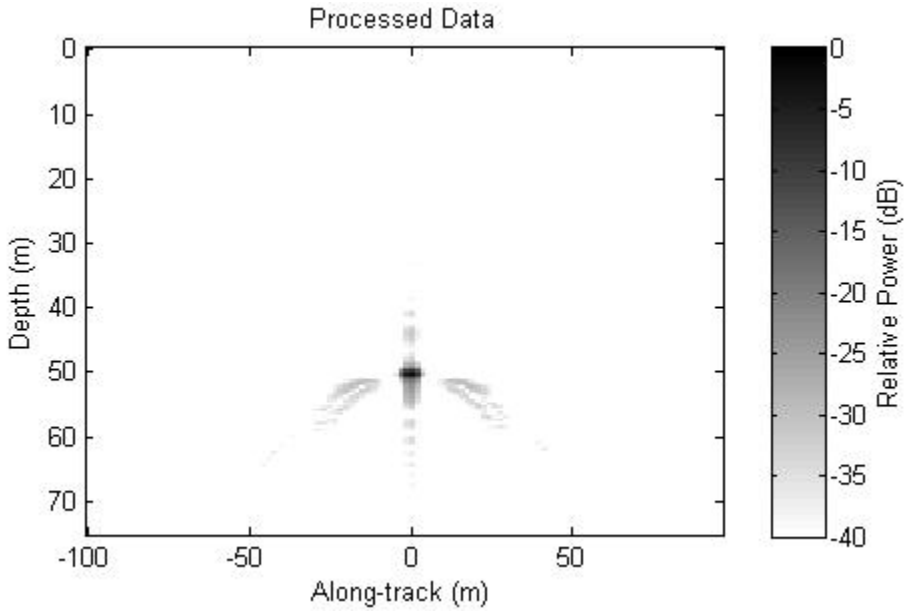

Fig. 5-9. Migration with pre-summing and spatial filtering.

As explained in the previous section, the sample window delay of the radar system is greater than zero. The effect of a non-zero sample window delay corresponding to approximately 30 m migrated with circular shifting is shown in Fig. 5-10. The migrated image starts at a larger depth, but there is no effect on signal quality.

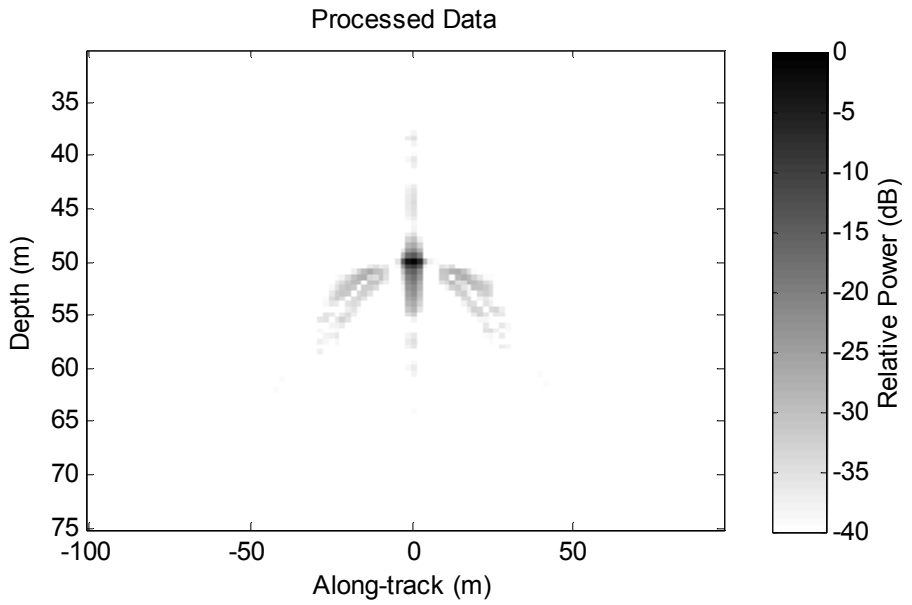

Fig. 5-10. Migration with circular shifts.

As explained in section 4.5, the radar platform velocity is not constant and the result was non-uniform along-track sampling. Simulations of along-track re-sampling of nonuniform data showed virtually no degradation in migrated image quality as shown by the results in Fig. 5-11.

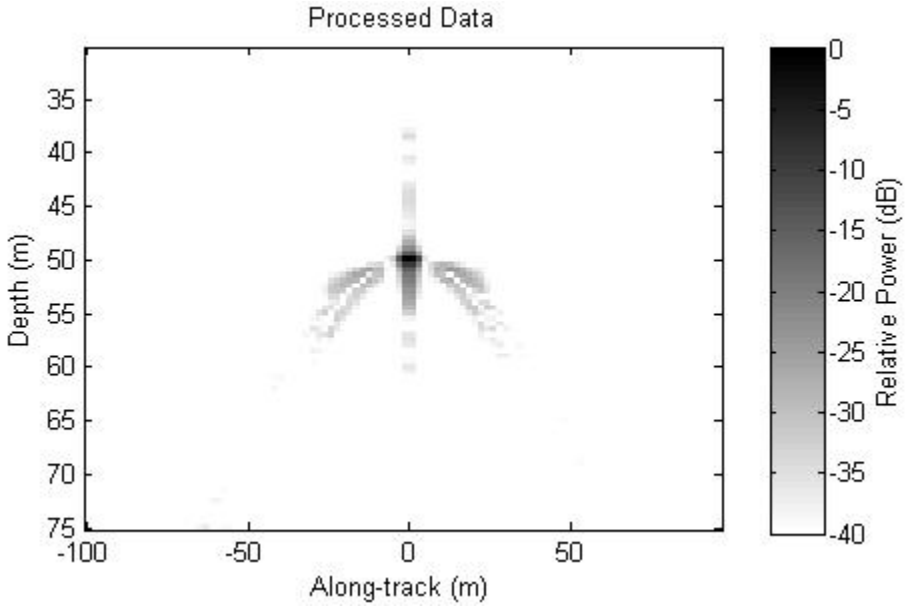

Fig. 5-11. Migration showing the effect of platform velocity variance for nonuniformly sampled data with differing amounts of variance in the platform velocity. Note that there is no visual degradation in the images.

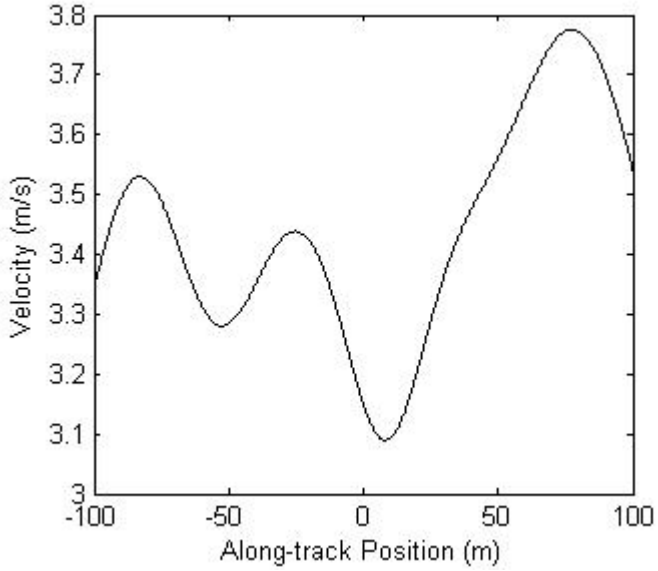

Fig. 5-12. Velocity profile used to generate the above migrated image.

5.3 RESULTS

Fig. 5-13 shows a log-detected echogram of radar data. Pulse compression/match filtering in the time domain has been applied. The eight receive channels are combined and only 1 meter of pre-summing is performed to minimize the effect on the along-track radiation pattern. Internal ice layers can be seen as specular layers in the upper part of the echogram. The specular reflections are identified by a lack of hyperbolas and the range-extent is small. The ice-bed interface is identified by the strong continuous scatterer along the base of the figure. Many hyperbolas can be seen along the whole length of the ice-bed interface and the range-extent is ~1000 meters.

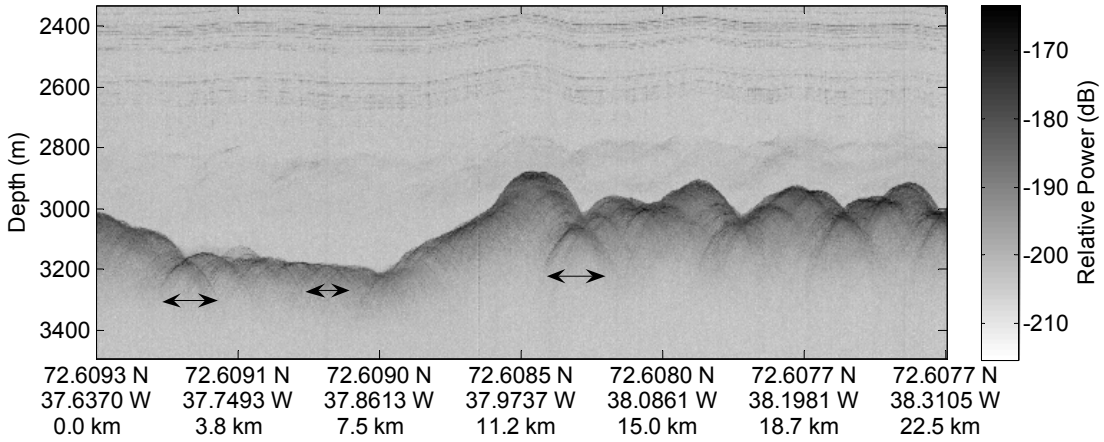

Fig. 5-13. Echogram with minimal pre-summing. The along-track extents of several hyperbolas are indicated in the figure.

The along-track extent of several hyperbolas were measured to be about 1000 m. The along-track spectral content of the basal signal is shown in Fig. 5-14. This is a rough estimate found by taking the power–averaged discrete Fourier transform in the along-track dimension. The spectral axis has been converted to along-track extent by converting the spatial frequency to angle of arrival and then to x-offset for a depth of 3000 m. The reason for measuring the along-track extent is that the nature of the backscatter, ice dielectric loss, spherical spreading loss, and antenna pattern directivity limit the along-track extent. If the synthetic aperture length is allowed to be too large, the extra length will only add in noise rather than signal. Therefore, we spatially filter as explained in

section 4.3 so that the effective synthetic aperture length only includes signal energy. Another consideration was the error margin in our *a priori* knowledge of the permittivity as explained in section 2.1. Based on these limitations we chose a 600 m aperture which provides approximately 5-m along-track resolution.

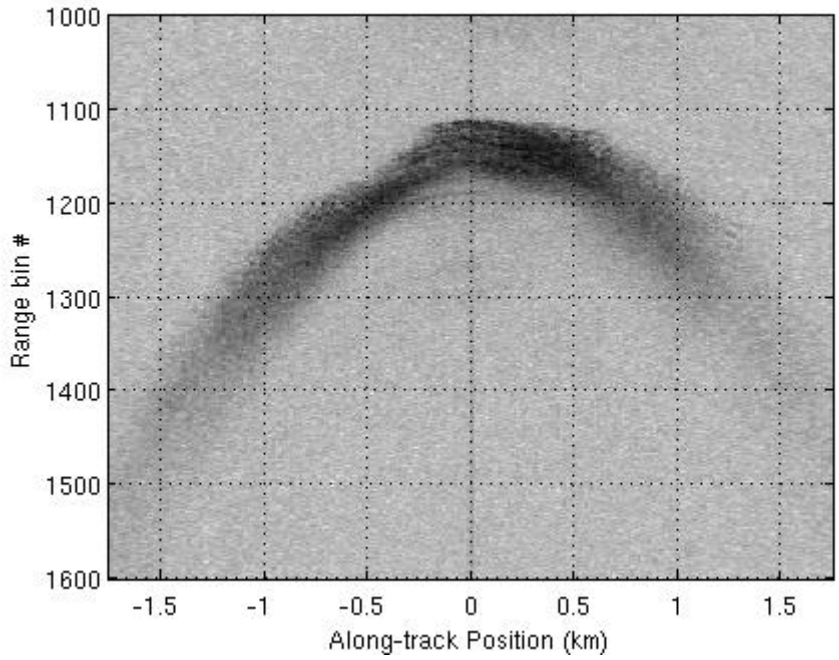

Fig. 5-14. Spectral content of basal signal.

Fig. 5-21 on page 126 through Fig. 5-36 on page 133 show the data after f-k migration with 5-m along-track resolution (corresponds to a 600 m synthetic aperture at 3000 m depth). Only the 8 long traverses are shown, but all of the data along straight line traverses exceeding 600 m have been migrated and used to generate the digital elevation map for the side-looking synthetic aperture radar processor. The first image from each traverse is a power-log-detected combination of all eight receive channels summed in-phase. These results were passed through a two-dimensional filter applied on the incoherent data (linear power) with the filter coefficients,

$$\frac{1}{15}\begin{bmatrix} 1 & 1 & 1 \\ 1 & 1 & 1 \\ 1 & 1 & 1 \\ 1 & 1 & 1 \\ 1 & 1 & 1 \end{bmatrix},$$

where the first dimension is along the depth axis and the second-dimension is parallel to the along-track axis. The effective resolution after filtering is 5 m in depth and 15 m in along-track. The second image from each traverse is an interferogram. The interferogram is formed by 1) summing the migrated image from channels 1 and 2, 2) summing the migrated images from channels 7 and 8, and 3) taking the component-wise conjugate multiplication of the resultant sums:

$$\{\text{receive channel 1} + \text{receive channel 2}\} \cdot \{\text{receive channel 7} + \text{receive channel 8}\}^{*}.$$

The effective baseline is small at 3.528 meters or $\frac{3.528}{\lambda} = \frac{3.528\, fn_{snow}}{c} = 2.5$ wavelengths, which is why only four fringes are seen. The magnitude of the interferogram is processed in the same way as the first image: filtering and power-log detection. The magnitude is an indication of the coherence between the two summed images and provides an indication of the interferometric quality of the phase information. The phase is magnitude detected and then median filtered with an extent of five pixels in each dimension. The reason for the magnitude detection is because there is left-right ambiguity in range. This means that scattering from either side of the radar in the cross-track dimension arrive simultaneously at the radar as shown in Fig. 5-15. Because of the simultaneous arrival of these two signals that have equal and opposite phase, the resultant plot tends to look cluttered. By taking the magnitude of the phase, the result tends to produce cleaner and more obvious fringes at the expense of having complete left-right ambiguity. The value of the phase is that it provides elevation angle information, albeit modulo 2π.

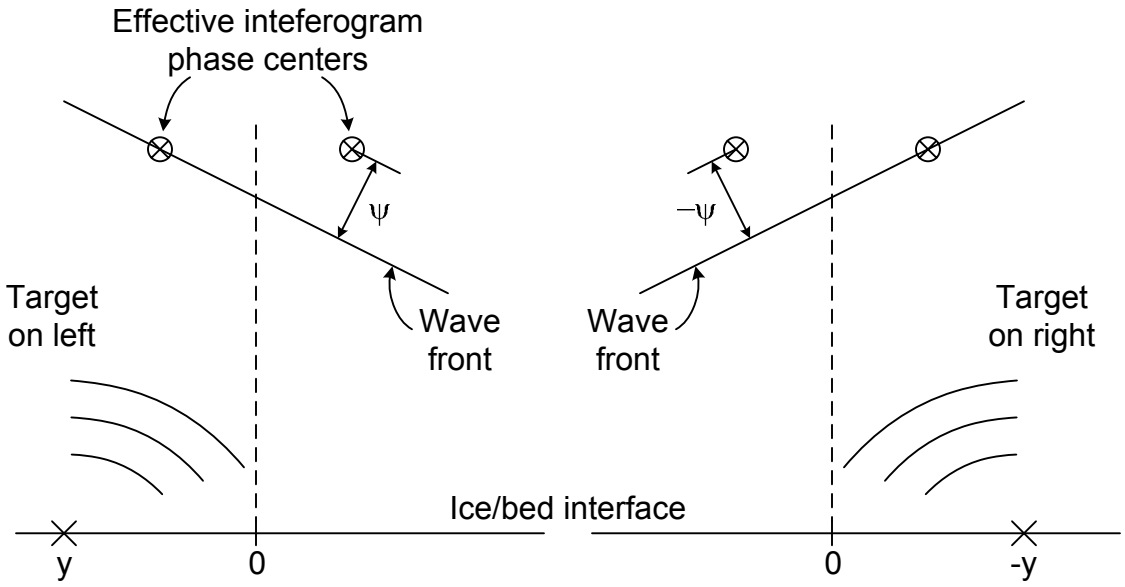

Fig. 5-15. Illustration of left-right ambiguity for a flat scattering surface.

Since we would like to view both the magnitude and phase of the interferogram together, a hue-saturation-value color scheme is used. The phase controls the hue or the color of the pixel, the saturation is always one so that no gray tones are used, and the value or brightness is set by the magnitude. Therefore, the darker a pixel is the lower its coherence and the more likely it is corrupted by noise. On the other hand, the brighter a pixel is, the higher its coherence is and the less likely its phase is corrupted. This provides an intuitive view of the interferogram since the brighter and more easily seen portions provide the best representation of the phase information. To enhance interpretation, the dynamic range of the magnitude is restricted by replacing all magnitude values above a maximum threshold or below a minimum threshold by the respective threshold which they exceeded.

Several interesting features and characteristics were observed in the data and our discussed in the following sections.

5.3.1 Analysis of Power Reflection Coefficient

In general, the magnitude of the basal return is linked to the ice thickness. This makes sense because of the dielectric loss of the ice. Fig. 5-16 shows a plot of the relative power

reflection coefficient (PRC) as a function of ice thickness. A first order polynomial is fit to the data – corrected for spherical spreading, the fit suggests a two-way ice loss of 80 dB/km. The polynomial fit excludes the effects of subglacial surface dielectric and roughness dependency on ice thickness, which are assumed to be independent. Based on the model described in section 2.1, the two-way ice loss from 2900-3200 m ice thickness should be between 30-50 dB/km. The loss is higher at the bed because of the increased temperature which both natural and impurity conductivities have positive correlation with. However, this predicted loss is over 1000 times smaller (30 dB) than the measured loss. This wide difference is probably a result of a combination of errors. The first and foremost is errors in the dielectric loss which are probably underestimated [60]. The second is that there may be a dielectric dependency versus ice thickness. This could be due to sediments getting trapped in valleys. This could account for 10 dB of the difference in scattered power since sediment has a dielectric very close to ice. A 10 dB difference is amplified by the fact that only 350 m of ice thickness variation is seen in the measurements, meaning that the loss per km would be affected by 20-30 dB/km.

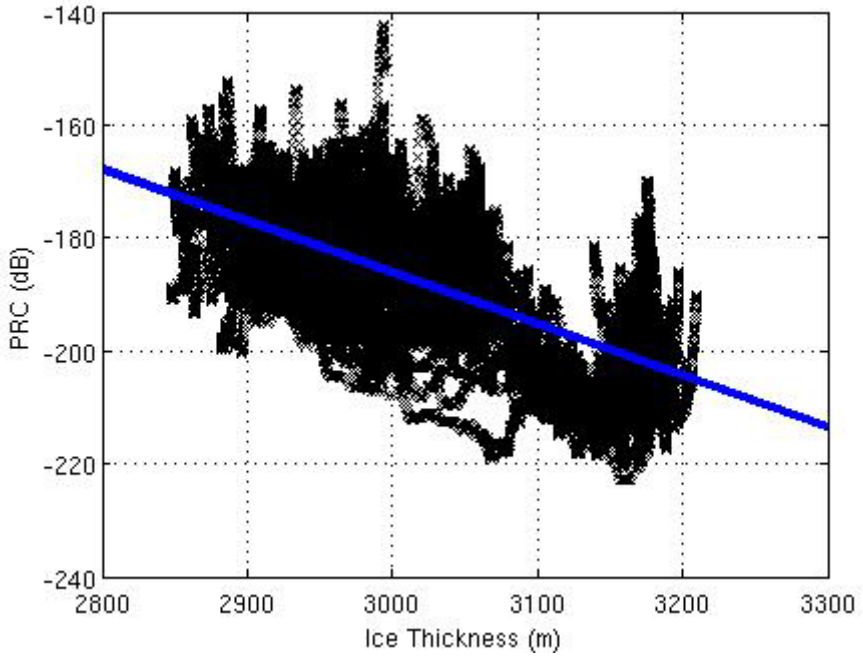

Fig. 5-16. Power reflection coefficient (PRC) as a function of ice thickness. The blue line is a first order polynomial fit to the data.

5.3.2 SURFACE SLOPE SIGNATURE IN INTERNAL LAYERS

The along-track slope of internal layers can be measured by tracking the phase of the slope as a function of the along-track radar position over long distances. The layers are very smooth with slopes that are much less than 1 deg. With the cross-track receive elements and sufficient SNR, the air-ice surface slope can be inferred from the interferogram if the internal layers are flat in comparison. Because the surface slopes are small, no wrapping of the interferometric phase occurs and the phase can be plotted without magnitude detection. This means that positive and negative slopes can be distinguished. An interferogram showing the interferometric phase of the internal layers is given in Fig. 5-17. The phase deviations when converted into slope show that the surface slope is oscillating between ±2.5 deg.

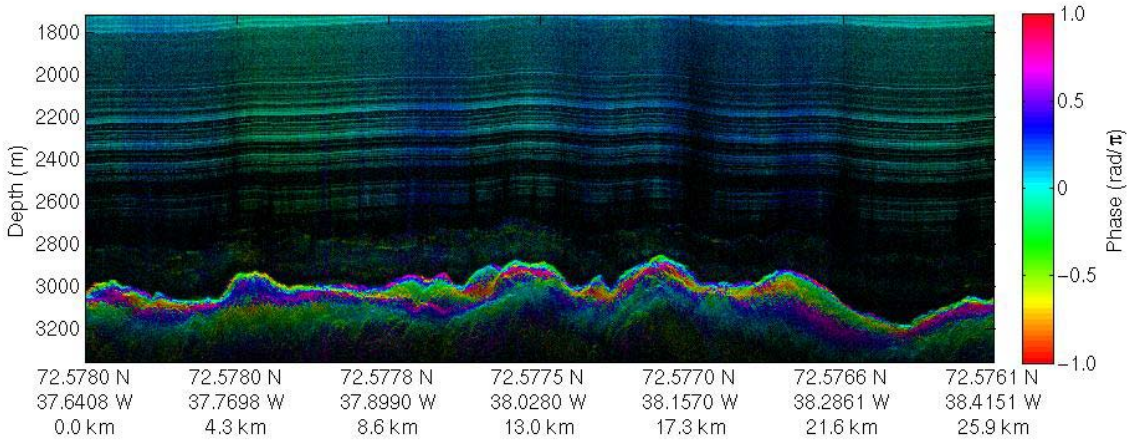

Fig. 5-17. Interferogram showing surface slope.

5.3.3 POINT TARGET

In Fig. 5-21 there is a point target located in the trench on the right hand side of the figure. A magnified view of the point target is shown in Fig. 5-18 before and after migration. The point target may be a nearby hill which happens to have a slope and surface that produces a specular-like response explained by facet scattering theory. The significance of this point target is two-fold. First, it shows that the migration algorithm is compressing the hyperbolas. Isolated targets such as this present a possibility for testing and refining other procedures such as autofocus algorithms in lieu of manmade

calibration targets. Secondly, this point target is at the apex of a very large hill nearby that would prevent some radar systems with poor cross-track resolution from properly estimating the nadir return. As a side note, the interferogram shows that the point target is off to one side of the platform because its phase is non-zero.

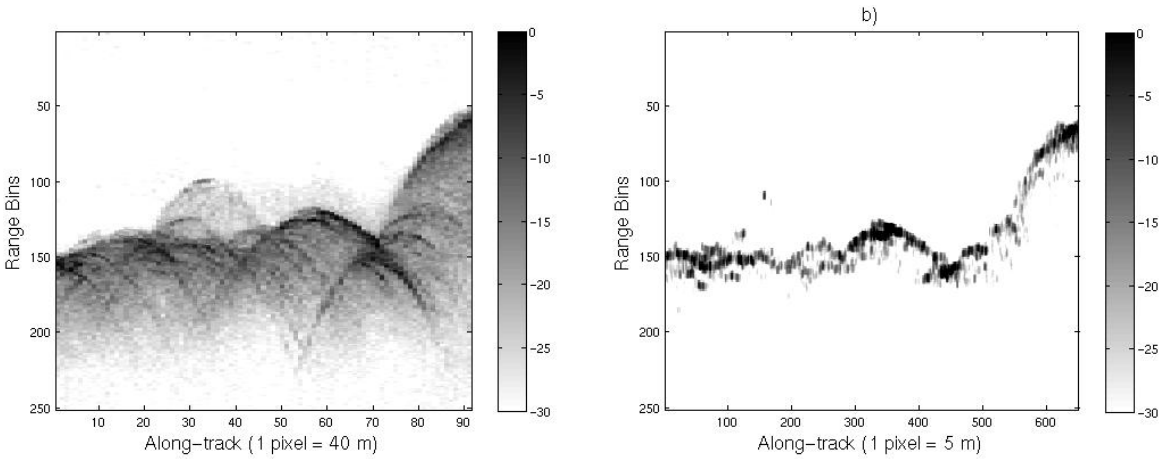

Fig. 5-18. Magnified view of point target in sequence 5, July 20, 2005 a) before and b) after migration. One range bin is 1.05 m in ice.

5.3.4 SCATTERING BETWEEN INTERNAL ICE LAYERS AND THE BEDROCK

In every migrated image, there appears to be weak scattering between the internal ice layers and the bedrock. To discount the possibility that this energy is actually range-sidelobes of the bedrock return we make two observations. 1) The scattering only partly tracks the bedrock return whereas sidelobes would show a much stronger correlation. This is especially noticeable over the deep trench in each image – the bed elevation drops hundreds of meters, but the scattering does not drop as much. 2) The scattering strength seems to depend more on the roughness of the bedrock rather than the power of the basal scattering. On the other hand, sidelobes would track very closely to changes in signal strength. This lack of correlation is most noticeable in sequence 6, July 22nd near the bright scatterer in the trench (see Fig. 5-31).

Two different causes of this scattering are considered. The scattering appears to be from distributed point targets, but there is some structure that roughly follows the bed.

Unlike the specular layers above the scattering which have angles of arrival concentrated in the nadir direction, an interferogram formed using the first and last receive channels shows a wide range of angles of arrival. If the scattering is due to layers, the layering has been disrupted – most likely because of ice flow so close to the very rough bed. An interesting note is the rather rapid change from specular layering to this diffuse scattering. It is almost as if there is a sudden change in the flow regimes of the ice. The other possibility for scattering is englacial debris, but this seems unlikely given that both the GRIP and GISP2 cores contained very low concentrations of debris [53].

5.3.5 BRIGHT TARGET AT BOTTOM OF TRENCH

A 250 m long bright target with a slope of 1-2 deg is located at the bottom of the trench that runs aside the GRIP borehole. In the region surveyed, this target is located in the narrowest portion of the trench as shown by the digital bed elevation map in Fig. 5-38. The relative signal strength is plotted in Fig. 5-19 after being passed through a 100 m moving average filter and is approximately 30 dB stronger than neighboring targets. Based on the interferogram, the target is directly beneath the radar platform since the phase is zero. The pre-migrated data show that the raw scattered energy is also significantly higher. There are also hyperbolas present – suggesting that the surface may not specular. Because the GRIP bore hole is only a few km from the target, we used the bottom 50 m of the temperature profile from GRIP to extrapolate the temperature down to the target depth of 3185 m as shown in Fig. 5-20. The estimated pressure melting temperature is about -2.4 C [46]. If the linear approximation for temperature is correct, the temperature at the base is -4 C or 1.6 C above the melting point. With radiometrically calibrated basal scattering data, the absolute scattering strength could be inferred and thereby an estimate of the dielectric of the basal material. Unfortunately, due to the large error bars associated with the ice loss only a relative measure is possible.

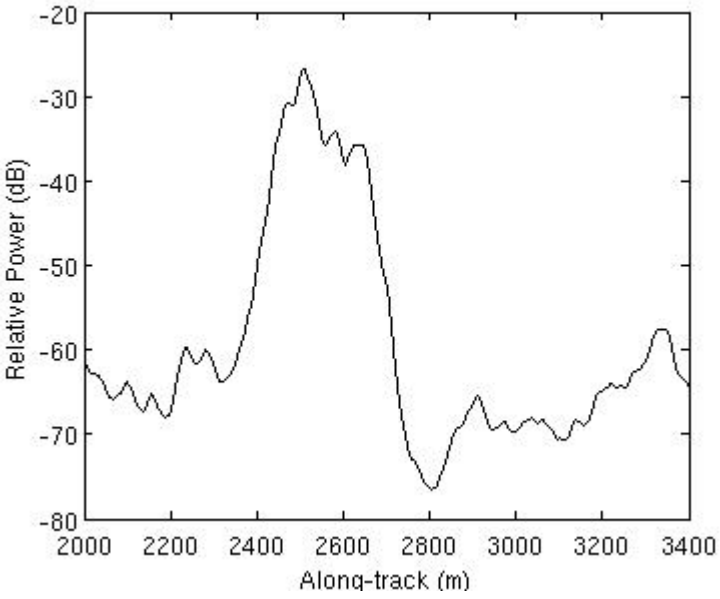

Fig. 5-19. Shows signal strength of peak return as a function of along-track position. The brightness of the target is about 30 dB stronger than neighboring targets after f-k migration.

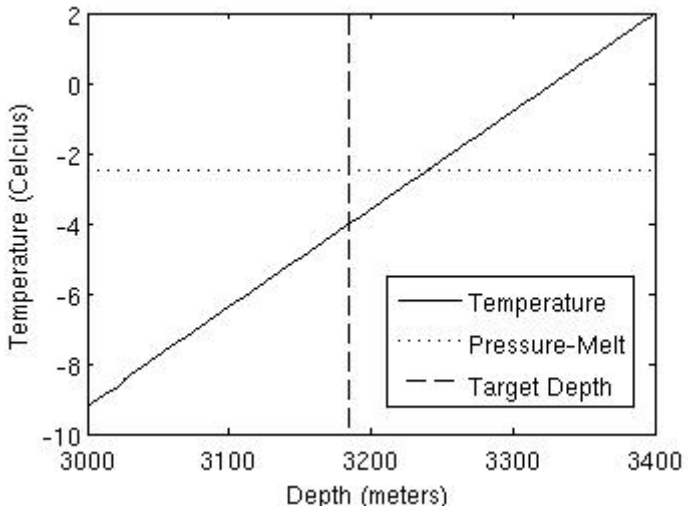

Fig. 5-20. Temperature of basal ice extrapolated to 3400 m ice thickness from the last 50 m of the temperature record at GRIP. The expected pressure melting temperature (approximated at -2.4 C is shown) as is the target depth of 3185 m.

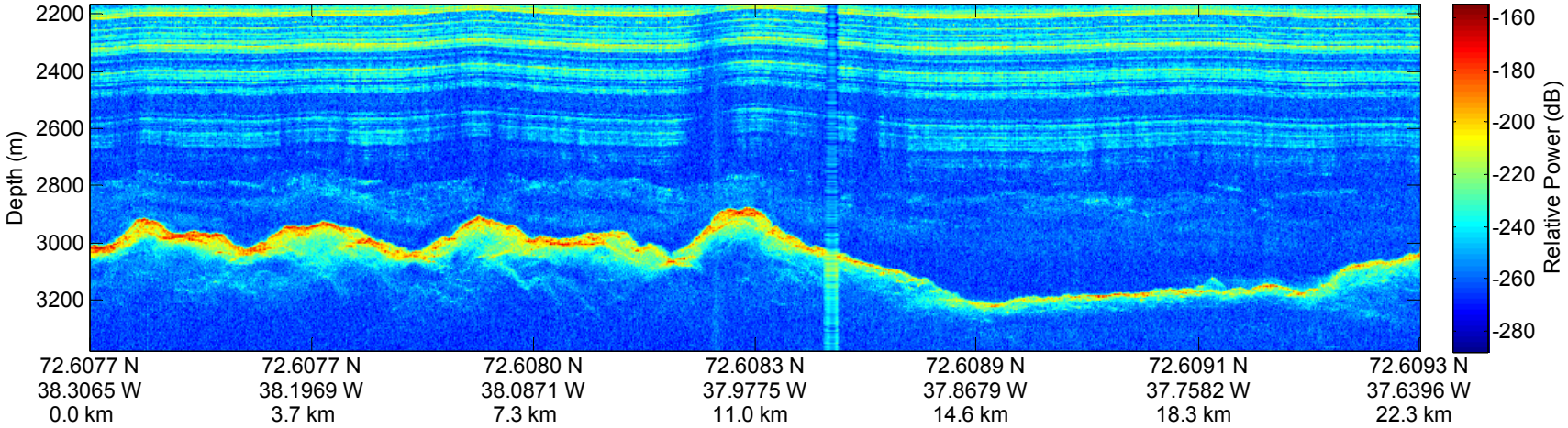

Fig. 5-21. f-k migrated data sequence 5 from July 20, 2005.

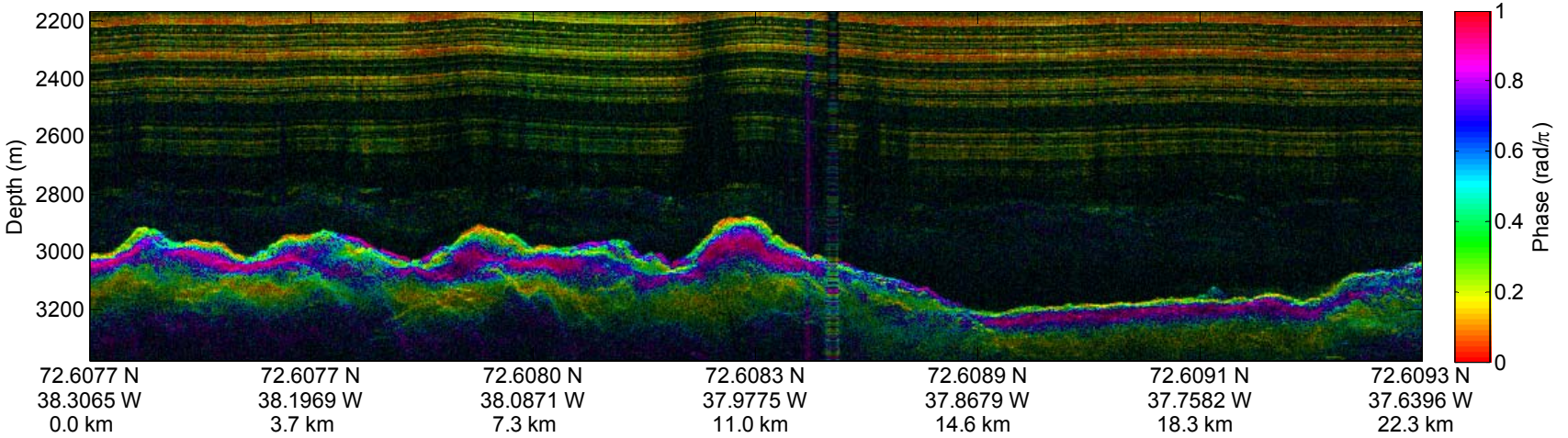

Fig. 5-22. Interferogram of f-k migrated data sequence 5 from July 20, 2005.

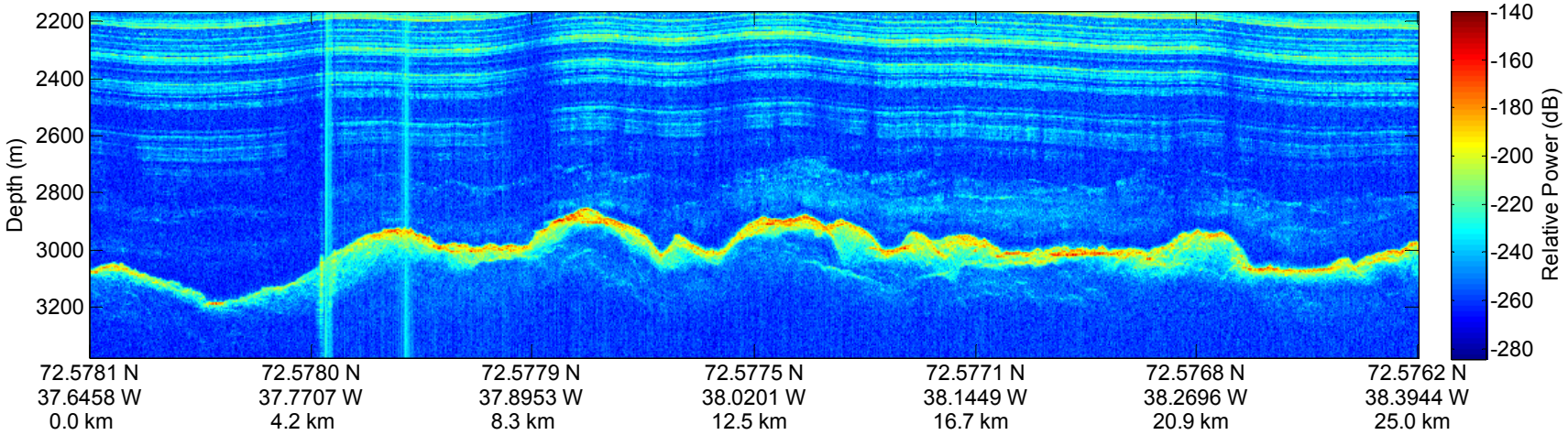

Fig. 5-23. f-k migrated data sequence 9 from July 20, 2005.

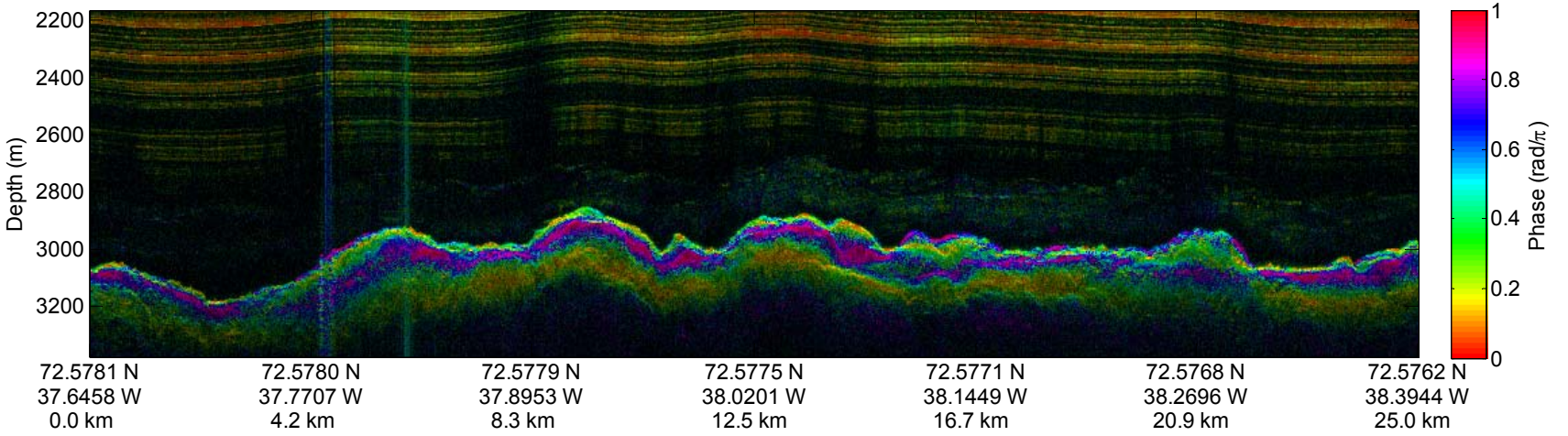

Fig. 5-24. Interferogram of f-k migrated data sequence 9 from July 20, 2005.

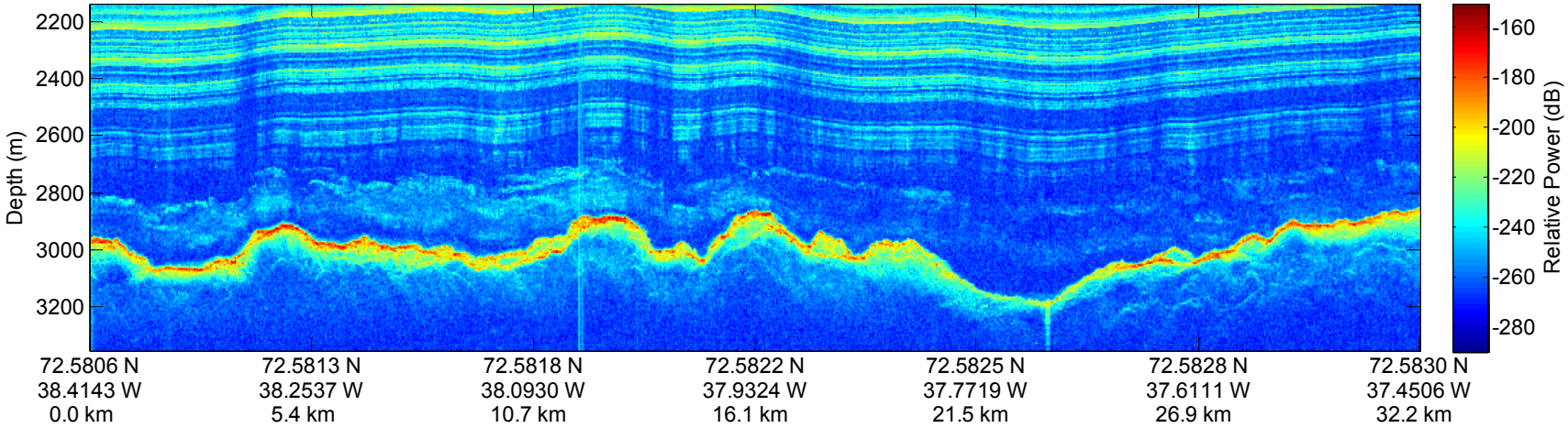

Fig. 5-25. f-k migrated data sequence 2 from July 21, 2005.

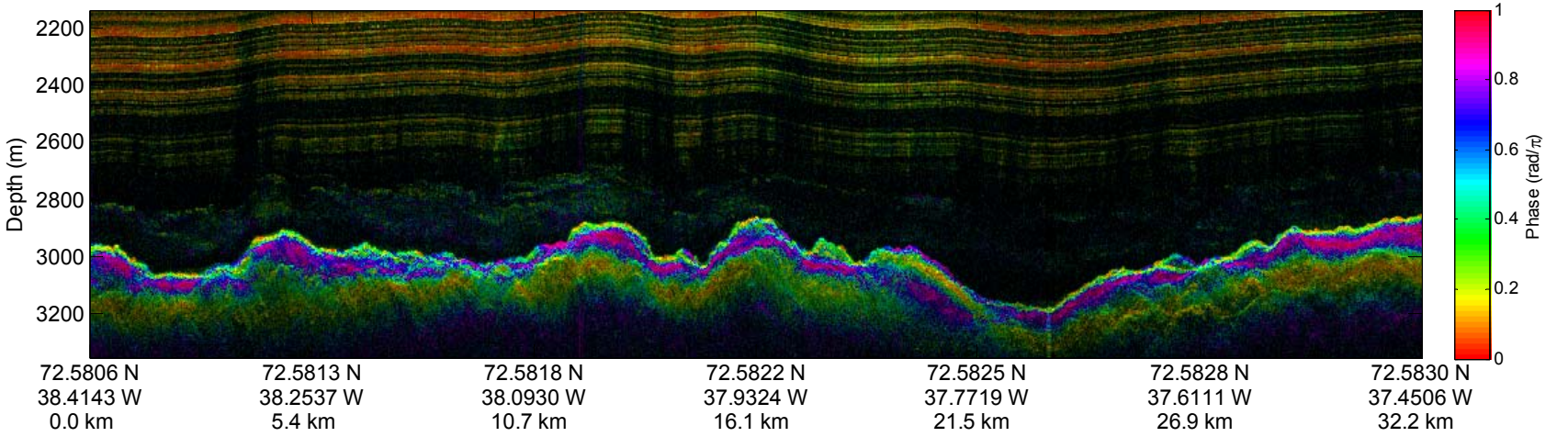

Fig. 5-26. Interferogram of f-k migrated data sequence 2 from July 21, 2005.

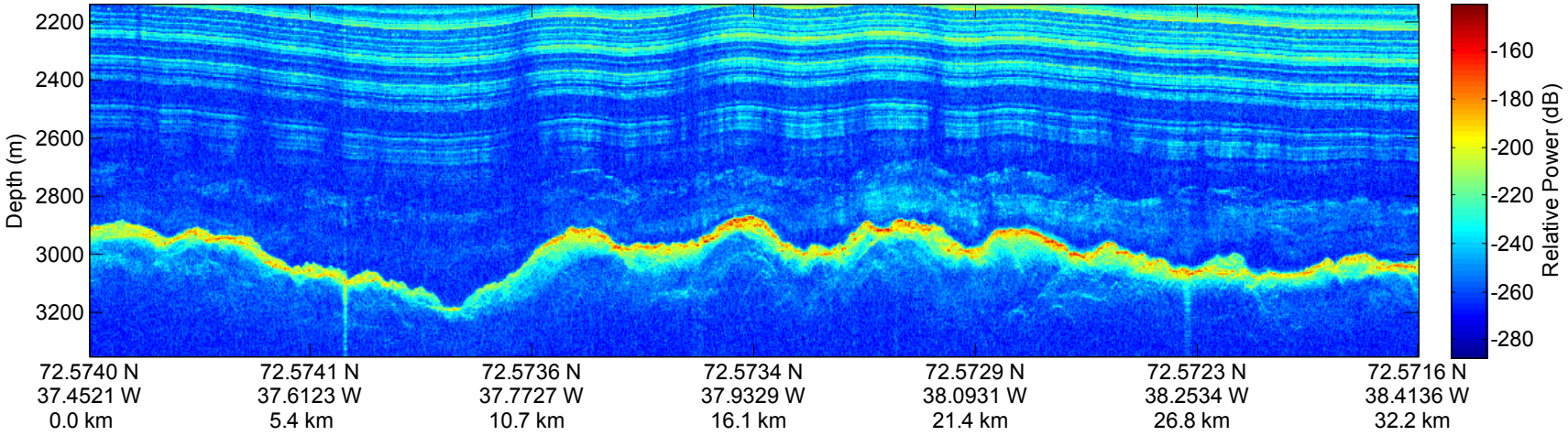

Fig. 5-27. f-k migrated data sequence 6 from July 21, 2005.

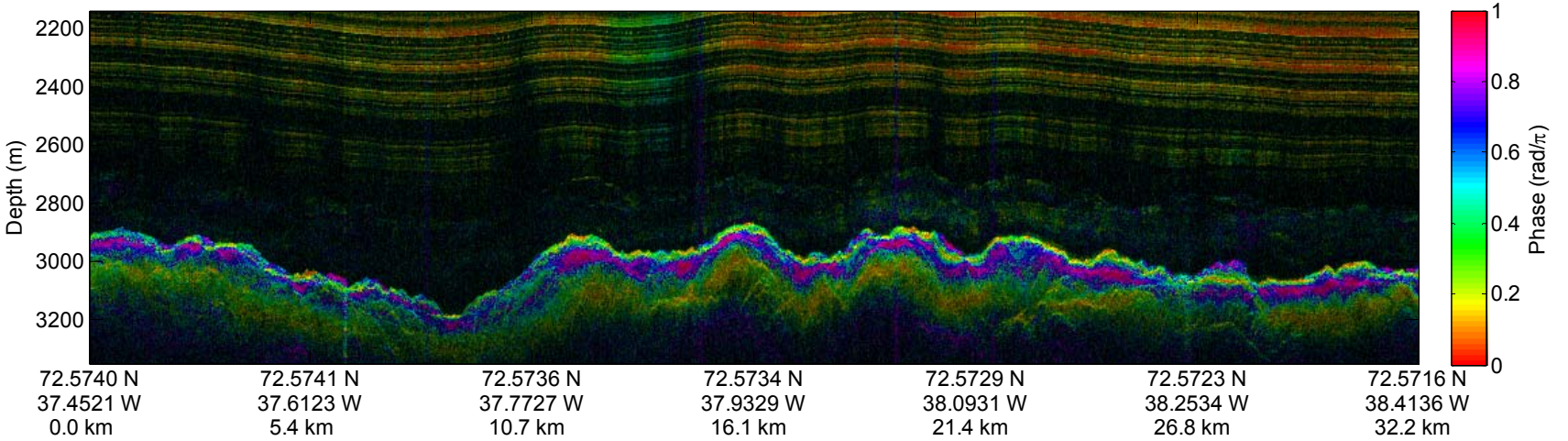

Fig. 5-28. Interferogram of f-k migrated data sequence 6 from July 21, 2005.

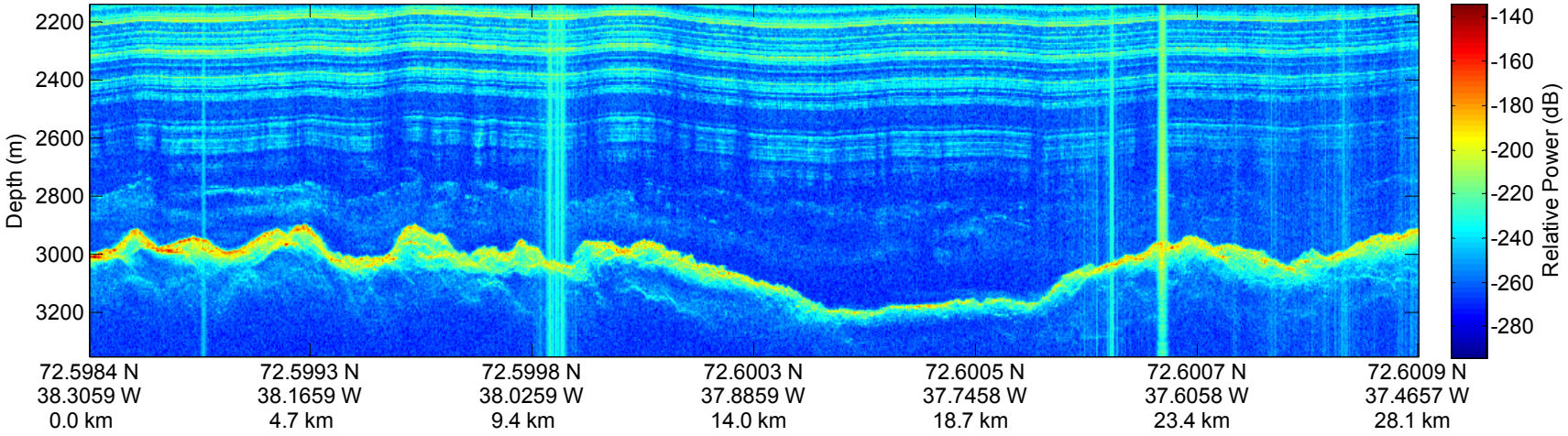

Fig. 5-29. f-k migrated data sequence 3 from July 22, 2005.

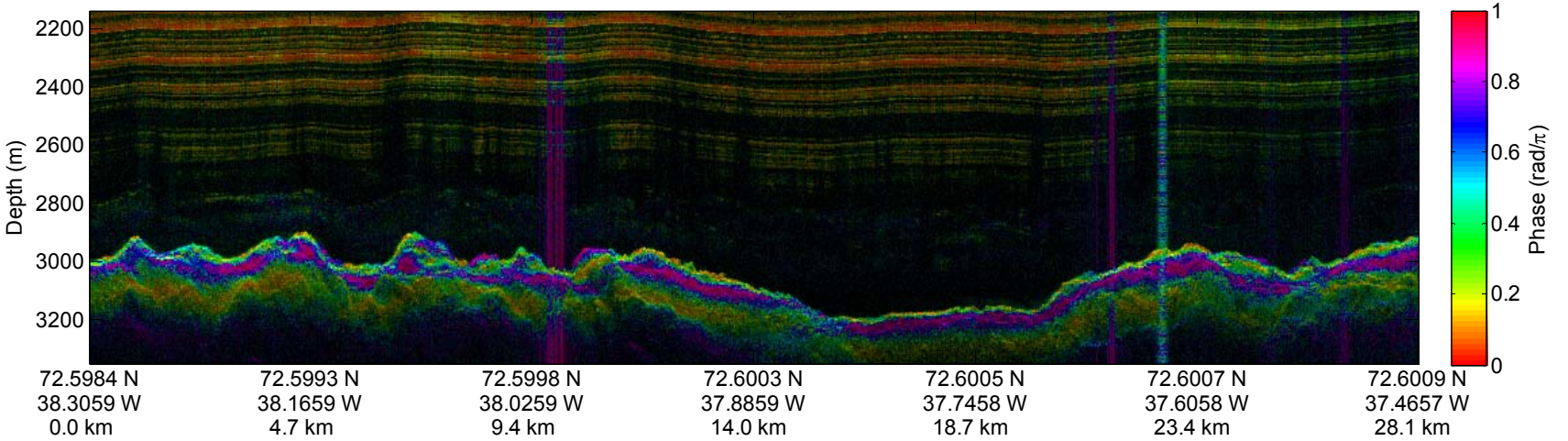

Fig. 5-30. Interferogram of f-k migrated data sequence 3 from July 22, 2005.

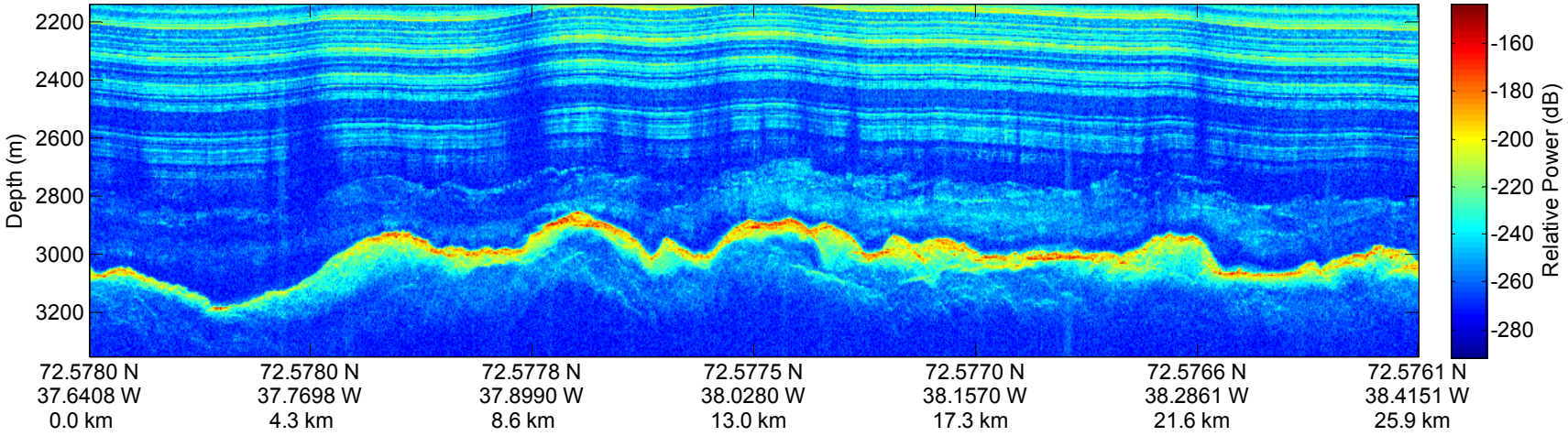

Fig. 5-31. f-k migrated data sequence 6 from July 22, 2005.

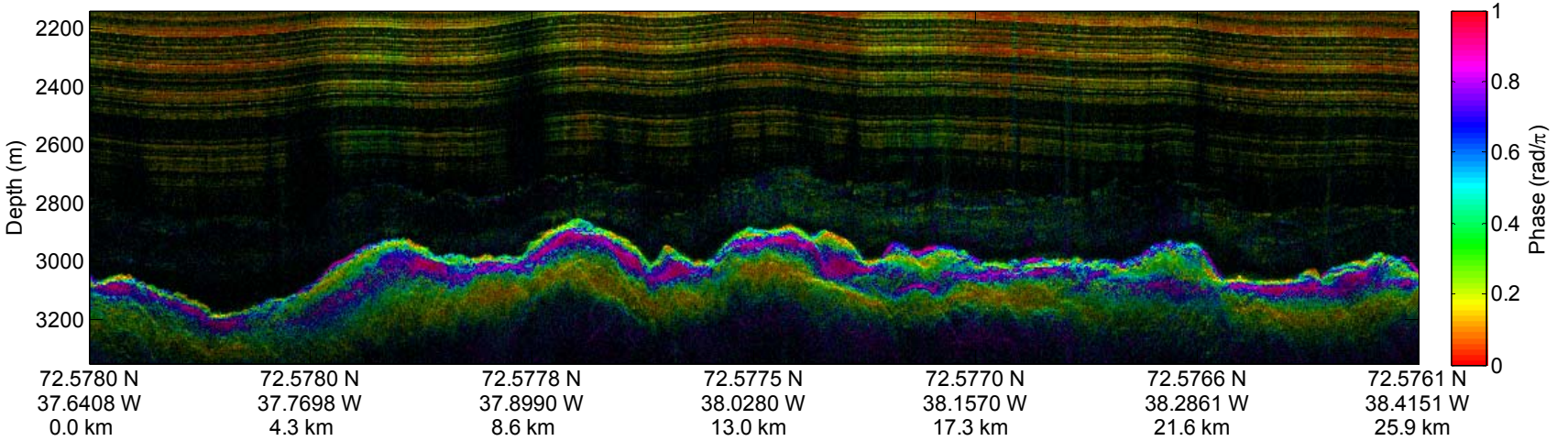

Fig. 5-32. Interferogram of f-k migrated data sequence 6 from July 22, 2005.

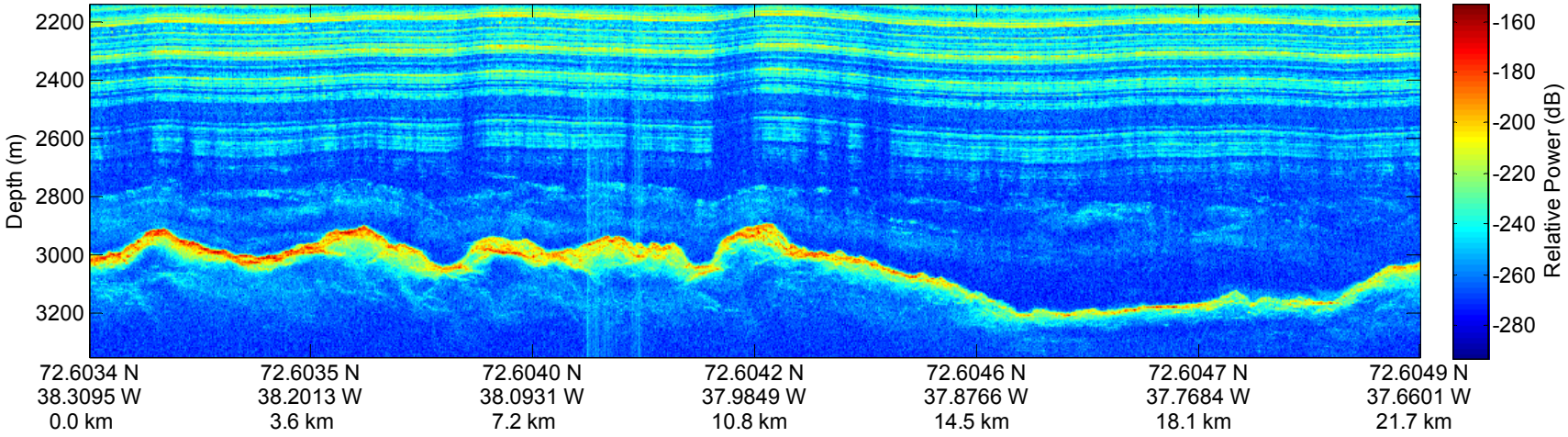

Fig. 5-33. f-k migrated data sequence 18 from July 23, 2005.

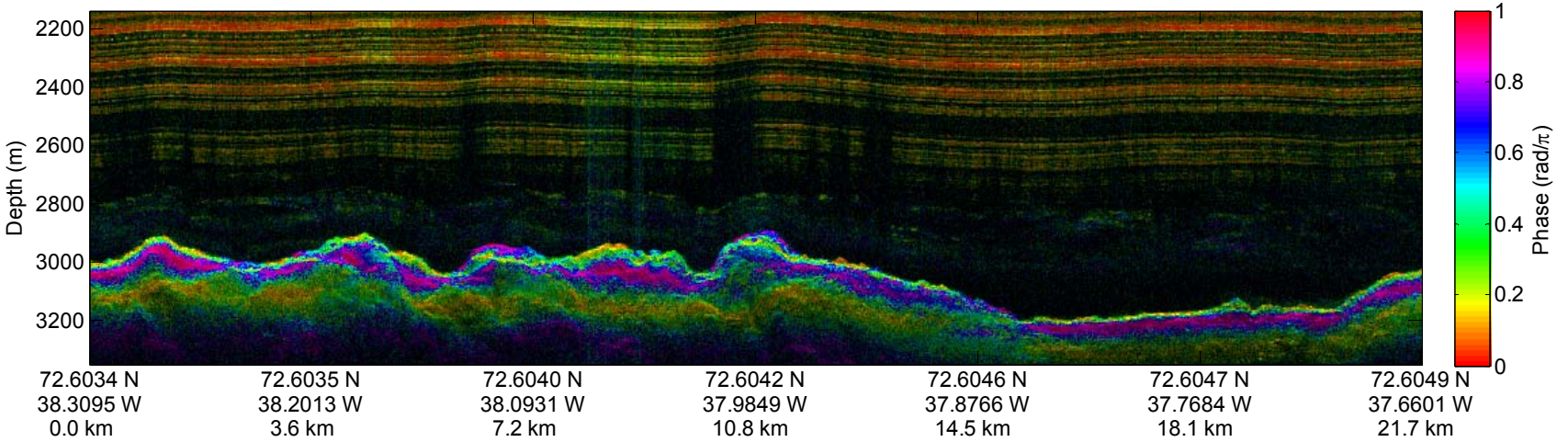

Fig. 5-34. Interferogram of f-k migrated data sequence 18 from July 23, 2005.

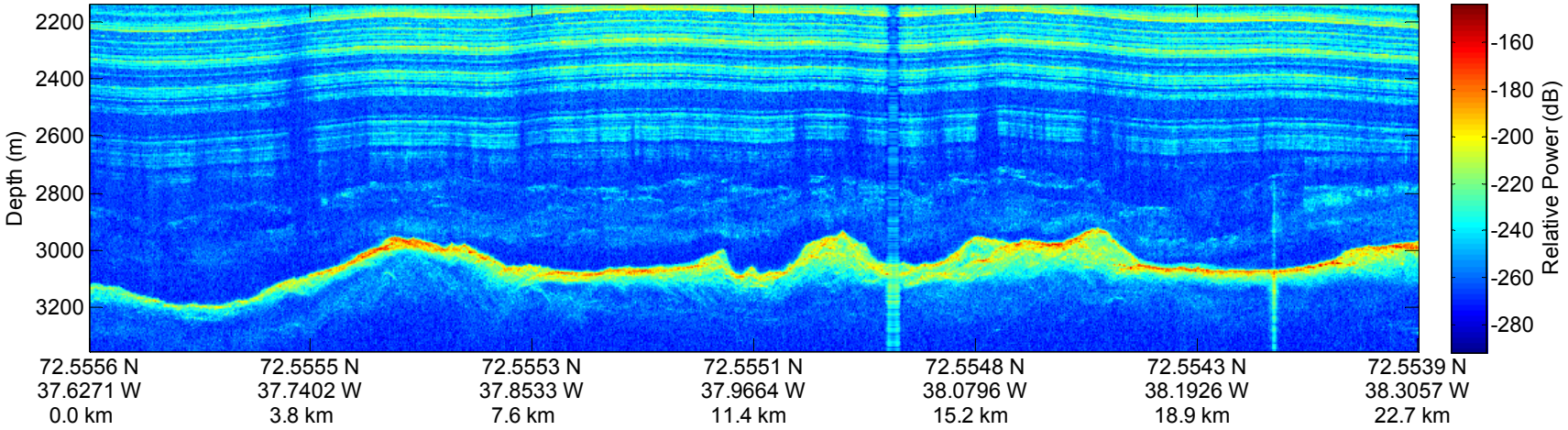

Fig. 5-35. f-k migrated data sequence 22 from July 23, 2005.

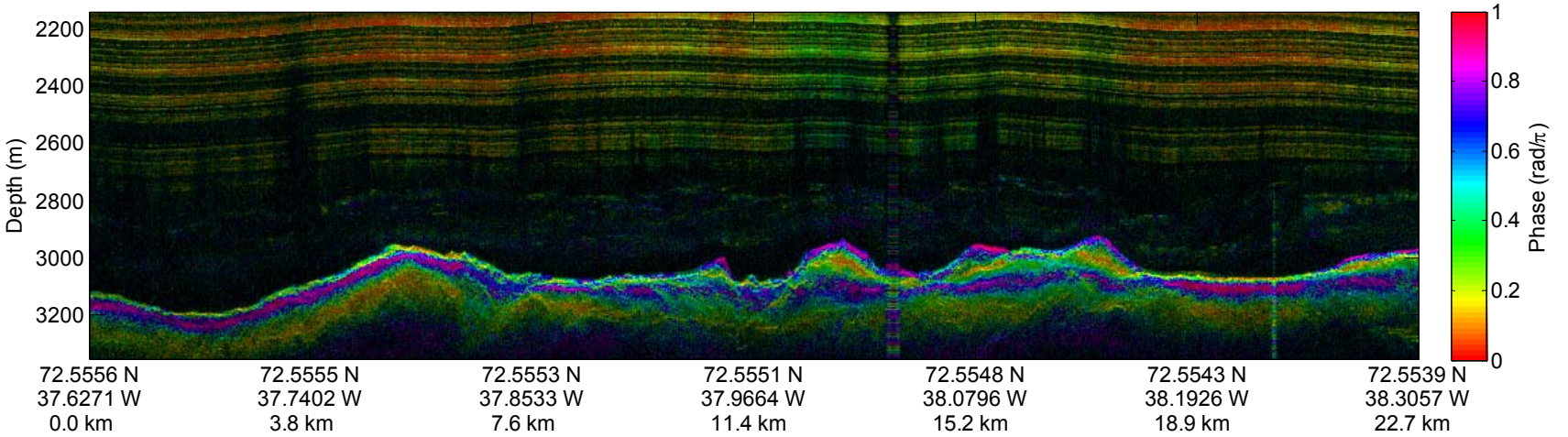

Fig. 5-36. Interferogram of f-k migrated data sequence 22 from July 23, 2005.

5.4 DIGITAL ELEVATION MODEL: DELAUNAY TRIANGULATION

The migrated images are used to determine the bed elevation that is needed to generate the SAR geometry. Because of the large SNR, a simple algorithm is used to track the bed. The migrated image is power detected and then filtered using a simple two-dimensional boxcar-like filter with a final resolution of 5 m in depth and 15 m in along-track. The bed is taken to be the first range bin that exceeds a threshold value set by the noise level of the prior record (typical value used is 25 dB above the noise of the previous record). The algorithm handles low SNRs by dropping the threshold so that it is 10 dB below the peak signal in the record – the threshold is reset to its normal value when the SNR returns to normal. Since the bed elevation should be contiguous, the algorithm restricts the maximum change in bed elevation from one record to the next to 20 meters. This value is small enough that it keeps the bed tracker from jumping all over, but large enough to allow it to re-lock to the bed when it gets off track. An example of the bottom detection is given in Fig. 5-37. The dark black line is the bed detection algorithm's output. The output is filtered over 40 records or 200 meters.

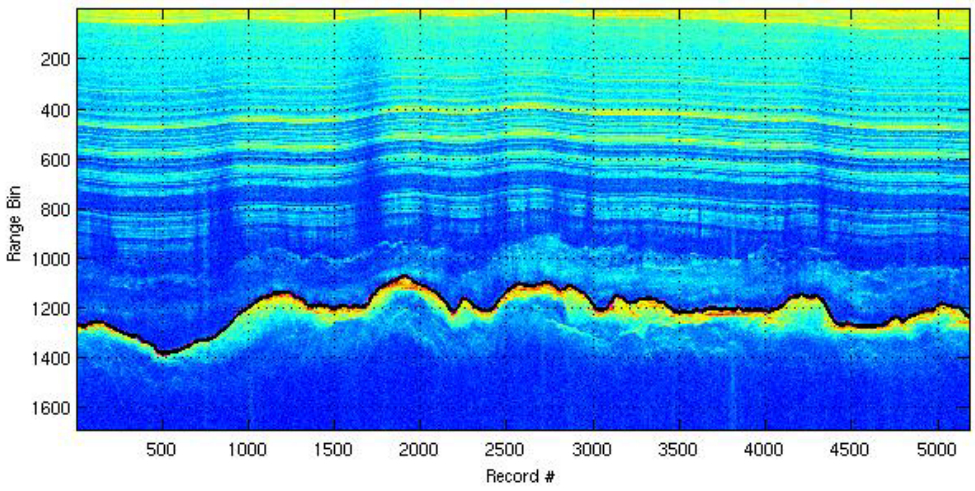

Fig. 5-37. Result of bed detection (black line) superimposed on the f-k migrated image.

Once all the migrated images are run through the bed tracking algorithm a digital elevation map is generated from the traverse lines using the linear Delaunay triangulation algorithm. The results are shown in Fig. 5-38. The traverse lines are in black and represent the locations of the data points. The areas in between are interpolated. Since ground truth data exist for the ice thickness at GISP2 and GRIP, a comparison with the ice thickness used to generate the DEM is given in Table 5-1. There appears to be a bias of about -15 meters in the ice thickness estimate. If the error is caused by a velocity error in ice, a permittivity change of -0.03 would be needed to correct it. The difference may be attributable to three other sources of error. The first is that the data are low-pass filtered after bed tracking. The second is that a nearby hill would mask the actual bed location. Finally, the bed estimate may be biased because the tracker chooses the first range bin that exceeds a threshold set relative to the noise floor – if the signal is very strong this may actually be a sidelobe of the actual bed reflection.

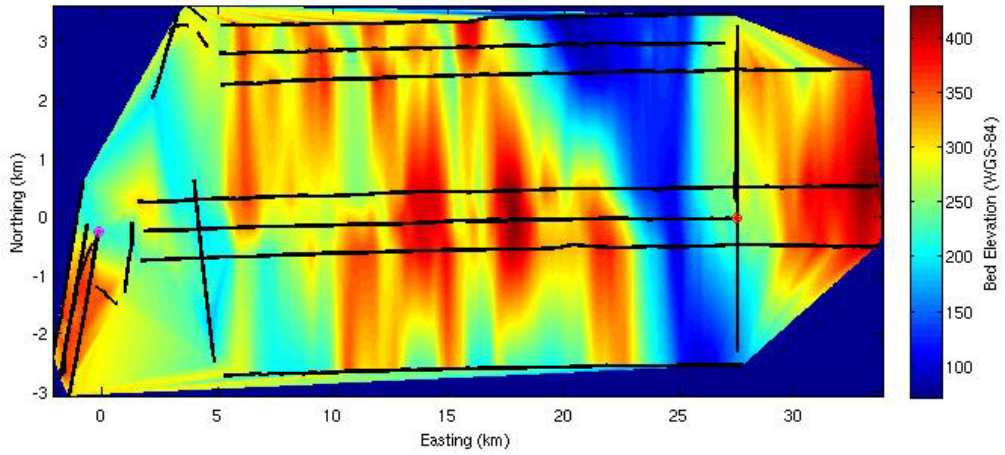

Fig. 5-38. Digital elevation map of subglacial bed generated from migrated images. GISP2 is marked by a magenta circle and GRIP is marked by a red circle.

Table 5-1: Comparison of DEM with GRIP and GISP2 ground truth data.

Borehole	Ground Truth	DEM	Error
GRIP	3027.6 m	3015.3 m	-12.3 m
GISP2	3047.9 m	3029.9 m	-18.0 m

Chapter 6: SYNTHETIC APERTURE RADAR PROCESSING

6.1 SAR PROCESSING ALGORITHM

The synthetic aperture radar (SAR) processing algorithm used is time-domain correlation [144]. This is essentially a matched filter applied in the space-time domain so the operation is similar to a standard two-dimensional linear time-invariant filter (i.e. convolution). We assume that the scene of interest is linear, and therefore the total radar response for each measurement can be found from adding the individual responses from each target. Additionally, the noise is assumed to be complex additive Gaussian noise. Based on these assumptions we take the form of the measurements to be

$$\mathbf{x} = \mathbf{G}\mathbf{s} + \mathbf{n}$$

where $\mathbf{x}$ is an N-by-1 vector of space-time measurements, $\mathbf{G}$ is an N-by-M matrix relating the image pixel backscattering to the space-time measurements, $\mathbf{s}$ is an M-by-1 random vector representing zero-mean backscatter signal from each of the M image pixels, and $\mathbf{n}$ is an N-by-1 random vector of zero-mean additive Gaussian noise. All vectors and matrices are complex. Additionally, the elements of $\mathbf{s}$ are assumed to have unity variance and be independent of each other. This is not really as restrictive as it sounds because the linear map, $\mathbf{G}$, captures correlation and non-unity variance. $\mathbf{n}$ is assumed to be independent and identically distributed with no assumptions about variance. Finally, the elements of $\mathbf{s}$ and $\mathbf{n}$ are independent.

For this form of measurements, the matched filter is derived in section 4.5.1 to be

$$\mathbf{l}_{MF,m} = \frac{\mathbf{G}_{:,m}}{\left|\mathbf{G}_{:,m}\right|^2}.$$

The filter coefficients for a target are referred to as the target's "reference function." The estimate of the backscattering from pixel m is then the inner product of the target's

reference function and the measurements: $\hat{s}_m = \mathbf{l}_{MF,m}^H \mathbf{x}$. This result is the same as the traditional matched filter in that the filter coefficients are the conjugate of the expectation of the SNR. The only difference is that a generic linear map is used to associate the measurements with the image pixels. The linear map is determined using the radar equation described in section 0. The targets in the SAR processor are approximated by a set of isotropic point scatterers with frequency-independent complex weights. Therefore, the scattering term in the radar equation, $A\sigma_0$, is represented as a single isotropic point scatterer.

Note that the radar equation only gives the magnitude response. To determine the phase response of the system, propagation delays and equipment phase information must be known. The propagation delay is found from refraction, path length and changes in velocity. The equipment phase delay is determined from the measured S_{21} parameters of the transmitter and receiver responses. To determine the path lengths requires knowledge of how the ray was refracted along its traverse. This is dealt with using the ice sheet model described in section 2.1.

The reason for operating in the space-time domain is to avoid traditional motion compensation techniques that are required to uniformly fit the data to a straight line trajectory in order to use Fourier techniques. In the case of nadir sounding, cross-track motion produces virtually no effect on the imaging algorithm. On the other hand, cross-track motion has a large effect on side-looking imaging algorithms. Because the ice sheet is barren of visually identifiable objects that can be used to track off while driving, the radar trajectory in this work has significant cross-track movement[21]. By processing in space-time, $\mathbf{G}$ can easily account for these variations.

To keep the processing tractable in terms of computational complexity, several techniques were used. The first is that the data are pulse compressed before SAR processing to reduce the time-extent of a target's scattered energy. Ideally, every measurement is placed inside the measurement vector $\mathbf{x}$. However, only a few samples as determined by $\mathbf{G}$ actually contain significant energy from the target. This means that

[21] A handheld GPS was used and provided heading information, but the resolution was coarse.

the size of $\mathbf{x}$ and $\mathbf{G}$ can be much smaller during the solution for a particular target. In the algorithm used for this work, only eleven time samples – five on each side of the main lobe – are used. This allows the magnitude and phase information of the main lobe and the first few side lobes to be included.

The second simplification was to use along-track low-pass filtering followed by down-sampling to reduce the number of spatial measurements included in $\mathbf{x}$ and $\mathbf{G}$. Decimation is limited by two factors:

1) The along-track filtering process removes the high spatial-frequency energy on the edges of the hyperbola and thereby limits the maximum SAR aperture length.

2) The uniform re-sampling of the data required by the Fourier transform to apply standard filtering techniques does not account for cross-track movement.

The two limitations interact with one another and both enforce requirements that need to be satisfied. Limitation 1) is a standard trade-off that must be made in any SAR application and is sometimes referred to as pre-summing (although we apply a true spatial filter for reasons explained in section 5.2). The second limitation is dependent on the accuracy of the platform heading. Since the averaging lengths to be considered are less than 10 meters and given the limited mobility of the platform, the cross-track movement is linear during averages. In other words, the vehicle does not change directions fast enough to allow for significant oscillations in cross-track movement during a single averaging interval. The filter before decimation then becomes not only a low-pass filter in the along-track domain, but a low-pass filter in the cross-track domain. Essentially, a rotation of the filter in the spatial domain corresponds to a rotation in the wavenumber domain. For side-looking operation this can have serious implications because we are interested in keeping the cross-track beamwidth wide enough to always "see" the whole scene for the entire SAR aperture length. This is illustrated in Fig. 6-1. If the heading was always zero, the filter width could be set exactly equal to the SAR aperture length. However, for a non-zero heading the filter width must be enlarged so that even after rotation the entire scene (hashed area) is still in the filter.

For over 99% of the measurements, the platform heading error from a straight line trajectory is less than 10 deg. The swath width stretches to 1000 m on each side of the

platform. Therefore the effective SAR aperture length considered in limitation 1) must be extended by $2 \cdot 1000 \tan(10 \text{ deg}) = 350 \text{ m}$ to allow for the non-zero headings.

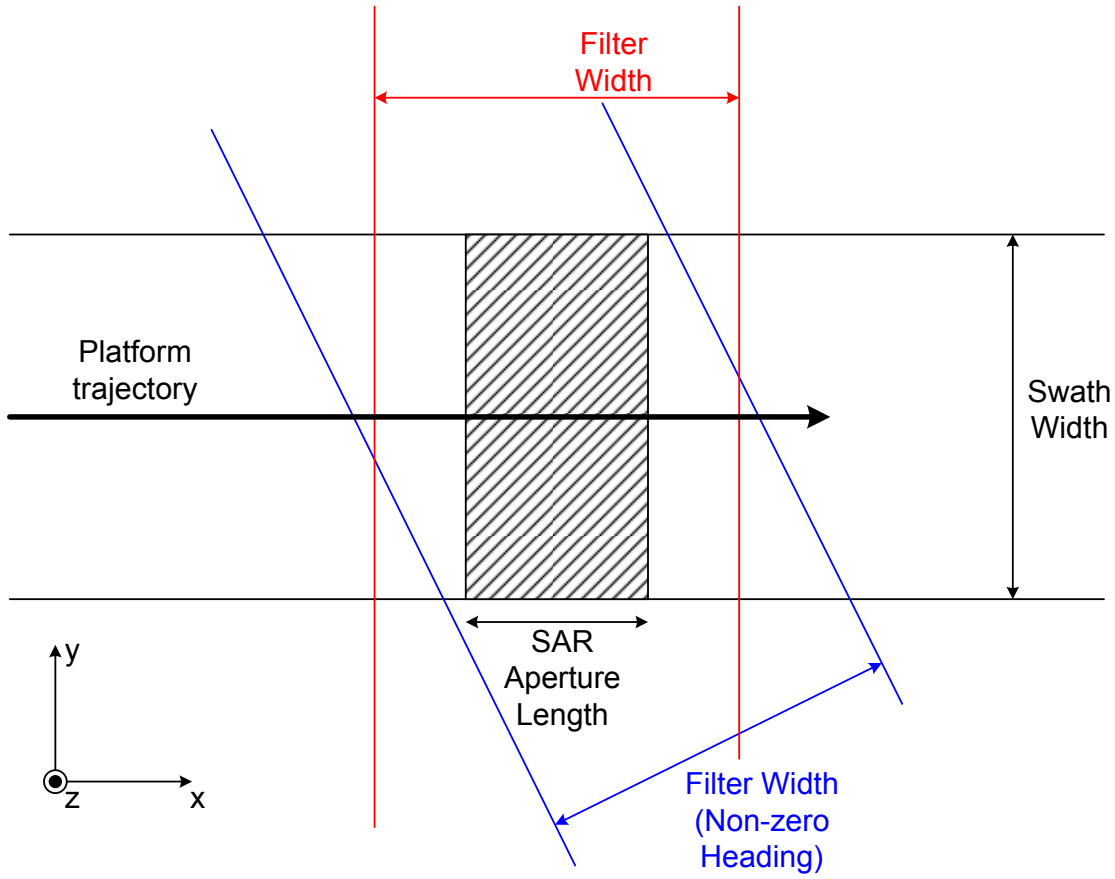

Fig. 6-1. Relationship between SAR aperture length and filter width for a non-zero heading.

The SAR aperture length was restricted to 300 m (resulting in 10 m image resolution) to keep the computational complexity at a manageable level. To increase it to 600 m would result in a four times increase in the computation time. Based on the current computation time of 560 hours for a 300 m aperture, the dataset would take more than 2000 hours to process. The primary purpose of this work is to show the feasibility and value of side-looking SAR to subglacial beds, which the shorter aperture length does effectively.

6.2 SIMULATIONS

As with the f-k migration routine, a target simulator is used to test the algorithm as well as to fine-tune choices in window size, pre-summing, etc. A simulation of a single point target is shown in Fig. 6-2 and the SAR processed result is shown in Fig. 6-3. Several points came out of these simulations and these are listed here:

1. As noted above, pulse compression was applied before the data were sent to the SAR processor. The time-domain windowing, Hanning, is also applied during the pulse compression. No additional time-domain windowing is needed during the SAR processing. The windowing could be applied in the SAR processor, but would be degraded by the truncated time-domain correlation of only 11 time samples. A small degradation in the cross-track/time-domain side lobe levels is seen when windowing is performed in the SAR processor.

2. A Hanning window is used for spatial filtering during the pre-sum process – the reasoning and purpose are the same as for f-k migration that are described in section 5.2. As explained above, because of the non-zero heading, the spatial filter's beamwidth used for the SAR processor is wider. The filter used is twice as wide as what would have been needed if we could have assumed zero-heading. Because the filter is twice as wide (600 m along-track versus 300 m along-track), the along-track decimation rate is also halved. The end result being that the SAR processor is fed twice as many spatial samples, because they are more finely spaced. The finer spacing, although doubling the processing time, also reduced along-track sidelobes. This is because of the improved control of the reference function over the synthetic aperture that finer sampling affords.

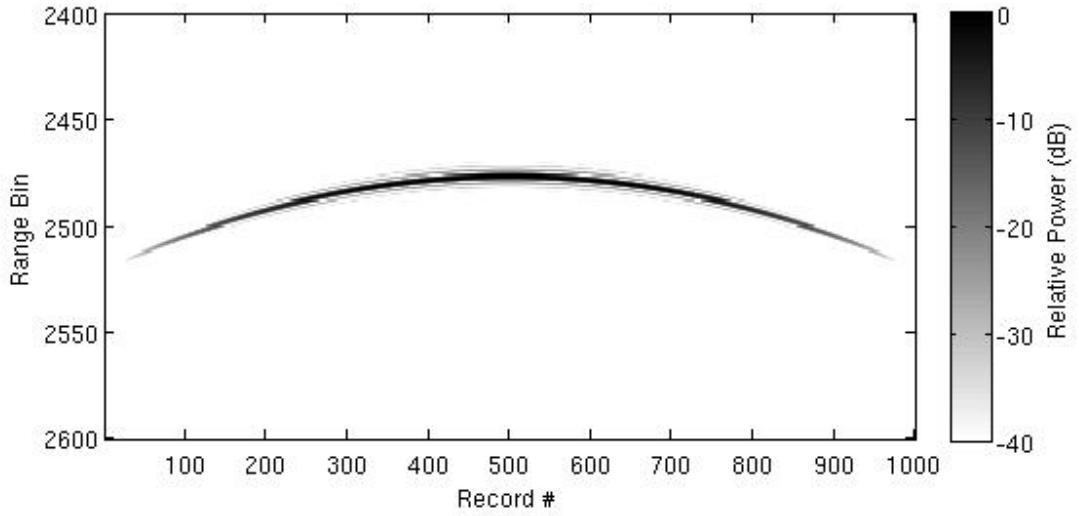

Fig. 6-2. Simulation of a single point target after pulse compression. The signal grows weaker towards the sides because of weaker reflectivity and greater signal loss.

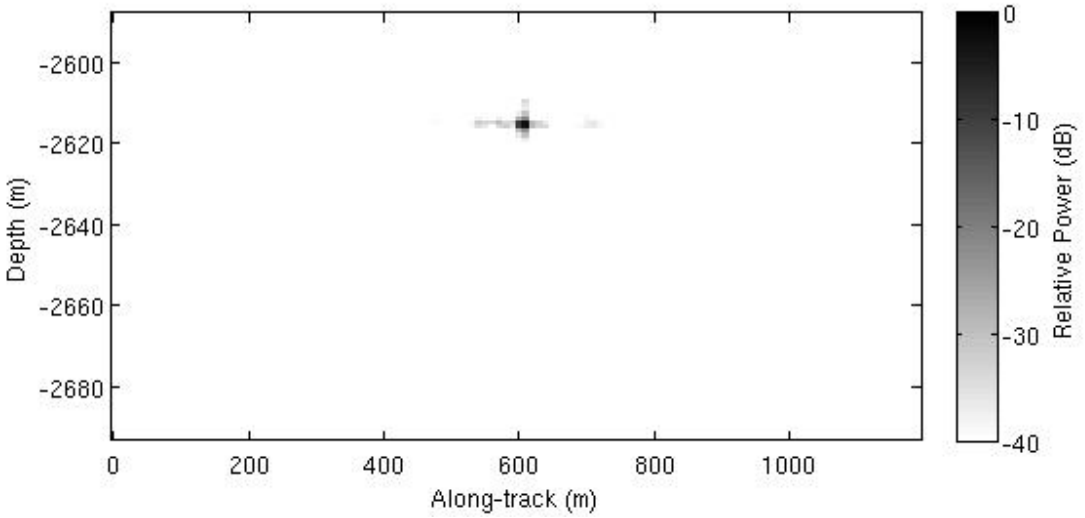

Fig. 6-3. SAR processed image of simulated point target.

6.3 RESULTS

The SAR processing routine independently processes each point target because it operates in the space-time domain. Because of this, the positions of each target are arbitrary and can be made to conform to a surface or aligned vertically to produce a depth sounder type of image. These two target distributions are shown in Fig. 6-4 and Fig. 6-5.

The conformal target distribution is based on the digital elevation map produced by interpolation of the f-k migrated bed elevation data product.

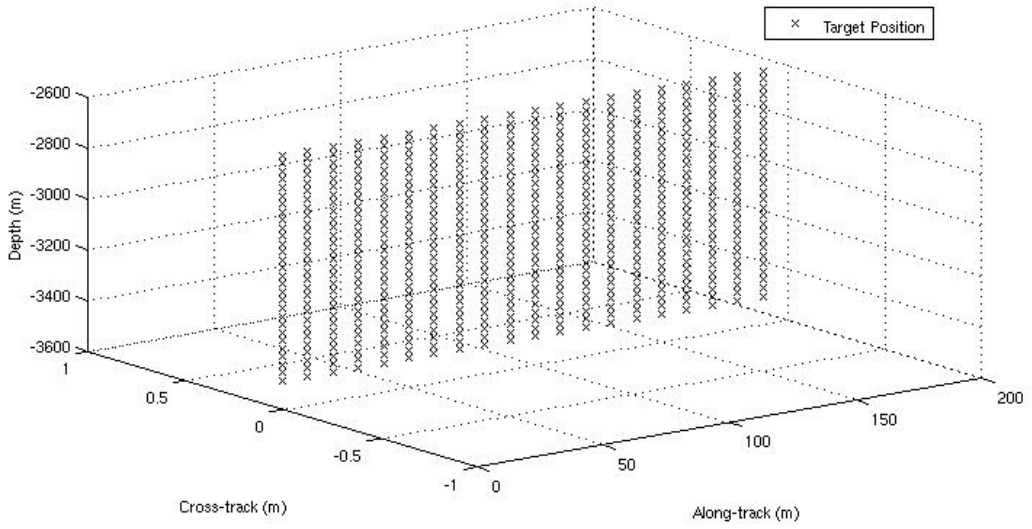

Fig. 6-4. Vertical target profile. The targets have been thinned along the z-axis (depth) and truncated in the along-track to better illustrate the structure of the target distribution.

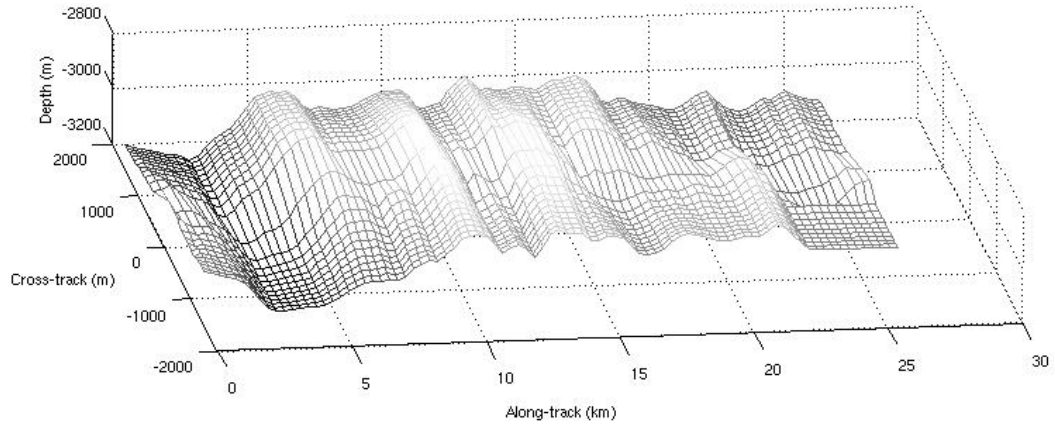

Fig. 6-5. Target profile contoured to the digital elevation map. Each cross in the mesh is a point target. The targets have been thinned along the cross and along-track to better illustrate the structure of the target distribution.

The vertical target profile was used to compare results with the f-k migration routine. These comparisons are shown in Fig. 6-6 and Fig. 6-7. Upon close examination, the f-k migration routine appears to produce slightly higher quality images due to the finer

resolution. However, the two images are almost identical with both images showing the same speckle structure. As a side note, if both images are processed with 5 m resolution the f-k migration routine is approximately 14 times faster than the SAR processing algorithm. This speed-up is dependent on the sizes of the matrices and the gap widens for finer along-track resolution. The two images are slightly different because the target profile passed to the SAR processor is a vertical column with no cross-track deviations. The f-k migration routine does not consider cross-track movement so it effectively looks directly beneath the vehicle and the image follows the cross-track deviations of the vehicle and is not a straight vertical wall of targets. However, absolute cross-track deviations are usually less than 40 m from the ideal straight path which corresponds to an elevation angle difference of less than 1 deg.

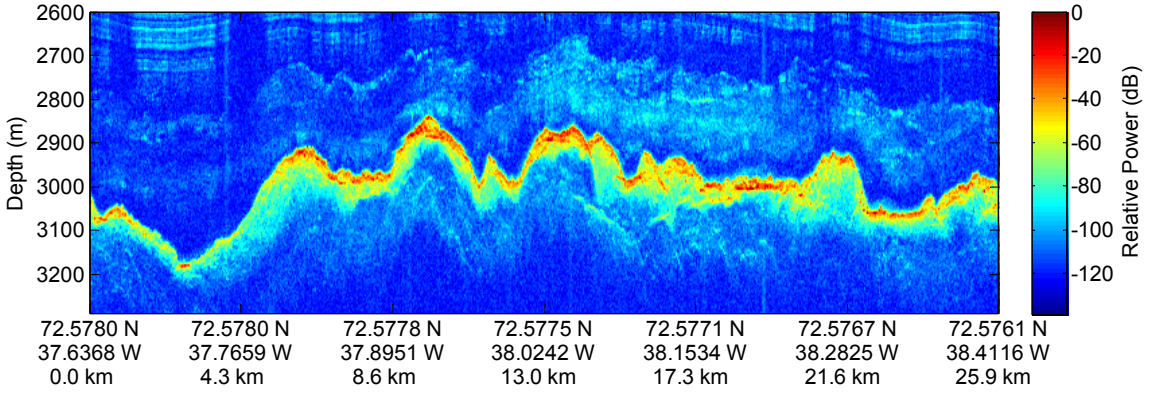

Fig. 6-6. Depth sounder image processed using time domain correlation SAR processing.

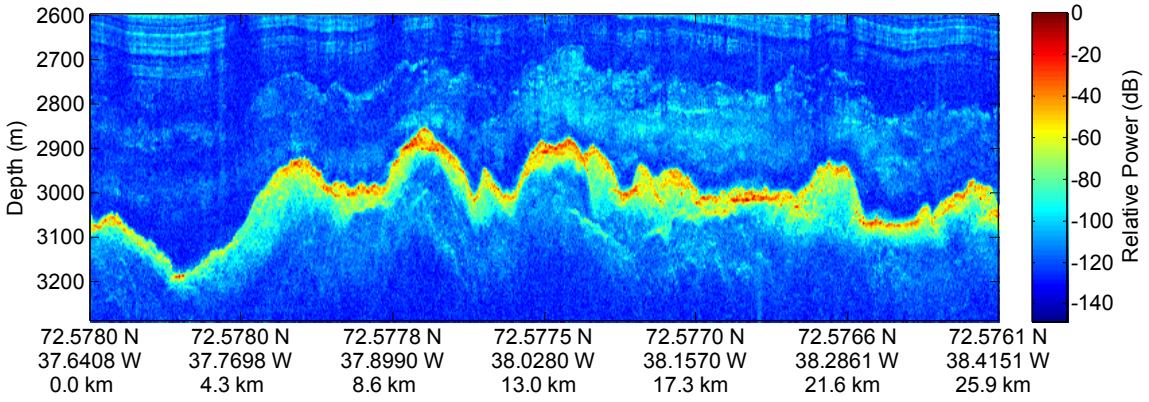

Fig. 6-7. Depth sounder image processed using f-k migration.

The conformal target distribution is used for creating the images of the subglacial bed. The along-track positions are spaced by 10 m, which is the along-track resolution for a 300 m aperture and 3000 m range. The cross-track positions are spaced so that the distance between two targets projected onto a flat surface is equal to the range resolution of the radar. Since there is substantial bed relief coupled with steep elevation angles (10 to 20 degrees incidence angle) a simple flat earth model could not be used. An example of the geometric error induced by using a flat earth approximation is shown in Fig. 6-8. For this simple example, a height error of z_{err} causes a cross-track position error of

$$y_{err} = \frac{z_{err}}{\tan\theta},$$

where θ is the incidence angle. Since the incidence angle is related to the target's position relative to the radar by $\theta = \tan^{-1}\left(\frac{\Delta y}{\Delta z}\right)$ where Δy and Δz are the relative offsets in each dimension, we have $y_{err} \to \infty$ as $\Delta y \to 0$. That is, targets close to nadir will have the largest cross-track position errors. In the opposite extreme, for grazing angles $\Delta y \to \infty$, then $\theta \to \frac{\pi}{2}$ and $y_{err} \to 0$. Height errors at grazing angles do not create cross-track position errors. Since we are operating with steep elevation angles, the cross-track position errors will be large.

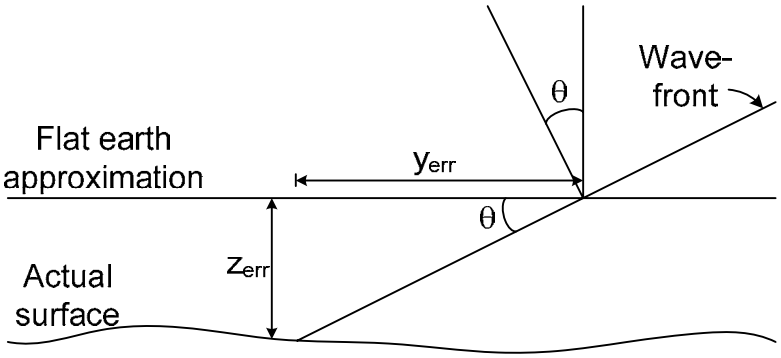

Fig. 6-8. Illustration of geometric errors induced by height errors in the scene.

Two common problems in SAR images are shadowing and layover and both are related to the surface slope, σ, and the incidence angle, θ. Examples of both are shown in Fig. 6-9. Shadowing occurs when the surface slope does not have line of sight with the

radar system. This requires the angle of the surface slope to satisfy $\sigma > \frac{\pi}{2} - \theta$. Therefore, shadowing is more likely to happen for large grazing angles. For this work, where the maximum incidence angle is 20 deg, a surface slope angle greater than $90 - 20 = 70$ deg is very unlikely and no shadowing is likely to occur. Layover, on the other hand, can be a serious problem for small incidence angles. Layover occurs when a target has a larger cross-track offset, but is closer in range to the radar than another target. The end of effect being that the ordering of the targets is interchanged in the image. This requires the angle of the surface slope to satisfy $\sigma > \theta$. Layover is certainly present in the SAR images, since the f-k migrated images show many places where the bed slope exceeds 10 deg which is the minimum incidence angle in the SAR images.

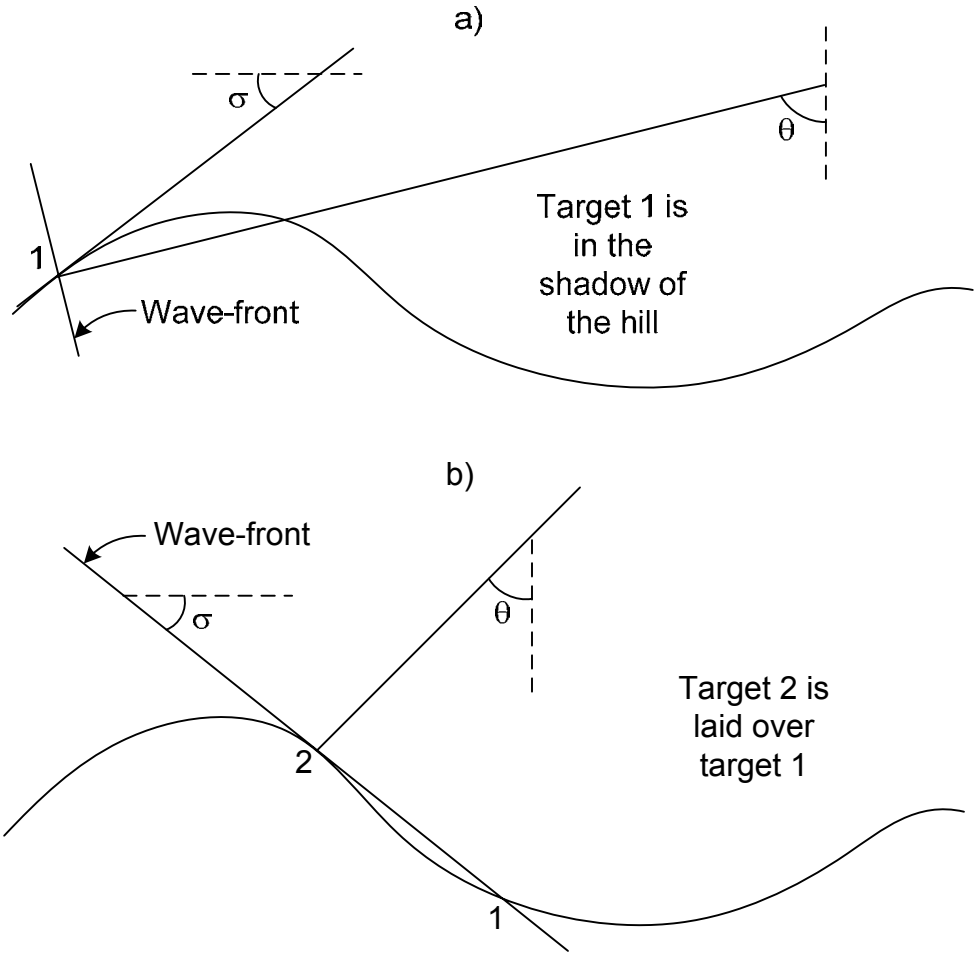

Fig. 6-9. Examples of a) shadowing and b) layover in cross-track SAR imagery.

The SAR imagery presented in Fig. 6-13 on page 151 through Fig. 6-28 on page 158 is processed with the conformally mapped target distribution. Occasionally the actual bed topography deviates far enough from the digital elevation map that the algorithm was focusing to points within the ice rather than on the ice/bed interface. These errors are identified by the dark blue patches on the side of the swath closest to the radar or 0 m cross-track. An example of a surface profile that could lead to this is shown in Fig. 6-10. The dark blue patches are caused by the SAR algorithm attempting to focus to points so far above the actual bed that the range shells contain no bed scatterers. These height errors are really a special case of layover where the swath targets are laid over the nadir target. Therefore, a target at cross-track position Δy which has a height error $z_{err} > \Delta y \tan\theta$ will not see any scatterers. Put another way, the average slope between the target and nadir exceeds the incidence angle. As can be seen in the SAR results there are a number of locations which are corrupted by this error.

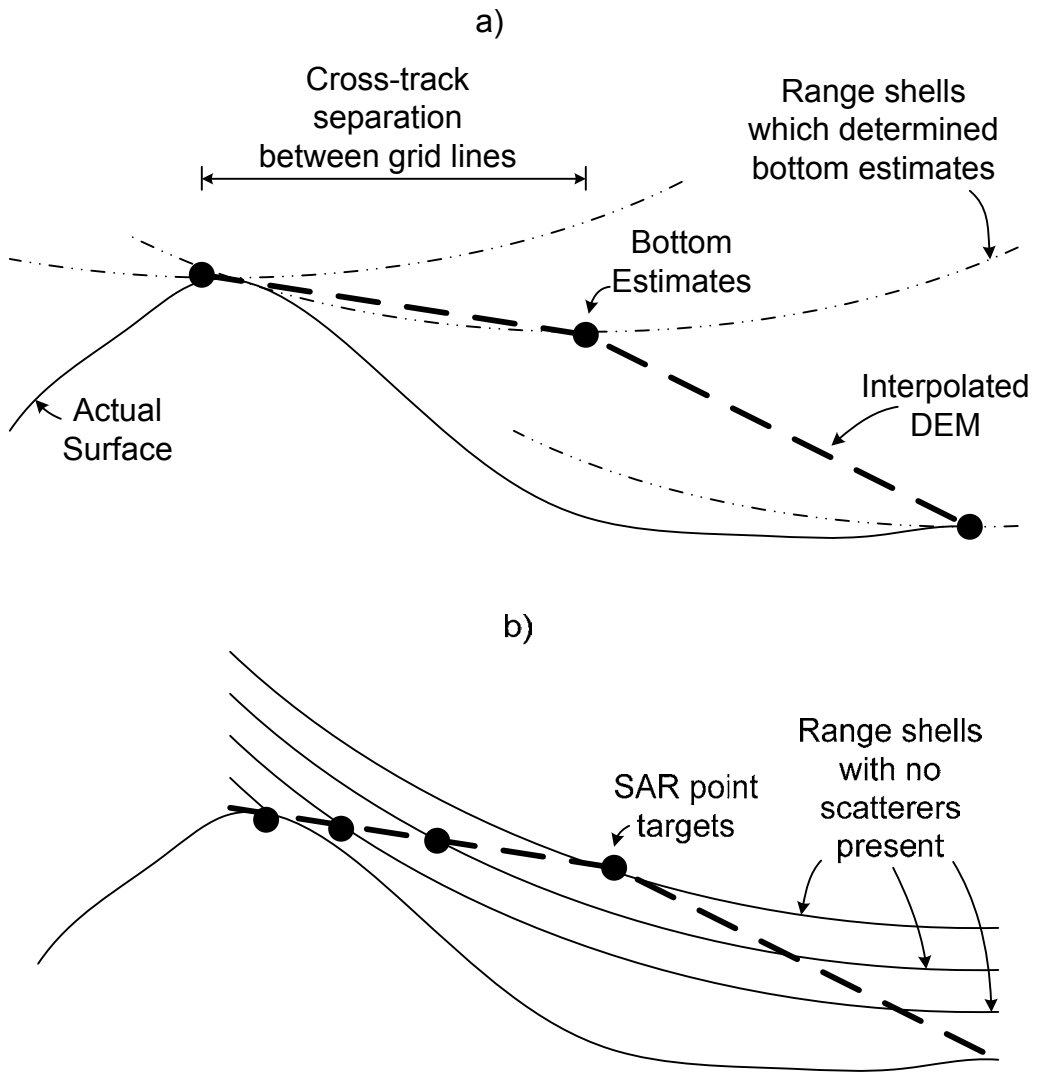

Fig. 6-10. Example of bed topography that could lead to severe DEM errors. The thickness estimate and interpolated surface from three depth sounding passes are shown in a) and the effect on the SAR processor is shown in b).

To illustrate a potential solution to this problem, a swath of SAR data are shown in Fig. *6-11* beside an interferogram from f-k migration. The interferogram is from the migrated data that was used to generate the digital elevation map the SAR image used at 500-m cross-track. Note how the patches of errors in the SAR line up with the largest non-zero surface phases in the interferograms. The dark magenta color riding on the top of the surface implies that the first echo in range is not from nadir, but from one side or

the other of the radar system. A method for improving the DEM is discussed in the summary and recommendations chapter that involves using spectral estimation and the interferograms rather than simply using the magnitude plot of the migrated data.

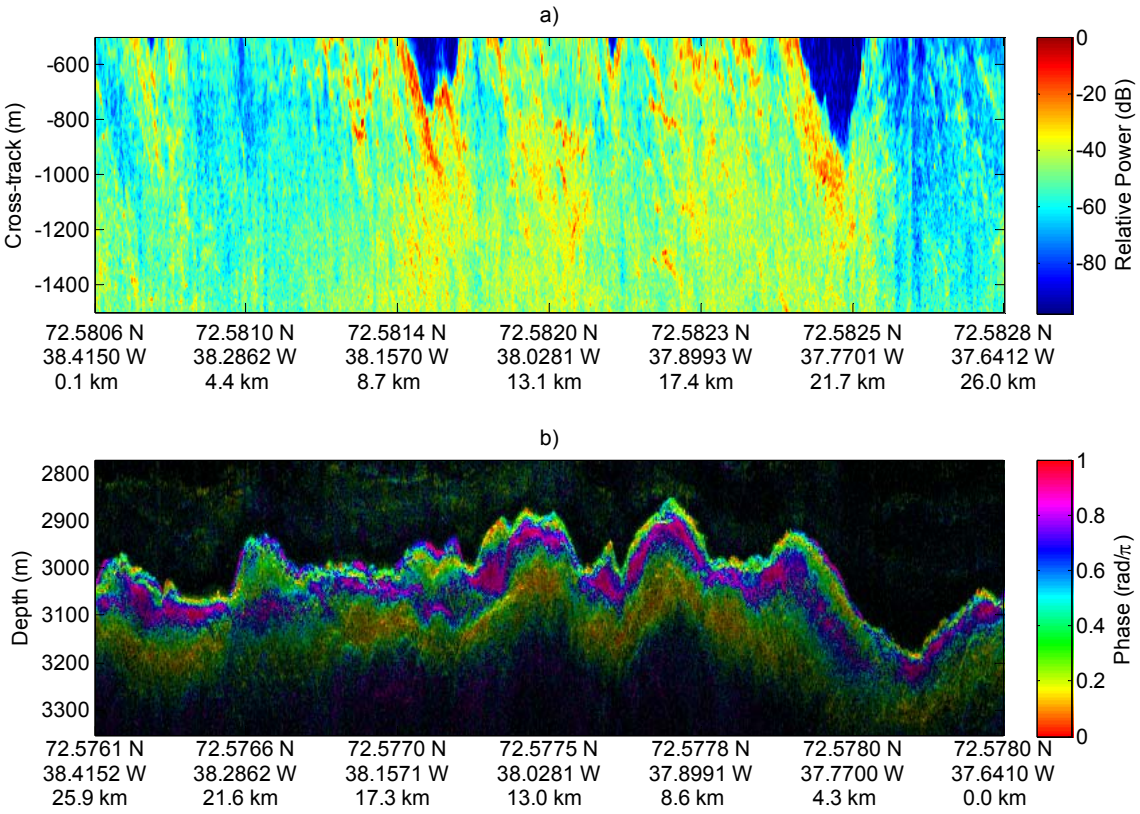

Fig. 6-11. a) SAR image showing areas of no bed scatter as indicated by the two dark blue patches at the top of the image (note longitudes 37.7 W and 38.1 W) and b) the corresponding interferogram.

The radar system operates with a bandwidth of 180 MHz which has been divided into two subbands, 120-200 MHz and 210-290 MHz. Each band is processed separately and the results are displayed in alternating figures on pages 151 through 158. The images formed from the two different bands show the same dominant features, but there are some regional differences in backscatter power. From the discussion in section 2.4, regions where no difference is seen are following the geometric optics model and/or the small-scale roughness is scaling inversely with frequency. Regions showing increased scattering for smaller incidence angles suggest that one of the small-scale roughness models is the dominant mechanism.

To reduce the effects of fading, 15 looks are taken. To do this, the data are passed through a two-dimensional boxcar filter with 5 cross-track looks and 3 along-track looks. The raw imaging resolution is 2-6 m in the cross-track by 10 m in the along-track. The variation in the cross-track resolution is because of the relationship between the slant range resolution, which is constant at 1 m and directly related to the inverse of the bandwidth, and the ground range resolution, which is related to the slant range resolution divided by the sine of the incidence angle. After filtering, the resolution is 10-30 m in the cross-track by 30 m in the along-track.

For visualization the SAR images are normalized so that the mean power for each cross-track position is made equal. The normalization function for each band is shown in Fig. 6-12. The SAR processing algorithm actually focuses a continuous swath from -1500 to +1500, but due to left-right ambiguity issues the valid region excludes the center of the swath from -500 to +500 m. The normalization function is the mean of the power for each cross-track cell across all SAR images. As expected the signal power is strongest at nadir or for small incidence angles and is weaker for greater incidence angles. There is a slight left-right asymmetry which is probably due to the asymmetry in the feed structure of the TEM horn antennas which are fed from the right-hand side (towards negative cross-track position). The dip at nadir is due to height errors that place the nadir point target above the surface. The SNR is fairly low beyond 1000 m from the center of the swath as expected. The mosaic presented in section 6.4 uses the left and right portions of the swath that are 500 m to 1000 m from the center.

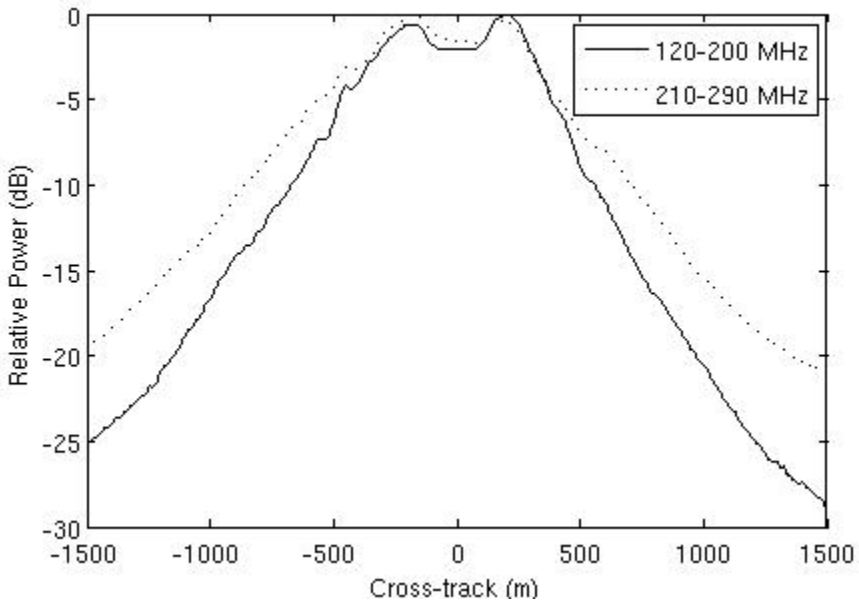

Fig. 6-12. Normalization function for 120-200 MHz and 210-290 MHz SAR images.

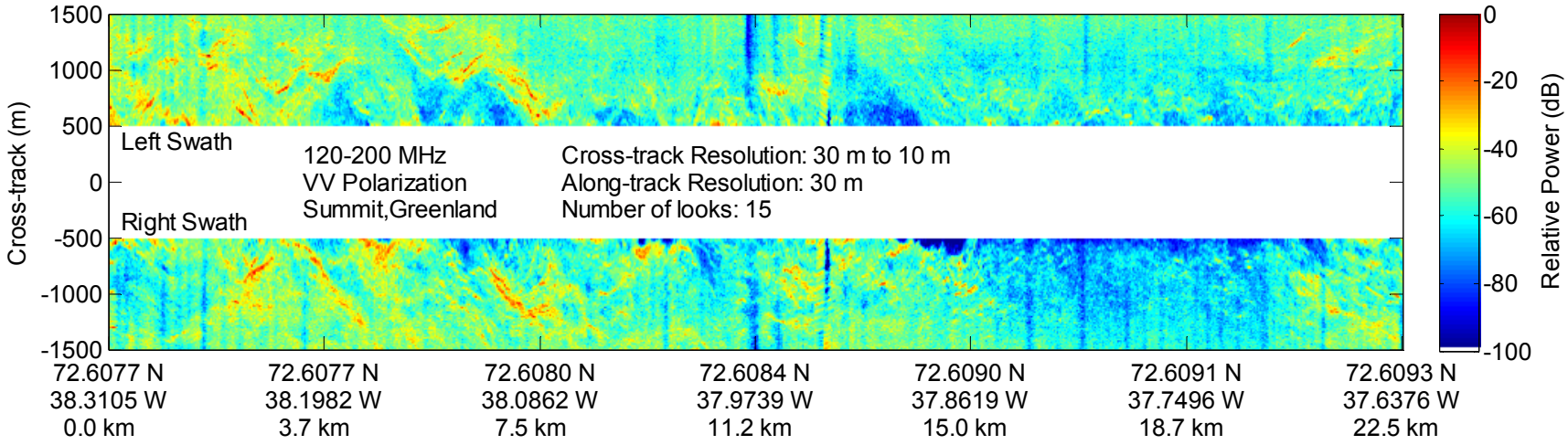

Fig. 6-13. SAR image (120-200 MHz) from data sequence 5 from July 20, 2005.

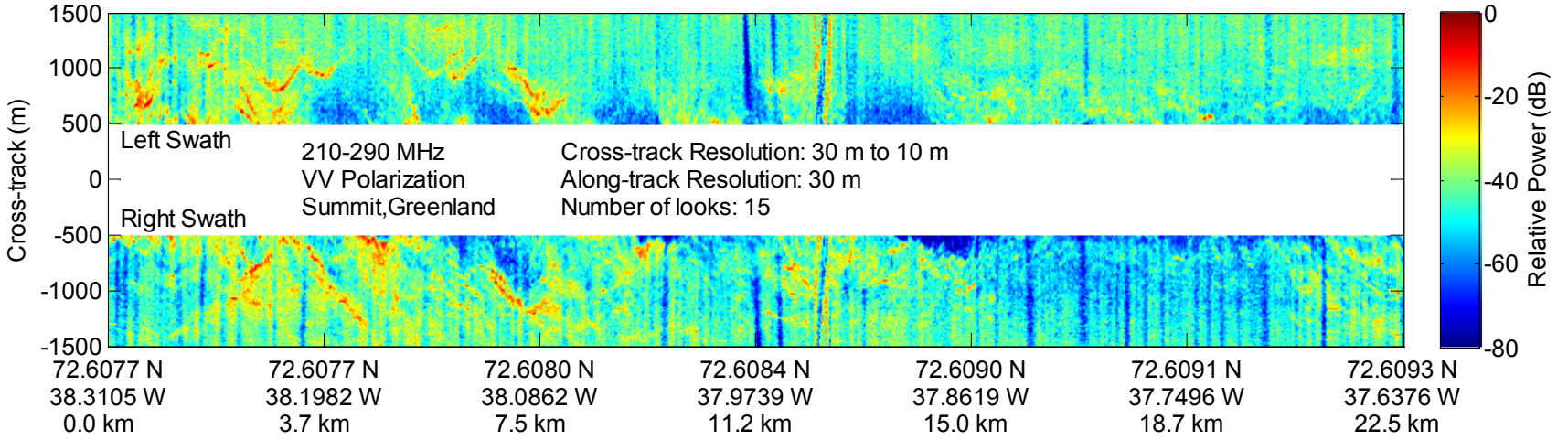

Fig. 6-14. SAR image (210-290 MHz) from data sequence 5 from July 20, 2005.

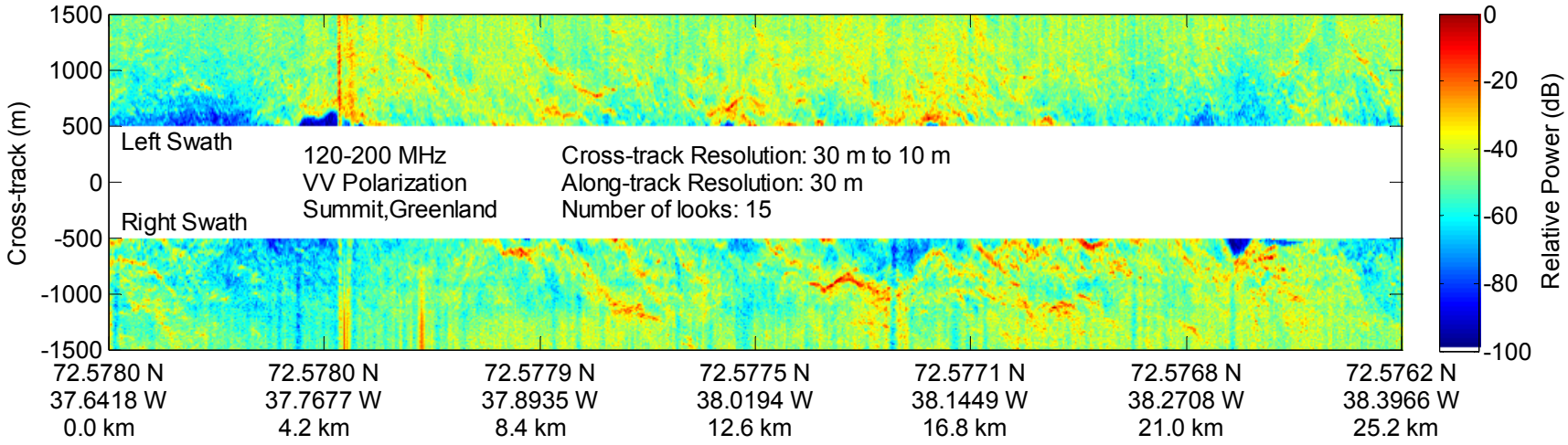

Fig. 6-15. SAR image (120-200 MHz) from data sequence 9 from July 20, 2005.

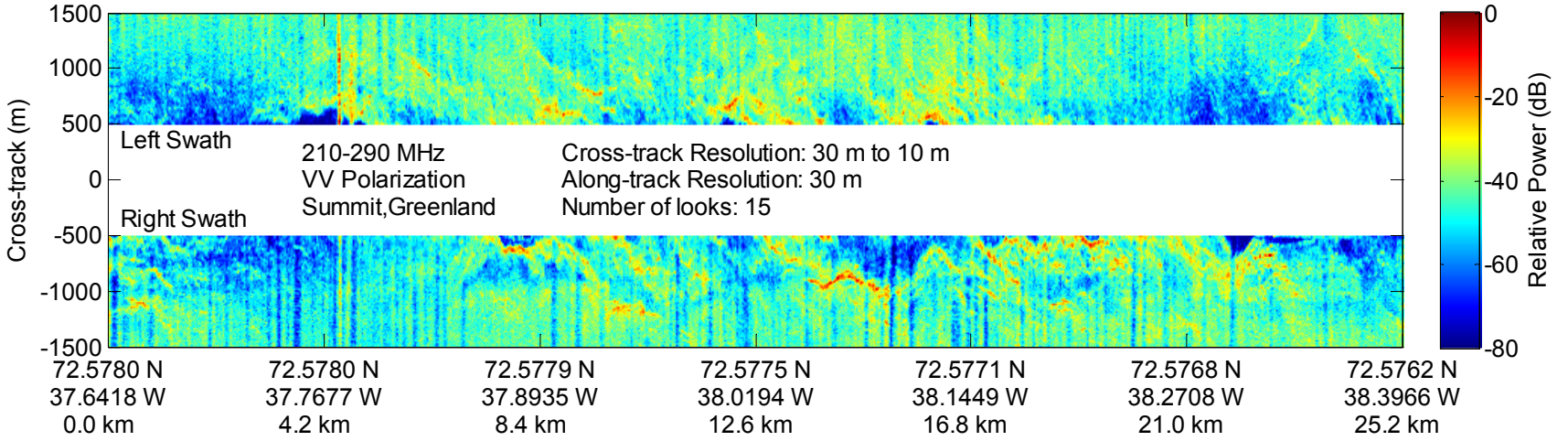

Fig. 6-16. SAR image (210-290 MHz) from data sequence 9 from July 20, 2005.

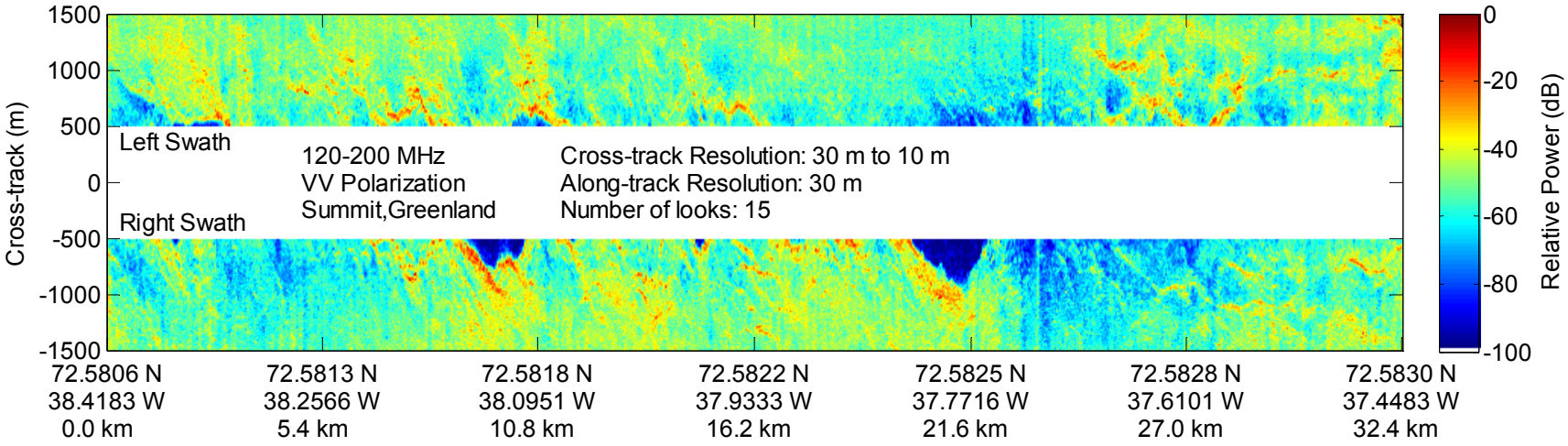

Fig. 6-17. SAR image (120-200 MHz) from data sequence 2 from July 21, 2005.

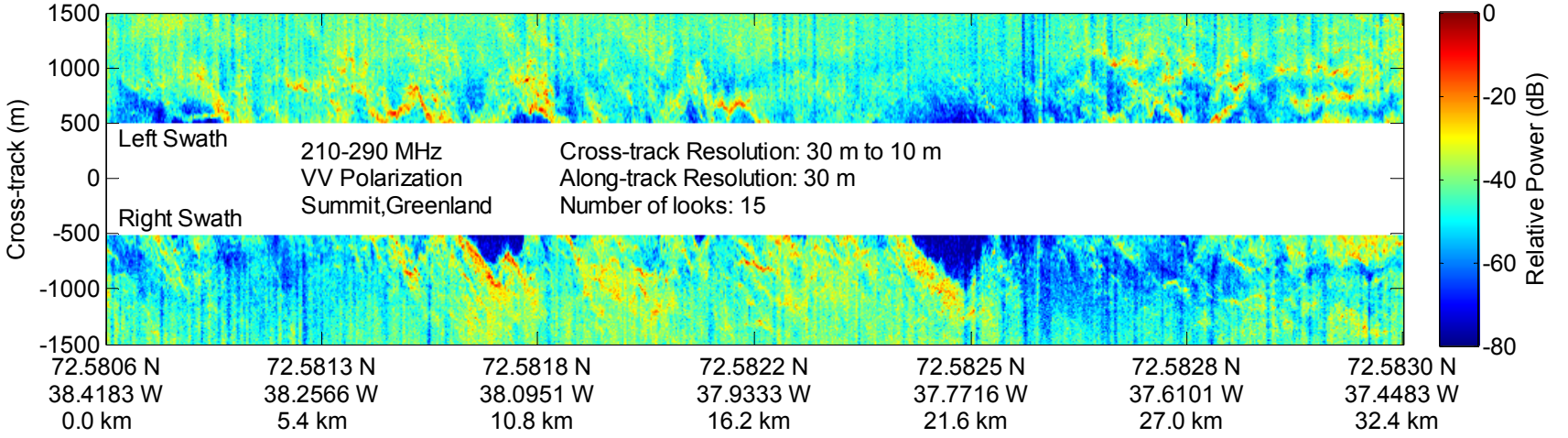

Fig. 6-18. SAR image (210-290 MHz) from data sequence 2 from July 21, 2005.

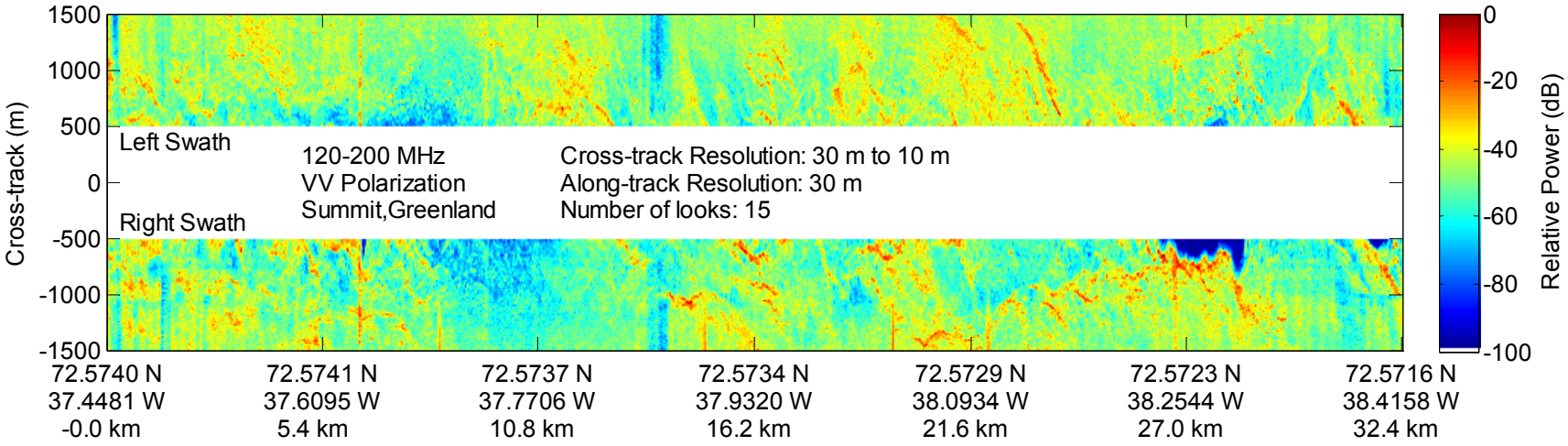

Fig. 6-19. SAR image (120-200 MHz) from data sequence 6 from July 21, 2005.

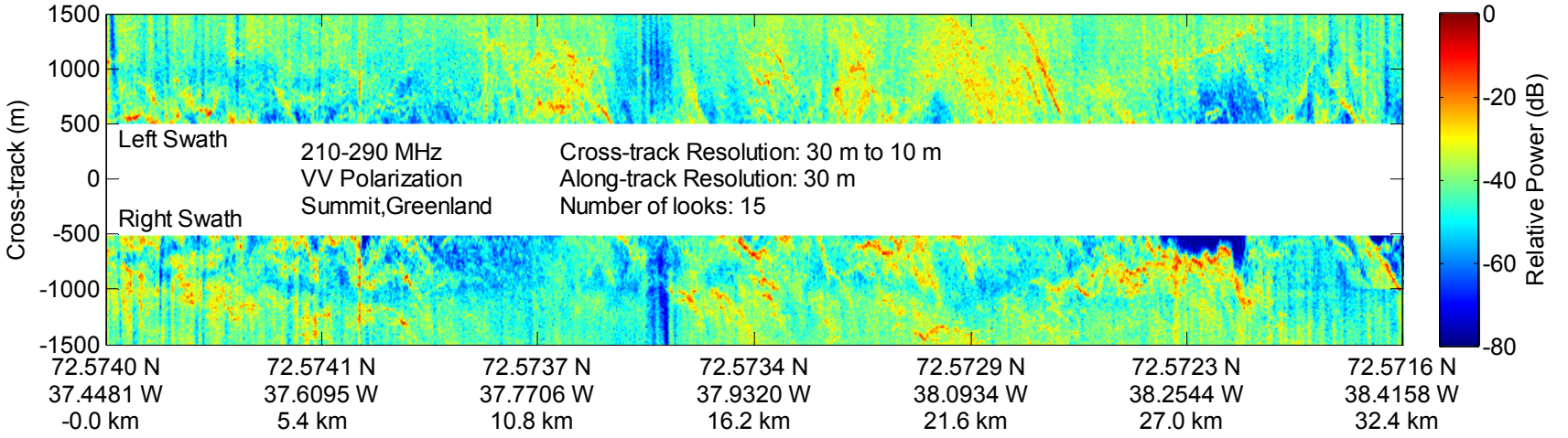

Fig. 6-20. SAR image (210-290 MHz) from data sequence 6 from July 21, 2005.

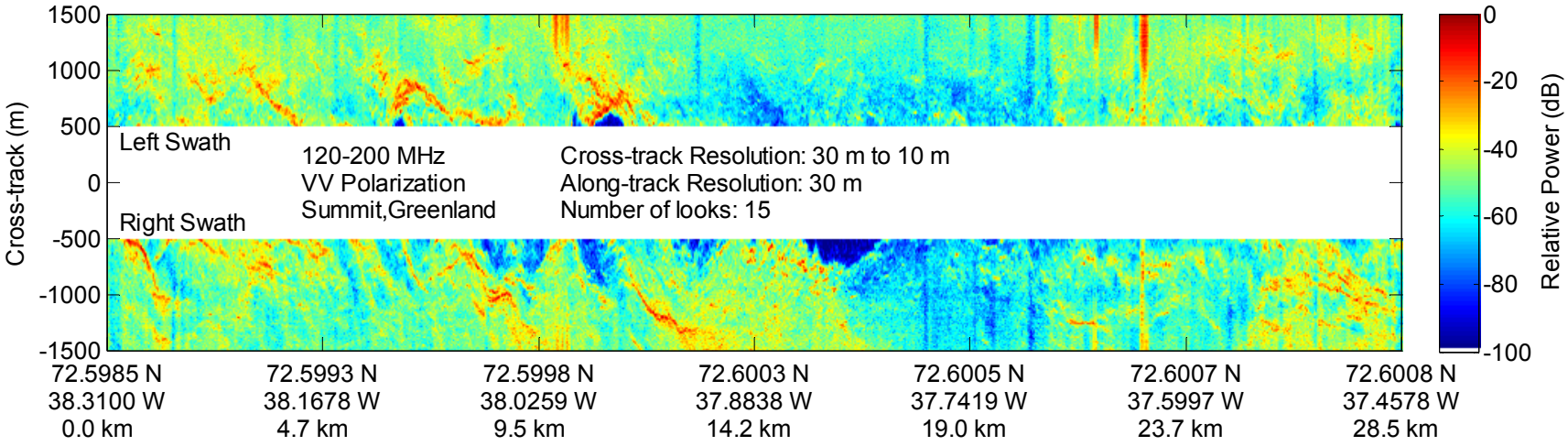

Fig. 6-21. SAR image (120-200 MHz) from data sequence 3 from July 22, 2005.

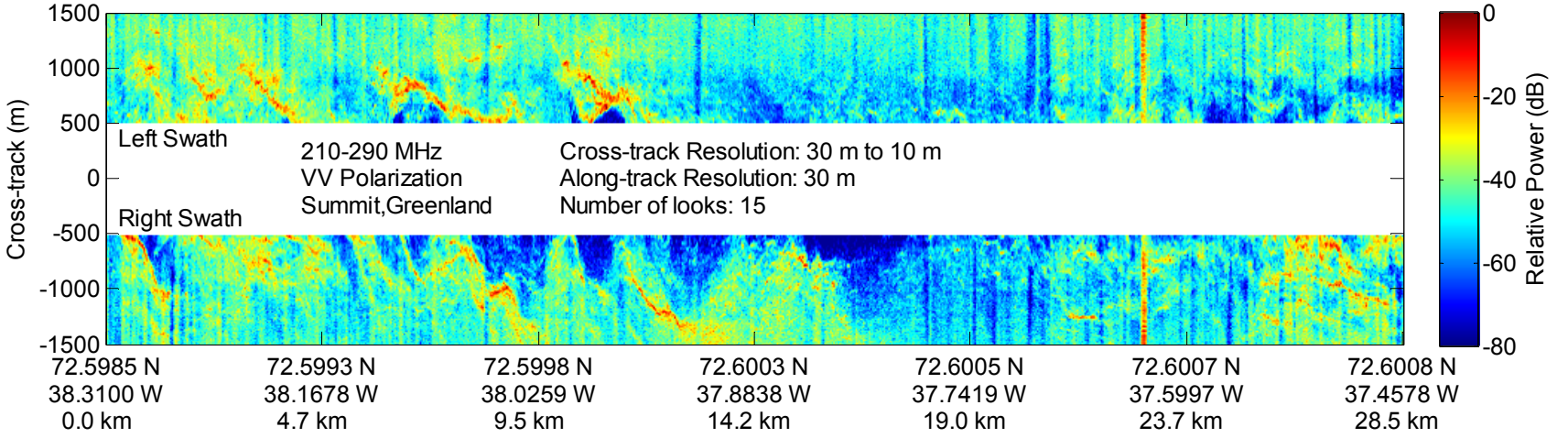

Fig. 6-22. SAR image (210-290 MHz) from data sequence 3 from July 22, 2005.

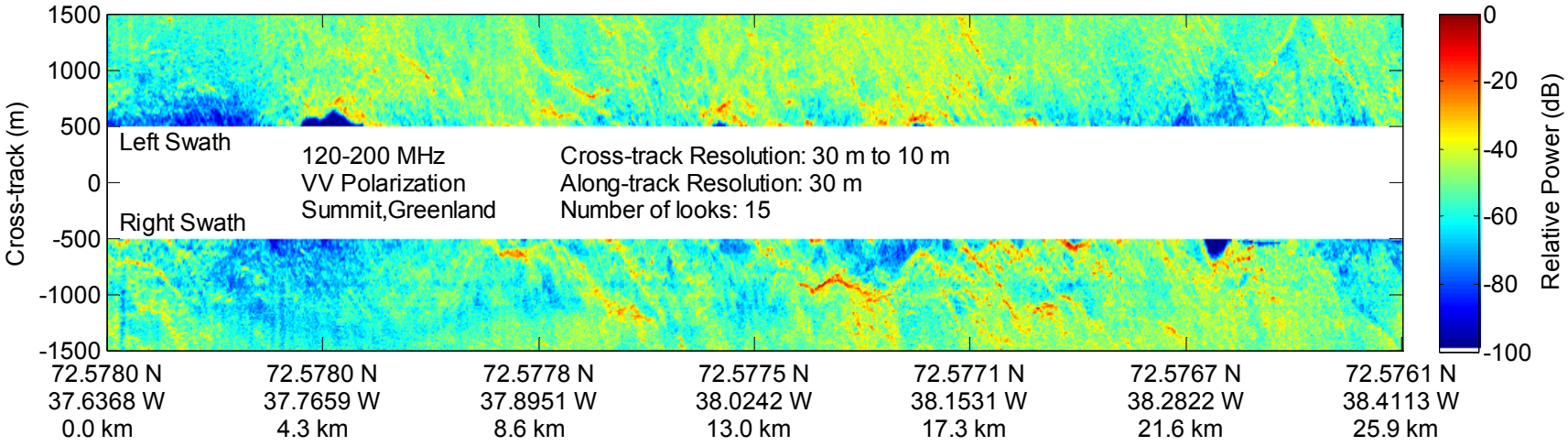

Fig. 6-23. SAR image (120-200 MHz) from data sequence 6 from July 22, 2005.

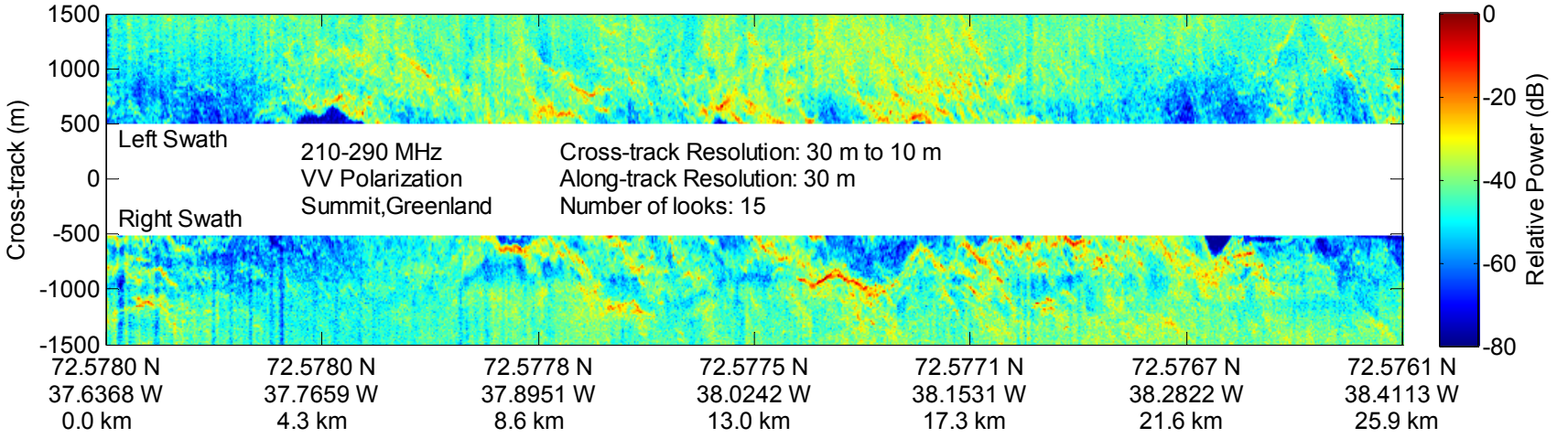

Fig. 6-24. SAR image (210-290 MHz) from data sequence 6 from July 22, 2005.

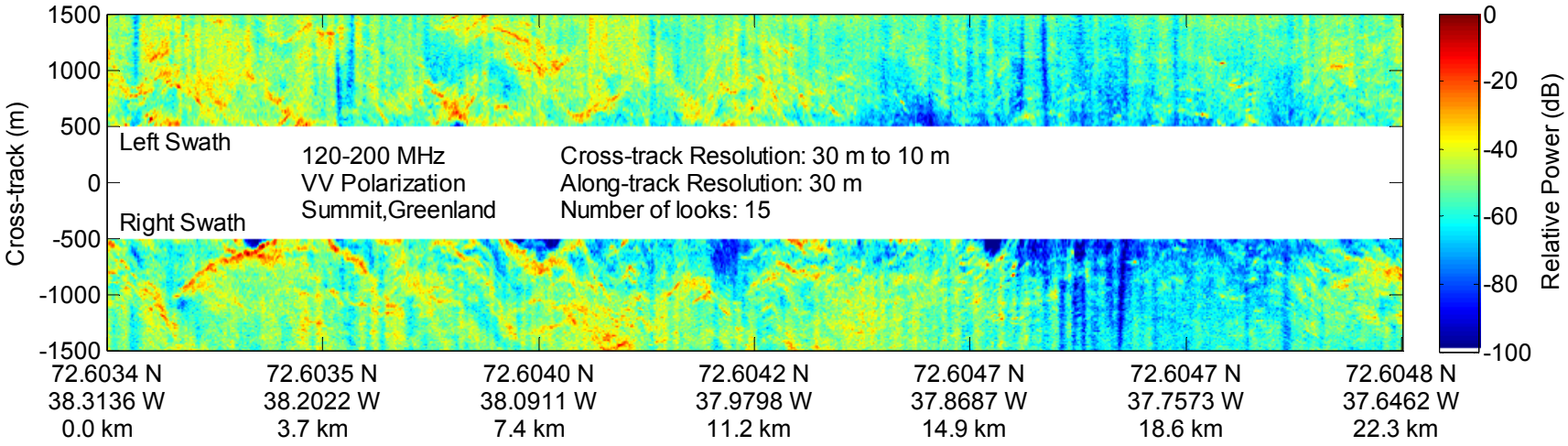

Fig. 6-25. SAR image (120-200 MHz) from data sequence 18 from July 23, 2005.

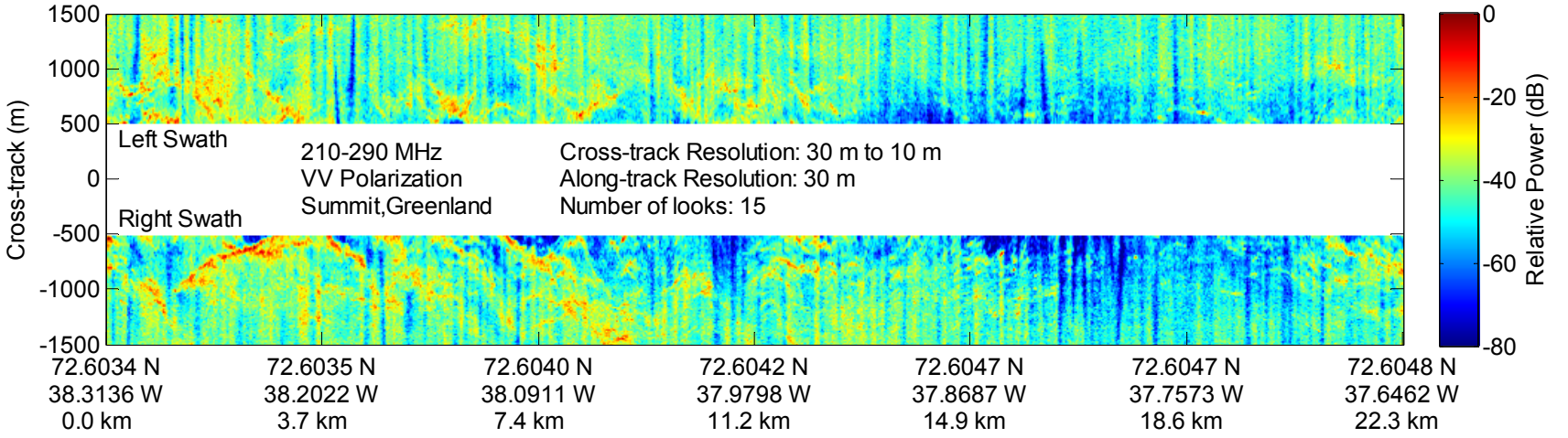

Fig. 6-26. SAR image (210-290 MHz) from data sequence 18 from July 23, 2005.

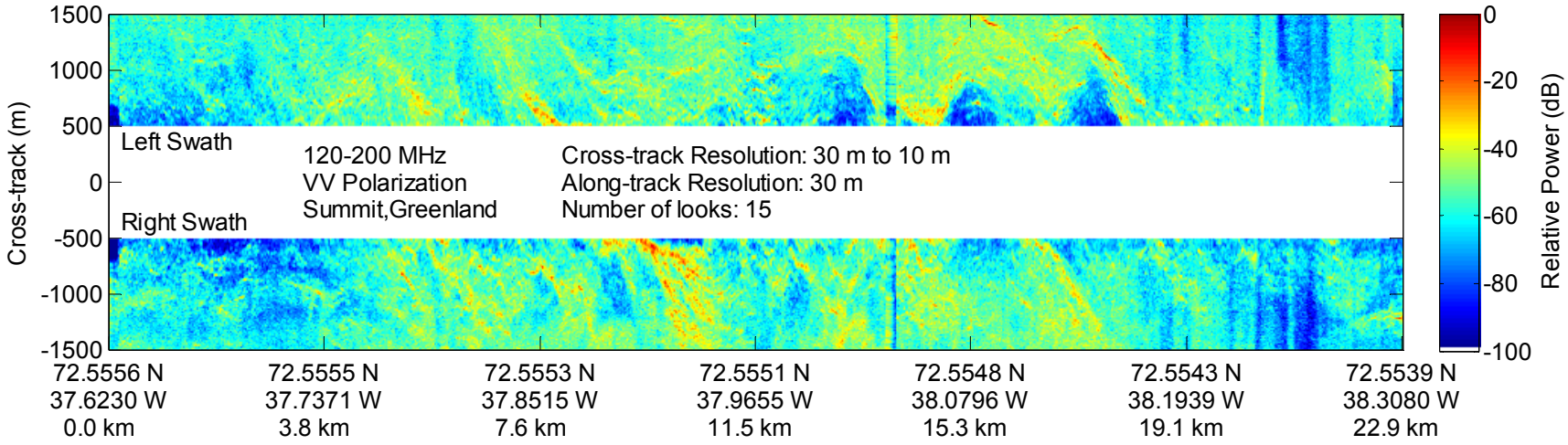

Fig. 6-27. SAR image (120-200 MHz) from data sequence 22 from July 23, 2005.

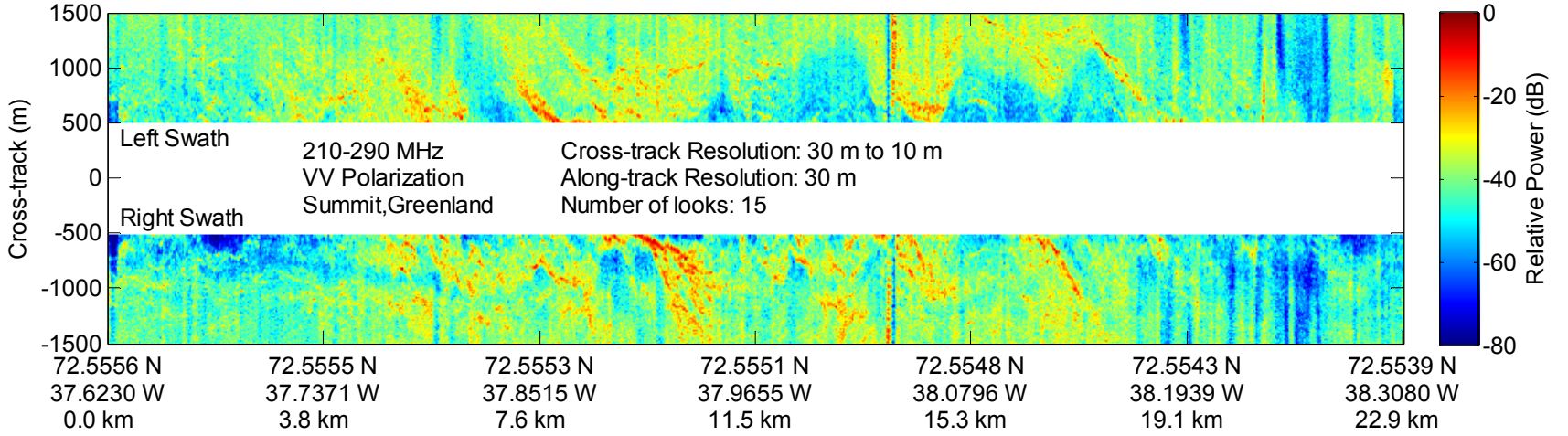

Fig. 6-28. SAR image (210-290 MHz) from data sequence 22 from July 23, 2005.

6.4 SAR MOSAIC METHOD

All the data sequences that formed the measurement grid are shown in Fig. 6-29. Each data sequence is processed independently and the lines not exactly parallel or registered with one another. To mosaic the images, a master grid is created which all the images are interpolated onto. Since each image is formed on a mesh grid in the sense that each pixel is rectilinear, simple two-dimensional interpolation is possible. The grid lines were spaced so that only the ideal portion of the image, 500 m to 1000 m cross-track, would need to be used. However, since the traverse lines are not exactly parallel the overlap is not perfect and gaps appear between the swaths. To bridge the gaps and to provide a smooth transition between SAR images, the swath used is extended to 400 m to 1200 m. In overlapping regions, the images are combined so that there is a linear transition from one image to the next. The resultant SAR mosaic is shown in Fig. 6-32 on page 162 for the 120-200 MHz band and Fig. 6-33 on page 163 for the 210-290 MHz band.

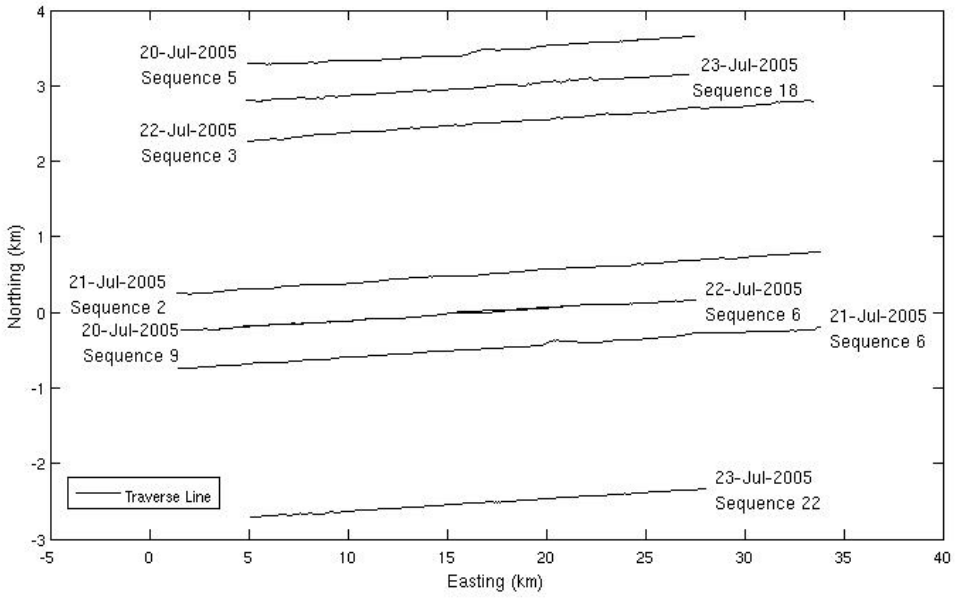

Fig. 6-29. Long traverse lines where SAR has been applied. All these traverses are used to generate the SAR mosaic. For the repeat passes from sequence 9, July 20, 2005 and sequence 6, July 22, 2005, only sequence 6 is used since the data quality appeared to be slightly better.

A number of discontinuities arise when creating a SAR mosaic. The two primary issues for this work, that have not been addressed, are height errors in the DEM (only layover was discussed above) and changes in look angle. The incidence angle is approximately 10 deg at the inside edge of swath and 20 deg at the outside edge of swath. As described in section 6.3, the cross-track error and height error are related by the tangent of the incidence angle. Therefore, if any height error exists, the pixels of adjacent swaths will not be the same as shown in Fig. 6-30 a). The geometric distortion is greatest when the incidence angles are of opposite sign because the errors are also of opposite sign as shown in Fig. 6-30 b).

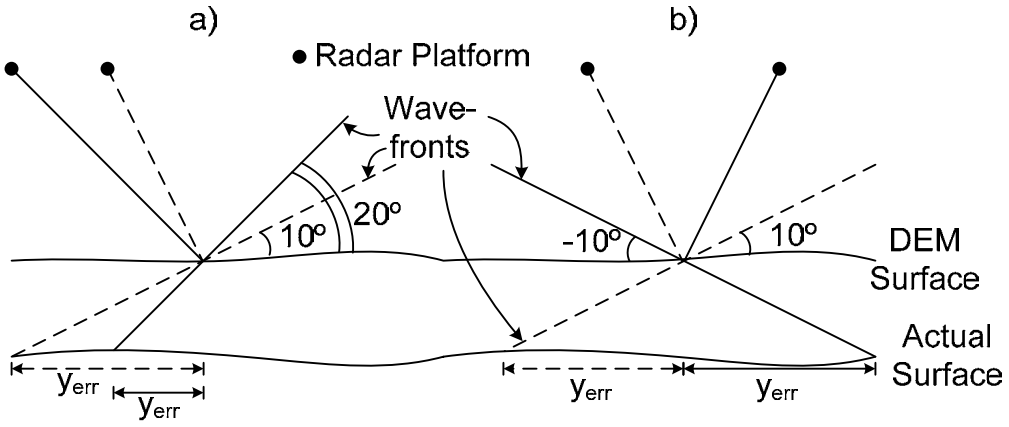

Fig. 6-30. Example of geometric distortion on mosaic process when a) the incidence angles from adjacent swaths have the same sign and b) when the incidence angles are of opposite sign..

The other discontinuity is caused by the change in the pixel scattering as a function of look angle. Even when there are no height errors, a pixel's backscattering is a function of look angle. Since the look angle on each edge of the swath is different, some discontinuity is expected. Two steps in the processing reduce this discontinuity: the normalization of the data in the cross-track dimension and the two-dimensional filtering of linear power data to reduce the fading.

Note that both image discontinuities are functions of incidence angle and grow worse for larger discontinuities in the incidence angle. Because of the way the images are fit together in the mosaic, there are groups of images that show the least amount of discontinuity. The meshing together of the images is shown relative to the traverse lines in Fig. 6-31. Each group of three designated in the figure has the smallest possible change

in the incidence angle at image boundaries. As expected, these groups of three in the SAR mosaics in Fig. 6-32 and Fig. 6-33 mesh better with each other.

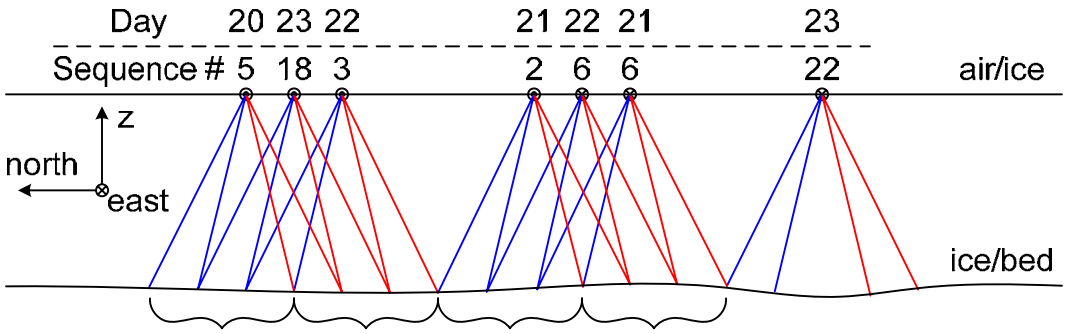

Fig. 6-31. Cross-section of the SAR mosaic showing the groups of three images that should have the least discontinuities because of the smallest change in incidence angle.

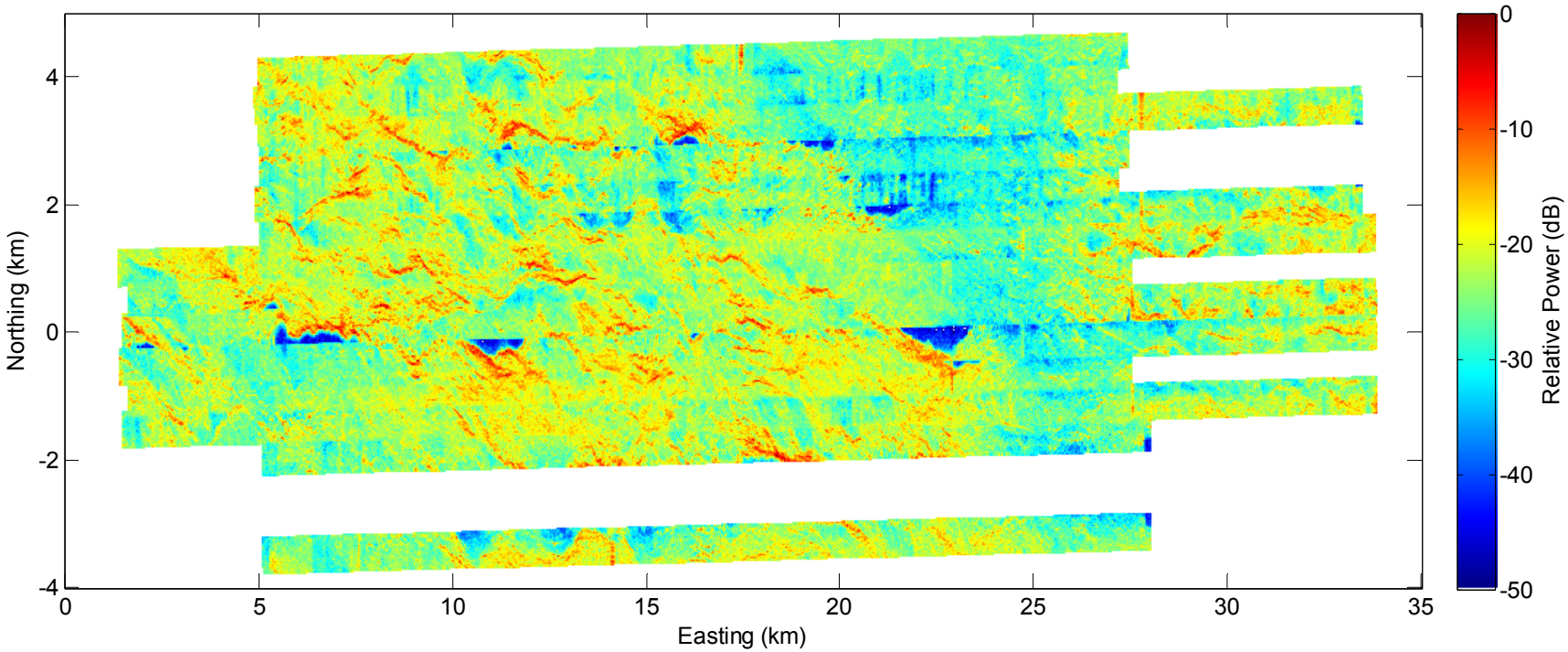

Fig. 6-32. SAR mosaic of 120-200 MHz images from the eight long data sequences. The origin is at Summit Camp, Greenland (72.5783°N and 38.4596°W). The polarization is VV and the resolution is 10-30 m cross-track and 30 m along-track with 15 looks.

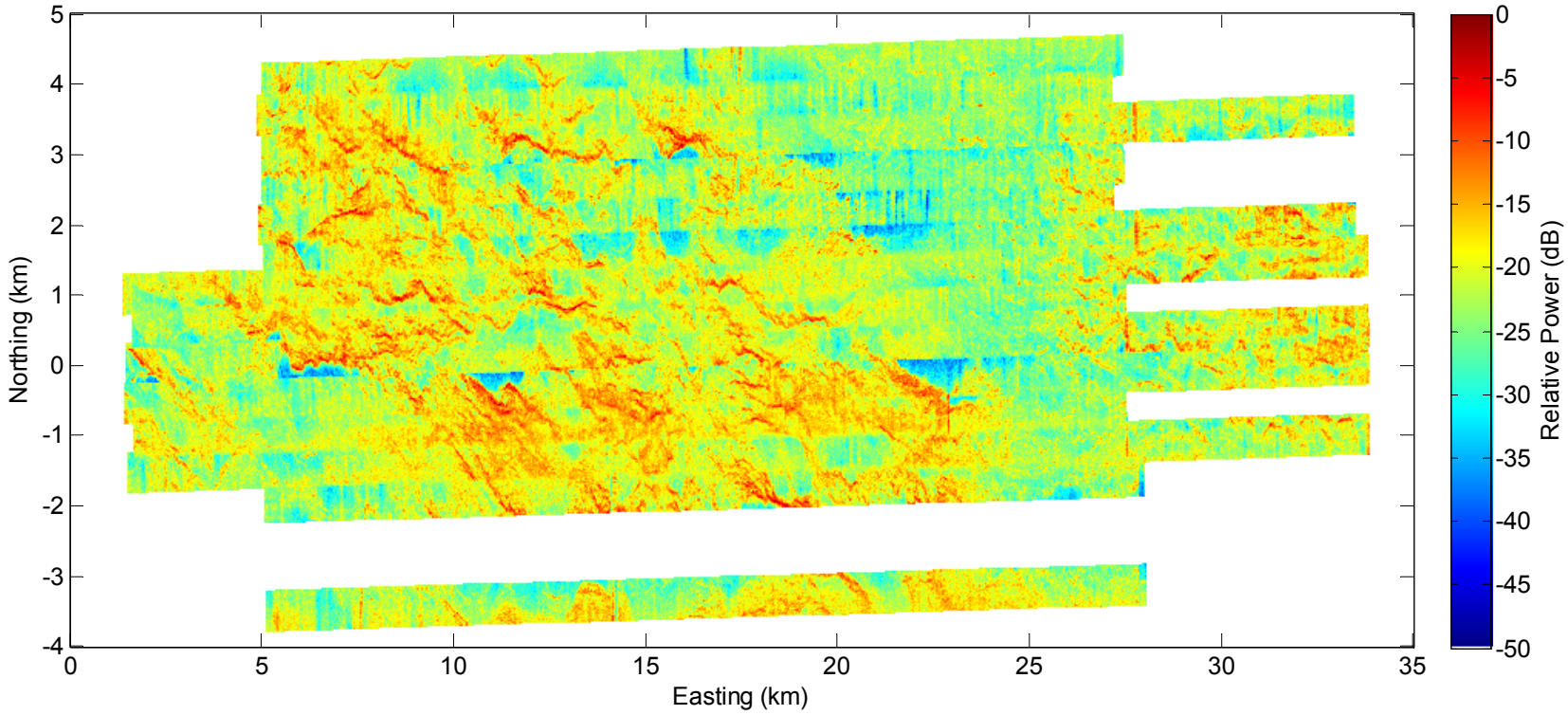

Fig. 6-33. SAR mosaic of 210-290 MHz images from the eight long data sequences. The origin is at Summit Camp, Greenland (72.5783 °N and 38.4596 °W). The polarization is VV and the resolution is 10-30 m cross-track and 30 m along-track with 15 looks.

Chapter 7: SUMMARY AND RECOMMENDATIONS

7.1 SUMMARY

This work covers the specification, design, development, fielding, and data processing of a multi-purpose VHF radar for radioglaciological work. The purposes of the radar are to image the subglacial bed, measure ice thickness, and map deep internal layers. The ability to form side-looking synthetic aperture radar (SAR) images of the subglacial bed in thick ice is demonstrated for the first time in this work. The utility of SAR for terrestrial and oceanic applications is unquestioned. The expansion of SAR into subglacial imaging brings an extensive set of tools developed for traditional SAR applications to bear on the glaciological problem of modeling the dynamics of the ice sheet. Roughness, surface dielectric, and topographic mapping are the primary SAR applications that address the science objectives outlined in this work. In addition to imaging, the radar system simultaneously provides a high-resolution ice thickness estimate and tracks internal layers at depth using a novel multi-waveform approach. Also, bistatic measurements are possible with the instrument and this configuration has been tested successfully in the field – although sensitivity-limiting temperature-stability issues need to be overcome.

In Chapter 2, the propagation model is developed which is used throughout the work. The propagation model relies on the assumption that the ice sheet may be modeled locally as a planarly layered media. Since direct measurements of ice properties are unavailable in the VHF range, we rely on geophysical profiles from nearby ice cores to model the permittivity of the ice sheet. Using this permittivity profile and previous radar datasets the required loop sensitivity and dynamic range required by the system to map deep internal layers and to the image the bed are derived. The f-k migration and SAR processors also make use of the propagation model as described in Chapter 5 and Chapter 6 respectively.

The radar specifications are derived and the system design is covered in Chapter 3. The final radar specifications pushed the envelope in many ways: broad bandwidth, high-sensitivity, large-dynamic range, multi-waveform, multi-channel, and bistatic capability. No previous radar system developed for ice research, has combined all these features into a single system and this radar system also provided the first multi-waveform approach to deep penetration ice radars. The broad bandwidth is needed to achieve fine resolution and map frequency sensitive parameters. The high sensitivity is needed to overcome the dielectric loss of ice. The large dynamic range is needed to capture the close-specular internal layers as well as the weak basal scattering. The multi-waveform approach allows the pulse duration, phase, and radar settings to be changed on a pulse-to-pulse basis allowing a single radar system to meet all these requirements. The multi-channel architecture allowed both left and right images to be formed while simultaneously collecting depth sounder data and solved the wide bandwidth problem caused by antenna array factor frequency dependence. It also opened the door to more powerful signal processing techniques such as spectral estimation and minimum mean-squared error (MMSE) channel combining.

In Chapter 4, the steps in data preconditioning are detailed. The SAR requires accurate positioning knowledge to reconstruct phase histories. The differential global positioning system (DGPS) provides the required trajectory information. The setup and data conditioning are explained including heuristic methods for overcoming poor results from the kinematic DGPS post-processor. Next, the calibration of the radar and matched filter processing are described. The calibration method described provides extremely accurate amplitude and phase accuracy in the measurement. Additional data conditioning steps to prepare the data for the imaging routines are also covered here. The data indexing scheme used to organize the data and provide a seamless dataset to the imaging routines is then described. Finally, a number of methods are tested for re-sampling of the nonuniform spatial data. It was found that spline interpolation of along-track filtered data followed by a fast Fourier transform was very efficient computationally and also provided near-optimal results in terms of the mean squared error criteria.

The f-k migration routine is described in Chapter 5. A number of modifications to the basic migration method are covered, such as spatial filtering, spatial decimation, time-

domain truncation, and nonuniform spatial sampling. The results from the f-k migrated data show a number of important glaciologically-significant features. These include a large trench running north and south beside the GRIP bore hole, a bright target in the bottom of the trench as it passes next to the GRIP site, isolated point targets, and the very high ice loss near the bed of the ice – significantly higher than predicted by models derived from laboratory experiments. While the primary purpose of the f-k migration was to derive the digital elevation map (DEM) for the SAR routine, due to the high sensitivity of the instrument, a potentially new glaciological feature was uncovered. The layers in the bottom few hundred meters of the ice sheet appear to be very deformed and to have lost most of their specular character. The change from specular layers to deformed layers is rather abrupt and occurs at about 2700-2800 m depth. In the 25-50 m next to the bed the deformed layers all but disappear. This may provide a link to why the GRIP and GISP2 cores are highly correlated along their whole lengths until they reach this region of the ice.

In Chapter 6, a time domain correlation SAR processor is used to form the images. The reason for working in the space-time domain is because it allows complete flexibility in both antenna and target positioning which traditional frequency domain techniques do not allow. Due to the short range and small incidence angles in the system geometry, the use of a conformally mapped target distribution is necessary for generating images. It is also important to include the height in the target distribution when creating a mosaic of images because height estimation errors during the meshing processes cause discontinuities. Additionally, because of the cross-track meandering of the platform, motion compensation required for frequency-domain methods would have been very difficult to apply without deteriorating the image quality. The SAR results are presented for two different subbands: 120-200 and 210-290 MHz. Both simulated and measured results show that left-right ambiguity and SNR are not an issue across the scene. The SAR mosaic shows that the images can be fused together successfully into a mosaic, although height errors in the DEM mean that some images with significantly different look angles do not match up as well.

Although the primary missions of this work were successful, several failures occurred and lessons were learned from the experience. Also, recommendations for future work

with the dataset are worth noting. The final portion of this chapter, attempts to cover these final topics.

7.2 RADAR SYSTEM IMPROVEMENTS

A number of hardware related problems and limitations are described in this section. Some of these problems occurred during the first field season and were fixed for the second field season. Others would have required a large expense to fix, but were taken as lessons learned that should be incorporated into future systems.

During the first field season, we had two hardware failures. Both were fixed for the second field season and no further problems were found. The first failure happened during the field calibration: both high-power transmit amplifier switches failed and only one backup was available. Because of this, the system was operated without transmit antenna switching which reduced the cross-track resolution by two. The switches had been tested extensively in the laboratory. When returned to the manufacturer, faulty isolation between the control circuitry and the high power RF path were blamed. A different manufacturer was used for the replacement switches.

The second failure had to do with vibration-induced noise. Later in the laboratory, it was found that the multiplexer and voltage regulators were not properly isolated through the DC bias. We suspect that the multiplexer's biasing was affected by low-frequency signals from the voltage regulator. Insertion of another DC-block capacitor and a 3 dB attenuator fixed the problem. Although not thoroughly tested, we think the vibrations during vehicle movement or upsetting the cables may have occasionally disrupted the DC path which set-off the noise. We suspect that the use of SMA connectors was not a good choice due to the exposure and the weight and size of the low-loss cables. Subsequent analysis of the noise showed that it occurred as spurs in the frequency domain. Fortunately, this allowed for automated suppression of the noise with only moderate degradation of the radar performance. First a detection routine was created which detected the presence of noise spikes and then the offending frequency bins were set to zero. Fig. 6-1 shows a SAR image before and after correction.

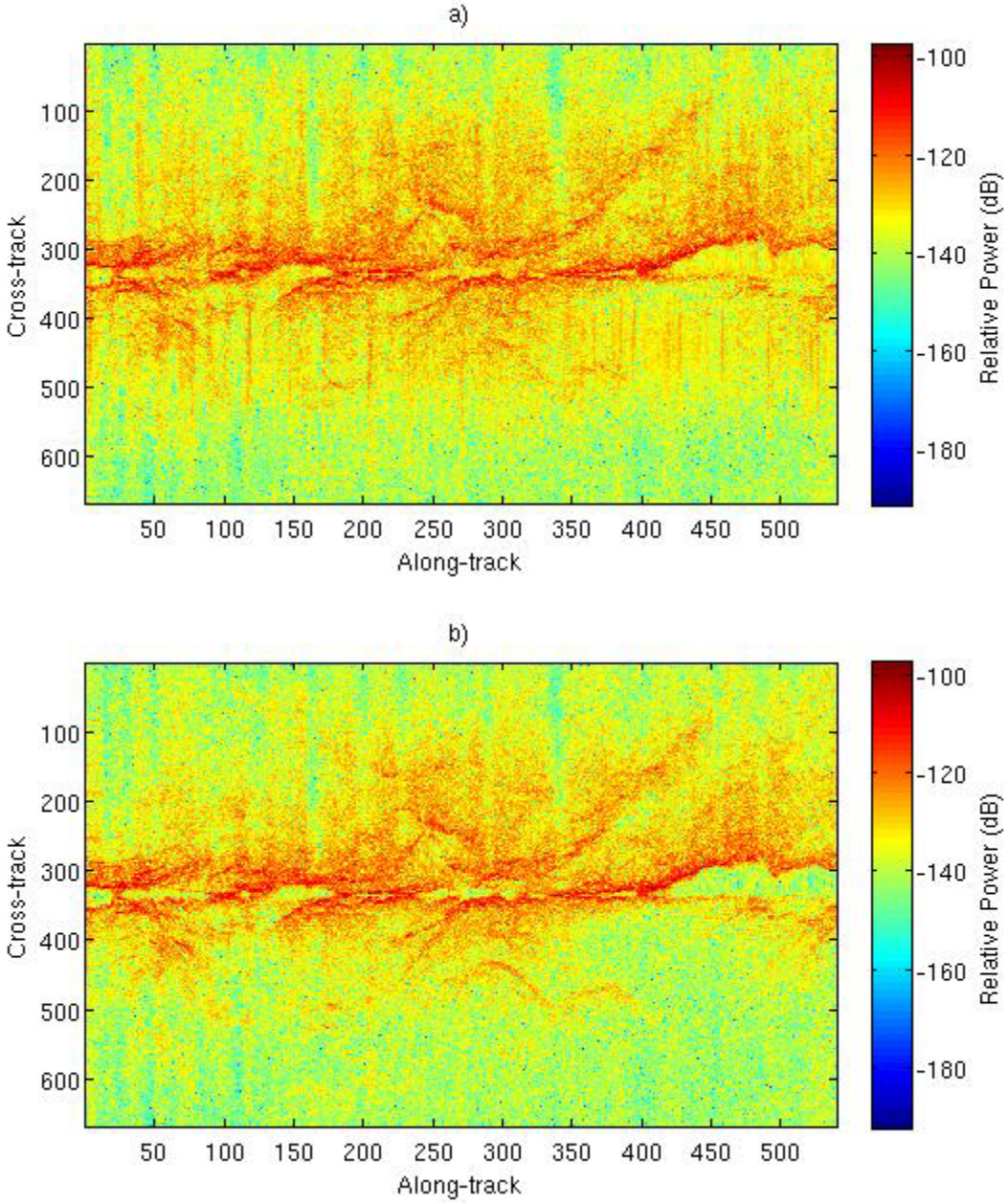

Fig. 7-1. SAR image a) before and b) after removal of noise spurs. The noise spurs show up as bright red vertical lines in a).

During the first field season of the radar system, we ran into electromagnetic interference (EMI) problems with the bistatic measurements due to a small separation between the system and the receive antenna. Even though the radar system is enclosed in a commercial ruggedized EMI box – significant signal power was able to couple into the receive antenna. This was validated in the RF-quiet Sprint anechoic chamber by

operating with the receive antenna and system inside the chamber and with just the antenna in the chamber. With just the antenna in the chamber, the measured noise floor matched the thermal noise floor. With the system and antenna in the chamber, the noise floor was 10 dB higher and contained both coherent and incoherent components. The coherent component is particularly problematic because even with the long-dwell times possible with ground-work, this energy can not be removed unless it is coherent over long periods of time. Given the nature of EMI and the drift in the bistatic receiver's stable local oscillator (STALO) relative to the transmitter's STALO, removal of the noise is a nontrivial task. For future operations, special attention should be paid to unintentional coupling of signal power into the receive antennas. In our case, we simply increased the separation between the receive antenna and the system.

During the second field season, the extreme cold and variations in temperature caused locking issues with the bistatic system. A temperature-stable system would not only solve the bistatic system's problem, but would also provide more accurate results in general. Plus it would alleviate the time-consuming process of checking the phase stability of the high speed data acquisition system before and after measurements every day and the arduous task of trying to keep the cabin-temperature stable during measurements.

All external connectors are SMA. Due to vibrations, the physical size and weight of low-loss cables, and the difficulty of working with small connectors in the cold, all external connectors should be replaced with Type-N connectors. As mentioned in the preceding paragraph, the SMA connectors may have also contributed to the vibration-induced noise spurs. Aside from greatly improved mechanical performance, Type-N connectors can also carry more RF power which would allow the system's power amplifiers to be upgraded without having to replace the antenna feed network.

The post-processed DGPS data had many errors in them. An in-house algorithm was used to partially circumvent these errors, but is a less than satisfactory solution. Limited testing of the DGPS system before the field experiment and in the field before the traverse runs showed no problems. We suspect that the mounting structure for the DGPS antennas may have been responsible for the problems. The antennas were mounted on masts as shown in Fig. 3-18. This mounting technique was problematic because the masts

vibrated constantly during platform movement which may have contributed to problems with the post-processing. This hypothesis has not been tested however and is left as future work. Although possibly cost prohibitive, other manufacturers such as Ashtech may be more appropriate for kinematic work (e.g. the Jet Propulsion Laboratory uses Ashtech).

7.3 COMMON MID-POINT (CMP) MEASUREMENTS

Common mid-point (CMP)[22] measurements on an ice sheet measure scattered energy from a common reflecting layer along different propagation paths as shown in Fig 7-2a. An estimate of velocity and attenuation can be determined by monitoring the behavior of the scattered energy from the layer as a function of the transmitter and receiver baseline. The permittivity of the ice sheet changes continuously with depth, so reflecting horizons at many depths are required to adequately determine the profile. Fortunately, there are detectable layers starting from the air/ice interface down to the bed, which can be used for permittivity calculations. Because ice is a low loss material (i.e. dielectric), the problem of estimating the permittivity can be divided into two separate problems: one of estimating the real permittivity via the velocity [145], [146], [147], [148], [149], [150] and one of estimating the imaginary part by the attenuation [151], [152].

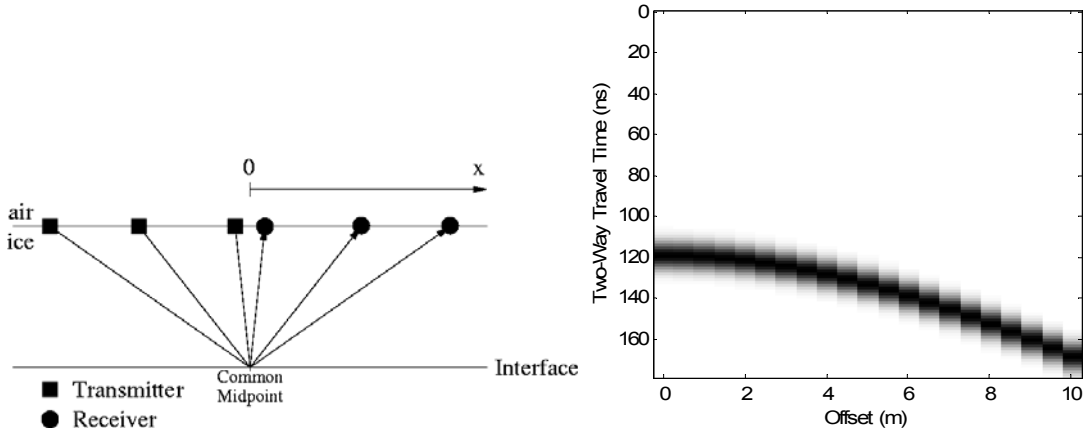

Fig 7-2. a) Illustration of common midpoint geometry. b) Idealized radar dataset using a Gaussian impulse for the transmit waveform with 1 m range resolution, depth to interface of 10 m, and $\sqrt{\varepsilon'} = 1.78$.

[22] Also known as common depth point (CDP) or wide-angle measurements.

7.3.1 VELOCITY

The phase velocity of an electromagnetic wave in a low-loss dielectric such as snow, may be approximated as $v = \frac{c}{\sqrt{\varepsilon'}}$ where c is the speed of light in a vacuum and ε' is the real part of the permittivity of snow. Snow is a mixture of air and ice and the real part of the permittivity is related empirically to the density by $\varepsilon' = (1 + 0.854\Delta)^2$ where Δ is the density of the snow [149], [153]. With a density profile, an accurate time-depth conversion can be made. In the absence of density information, CMP radar measurements provide a way to find the phase velocity needed for time-depth conversions. A simplified view of the situation is shown in Fig 7-2a where the medium is homogeneous. A simulated set of radar data are shown in Fig 7-2b. As the transmitter and receiver's separation is increased, the two-way time to the target's echo increases. The first step in the processing involves finding the normal moveout, which is the additional time-delay incurred by moving the transmitter and receiver apart. For a homogeneous media the two-way time as a function of receiver offset is

$$t(x) = \sqrt{t^2(0) + 4x^2/v^2}$$

where $4x^2/v^2$ is the normal moveout and $t^2(0)$ is the two-way time to the interface at zero offset. This correction is analogous to SAR processing. After the time offsets are processed, a velocity is fit to the normal moveout data (e.g. least squares technique). Future work should involve investigating techniques for converting normal moveout data generated from field measurements into velocity profiles (e.g. [154]).

Density models will be investigated to further improve empirical results from CMP radar measurements through forward modeling techniques. For example, Herron and Langway show that from estimates of mean annual surface temperature in Kelvin, T, accumulation rate in m of water equivalent snow fall per year, A, and surface snow density measurements, Δ_0, we can estimate the density profile at depth z in a region with Herron et al.'s semi-empirical formula [73]

$$\Delta(z) = \begin{cases} \dfrac{\Delta_i Z_0}{1+Z_0} & \Delta(z) < \Delta_c \\ \dfrac{\Delta_i Z_1}{1+Z_1} & \Delta(z) \geq \Delta_c \end{cases}$$

where

$\Delta_i = 0.917\ \mathrm{g \cdot cm^3}$ is the density of pure ice,

$\Delta_c = 0.55\ \mathrm{g \cdot cm^3}$ is the critical density where the form of $\Delta(z)$ changes,

$Z_0 = \exp\left[\Delta_i k_0 z + \ln\{\Delta_0/(\Delta_i - \Delta_0)\}\right]$,

$Z_1 = \exp\left[\Delta_i k_1 z / A^{0.5} + \ln\{\Delta_c/(\Delta_i - \Delta_c)\}\right]$,

$k_0 = 11 \exp\left[\dfrac{-10160\ \mathrm{mol \cdot J^{-1}}}{RT}\right]$,

$k_1 = 575 \exp\left[\dfrac{-21400\ \mathrm{mol \cdot J^{-1}}}{RT}\right]$,

and

$R = 8.314\ \mathrm{J \cdot K^{-1} \cdot mol^{-1}}$ is the universal gas constant.

7.3.2 ATTENUATION

Assuming specular reflections from internal layers, we can use the specular radar equation to model the power received from a layer as a function of radar offset:

$$P_r = \frac{P_t(f) G_t(f, \theta_t, \phi_t) G_r(f, \theta_r, \phi_r) c^2}{64 \pi^3 (f n_{ice} R_t)^2} L_t^2(f, \theta_t, R_t) \left\langle \left| \Gamma_{pp} \right|^2 \right\rangle .$$

Assuming accurate knowledge of the transmit power, gain, and range; the only two unknowns are the dielectric loss and Fresnel reflection coefficient. The reflection coefficient is, however, a weak function of the offset position when the incidence angle is small. To demonstrate this, the power reflection coefficient versus receiver offset from a typical internal layer at 500 m depth is shown in Fig 7-3. Therefore, by monitoring power

returns from various layers in the ice, we can approximate the loss to each layer and then iteratively solve for the loss profile, one layer at a time.

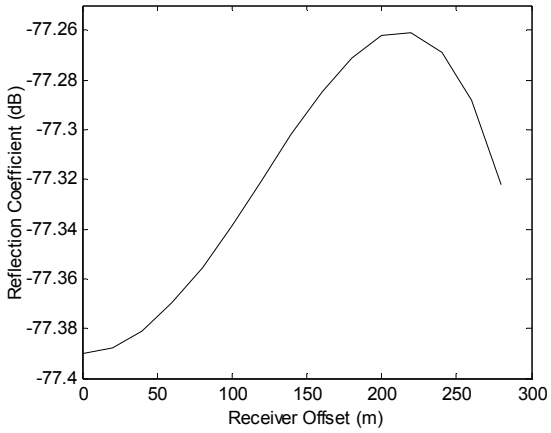

Fig 7-3. Power reflection coefficient versus receiver offset for a 1 m acid layer with a 10 μS increase in conductivity.

7.4 DIGITAL ELEVATION MAP GENERATION FROM SPECTRAL ESTIMATION AND INTERFEROMETRIC SYNTHETIC APERTURE RADAR

As shown in the SAR images and in the mosaic, errors in the digital elevation map cause geometric distortion of the images. The current method for creating the digital elevation map involves a simple magnitude detection process. The multi-channel nature of the data is not currently exploited, but the interferograms formed from the complex migrated images indicate that improved height estimation is possible. Here we show the results of an Eigen-based spectral estimator using the migrated images as the input. The method used is called multiple signal classification or MUSIC [155]. The reason for choosing an Eigen-based approach for spectral estimation is that the problem-at-hand is essentially a direction of arrival problem which Eigen methods are especially well-suited for. Eigen methods work best when the number of sources is small compared to the number of measurements. To ensure this, each channel is separately migrated so that for a given record and range bin, power should only be coming from two directions: the left

side and the right side as shown in Fig. 7-4. This assumes that there is no or very little volume scattering from beneath the ice-bed interface. To improve the results, the spectral estimator is told to find three sources of energy (three sources are found to be sure there are no unexpected sources of energy). Furthermore, we assume that the surface height is not changing abruptly and several records are passed in at a time to improve the estimation process. The results of the spectral estimation are shown in Fig. 7-5. As expected, near the nadir return the music algorithm breaks down to some degree because there are many angles of arrival due to the roughness of the bed. However, as the constant range circle extends outward (i.e. later range bins) the chance for ambiguity decreases and two very distinct lines form in the spectral estimation image. Note that the nearest return is not at zero spatial frequency and that the nadir return (zero spatial frequency) is showing up nearly 30 range bins below the first return. This clearly shows why the SAR images do not always mesh together well in the mosaic. Automating this height estimation process so that a digital elevation map could be produced would likely improve the SAR imaging results significantly.

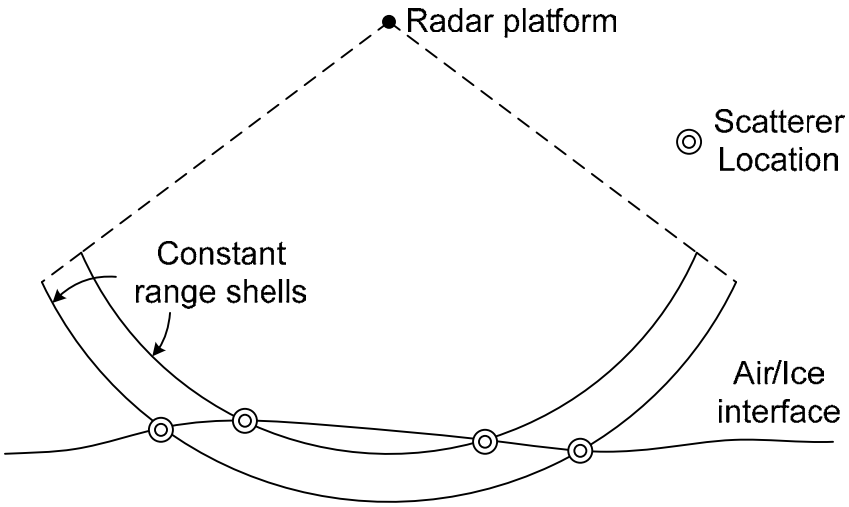

Fig. 7-4. Illustration of directional of arrival problem for surface height estimation. Note that each range shell only includes two sources of scattering.

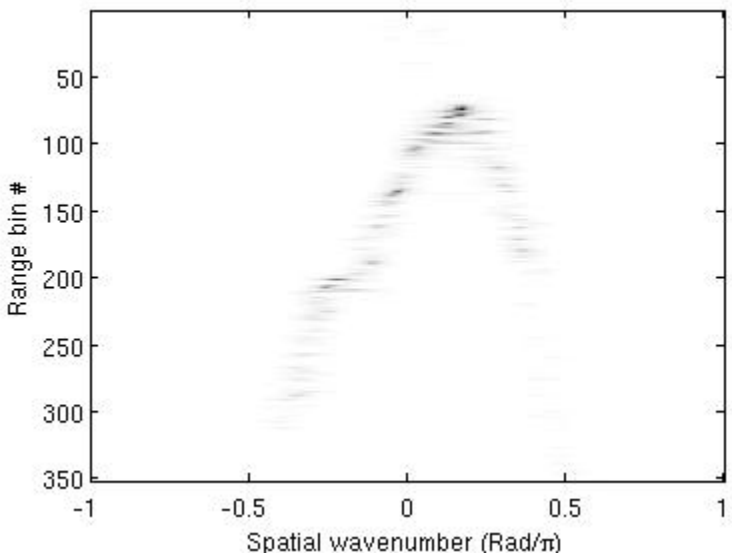

Fig. 7-5. MUSIC spectral estimation results.

7.5 MINIMUM MEAN SQUARED ERROR

The channel combination method used in the SAR processor is simple matched filtering. MMSE channel combining may allow finer resolution than provided by the matched filter "beamwidth" at the cost of increased complexity. The finer resolution would be useful in improving left/right ambiguity especially near nadir where the angular separation between the left and right side is the least. The signal levels near nadir are also the strongest (>30 dB SNR on average as shown in Fig. 6-12). The high SNR should be exploited with MMSE to recover a larger swath are as well as a larger range of incidence angles. The difficulty in exploiting this algorithm will be determining the spatial correlation matrices of the signal and noise without running into self-nulling problems that are inherent to data-dependent methods.

REFERENCES

[1] Douglas, Bruce C., Michael S. Kearney, and Stephen P. Leatherman, *Sea Level Rise: History and Consequences*, International Geophysics Series Vol. 75, Academic Press, San Diego, 2001.

[2] Douglas, Bruce C., and W. Richard Peltier, "The puzzle of global sea-level rise," *Physics Today*, pp. 35-40, March 2002.

[3] IPCC, *Climate Change 2001: The Scientific Basis*, IPCC, Geneva, Switzerland, 2001.

[4] IPCC, *Climate Change 2001: The Scientific Basis*, IPCC, Geneva, Switzerland, 2001, pg 26.

[5] Waggoner, Paul E., *Climate Changes and U.S. Water Resources*, John Wiley and Sons, New York, 1990.

[6] Rignot, Eric and Robert H. Thomas, "Mass Balance of Polar Ice Sheets," *Science*, vol 297, pp. 1502-1506, 30 August 2002.

[7] Terence J. Hughes, *Ice Sheets*, Oxford University Press, New York, 1998.

[8] Houghton, J. T., B. A. Callander, and S. K. Varney. The 1992 IPCC Supplement: Scientific Assessment. In Climate Change 1992: The Supplementary Report to the IPCC Scientific Assessment, Cambridge University Press, Cambridge, England, 1992.

[9] Nesje, Atle and Svein Olaf Dahl, *Glaciers and Environmental Change*, pp 48, Oxford University Press, New York, 2000.

[10] NASA Ocean and Ice Branch, http://neptune.gsfc.nasa.gov/moceansice.html, Chester J. Koblinsky, March 2003.

[11] NASA Earth Science Enterprise, http://www.earth.nasa.gov/visions/researchstrat/Research_Strategy.htm, "Understanding earth system change NASA's Earth science enterprise research strategy for 2000-2010", NASA Earth Systems Science Research Strategy, October 2001.

[12] Van der Veen, Cornelis J., *Fundamentals of Glacier Dynamics*, A. A. Balkema, Rotterdam, Netherlands, 1999.

[13] Krabill, William B., Waleed Abdalati, Earl Frederick, Serdar Manizade, Chreston Martin, John G. Sonntag, Robert N. Swift, Robert H. Thomas, W. Wright, J. Yungel, "Greenland ice sheet: high elevation balance and peripheral thinning," *Science*, vol 289, no 5478, pp. 428-430, 21 July 2000.

[14] Kanagaratnam, Pannir, Silvaprasad Gogineni, Niels Gundestrup, and Lars Larsen, "High-resolution radar mapping of internal layers at the North Greenland Ice Core Project", *Journal of Geophysical Research*, vol 106, no. D24, pp. 33799-33811, Dec 27, 2001.

[15] Gogineni, Silvaprasad, Dilip Tammana, David Braaten, Carl Leuschen, Torry Akins, Justin Legarsky, Pannir Kanagaratnam, Jim Stiles, Christopher T. Allen, and Kenneth C. Jezek, "Coherent radar ice thickness measurement over the Greenland ice sheet", *Journal of Geophysical Research*, vol 106, no. D24, pp. 33761-33772, Dec 27, 2001.

[16] Bamber, Jonathan L., Russell L. Layberry and Silvaprasad Gogineni, "A new ice thickness and bed data set for the Greenland ice sheet, 1. Measurement, data reduction, and errors", *Journal of Geophysical Research*, vol 106, no. D24, pp. 33773-33780, Dec 27, 2001.

[17] Arendt, Anthony A., Keith A. Echelmeyer, William D. Harrison, Craig S. Lingle, and Virginia B. Valentine, "Rapid wastage of Alaska glaciers and their contribution to rising sea level," *Science*, vol 297, pp. 382-386, 19 July 2002.

[18] Bentley, Charles R., N. Lord, C. Liu, "Radar reflections reveal a wet bed beneath stagnant ice stream C and a frozen bed beneath ridge BC, West Antarctica," *Journal of Glaciology*, vol. 44, no. 146, 1998, pp. 149-156.

[19] Gades, Anthony M., Charles F. Raymond, Howard B. Conway, and Robert W. Jacobel, "Bed properties of Siple Dome and adjacent ice streams, West Antarctica, inferred from radio-echo sounding measurements," *Journal of Glaciology*, vol .46, no. 152, 2000, pp. 88-94.

[20] Gades, Anthony M., "Spatial and temporal variations of basal conditions beneath glaciers and ice sheets inferred from radio echo-sounding measurements," Ph. D. Thesis, University of Washington, 1998.

[21] Ohmae, Hirokazu, Fumihiko Nishio, and Shinji Mae, "Distribution of reflected power from the bed by radio echo-sounding in the Shirase Glacier drainage area, East Dronning Maud Land, Antarctica," *Annals of Glaciology*, vol. 12, 1989, pp. 124-126.

[22] Neal, C. S., "The dynamics of the Ross Ice Shelf revealed by radio echo-sounding," *Journal of Glaciology*, vol. 24, no. 90, 1979, pp. 295-307.

[23] Winebrenner, Dale P., Benjamin E. Smith, Ginny A. Catania, Howard B. Conway, Charles F. Raymond, "Radio-frequency attenuation beneath Siple Dome, West Antarctica, from wide-angle and profiling radar observations," *Annals of Glaciology*, vol. 37, 2003, pp. 226-232.

[24] Allen, Chris T., M. Gandhi, Silvaprasad Gogineni, and Kenneth C. Jezek, "Feasibility study for mapping the polar ice bottom topography using interferometric synthetic-aperture radar techniques," RSL Technical Report 11680-1, 1997.

[25] Neal, C. S., "Radio echo determination of basal roughness characteristics on the Ross Ice Shelf," *Annals of Glaciology*, vol. 3, 1982, pp. 216-221.

[26] Oswald, Gordon K. A., "Investigation of sub-ice bedrock characteristics by radio-echo sounding," *Journal of Glaciology*, vol. 15, no. 73, 1975, pp. 75-87.

[27] Peters, Matthew E., Donald D. Blankenship, and David L. Morse, "Analysis techniques for coherent airborne radar sounding: application to West Antarctica ice streams," *Journal of Geophysical Research*, vol. 110, 9 Jun 2005, B06303, doi:10.1029/2004JB003222.

[28] Retzlaff, R., N. Lord, and Charles R. Bentley, "Airborne-radar studies: ice streams A, B, and C, West Antarctica," *Journal of Glaciology*, vol. 39, no. 133, 1993.

[29] Shabtaie, Sion, Ian M. Whillans, Charles R. Bentley, "The morphology of ice streams A, B, and C, West Antarctica, and their environs," *Journal of Geophysical Research*, vol. 92, no. B9, 10 Aug 1987, pp. 8865-8883.

[30] Rose, K. E., "Characteristics of ice flow in Marie Byrd Land, Antarctica," *Journal of Glaciology*, vol. 24, 1979, pp. 63-75.

[31] Englehardt, Hermann, Neil Humphrey, and Barclay Kamb, "Borehole geophysical observations on ice stream B, Antarctica," *Antarctic Journal*, vol. 25, no. 5, 1990, pp. 80-82.

[32] Blankenship, Donald D., Charles R. Bentley, S. T. Rooney, and Richard B. Alley, "Till beneath ice stream B 1. Properties derived from seismic travel times," *Journal of Geophysical Research*, vol. 92, no. B9, Aug 10, 1987, pp. 8903-8911.

[33] Alley, Richard B., Donald D. Blankenship, Charles R. Bentley, and S. T. Rooney, "Deformation of till beneath ice stream B, West Antarctica," *Nature*, vol 322, Jul 3, 1986, pp. 57-59.

[34] Barclay Kamb, "Basal zone of the west Antarctic ice streams and its role in lubrication of their rapid motion," in *The West Antarctic Ice Sheet: Behavior and Environment*, Antarctic Research Series, vol. 77, American Geophysical Union, Washington, D.C., 2001, pp. 157-199.

[35] Paterson, W. S. B., *The Physics of Glaciers*, Third Edition, Butterworth-Heinemann, Jordan Hill, Oxford, 1998, pp. 301.

[36] Fahnestock, Mark, Robert Bindschadler, Ron Kwok, and Ken Charles Jezek, "Greenland ice sheet surface properties and ice dynamics from ERS-1 SAR imagery," *Science*, vol. 262, no. 5139, 3 Dec 1993, pp. 1530-1534.

[37] Joughin, Ian, Laurence Gray, Robert Bindschadler, Stephen Price, David Morse, Christina Hulbe, Karim Mattar, Charles Werner, "Tributaries of West Antarctic ice streams revealed by RADARSAT interferometry," *Science*, vol. 286, no. 5438, 8 Oct 1999, pp. 283-286.

[38] Paterson, W. S. B., *The Physics of Glaciers*, Third Edition, Butterworth-Heinemann, Jordan Hill, Oxford, 1998, pp. 140-2.

[39] Paterson, W. S. B., *The Physics of Glaciers*, Third Edition, Butterworth-Heinemann, Jordan Hill, Oxford, 1998, Chapter 7.

[40] Paterson, W. S. B., *The Physics of Glaciers*, Third Edition, Butterworth-Heinemann, Jordan Hill, Oxford, 1998, pp. 158.

[41] Paterson, W. S. B., *The Physics of Glaciers*, Third Edition, Butterworth-Heinemann, Jordan Hill, Oxford, 1998, pp. 154.

[42] Jezek, Kenneth C., Personal Communication, Oct 1, 2005.

[43] Gogineni, Silvaprasad, "A mobile sensor web for polar ice sheet measurements," NSF Proposal, October 2001.

[44] Schoof, Christian, "Basal perturbations under ice streams: form drag and surface expression," *Journal of Glaciology*, vol. 48, no. 162, 2002, pp. 407-416.

[45] Dahl-Jensen, Dorthe, "Enhanced: The Greenland Ice Sheet Reacts," Science, vol. 289, no. 5478, 21 July 2000, pp. 404-5.

[46] Dahl-Jensen, Dorthe, Niels S. Gundestrup, Siva Prasad Gogineni, Heinz Miller, "Basal melt at NorthGRIP modeled from borehole, ice-core and radio-echo sounder observations," *Annals of Glaciology*, vol. 37, 2003, pp. 207-212.

[47] Englehardt, Hermann and Barclay Kamb, "Basal hydraulic system of a West Antarctica ice stream: constraints from borehole observations," *Journal of Glaciology*, vol 43, no 144, pp 207-229, 1998.

[48] Anandakrishnan, Sridhar, personal communication, Sept 30, 2005.

[49] Anandakrishnan, Sridhar, Richard B. Alley, Robert W. Jacobel, and Howard Conway, "The flow regime of ice stream C and hypothesis concerning its recent stagnation," in *The West Antarctic Ice Sheet: Behavior and Environment*, Antarctic Research Series, vol. 77, American Geophysical Union, Washington, D.C., 2001, pp. 283-294.

[50] Gogineni, Silvaprasad, "Center for Remote Sensing of Ice Sheets," NSF Proposal, October 2004.

[51] Parthasarathy, Rohit, "Fine-resolution radar for near-surface layer mapping," M.S. Thesis, University of Kansas, Aug. 25, 2004.

[52] Clow, Gary D., R. W. Saltus, and E. D. Waddington, "A new high-precision borehole-temperature logging system used at GISP2, Greenland, and Taylor Dome, Antarctica," *Journal of Glaciology*, vol. 42, 1996, pp. 576-584.

[53] Gow, Anthony J. and Debra A. Meese, "Nature of basal debris in the GISP2 and Byrd ice cores and its relevance to bed processes," *Annals of Glaciology*, vol. 22, 1996, pp 134-140.

[54] Harrison, C. H., Radio echo sounding of horizontal layers in ice," *Journal of Glaciology*, vol. 12, no. 66, 1973, pp. 383-397.

[55] Fujita, Shuji, Takeshi Matsuoka, Toshihiro Ishida, Kenichi Matsuoka, and Shinji Mae, "A summary of the complex dielectric permittivity of ice in the megahertz range and its application for radar sounding of polar ice sheets," *Physics of Ice Core Records*, Edited by T. Hondoh, Hokkaido University Press, 2000, Sapporo, pp. 185-212.

[56] E. Wolff, J. Moore, H. Clausen, C. Hammer, J. Kipfstuhl, and K. Fuhrer, "Long-term changes in the acid and salt concentrations of the Greenland Ice Core Project ice core from electrical stratigraphy," *Journal of Geophysical Research*, vol. 100, no. D8, pp. 16249-16263, Aug. 20, 1995. Data archived at the World Data Center for Paleoclimatology, Boulder, Colorado, USA.

[57] J. Bolzan and M. Strobel, "Accumulation-rate variations around Summit, Greenland," *Journal of Glaciology*, vol. 40, pp. 56-66, 1994. Data archived at the World Data Center for Paleoclimatology, Boulder, Colorado, USA.

[58] Twickler, Mark, personal communication, Aug. 30, 2004.

[59] Kanagaratnam, Pannirselvam, "Airborne radar for high-resolution mapping of internal layers in glacial ice to estimate accumulation rate," Ph. D. Thesis, University of Kansas, 2002.

[60] Paden, John D., Christopher T. Allen, Sivaprasad Gogineni, Kenneth Charles Jezek, Dorthe Dahl-Jensen, Lars B. Larsen, "Wideband measurements of ice sheet attenuation and basal scattering," *IEEE Geoscience and Remote Sensing Letters*, vol. 2, no. 2, Apr 2005, pp. 164-168.

[61] Matzler, Christian and Urs Wegmuller, "Dielectric properties of fresh-water ice at microwave frequencies," *Journal of Physics D: Applied Physics*, vol. 20, 1987, pp. 1623-1630.

[62] Matsuoka, Takeshi, Shuji Fujita, and Shinji Mae, "Effect of temperature on dielectric properties of ice in the range 5-39 GHz," *Journal of Applied Physics*, vol. 80, no. 10, 15 Nov 1996, pp. 5884-5890.

[63] Wolff, Eric W., John C. Moore, Henrik B. Clausen, Claus U. Hammer, Josef Kipfstuhl, and Katrin Fuhrer, "Long-term changes in the acid and salt

concentrations of the Greenland Ice Core Project ice core from electrical stratigraphy," *Journal of Geophysical Research*, vol. 100, no. D8, 20 Aug 1995, pp. 16249-16263.

[64] Corr, Hugh F J, John C Moore, and Keith W. Nicholls, "Radar absorption due to impurities in Antarctic ice," *Geophysical Research Letters*, vol. 20, no. 11, pp. 1071-1074, Jun 7, 1993.

[65] Tiuri, Martti E., Ari H. Sihvola, Ebbe G. Nyfors, Martti T. Hallikaiken, "The complex dielectric constant of snow at microwave frequencies," *IEEE Journal of Oceanic Engineering*, vol. OE-9, no. 5, Dec 1984, pp. 377-382.

[66] Berizzi, F., G. Corsini, M. Diani, M. Veltroni, "Autofocus of wide azimuth angle SAR images by contrast optimization," IEEE Conference on Acoustics, Speech, and Signal Processing (ICASSP) , Albequerque, NM, 3-6 Apr 1990, pp. 1230-1232.

[67] Elachi, Charles, *Spaceborne Radar Remote Sensing: Applications and Techniques*, Institute of Electrical and Electronics Engineers, New York, NY, 1988, pp. 144-145.

[68] Green, J. F. and C. J. Oliver, "The limits on autofocus accuracy in SAR," *International Journal of Remote Sensing*, vol. 13, no. 14, 1992, pp. 2623-2641.

[69] Marechal, Nick, "High frequency phase errors in SAR imagery and implications for autofocus," IEEE International Geoscience and Remote Sensing Symposium, IGARSS 96, vol. 2, 27-31 May 1996, pp. 1233-1240, Digital Object Identifier 10.1109/IGARSS.1996.516625.

[70] Monti-Guarnieri, A. and C. Prati, "Autofocusing and residual migration of SAR images," IEEE International Conference on Acoustics, Speech, and Signal Processing (ICASSP), Albequerque, NM, vol. 4, 3-6 Apr 1990, pp. 1953-1956.

[71] Ping, Bai and Chen Zongzhi, "A new synthetic aperture radar autofocusing approach," CIE International Conference of Radar Proceedings, ICR 96, Beijing, China, 8-10 Oct 1996, pp. 326-329.

[72] Rao, M. S. Ranga and P. R. Mahapatra, "Synthetic aperture radar: a focus on current problems," *Defense Science Journal*, vol. 47, no. 4, Oct 1997, pp. 517-536.

[73] Herron, Michael M. and Chester C. Langway, Jr., "Firn densification: an empirical model," *Journal of Glaciology*, vol. 25, no. 93, 1980.

[74] Munk, J., Kenneth Charles Jezek, R. R. Forster, Sivaprasad Gogineni, "An accumulation map for the Greenland dry-snow facies derived from spaceborne radar," *Journal of Geophysical Research*, vol. 108, no. D9, 4280, doi: 10.1029/2002JD002481, 2003, pp. 8-1 – 8-12.

[75] Ohmura, Atsuma and Neils Reeh, "New precipitation and accumulation maps for Greenland," *Journal of Glaciology*, vol. 37, no. 125, 1991, pp. 140-148.

[76] Maule, Cathrine Fox, Michael E. Purucker, Nils Olsen, and Klaus Mosegaard, "Heat flux anomalies in Antarctica revealed by satellite magnetic data," *Science*, vol. 309, 15 Jul 2005, pp. 464-467.

[77] Payne, A. J., "A thermomechanical model of ice flow in West Antarctica," *Climate Dynamics*, vol. 15, 1999, pp. 115-125.

[78] Ulaby, Fawwaz T., Richard K. Moore, and Adrian K. Fung, *Microwave Remote Sensing: Active and Passive, Volume I, Microwave Remote Sensing Fundamentals and Radiometry*, Artech-House, Norwood, MA, 1986, pp. 78-82.

[79] Ruck, George T., Donald E. Barrick, William D. Stuart, Clarence K. Krichbaum, *Radar Cross Section Handbook, Volume 2*, Plenum Publishers, New York, NY, 1970, pp. 479-484.

[80] West, James C. and Kenneth R. Demarest, "The radiation characteristics of an arbitrary antenna positioned on a polar ice sheet," *Geophysics*, vol. 52, no. 12, Dec 1987, pp. 1689-1696.

[81] Robin, G. De Q., S. Evans, J. T. Bailey, "Interpretation of Radio Echo Sounding in Polar Ice Sheets," *Philosophical Transactions of the Royal Society of London. Series A, Mathematical and Physical Sciences*, vol. 265, no. 1166, Dec 18, 1969, pp. 437-505.

[82] Gradshteyn, I. S. and I. M. Ryzhik, *Table of Integrals, Series, and Products, Sixth Edition*, Academic Press, San Diego, CA, 2000, pp. 95,97.

[83] Englehardt, Hermann, Mark Fahnestock, Neil Humphrey, and Barclay Kamb, "Borehole drilling and measurements in ice stream B, Antarctica," *Antarctic Journal*, vol. 24, no. 5, 1989, pp. 83-84.

[84] Gades, Anthony M., “Spatial and temporal variations of basal conditions beneath glaciers and ice sheets inferred from radio echo-sounding measurements,” Ph. D. Thesis, University of Washington, 1998.

[85] Gow, Anthony J., and Debra A. Meese, "Nature of basal debris in the GISP2 and Byrd ice cores and its relevance to bed processes," *Annals of Glaciology*, vol. 22, 1996, pp 134-140.

[86] Hoekstra, P. and A. Delaney, “Dielectric properties of soils at UHF and microwave frequencies,” vol. 79, no. 11, *Journal of Geophysical Research*, 10 Apr 1974, 1699-1708.

[87] Keller, George V., “Electrical properties of rocks and minerals,” Handbook of Physical Constants, The Geological Survey of America Memoir 97, U.S. Geological Survey, 1966.

[88] Olhoeft, Gary R., “Tables of room temperature electrical properties for selected rocks and minerals with dielectric permittivity statistics,” Denver U. S. Department of the Interior, Geological Survey, 1979.

[89] Dielectric Materials and Applications, Edited by Von Hippel, MIT Press, 1954.

[90] Ulaby, Fawwaz T., Richard K. Moore, and Adrian K. Fung, *Microwave Remote Sensing: Active and Passive, Volume I, Microwave Remote Sensing Fundamentals and Radiometry*, Artech-House, Norwood, MA, 1986, pp. 78-82.

[91] Ulaby, Fawwaz T., Richard K. Moore, and Adrian K. Fung, *Microwave Remote Sensing: Active and Passive, Volume III, From Theory to Applicationy*, Artech-House, Norwood, MA, 1986, pp. 2020-2022.

[92] Fung, Adrian K., *Microwave Scattering and Emission Models and Their Applications*, Artech House, Boston, London, 1994, Chapter 2.

[93] Looyenga, H., “Dielectric constant of heterogeneous mixtures,” *Physica*, vol. 21, pp. 401-406, 1965.

[94] Ulaby, Fawwaz T., Richard K. Moore, and Adrian K. Fung, *Microwave Remote Sensing: Active and Passive, Volume II, Radar Remote Sensing and Surface Scattering and Emission Theory*, Artech-House, Norwood, MA, 1986, pp. 457-463.

[95] Jayaraman, Gunashekar, personal communication, Aug 31, 2005.

[96] Moore, Richard K. and C. S. Williams, "Radar terrain return at near-vertical incidence," *Proceedings of IRE*, vol. 45, 1957, pp. 228-238.

[97] Elachi, Charles, Spaceborne *Radar Remote Sensing: Applications and Techniques, Institute of Electrical and Electronics Engineers*, New York, NY, 1988, pp. 187-190.

[98] Harrington, Roger, *Time-harmonic Electromagnetic Fields*, John Wiley and Sons, New York, NY, 2001, pp. 103-106.

[99] Ulaby, Fawwaz T., Richard K. Moore, and Adrian K. Fung, *Microwave Remote Sensing: Active and Passive, Volume II, Radar Remote Sensing and Surface Scattering and Emission Theory*, Artech-House, Norwood, MA, 1986, pp. 951.

[100] Ruck, George T., Donald E. Barrick, William D. Stuart, Clarence K. Krichbaum, *Radar Cross Section Handbook, Volume 2*, Plenum Publishers, New York, NY, 1970, pp. 700-701.

[101] Peebles, Peyton Z., *Radar Principles*, John Wiley and Sons, New York, NY, 1998, pp.64-65.

[102] Olaf Eisen, Frank Wilhelms, Uwe Nixdorf, and Heinrich Miller, "Revealing the nature of radar reflections in ice: DEP-based FDTD forward modeling," *Geophysical Research Letters*, vol. 30, no. 5, 2003, pp. 1218, doi:10.1029/2002GL016403.

[103] Hempel, Ludwig, Franz Thyssen, Niels S. Gundestrup, Henrik B. Clausen, and Heinz Miller, "A comparison of radio-echo sounding data and electrical conductivity of the GRIP ice core," *Journal of Glaciology*, vol. 46, no. 154, 2000, pp. 369-374.

[104] Doake, C S M, Hugh F J Corr, A Jenkins, K W Nicholls and C. Stewart, "Interpretation of polarimetric ice penetrating radar data over Antarctic ice shelves," FRISP Report No. 14, 2003.

[105] Fujita, Shuji, Shinji Mae, and Takeshi Matsuoka, "Dielectric anisotropy in ice Ih at 9.7 GHz," *Annals of Glaciology*, vol. 17, 1993, pp. 276-280.

[106] Fujita, Shuji, and Shinji Mae, "Relation between ice sheet internal reflections and ice fabric at Mizuho Station, Antarctica," *Annals of Glaciology*, vol. 17, 1993, pp. 269-275.

[107] Fujita, Shuji, and Shinji Mae, "Causes and nature of ice-sheet radio-echo internal reflections estimated from the dielectric properties of ice," *Annals of Glaciology*, vol. 20, 1994, pp. 80-86.

[108] Fujita, Shuji, Hideo Meano, Seiho Uratsuka, Teruo Furukawa, Shinji Mae, Yoshiyuki, and Okitsugu Watanabe, "Nature of radio echo layering in the Antarctic ice sheet detected by a two-frequency experiment," *Journal of Geophysical Research*, vol. 104, no. B6, 10 Jun 1999, pp. 13013-13024.

[109] Fujita, Shuji, Kenichi Matsuoka, Hideo Maeno, and Teruo Furukawa, "Scattering of VHF radio waves from within an ice sheet containing the vertical-girdle-type ice fabric and anisotropic reflection boundaries," *Annals of Glaciology*, vol. 37, 2003, pp. 305-316.

[110] Hargreaves, N. D., "The polarization of radio signals in the radio echo sounding of ice sheets," *Journal of Physics D: Applied Physics*, vol. 10, 1977, pp. 1285-1304.

[111] Hargreaves, N. D., "The radio-frequency birefringence of polar ice," *Journal of Glaciology*, vol. 21, no. 85, 1978, pp. 301-313.

[112] Johari, G. P. and S. J. Jones, "The orientation polarization in hexagonal ice parallel and perpendicular to the c-axis," *Journal of Glaciology*, vol. 21, no. 85, 1978, pp. 259-276.

[113] Kawada, Syuji, "Dielectric anisotropy in Ice Ih," *Journal of the Physical Society of Japan*, vol. 44, no. 6, Jun 1978, pp. 1881-1886.

[114] Matsuoka, Takeshi, Shuji Fujita, Shigenori Morishima, and Shinji Mae, "Precise measurements of dielectric anisotropy in ice Ih at 39 GHz," *Journal of Applied Physics*, vol. 81, no. 5, 1 Mar 1997, pp. 2344-2348.

[115] Yoshida, Minoru, Kazunobu Yamashita, and Shinji Mae, "Bottom topography and internal layers in East Dronning Maud Land, East Antarctica, from 179 MHz radio echo-sounding," *Annals of Glaciology*, vol. 9, 1987, pp. 221-224.

[116] Ulaby, Fawwaz T., Richard K. Moore, and Adrian K. Fung, *Microwave Remote Sensing: Active and Passive, Volume I, Microwave Remote Sensing Fundamentals and Radiometry*, Artech-House, Norwood, MA, 1986, chapter 12.

[117] Ruck, George T., Donald E. Barrick, William D. Stuart, Clarence K. Krichbaum, *Radar Cross Section Handbook, Volume 2*, Plenum Publishers, New York, NY, 1970, chapter 9.

[118] Fung, Adrian K., *Microwave Scattering and Emission Models and Their Applications*, Artech House, Boston, London, 1994, Chapter 5.

[119] Musil, George Jiri and C. S. M. Doake, "Imaging subglacial topography by a synthetic aperture radar technique," *Annals of Glaciology*, vol. 9, 1987, pp. 170-175.

[120] Musil, George Jiri, "On the underside scarring of floating ice sheets," *Annals of Glaciology*, vol. 12, 1989, pp. 118-123.

[121] Musil, George Jiri, "Synthetic aperture radar sounding through ice," Ph. D. Thesis, University of Cambridge, December 1985.

[122] Mader, Ralph E., "Synthetic-aperture radar imaging of glacial ice," University of Kansas, M. S. Thesis, 1992.

[123] Hamran, Svein-Erik and Eldar Aarholt, "Glacier study using wavenumber domain synthetic aperture radar," *Radio Science*, vol. 28, no. 4, July-August 1993, pp. 559-570.

[124] Legarsky, Justin J., Siva Prasad Gogineni, and Torry L. Akins, "Focused synthetic aperture radar processing of ice-sounder data collected over the Greenland ice sheet," *IEEE Transactions on Geoscience and Remote Sensing*, vol. 39, no. 10, Oct 2001, pp. 2109-2117.

[125] Leuschen, Carl, Prasad Gogineni, and Dilip Tammana, "SAR Processing of Radar Echo Sounder Data," International Geoscience and Remote Sensing Symposium (IGARSS) 2000 Digest, OOCH37120, Honolulu, July 24-28, 2000, pp. 2570-2572.

[126] Murray, Tavi, Graham W. Stuart, Paul J. Miller, John Woodward, Andrew M. Smith, Philip R. Porter, and Hester Jiskoot, "Glacier surge propagation by thermal evolution at the bed," *Journal of Geophysical Research*, vol. 105, no. B6, 10 Jun 2000, pp. 13491-13507.

[127] Walford, M. E. R. and M. F. L. Harper, "The detailed study of glacier beds using radio-echo techniques," *Geophysics Journal of Radio Astronomy Society*, vol. 67, pp. 487-514, 1981.

[128] Corr, Hugh, personal communication, Sept 30, 2005.

[129] Blankenship, Donald D., personal communication, Sept 30, 2005.

[130] Choi, Hyoungjin and Sangseol Lee, "Design of an exponentially-tapered TEM horn antenna for the wide broadband communication," *Microwave and Optical Technology Letters*, vol. 40, no. 6, Mar 20, 2004, pp. 531-534.

[131] Chung, Kyung-Ho, Sung-Ho Pyun, Chung, S.-Y., Jae-Hoon Choi, "Design of a wideband TEM horn antenna," Antennas and Propagation Society International Symposium, 2003, vol. 1, June 22-27, 2003, pp. 229-232.

[132] Ulaby, Fawwaz T., Richard K. Moore, and Adrian K. Fung, *Microwave Remote Sensing: Active and Passive, Volume II, Radar Remote Sensing and Surface Scattering and Emission Theory*, Artech-House, Norwood, MA, 1986, pp. 569-571.

[133] DeRego, Paul, personal communication, Jul 05, 2005.

[134] Bamler, Richard and Philipp Hart, "Synthetic aperture radar interferometry," *Inverse Problems*, vol. 14, 1998, R1-R54.

[135] Rodriguez, E, and J M Martin, "Theory and design of interferometric synthetic aperture radars," *IEE Proceedings F*, vol. 139, no. 2, Apr 1992, pp. 147-159.

[136] Peebles, Peyton Z., *Radar Principles*, John Wiley and Sons, New York, NY, 1998, pp. 390-396.

[137] Atmel Datasheet, model number TS83102G0B.

[138] Allen, Christopher T., Shadab N. Mozaffar, Torry L. Akins, "Suppressing coherent noise in radar applications with long dwell times," *IEEE Geoscience and Remote Sensing Letters*, vol. 2, no. 3, Jul 2005, pp. 284-286, Digital Object Identifier 10.1109/LGRS.2005.847931.

[139] Dunson, David, "A wideband synthetic aperture radar for ice sheet basal measurements," M.S. Thesis, University of Kansas, May 5, 2006.

[140] Paden, John D., "DGPS Measurements and Post-Processing for Topcon Receivers," CReSIS Technical Report, Aug 2006.

[141] Shampine, L. F., R. C. Allen, Jr., S. Pruess, *Fundamentals of Numerical Computing*, New York, John Wiley and Sons, Inc., 1997.

[142] Gazdag, Jeno and Piero Sguazzero, "Migration of seismic data," *Proceedings of the IEEE*, vol. 72, no. 10, Oct 1984, pp. 1302-1315.

[143] Stolt, R. H., "Migration by Fourier transform," *Geophysics*, vol. 43, no. 1, Feb. 1978, pp. 23-48.

[144] Soumekh, Mehrdad, *Synthetic Aperture Radar Signal Processing with MATLAB Algorithms*, John Wiley and Sons, Inc., New York, NY, 1999.

[145] Jezek, Kenneth Charles and John W. Clough, "Dielectric permittivity of glacier ice measured in situ by radar wide-angle reflection," *Journal of Glaciology*, vol. 21, no. 85, 1978, pp. 315-329.

[146] Macheret, Yu. Ya., M. Yu. Moskalevsky, and E. V. Vasilenko, "Velocity of radio waves in glaciers as an indicator of their hydrothermal state, structure and regime," *Journal of Glaciology*, vol. 39, no. 132, 1993, pp. 373-384.

[147] Popov, Sergey V., Alexander N. Sheremet'yev, Valery N. Masolov, Valery V. Lukin, Anatoliy V. Mironov, and Vadim S. Luchininov, "Velocity of radio-wave propagation in ice at Vostok station, Antarctica," *Journal of Glaciology*, vol. 49, no. 165, 2003, pp. 179-183.

[148] Fisher, Elizabeth, George A. McMechan, and A. Peter Annan, "Acquisition and processing of wide-aperture ground-penetrating radar data," *Geophysics*, vol. 57, no. 3, Mar 1992, pp. 495-504.

[149] Eisen, Olaf, Uwe Nixdorf, Frank Wilhelms, and Heinz Miller, "Electromagnetic wave speed in polar ice: Validation of the CMP technique with high resolution dielectric-profiling and gamma-density measurements," *Annals of Glaciology*, vol. 34, 2002, pp. 150-156.

[150] Hempel, Ludwig, Franz Thyssen, Niels S. Gundestrup, Henrik B. Clausen, and Heinz Miller, "A comparison of radio-echo sounding data and electrical conductivity of the GRIP ice core," *Journal of Glaciology*, vol. 46, no. 154, 2000, pp. 369-374.

[151] Pettersson, Rickard and Robert Jacobel, "Radar wave speed and attenuation studies using constant midpoint profiles on Kamb Ice Stream," West Antarctic Ice Sheet Initiative Twelfth Annual Workshop, Sept, 2005, Poster.

[152] Winebrenner, Dale P., Benjamin E. Smith, Ginny A. Catania, Howard B. Conway, Charles F. Raymond, "Radio-frequency attenuation beneath Siple Dome, West Antarctica, from wide-angle and profiling radar observations," *Annals of Glaciology*, vol. 37, 2003, pp. 226-232.

[153] Kovacs, Austin, Anthony J. Gow, Rexford M. Morey, "The in-situ dielectric constant of polar firn revisited," *Cold Regions Science and Technology*, vol. 23, 1995, pp. 245-256.

[154] Yilmaz, Ozdogan, *Seismic Data Processing*, Investigations in Geophysics, no. 2, Society of Exploration Geophysicists, Tulsa, OK, 1987.

[155] Proakis, John G., Dimitris G. Manolakis, *Digital Signal Processing: Principles, Algorithms, and Applications*, Englewood Cliffs, NJ. : Prentice Hall, 1996.